Ultrasonic Histotripsy for Cell Therapy

by

Ki Joo Pahk

A dissertation submitted for

the degree of Doctor of Philosophy

at University College London

Department of Mechanical Engineering

University College London

Torrington Place

London WC1E 7JE

Declaration

I, Ki Joo Pahk, confirm that the work presented in this thesis is my own. Where information has been derived from other sources, I confirm that this has been indicated in the thesis.

Abstract

Liver transplantation is the mainstay of the treatment for end stage liver diseases including metabolic and congenital liver diseases. The number of suitable donor organs is, however, limited. Intra-portal hepatocytes transplantation has been considered as a bridging therapy to liver transplantation but has shown a mixed clinical outcome with limited success including low level of engraftment of transplanted hepatocytes. To enhance the level of cell engraftment, this thesis introduces an alternative and novel approach to traditional intra-portal cell therapy mediated by High Intensity Focused Ultrasound (HIFU) histotripsy. The proposed novel strategy is to create damage to the recipient liver by producing a number of cavities inside the liver parenchyma through histotripsy and then delivering donor hepatocytes into the cavities. The aim of histotripsy is to mechanically fractionate soft tissue as an alternative to thermal ablation for therapeutic applications. While a number of studies have demonstrated the efficacy of histotripsy for fractionating solid tumours, the exact mechanisms underpinning this phenomenon are poorly understood. The main objectives of this thesis are to (a) investigate the major mechanisms involved in histotripsy and (b) demonstrate the feasibility of the proposed new cell therapy. A high-speed camera with a passive cavitation detection (PCD) system were used to observe the dynamics of bubbles produced in optically transparent tissue phantoms exposed to HIFU fields. Numerical studies on the bubble dynamics and both *ex*- and *in vivo* liver experiments were conducted with histological and serological analyses. Boiling bubbles were generated in a localised super-heated region and cavitation clouds were subsequently induced ahead of the expanding bubble. This process was repeated with HIFU pulses and eventually resulted in a tadpole shaped lesion. The *in vivo* experimental results together with histological observations showed that direct injection of cells inside the cavity facilitated successful uptake, proliferation and integration of the transplanted hepatocytes in the recipient liver. A week after the transplantation, the plasma albumin level was partially restored to 50% of the normal level in Nagase analbuminemic rats (serum albumin level was initially nil) by cell therapy after HIFU histotripsy. This novel method of intra-hepatic hepatocyte transplantation might be an invaluable tool for cell therapy in the future.

Table of Contents

Acknowledgements

First and foremost, I would like to express my sincere gratitude to my supervisor Professor Nader Saffari for his constant support, guidance, assistance, encouragement and enlightened mentorship throughout the duration of this work. It has been an honour and a privilege to work with him over the past six years including my undergraduate and master's years. I have learned and experienced so much both professionally and personally. There are no adequate words to express my appreciation to him.

I would also like to thank Dr. Dipok Kumar Dhar for his help in performing the *in vivo* animal experiments for cell therapy and for his expertise in teaching me histology. I wish to extend my gratitude to Dr. Pierre Gélat (Department of Mechanical Engineering, UCL) for his invaluable guidance and help which greatly improved the quality of this dissertation. Pierre's expertise in acoustic field simulation, especially HIFU scattering by ribs, helped me to interpret the experimental results obtained with a high-speed camera and to gain the improved understanding of the mechanisms involved in HIFU boiling histotripsy. Further thanks go to Dr. Elly Martin (Medical Physics and Biomedical Engineering, UCL) for her time helping with the acoustic characterisation of the HIFU transducer.

Additionally, many thanks to my colleagues at the UCL Ultrasonics Group, including Reza Haqshenas, Christopher Wright and Antonio Gómez, who have encouraged my work and made it such a pleasant research environment.

Last but not least, I would like to thank my beloved parents, Prof. Heui Jae Pahk and Eun Hyun Nam, and brother, Dr. Kisoo Pahk, in Korea for their unlimited and everlasting support and love. Without their support, I could not have had the great opportunity to study at UCL.

List of acronyms

ALT	alanine transaminase
APS	ammonium persulfate
BC	boundary condition
BEM	boundary element method
BH	boiling histotripsy
BHT	bioheat transfer
BSA	bovine serum albumin
CNS	Crigler-Najjar syndrome
dB	decibel
ECM	extracellular matrix
FDA	Food and Drug Administration
FFT	fast Fourier transform
FWHM	full width half maximum
fps	frames per second
HIFU	high intensity focused ultrasound
HT	Herring-Trilling
IC	inertial cavitation
ILD	inherited liver disorder
IVIS	in vivo imaging system
KZK	Khokhlov-Zabolotskaya-Kuznetsov
MR	magnetic resonance
MRI	magnetic resonance imaging
NAR	Nagase analbuminemic rat
NHS	National Health Service
ODE	ordinary differential equation
OLT	orthotopic liver transplantation
PAM	passive cavitation mapping
PBS	phosphate buffered saline
PCD	passive cavitation detector
PD	Parkinson’s disease

PRF	pulse repetition frequency
PVDF	polyvinylidene fluoride
RBC	red blood cell
RF	radiofrequency
RMS	root mean square
RP	Rayleigh-Plesset
SBSL	single bubble sonoluminescence
SC	stable cavitation
SD	standard deviation
SDR	Sprague-Dawley rat
TA	thermal ablation
TEMED	tetramethylethylenediamine
TMM	tissue mimicking material
UDPGT	uridine diphosphate glucuronyltransferase
WF1	waveform 1: sinusoidal waves
WF2	waveform 2: slightly distorted nonlinear waves
WF3	waveform 3: nonlinear-shocked waves

List of symbols

A	first coefficient in Taylor series expansion of the pressure as a function density
A_{m}	medium-dependent empirical constant for pressure-density relation
Ar	argon
A_{s}	shock pressure amplitude
a	decay constant to approximate a lithotripter waveform
a_{a}	constant in ultrasonic attenuation coefficient power law
a_{air}	van der Waals constant of air
a_{h}	initial radius of the heated region
a_{s}	sound source radius
a_{v}	van der Waals constant for attraction between air and water vapour molecules
a_{vap}	van der Waals constant of water vapour
B	second coefficient in Taylor series expansion of the pressure as a function density
B_{m}	medium-dependent empirical constant for pressure-density relation
b_{a}	exponent in ultrasonic attenuation coefficient power law
b_{air}	van der Waals constant of air
b_{v}	van der Waals constant for volume occupied by air and water vapour molecules
b_{vap}	van der Waals constant of water vapour
C	third coefficient in Taylor series expansion of the pressure as a function density
C_{B}	specific heat capacity of blood at constant pressure
C_{T}	specific heat capacity of soft tissue at constant pressure
$C_{v,\mathrm{mix}}$	heat capacity of air-water vapour mixture at constant volume
c	speed of sound
c_0	equilibrium speed of sound
c_L	speed of sound in the surrounding liquid

c_p	specific heat capacity at constant pressure
c_s	concentration of molecules at the bubble wall
c_v	specific heat capacity at constant volume
c_∞	concentration of dissolved gas
$\bar{c}$	average velocity of molecules
D	diffusivity of gas
d_{rc}	radius of curvature of the source
$\dot{E}$	rate of total energy change
f	frequency
f_0	insonation frequency
f_{i}	number of translational and rotational degrees of freedom of gas
G	invariant of the bubble motion
G_f	focal gain
H	enthalpy
H_{heat}	heat source term
H_{linear}	linear heat deposition
H_{shock}	heat deposition by shocks
$\mathrm{H_2O}$	water vapour
h_{i}	molecular enthalpy
I	ultrasonic intensity
I_L	ultrasonic intensity under linear wave propagation
I_N	ultrasonic intensity under nonlinear wave propagation
I_{tot}	total ultrasonic intensity
i	different gas species
i	unit imaginary number
K_{B}	Boltzmann constant
K_{H}	Henry's constant
K_{mix}	thermal diffusivity of air-vapour mixture
k	thermal diffusivity
k_{w}	acoustic wave number
L	nondimensionalisation parameter for length

L_g	characteristic diffusion length
L_{th}	thermal boundary layer thickness
M	nondimensionalisation parameter for mass
MOL	nondimensionalisation parameter for mole
M_{Ar}	molar mass of argon
M_{air}	molar mass of air
M_{O2}	molar mass of oxygen
M_{N2}	molar mass of nitrogen
M_{vap}	molar mass of water vapour
m	medium-dependent empirical constant for pressure-density relation
N	number of molecules
N_A	Avogadro's number
N_{Ar}	number of argon molecules
N_{air}	number of air molecules
N_{N2}	number of nitrogen molecules
N_{O2}	number of oxygen molecules
N_{tot}	total number of molecules
N_{vap}	number of water vapour molecules
$\dot{N}$	the change of number of molecules
N_2	nitrogen
n	number of the characteristic vibrational temperatures of gas
n_0	initial number of moles
n_{Ar}	number of argon moles
n_{air}	number of air moles
nf_0	nth harmonic, where n is a positive integer
n_g	number of non-condensable gas (air) moles
$\dot{n}_g$	change of molar rate of non-condensable gas (air)
n_{N_2}	number of nitrogen moles
n_{O_2}	number of oxygen moles
n_s	number of samples
n_{tot}	total number of moles

n_{vap}	number of water vapour moles
$\dot{n}_{\text{vap}}$	change of molar rate of water vapour
$\dot{n}_{\text{vap}}^{\text{cond}}$	molar rate of condensation of water vapour
$\dot{n}_{\text{vap}}^{\text{evap}}$	molar rate of evaporation of water vapour
$\vec{n}$	unit normal vector on the surface of a HIFU transducer
O_2	oxygen
P	total pressure
P_{elect}	electrical power supplied to a HIFU transducer
P_+	peak positive pressure
P_-	peak negative pressure
p	pressure
p_0	ambient pressure
p_a	acoustic pressure
p_i	pressure in the bubble
p_L	pressure in the surrounding medium at the bubble wall
p_{rad}	radiated pressure
p_v	vapour pressure
p_w	pressure at the bubble wall
p_∞	pressure far from the bubble
$\dot{Q}$	rate of heat transferred to the bubble
R	instantaneous bubble radius
R_0	initial bubble radius
$\dot{R}$	velocity of the bubble wall
$\ddot{R}$	acceleration of the bubble wall
R_{gas}	universal gas constant
R_{max}	maximum bubble radius
R_{min}	minimum bubble radius
r_d	distance away from the centre of a bubble

$\vec{r}$	a position vector
$\vec{r}_0$	position on the surface of a HIFU transducer
S	radiating surface of a HIFU source
s	specific entropy
T	nondimensionalisation parameter for time
T_0	ambient temperature
T_0(K)	ambient temperature in Kelvin
T_T	instantaneous tissue temperature
T_B	arterial blood temperature
T_b	instantaneous bubble temperature
T_{b0}	initial bubble temperature
$\dot{T}_b$	rate of bubble temperature change
T_c	temperature in Celsius
T_s	bubble surface temperature
t	time
t_0	$t = 0$
t_b	time to reach a boiling temperature of 100$^\mathrm{o}$C
t_d	characteristic heat diffusion time
U	average bubble growth rate
u	particle velocity
$\vec{u}$	velocity vector
u_i	molecular internal energy
u_n	normal component of the particle velocity vector
V	bubble volume
V_m	diffusion volume of gas
$\dot{V}$	rate of bubble volume change
$\dot{W}$	work done by the bubble expansion
w_B	perfusion rate of blood
x_sh	distance at which shockwaves form
y	lateral direction with respect to the direction of wave propagation

z	direction of the sound beam propagation
z_l	distance from the sound source.
α	ultrasonic attenuation coefficient
α_0	absorption coefficient at the fundamental ultrasonic frequency f_0
α_a	absorption coefficient
$\alpha_a(f)$	absorption coefficient at a frequency f
α_{air}	constant for temperature dependence of thermal conductivity of air
α_m	accommodation coefficient for evaporation or condensation
α_{vap}	constant for temperature dependence of thermal conductivity of vapour
β	coefficient of nonlinearity
β_{air}	constant for temperature dependence of thermal conductivity of air
β_{vap}	constant for temperature dependence of thermal conductivity of vapour
γ	polytropic index for the filling gas
δ	sound diffusivity
ε	ratio of the particle velocity amplitude at the sound source to the small-signal sound speed c_0
θ	nondimensionalisation parameter for temperature
θ_n	characteristic vibrational temperatures of gas
κ	thermal conductivity of medium
κ_{T}	thermal conductivity of soft tissue
λ_{mix}	temperature and density dependence of thermal conductivity of air-vapour mixture
λ'_{air}	temperature dependence of thermal conductivity of air
λ'_{vap}	temperature dependence of thermal conductivity of water vapour
λ'_{mix}	temperature dependence of thermal conductivity of air-vapour mixture
μ_0	equilibrium viscosity
μ_L	viscosity of the surrounding medium

μ_s	shear viscosity
μ_B	bulk or volume viscosity
v	mixture molar volume
ρ_0	equilibrium mass density
ρ_{T}	density of soft tissue
ρ_{vap}	water vapour density
$\rho_{\mathrm{vap}}^{\mathrm{sat}}$	saturated water vapour density
ρ_L	density of the liquid surrounding the bubble
σ	surface tension at the bubble wall
σ_{sh}	shock parameter
τ	retarded time variable
ω	angular frequency

List of figures

Figure 2.7. An example of a "tadpole" shaped lesion produced by HIFU boiling histotripsy in an *ex vivo* liver. The HIFU beam propagates from left to right.

Figure 2.8. Mechanisms of tissue fractionation involved in boiling histotripsy proposed by Canney *et al* (2010a), Khokhlova *et al* (2011), Simon *et al* (2012) and Wang *et al* (2013). (a) A localised super-heated region by shocks. (b) Formation of a boiling vapour bubble or a vapour cavity at the HIFU focus. (c) Ultrasonic micro-fountains and tissue atomisation. (d) Tissue atomisation together with the streaming of the liquefied tissue within the forming "head".

Figure 3.1. Calculated properties of water (solid line) and of liver (dashed line) as a function of temperature from 20ºC to 100ºC. (a) density, (b) speed of sound, (c) viscosity and (d) surface tension. The blue circles indicate experimental measurements of properties of water as a function of temperature variation. These values were obtained from Haar *et al* (1984) for density, Delgrosso *et al* (1972) for speed of sound, Korson *et al* (1969) for viscosity and Vargaftik *et al* (1983) for surface tension.

Figure 3.2. Comparisons of radius vs time (a,b) and number of vapour molecules (c,d) for SBSL. A single argon-vapour bubble in water was excited by a sinusoidal wave over one acoustic cycle with parameters f_0 = 26.5 kHz, R_0 = 4.5 μm, p_a = 120 kPa and T_0 = 298K as used by Storey and Szeri (2000). (a) and (c) are taken from Storey and Szeri (2000), whereas (b) and (d) are obtained from the present model. The vapour trapping was controlled by setting $\alpha_m = 0.1$.

Figure 3.3. The analytical approximation for the lithotripter pulse with P_+ of 33 MPa and P_- of –11 MPa.

Figure 3.4. Comparison of radius vs time (a,b) and molecular contents (c,d) for a lithotripsy bubble. (a) and (c) are taken from Matula *et al* (2002); while (b) and (d) are obtained with the present model. The present calculations included the same parameters used by Matula *et al* (2002) i.e. a 4.5 μm air-vapour bubble in water at

298K. The peak positive and negative acoustic pressures used in the lithotripter shockwave were P_+ = 33 MPa and P_- = –11 MPa, respectively (see Figure 3.3). The vapour trapping was controlled by setting α_m = 0.15.

Figure 3.5. An example of the piecewise constant approach used in the thesis. R_0, $\dot{R}_0$, $N_{i,0}$ at t_0 are obtained from equation (3.61). Saturated water vapour density, Henry's constants for incondensable gases and the physical properties of liver are calculated using equations (3.41), (3.45) and (3.65)–(3.70), respectively.

Figure 3.6. Illustrating the methods for quantifying IC and SC. (a) Radius vs time curve. (b) Corresponding simulated radiated pressures. The large amplitude short-duration pressure spikes are due to the collapses of bubble. (c) Corresponding FFT plot with the specified windows for IC (within the black solid line) and SC (within the red solid line). Cavitation activity is quantified by integrating the areas under the specified frequency windows and these are cumulated to obtain the "amount" of SC and IC.

Figure 4.1. (a) Sinusoidal (WF1, black solid line, P_+ = 7.5 MPa), slightly distorted nonlinear (WF2, blue solid line, thermal ablation, P_+ = 13.4 MPa, P_- = –7.5 MPa) and nonlinear-shocked (WF3, red solid line, boiling histotripsy, P_+ = 82 MPa, P_- = –15 MPa) waveforms at the HIFU focus with a driving frequency of 1.1 MHz. P_+ and P_- are within the range of required pressure values reported by other boiling histotripsy studies (Khokhlova *et al* 2011, Wang *et al* 2013). (b) Corresponding frequency spectra over 100 acoustic cycles. f_0 is the fundamental frequency.

Figure 4.2. Radius vs time curves at T_0 = 20ºC in the absence of any heat or mass transfer at the bubble wall. (a) resulting from the sinusoidal waves (WF1, black solid line, P_- = –15 MPa) and the nonlinear-shocked waveforms (WF3, red solid line, boiling histotripsy, P_+ = 82 MPa, P_- = –15 MPa at the focus). (b) with the sinusoidal waves (WF1, black solid line, P_- = –7.5 MPa) and the slightly distorted nonlinear waves (WF2, blue solid line, thermal ablation, P_+ = 13.4 MPa, P_- = –7.5 MPa at the focus). The initial radii were 15 μm in the simulations.

Figure 4.3. (a) Simulated acoustic waveforms with σ_{sh} = 5 to 9. (b) Radius vs time curves with σ_{sh} = 5, 7 and 9 over 100 acoustic cycles. The initial bubble radii were 15 μm in the simulations.

Figure 4.4. Dynamics of a 1 μm gas-vapour bubble in the liver at 100ºC with the nonlinear-shocked waveforms (WF3, P_+ = 82 MPa, P_- = –15.1 MPa) over 100 acoustic cycles. (a) Radius vs time curves with (red solid line) and without (blue solid line) heat and mass transfer. (b) Corresponding molecular contents of water vapour and gas of (a). (c) Radius vs time curve without gas diffusion. (d) Corresponding molecular contents of (c). (e) Radius vs time curve without water vapour transport. (f) Corresponding molecular contents of (e).

Figure 4.5. (a) Radius vs time curves with the sinusoidal waves (WF1, P_- = –15 MPa) at temperatures of 95ºC (blue solid line) and 105ºC (red solid line) over 100 acoustic cycles. (b) Corresponding molecular contents of (a) at 105ºC. The initial bubble radii were 1 μm.

Figure 4.6. Dynamics of a 1 μm gas-vapour bubble as a function of temperature variation from 20ºC to 100ºC with ΔT_0 = 10ºC/200 acoustic cycles. Radius vs time curves with (a) the nonlinear-shocked waves (WF3, boiling histotripsy, P_+ = 82 MPa, P_- = –15 MPa) and (b) the slightly distorted nonlinear waveforms (WF2, thermal ablation, P_+ = 13.4 MPa, P_- = –7.5 MPa). The liver properties (density, speed of sound, viscosity and surface tension) that change with temperature were calculated using equations (3.65)–(3.70).

Figure 4.7. Radius vs time curve under the nonlinear-shocked waves (WF3, P_+ = 82 MPa, P_- = –15 MPa) at temperatures of 100ºC, 90ºC, 80ºC and 70ºC.

Figure 4.8. Simulated radiated pressures and spectrograms with the thermal ablation (WF2, slightly distorted nonlinear waveforms, P_+ = 13.4 MPa, P_- = –7.5 MPa) and the boiling histotripsy (WF3, nonlinear-shocked waves, P_+ = 82 MPa, P_- = –15 MPa) exposures. (a) Radiated acoustic pressures during the boiling

histotripsy (WF3, red solid line) and the thermal ablation (WF2, blue solid line) insonations. (b) and (c) are the corresponding spectrograms for the boiling histotripsy and the thermal ablation exposures, respectively. A sampling frequency of 22 GHz was used in the simulations.

Figure 4.9. Corresponding amounts of (a) SC and (b) IC during the boiling histotripsy (red solid line, P_+ = 82 MPa, P_- = –15 MPa) and the thermal ablation (blue solid line, P_+ = 13.4 MPa, P_- = –7.5 MPa) exposures.

Figure 4.10. Corresponding simulated frequency spectra of the radiated pressures plotted in Figure 4.8(a) during the boiling histotripsy (red solid line, P_+ = 82 MPa, P_- = –15 MPa) and the thermal ablation (blue solid line, P_+ = 13.4 MPa, P_- = –7.5 MPa) exposures.

Figure 4.11. Saturated density of water vapour H_2O and gas (Nitrogen N_2 + Oxygen O_2 + Argon Ar) in the liver with temperature. Equations (3.41) and (3.45) were used to calculate the molecular concentrations for water vapour and gas, respectively.

Figure 5.1. HIFU experimental set up used for investigating the generation of tadpole shaped lesions resulting from boiling histotripsy.

Figure 5.2. Experimental setup for the acoustic characterisation of the HIFU transducer.

Figure 5.3. Comparison of (a) axial and (b) lateral focal pressure fields (under linear propagation conditions) measured in water by the needle hydrophone and calculated with the linearised KZK equation.

Figure 5.4. An example of a cross section of a HIFU-induced thermal lesion in the tissue phantom. The HIFU beam propagates from left to right.

Figure 5.5. An example of captured optical images (a) before and (b) during HIFU exposure.

Figure 5.6. Simulated acoustic waveforms and peak temperatures at the HIFU focus in the tissue phantom. (a) Acoustic wavefronts with P_{elect} = 200 W (P_+ = 85.4 MPa, P_- = –15.6 MPa at focus). (b) Corresponding peak temperature. The time to reach a boiling temperature of 100ºC is predicted to be 3.66 ms.

Figure 5.7. Simulated acoustic pressure magnitudes at the HIFU focus using BEM. The contour plots of the incident acoustic pressure (a) without and (b) with a scatterer. The presence of a vapour bubble is indicated by an arrow in (b). The HIFU beam propagates from top to bottom.

Figure 5.8. A sequence of high speed camera images (a), (b), (d)-(h) obtained in an optically transparent tissue phantom during the single 10 ms HIFU insonation with an electrical power of P_{elect} = 200W (P_+ = 85.4 MPa; P_- = –15.6 MPa at the HIFU focus). Images were captured at a 15,000 fps. (c) Simulated temperature contour plot at t = 3.4 ms. The HIFU beam propagates from left to right. The vertical dashed lines indicate the HIFU focus. The time at 0 ms corresponds to the start of the HIFU exposure.

Figure 5.9. Acoustic emission emitted at the HIFU focus in the gel during the single 10 ms HIFU pulse. (a) shows the PCD voltage vs time plot and (b) is the corresponding spectrogram. Acoustic emissions were recorded at a sampling rate of 0.5 GHz. The time at 0 ms represents the start of the HIFU insonation.

Figure 5.10. A series of camera images acquired at 100,000 fps during a single 10 ms HIFU exposure. (a)-(f) are captured high speed images over 4.69 to 4.74 ms (1 frame per 20 acoustic cycles). The HIFU beam propagates from left to right. The red arrow in (b) indicates the formation of a boiling bubble. (g) A comparison between the experimentally measured bubble radius and the simulated radius vs time curve. Photron FASTCAM Viewer (Photron, San Diego, CA, USA) was used

to measure the size of the bubble (24 μm/pixel). The initial bubble radius was chosen as R_0 = 132 μm at a temperature of 100ºC in the bubble simulation.

Figure 5.11. High speed images taken over the course of five HIFU pulses. (a) Images acquisition of the formation of a boiling bubble at the beginning of each HIFU pulse (left column). (b) Images-captured at the end of each pulse (middle column). (c) Corresponding mechanical damage induced in the gel prior to the subsequent arrival of HIFU pulse (right column). The HIFU beam propagates from left to right. The images were captured at the frame rate of 15,000 fps. The vertical dashed lines indicate the HIFU focus.

Figure 5.12. (a)-(e) high speed images taken over the course of 50 HIFU pulses. (f) is the cross-sectioned lesion after the 50^{th} HIFU pulse and (g) is the same lesion as (f) but with an added dye. An acquisition rate of 1000 fps was used. Images on the left and right columns represent bubbles activities at the end of each 10 ms HIFU pulse and the corresponding mechanical damage induced in the gel, respectively. The HIFU beam propagates from left to right. The vertical dashed lines indicate the HIFU focus.

Figure 5.13. Length measurement (mean ± SD) along the *z*-axis (the direction of wave propagation) and the width along the *y*-axis (the lateral direction) of the "head" and of the "tail" as a function of the HIFU pulse exposure. The reference measurement point was at the HIFU focus. Photron FASTCAM Viewer software (Photron, San Diego, CA, USA) was used for the size measurement (24 μm/pixel). Each measurement was repeated five times.

Figure 5.14. An illustration of a shift of the HIFU focus towards the transducer which can occur during boiling histotripsy.

Figure 5.15. Calculated acoustic pressure magnitudes resulting from the scattering of the HIFU field by a boiling bubble. The green arrow indicates the presence of partially shielded acoustic pressure field behind the vapour bubble. The red arrow

shows the backscattered pressures. The HIFU beam propagates from top to bottom. Inset: a captured high speed image showing a cavitation cluster in front of and a secondary boiling bubble behind the primary boiling bubble. This acoustic pressure field was simulated using equation (5).

Figure 5.16. Proposed mechanisms for boiling histotripsy. (a) Shock wave heating. (b) Formation of a primary boiling bubble at the HIFU focus. (c) Rectified growth of a boiling bubble. (d) Production of cavitation clouds (indicated by the green arrow) and secondary boiling bubbles (indicated by the red arrows). (e) Creation of a tadpole-shaped lesion resulting from HIFU boiling histotripsy.

Figure 5.17. The sum of the incident and the backscattered acoustic pressure magnitudes from a vapour bubble with a diameter of (a) 100 μm, (b) 200 μm, (c) 300 μm and (d) 500 μm. The HIFU beam propagates from top to bottom.

Figure 6.1. HIFU experimental set up used for producing thermally and mechanically induced lesions in an *ex vivo* liver.

Figure 6.2. Simulated peak temperatures at the HIFU focus in *ex vivo* liver. (a) Boiling histotripsy exposure with a 1.1 MHz and a 2.0 MHz HIFU transducers. (b) Thermal ablation insonation with a 1.1 MHz HIFU source. The inset in (b) represents the calculated temperature rise over 10 ms.

Figure 6.3. An illustration of a surface marking method used in this Chapter. (a) Two thermal "marker" lesions were produced on the liver surface facing the HIFU transducer in order to specify the lateral position of a histotripsy lesion produced within the sample. (b) After the HIFU experiments, the liver sample was cut along these two markers.

Figure 6.4. A schematic diagram of the *in vivo* HIFU experimental set up used in this Chapter.

Figure 6.5. Testing the *in vivo* HIFU experimental set-up with an *ex vivo* liver sample. (a) Targeting the HIFU beam on the liver surface laterally using a laser pointer. (b) shows the appearance of a "dimple" on the liver surface after the HIFU exposure. (c) The lateral position of the "dimple" on the surface matches that of a laser point. (d) shows a cross-section of a cavity. An electrical power of 200 W, 10 ms pulse length, 1% duty cycle, 1 Hz pulse repetition frequency and 50 HIFU pulses were used.

Figure 6.6. Photographs showing cross-sections of HIFU-induced lesions produced inside an *ex vivo* chicken liver. (a) A mechanically fractionated lesion (a cavity) with the 2.0 MHz HIFU transducer (P_{elect} = 200 W, P_+ = 80 MPa, P_- = –15.6 MPa at the HIFU focus). (b) A cavity produced by the 1.1 MHz HIFU source with P_{elect} = 350 W (P_+= 82.1 MPa, P_- = –15.1 MPa). The HIFU beam propagates from top to bottom. (c) A thermally ablated lesion induced by the 1.1 MHz HIFU source with P_{elect} = 60 W (P_+ = 13.4 MPa, P_- = –7.5 MPa). The HIFU beam propagates from left to right. Images (a), (b), (c)-i and (a), (b), (c)-ii represent the corresponding ultrasound B-mode images before and after the HIFU exposure, respectively. The hyperechoic regions on the B-mode images indicated by the yellow circles in (a), (b), (c)-ii represent the HIFU-induced lesions.

Figure 6.7. Recorded acoustic emissions resulting from cavitation activity at the HIFU focus during the boiling histotripsy and the thermal ablation exposures. (a) and (c) are the raw PCD voltage vs time plots obtained under the boiling histotripsy and the thermal ablation exposure conditions, respectively. (b) and (d) are the corresponding spectrograms. The time at 0 ms corresponds to the start of HIFU insonation.

Figure 6.8. (a) and (b) are the experimentally obtained SC and IC doses under the boiling histotripsy (mean ± SD with n_s = 9) and the thermal ablation (mean ± SD, n_s = 4) exposures, respectively. (c) and (d) are the simulated SC and IC doses. (e) and (f) are the predicted spectrograms under the boiling histotripsy and the thermal ablation excitations, respectively.

Figure 6.9. (a) A freshly created cavity by extracorporeal HIFU (i.e. the liver has not been exteriorised) with an electrical power of 200 W and 50 pulses. (b) Corresponding cross-sectioned lesion. The blue arrows indicate the cavity formation. The HIFU beam propagates from top to bottom.

Figure 6.10. Cross-section of a liver lobe showing freshly created cavity in the exteriorised *in vivo* liver by HIFU. Upper row (a): Cavities produced by 150 W HIFU electrical power and, 5, 10 and 50 pulses, respectively (left to right), lower row (b): Cavities induced with 200 W and, 5, 10 and 50 pulses, respectively (left to right). The HIFU beam propagates from top to bottom. (c) A microscopic view of the highlighted area in (a). The margin of a newly created cavity without any sign of thermal damage is shown. Scale bars in (a) and (b) represent 1 mm.

Figure 6.11. Examples of microscopic views of (a) a normal hepatic parenchyma and (b) a thermally ablated liver parenchyma by HIFU. The yellow arrows indicate blood vessels.

Figure 6.12. (a) Lysed RBCs (yellow arrows) and (b) intact hepatocytes nuclei (blue arrows) inside the cavity. The black arrows indicate cellular debris.

Figure 6.13. Histological examination around a freshly created cavity produced by an electrical power of 200 W (P_+ = 80 MPa, P_- = –15.6 MPa) with 10 HIFU pulses. (a) A photograph showing the cavity creation *in vivo*. The HIFU beam propagates from top to bottom. (b) Corresponding H&E stained lesion. Images (c) to (f) show the highlighted areas in (b) at higher magnifications. Arrows indicate broken hepatocyte plates.

Figure 6.14. (a) CD-31 stained decellularised cavity is shown. (b) shows the highlighted area in (a) at higher magnification (100×). Extracellular matrix in the cavity remained intact and vascular network was stained (brown colour) by anti-CD-31 antibody.

Figure 7.1. A photograph showing the *in vivo* experimental set-up used in this Chapter.

Figure 7.2. A graphical representation of the relationship between the *ex vivo* cavity volume and number of HIFU pulses is shown. The volumes are presented as the means ± standard deviations (SD) with $n_s = 5$. (b) Upper row: cavities produced by 150 W HIFU electrical power and 5, 10 and 50 pulses, respectively (left to right), lower row: cavities generated with 200 W and 5, 10 and 50 pulses, respectively (left to right). Each pulse contains a continuous 10 ms HIFU insonation.

Figure 7.3. (a) Direct injection of primary hepatocytes into a cavity using a 29G needle (0.33 mm in diameter) guided by a laser pointer. (b) A magnified view of the highlighted area in (a).

Figure 7.4. (a) IVIS image of the cavity in a Nagase rat at day 7 after injection of cells is shown. Cells were stained with DiR xenolyte (inset: IVIS image of the explanted liver showing elliptical cavity). (b) Corresponding cross-section of the cavity. (c) IVIS image of (b).

Figure 7.5. IVIS images of the injected cells in the recipient liver (a) at day 3 and (b) day 6. No dispersal of the transplanted cells to different organs is seen.

Figure 7.6. Healed margin with injected hepatocytes inside the cavity (stained with H&E). Red arrows show compressed hepatic plates at the boundary of the cavity and yellow arrows indicate intact blood vessels and bile ducts at the margin (100×). Blue and pink arrows represent transplanted hepatocytes and Matrigel scaffold inside the cavity, respectively.

Figure 7.7. (a) Colonies of DiR and H&E stained hepatocytes inside the cavity at day 7. (b) Proliferating cells stained by Ki-67. (c) The margin of the cavity stained by Ki-67 is shown. Red arrows show strongly positive bi-nucleated cells inside the

cavity. The area within the dashed yellow line indicates the untreated liver parenchyma. Magnification 100×.

Figure 7.8. Growing nascent vascular network in the vicinity of proliferating hepatocytes inside the cavity is shown. The proliferating vascular endothelial cells (i.e. angiogenesis) stained by CD-31 antibody formed lumen like structure (indicated by a black arrow). Magnification 25×.

Figure C.1. A sequence of high speed camera images (a)-(f) obtained in an optically transparent tissue phantom during the single 10 ms HIFU insonation with an electrical power of 200W (P_+ = 85.4 MPa; P_- = –15.6 MPa at the HIFU focus). Images were captured at a 15,000 fps. The HIFU beam propagates from left to right. The time at 0 ms corresponds to the start of the HIFU exposure. The corresponding PCD vs time plot as well as its spectrogram are shown in Figure C.2.

Figure C.2. Acoustic emission emitted at the HIFU focus in the gel during the single 10 ms HIFU pulse. (a) shows the PCD voltage vs time plot and (b) is the corresponding spectrogram. Acoustic emissions were recorded at a sampling rate of 0.5 GHz. The time at 0 ms represents the start of the HIFU insonation.

List of tables

Table 4.4. Physical properties of liver at T_0 = 100ºC used in the bubble model. These values were calculated using equations (3.65)–(3.70) described in Chapter 3. The material dependent constants m, A_m and B_m are shown in Table 4.2.

Table 4.5. The effects of water vapour on the bubble dynamics at a boiling temperature of 100ºC.

Table 4.6. The maximum bubble radius, average bubble growth rate and the number of molecular contents attained by the sinusoidal (WF1, P_- = –15 MPa) and the nonlinear-shocked excitations (WF3, P_+ = 82 MPa, P_- = –15 MPa) over 100 acoustic cycles.

Table 5.1. Composition of 50 mL gel with 7% concentration of BSA. APS = ammonium persulfate. TEMED = tetramethylethylenediamine.

Table 5.2. Properties of tissue phantom used in the acoustic and temperature fields simulations (Khokhlova *et al* 2011).

Table 6.1. HIFU exposure settings used in the *ex vivo* experiments. A continuous 5s HIFU insonation was used for the thermal ablation process whereas the duty cycle, pulse length, pulse repetition frequency and the number of HIFU pulses for the boiling histotripsy were 1%, 10 ms, 1 Hz and 50, respectively. Corresponding computed temperature fields are plotted in Figure 6.2.

Table 6.2. Properties of *ex vivo* liver used in the temperature field simulation. Acoustic properties listed in Table 4.1 in Chapter 4 were used in the acoustic field simulation.

Table 6.3. HIFU exposure conditions used in the *in vivo* experiments. Each HIFU pulse contains a continuous 10 ms HIFU insonation. The KZK equation (3.72) and the BHT equation (3.75) were used to simulate the peak positive and negative pressures at the HIFU focus and the time t_b to reach a boiling temperature of 100ºC

with P_{elect} = 150 W and 200 W. The physical parameters of the *in vivo* liver used in the temperature simulation are displayed in Table 6.4.

Table 6.4. Physical properties of *in vivo* liver used in the temperature simulation. The acoustic properties displayed in Table 4.1 in Chapter 4 were used in the acoustic field simulation.

Table 7.1. HIFU exposure settings used in the *ex vivo* experiments.

Table 7.2. Animals used in the cell therapy experiment. Eleven rats (7 Sprague–Dawley and 4 Nagase rats) were used in this Chapter.

List of publications

**Refereed Journal papers[1]:*

Pahk, K.J., Mohammad, G.H., Malago, M., Saffari, N. and Dhar, D.K. 2016. A novel approach to ultrasound-mediated tissue decellularization and intra-hepatic cell delivery in rats. *Ultrasound in Med. Biol.* **42**(8), pp.1958-1967. doi: 10.1016/j.ultrasmedbio.2016.03.020.

Pahk, K.J., Dhar, D.K., Malago, M. and Saffari, N. 2015. Ultrasonic histotripsy for tissue therapy. *J. Phys. Conf. Ser.* **581**, pp.012001. doi: 10.1088/1742-6596/581/1/012001.

**In Preparation:*

Pahk, K.J. and Saffari, N. 2016. Qualitative and quantitative study of bubble dynamics in high intensity focused ultrasound-mediated boiling histotripsy.

Pahk, K.J., Gélat, P., Sinden, D., Dhar, D.K. and Saffari, N. 2016. Numerical and experimental observation of mechanisms involved in boiling histotripsy.

**Conference Presentations:*

Pahk, K.J., Gélat, P. and Saffari, N. 2016. Formation of a mechanically fractionated lesion in histotripsy. *15th Anglo-French Physical Acoustics Conference (AFPAC2016), 13-15 January, Surrey, UK.*

Pahk, K.J., Dhar, D.K. and Saffari, N. 2015. Intrahepatic cell delivery in Nagase analbuminemic rats with HIFU mediated histotripsy. *3rd European Symposium on Focused Ultrasound Therapy (FUS), 15-16 October, London, UK*.

Pahk, K.J., Dhar, D.K. and Saffari, N. 2015. Ultrasonic histotripsy for cell therapy: an alternative novel method to intraportal hepatocyte transplantation for the treatment of metabolic liver diseases mediated by high-intensity focused ultrasound

[1] Reprints of the papers have been included in Appendix D.

(HIFU). *8th Euro-Korean Conference on Science and Technology (EKC2015), 22-24 July, Strasbourg, France.*

Pahk, K.J., Dhar, D.K. and Saffari, N. 2015. Restoration of serum albumin levels in Nagase analbuminemic rats by intrahepatic cell delivery with HIFU mediated histotripsy. *12th UK Therapy Ultrasound Interest Group (THUGS2015), 22 May, Middlesex, UK.*

Pahk, K.J., Dhar, D.K. and Saffari, N. 2015. Ultrasonic hepatotripsy for cell therapy: a novel approach to treatment of inherited liver disorders. *15th International Society for Therapeutic Ultrasound Conference (ISTU2015), 15-18 April, Utrecht, Netherlands.*

Pahk, K.J., Dhar, D.K. and Saffari, N. 2014. Ultrasonic histotripsy for paediatric liver cell therapy. *13th Anglo-French Physical Acoustics Conference (AFPAC2014), 15-17 January, Surrey, UK.*

**Invited Talks:*

Pahk, K.J. 2015. Cell transplantation in Nagase rats with high intensity focused ultrasound-mediated histotripsy. *Medical Solutions Institute, Sogang University, 2 December, Seoul, Korea. Hosted by Prof. Tai-kyong Song.*

Pahk, K.J. 2015. Restoration of serum albumin levels in Nagase analbuminemic rats by intrahepatic cell delivery with high intensity focused ultrasound. *1288th Research Ground Rounds (RGR1288), Dept. Radiology, Seoul National University Hospital, 24 September, Seoul, Korea. Hosted by Prof. Jae Young Lee.*

Pahk, K.J. 2015. Intrahepatic cell delivery with high intensity focused ultrasound (HIFU) mediated histotripsy. *Dept. Radiology, Samsung Medical Center, Sungkyunkwan University School of Medicine, 22 September, Seoul, Korea. Hosted by Prof. Young-sun Kim.*

Chapter 1. Introduction

1.1. Background

1.1.1. Liver transplantation and cell therapy

Liver transplantation is the mainstay treatment for the advanced stages of chronic and acute liver diseases as well as inherited metabolic liver disorders. The number of patients who can benefit from this treatment is, however, small because of the limited availability of suitable donor organs (Jorns *et al* 2012, Gramignoli *et al* 2015, Bartlett and Newsome 2015). Intra-portal hepatocyte transplantation has been considered as an alternative to liver transplantation, but has shown a mixed clinical outcome with limited success. One of its main limitations is the low level of engraftment of transplanted hepatocytes due to the innate immune reaction, the instant blood-mediated inflammatory reaction and the liver-to-body-weight ratio of the patient, which makes it difficult to achieve extensive proliferation of the transplanted cells (Baccarani *et al* 2005, Johansson *et al* 2005, Stéphenne *et al* 2006, Quaglia *et al* 2008, Dhawan *et al* 2010, Gustafson *et al* 2011, Zhou *et al* 2012, Forbes and Rosenthal 2014).

Cell therapy is much more challenging unless the recipient liver is damaged by iatrogenic methods. Liver irradiation, partial hepatectomy, reperfusion injury and types of noxious chemical agents have been used to increase the level of engraftment of the transplanted hepatocytes. So far, however, the overall clinical outcomes have been mixed, with side effects including radiation-induced liver disease, massive host hepatocyte proliferation, the risk of portal thrombosis and the development of hepatocellular carcinoma (Sigal *et al* 1999, Malhi *et al* 2002, Stéphenne *et al* 2006, Morán-Jiménez *et al* 2008, Fujii *et al* 2010, Turner *et al* 2011, Gramignoli *et al* 2015).

1.1.2. Histotripsy

High Intensity Focused Ultrasound (HIFU) is a non-invasive ablation technique which has been traditionally used to necrose solid tumours without damage to surrounding tissue (ter Haar and Coussios 2007, Al-bataineh *et al* 2012). In recent years, significant interest has been garnered in alternative applications of HIFU. HIFU techniques can be used to mechanically fractionate soft tissue with a high degree of precision (Kieran *et al* 2007, Khokhlova *et al* 2011). This technique is known as tissue fractionation or histotripsy. Histotripsy utilises a number of short ultrasound pulses (of the order of microseconds to milliseconds) with high acoustic pressure amplitudes to mechanically fractionate soft tissue (Hall *et al* 2005). Acoustic peak positive (P_+) and negative (P_-) pressures at the HIFU focus used in histotripsy are comparable to those in the shockwaves used in lithotripsy for kidney stone fragmentation (Zhu *et al* 2002, Pishchalnikov *et al* 2003). A well-defined lesion in the form of a cavity can be produced by histotripsy without any significant thermal damage at the periphery. Recent *in vivo* studies on kidney, prostate, heart and liver have shown that a lesion produced by histotripsy contains complete fragmentation of tissue and is sharply demarcated between treated and untreated regions (Roberts *et al* 2006, Hall *et al* 2008, Hall *et al* 2009, Styn *et al* 2010, Xu *et al* 2010, Vlaisavljevich *et al* 2013, Khokhlova *et al* 2014, Pahk *et al* 2015). Subcellular debris remaining inside a mechanically fractionated lesion can be absorbed as part of the physiologic healing mechanism (phagocytosis), whereas a thermally ablated lesion becomes fibrous scar tissue (Hoogenboom *et al* 2015).

Acoustic cavitation is believed to be one of the main mechanisms for histotripsy. Parsons *et al* (2006) showed that there is a strong correlation between acoustic cavitation and mechanical tissue fractionation. It is, however, unclear how cavitation interacts with tissue fractionation producing a well-defined cavity.

1.2. Proposed cell therapy mediated by histotripsy

To enhance the level of cell integration and proliferation, this thesis introduces an alternative and novel approach to traditional intra-portal cell therapy mediated by HIFU histotripsy, which is shown in Figure 1.1. This proposed novel strategy is to create damage to the recipient liver by producing a number of cavities inside the liver parenchyma through histotripsy and then delivering healthy donor hepatocytes into the cavities. The cavities provide sites for the enhanced engraftment and proliferation of donor cells. Histotripsy can be performed repeatedly to create damage to the liver without the risks associated with currently available alternative iatrogenic methods mentioned in section 1.1.1. Furthermore, in contrast with the intra-portal cell injection approach for cell therapy, the entrapment of the majority of the infused cells in the portal vein (Dhawan *et al* 2010), and the dispersal of the cells to a different organ (Turner *et al* 2013), can be prevented.

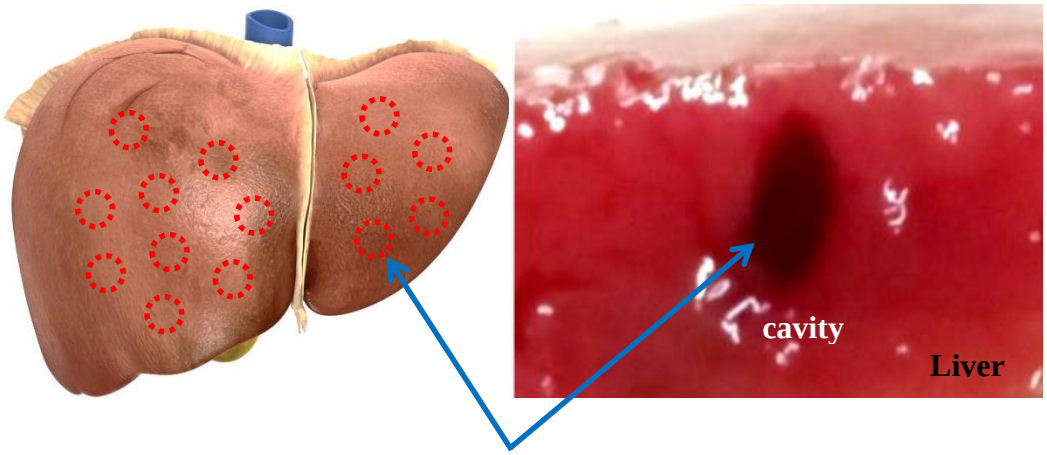

Figure 1.1. Proposed cell therapy mediated by ultrasonic histotripsy. Red circles represent mechanically fractionated lesions (cavities) inside the liver parenchyma in which healthy donor hepatocytes are to be injected.

1.3. Aims and objectives

1.3.1. Statement of problem

Hepatocyte transplantation is a promising alternative to liver transplantation for the treatment for end stage liver diseases including chronic liver diseases, acute liver failure and metabolic liver disorders. Despite its significant clinical benefits, one of the main limitations involved in the transplantation of intra-portal hepatocytes is their low level of integration in the recipient liver (Baccarani *et al* 2005, Stéphenne *et al* 2006, Dhawan *et al* 2010, Forbes and Rosenthal 2014, Bartlett and Newsome 2015). To improve the level of engraftment and proliferation of transplanted cells, this thesis proposes a new cell transplantation method mediated by HIFU histotripsy. This method involves producing a cavity inside the recipient liver by HIFU histotripsy and injecting primary donor hepatocytes into the cavity which acts as suitable hepatocyte receptor and which facilitates the successful uptake, proliferation and integration of the transplanted cells.

It is of important to understand the mechanisms of HIFU histotripsy in order to control as well as to optimise the size of a cavity for the proposed cell therapy. While a number of *in vivo* studies have demonstrated the efficacy of histotripsy for fractionating solid tumours (Roberts *et al* 2006, Hall *et al* 2008, Hall *et al* 2009, Styn *et al* 2010, Xu *et al* 2010, Vlaisavljevich *et al* 2013, Khokhlova *et al* 2014), there has been little research reported on the mechanisms underpinning this phenomenon (Khokhlova *et al* 2011, Simon *et al* 2012, 2015).

This thesis is, therefore, concerned with the investigation of mechanisms involved in histotripsy and the demonstration of feasibility of the proposed hepatocyte transplantation in animal models.

1.3.2. Objectives

The aims of this thesis are to: (a) help provide a better understanding of the mechanisms behind the formation of a mechanically-induced lesion produced by histotripsy and (b) demonstrate the proposed new cell therapy.

The specific objectives are as follows:

- To develop a suitable numerical model describing the dynamics of a single bubble excited by HIFU.

- To validate the bubble model against other published numerical and experimental results.

- To investigate the behaviour of a single bubble in the liver exposed to HIFU histotripsy insonation.

- To evaluate and distinguish between the different types of cavitation activity for either a thermally or a mechanically induced lesion both numerically and experimentally.

- To observe the dynamics of histotripsy bubbles induced in an optically transparent tissue phantom using a high speed camera.

- To produce a mechanically induced lesion in both *ex*- and *in vivo* liver.

- To inject primary hepatocytes into a mechanically fractionated lesion in an *in vivo* liver to (a) demonstrate the proposed intra-hepatic hepatocyte transplantation and (b) examine the viability and functionality of the transplanted hepatocytes.

1.3.3. Thesis outline

Previous work on hepatocyte transplantation and HIFU histotripsy will be reviewed in Chapter 2.

Numerical approaches to modelling the response of a single spherical gas-vapour bubble exposed to HIFU fields will be described and validated in Chapter 3. The bubble model will then be implemented to investigate the dynamics of bubbles induced by HIFU histotripsy exposure. Numerical results will be presented and discussed in Chapter 4.

In Chapter 5, a high-speed camera with a passive cavitation detection (PCD) system will be used to (a) observe the dynamics of bubbles induced in tissue mimicking gel phantoms exposed to HIFU fields and (b) record the corresponding acoustic emissions. Tissue phantoms will be cross-sectioned after HIFU histotripsy exposure for morphological analysis.

For Chapter 6, experiments performed in *ex*- and *in vivo* livers will be described. Acoustic emissions emitted from both thermally and mechanically induced lesions will be recorded using a PCD system. Animals will be euthanised on the same day as the experiment. Upon sacrifice, HIFU exposed liver tissues will be sliced and collected for morphological and histological analyses.

Chapter 7 will describe cell therapy experiments performed on Nagase analbuminemic rats to demonstrate the feasibility of the proposed intra-hepatic hepatocyte transplantation mediated by HIFU histotripsy. Animals will be sacrificed at 96 hours and one week time points. The viability and functionality of transplanted hepatocytes will be investigated with histological and serological examinations.

Finally, the findings and conclusions from this thesis will be addressed with the areas for future work in Chapter 8.

1.4. Statement of contributions

The contributions made in this thesis (which will be detailed in the subsequent chapters) can be divided into two parts: (A) the investigation of the major mechanisms involved in HIFU histotripsy and (B) the demonstration of the high potential of HIFU for improving the outcome of cell therapy in treating metabolic liver diseases. The specific original contributions are as follows:

A) Mechanisms of HIFU histotripsy

- A numerical model describing the dynamics of a single spherical gas-vapour bubble in the liver exposed to HIFU fields as a function of temperature variation has been developed.

- It has been observed that the asymmetry in shockwave and water vapour transport are the key parameters that lead a bubble to undergo rectified growth at a boiling temperature of 100^{o}C. The extent of this explosively growing bubble is spatially confined to the volume defined by the super-heated region.

- It has been shown that the onset of the formation of a boiling bubble at the HIFU focus can be monitored in the course of HIFU histotripsy. This is due to the reflection and inversion of an incident wave from the bubble and due to its highly nonlinear radial oscillation. A significant increase in amplitude of the PCD output and a sudden appearance of higher order multiple harmonic components of the fundamental frequency in the frequency domain, are the indications of a boiling bubble.

- It has been observed that the creation of a “tadpole” shaped lesion by HIFU histotripsy is due to the production of a boiling bubble at the HIFU focus and the generation of a cavitation cluster in front of the bubble towards the HIFU source. It has been suggested that the overall size of a histotripsy-induced lesion is dependent upon the sizes of the super-heated region at the HIFU focus and the backscattered acoustic fields by the original vapour bubble.

- Acoustic emissions emitted during HIFU thermal ablation and HIFU histotripsy exposures have been distinguished both numerically and experimentally. The presence of a shock in an acoustic waveform resulting from histotripsy exposure condition leads to a high degree of nonlinearity in the radial bubble oscillations and violent bubble collapses with larger amplitude short-duration pressure spikes. Therefore, higher order multiple harmonic components with the elevation of broadband emissions appear in the frequency domain during histotripsy exposure compared to those under thermal ablation insonation.

B) Hepatocyte transplantation mediated by HIFU histotripsy

- A novel approach for intra-hepatic cell delivery mediated by HIFU histotripsy has been proposed and its efficacy demonstrated in Nagase analbuminemic rats.

- It has been shown that direct injection of donor hepatocytes inside the cavity can facilitate the successful uptake, proliferation and integration of the transplanted cells in the recipient liver with the prevention of proliferation of native hepatocytes.

- The proposed cell therapy has led to a reversal of liver functional deficiency. A week after the transplantation, the plasma albumin level was partially restored to 50% of the normal level in Nagase rats (serum albumin level of the Nagase rats was initially nil).

- A completely acellular or partially decellularised cavity with intact extracellular matrix and vascular network can be produced by HIFU. HIFU histotripsy can potentially be used as a tissue or cell selective fractionation method.

To summarise the above, this thesis (a) provides a deeper insight into the formation of a mechanically induced lesion by HIFU histotripsy and (b) demonstrates the high potential for the non-invasive use of HIFU in tissue engineering.

Chapter 2. Literature review

The objective of this chapter is to review hepatocyte transplantation and high intensity focused ultrasound-mediated histotripsy to identify area requiring further research. The findings from this Chapter will form the basis of the original contributions of the thesis presented in the subsequent chapters.

2.1. Liver transplantation

Orthotopic liver transplantation (OLT) is currently the mainstay treatment for end-stage liver diseases including inherited liver disorders (ILDs) (Bartlett and Newsome 2015). ILDs are characterised by a deficiency in a hepatic enzyme or protein resulting in life-threatening disease. The first human liver transplantation was performed in 1963 by Starzl *et al* (1963). Three patients with congenital biliary atresia, Laennec's liver cirrhosis and a primary hepatoma, progressive jaundice were treated. Despite the improvement in hepatic function after transplantation, all patients died within three weeks due to gastrointestinal haemorrhage, multiple emboli and respiratory insufficiency. Over the following 15 years, liver transplantation developed slowly, and it was not until the introduction of the immunosuppressant drug cyclosporin A in 1978 that significant progress was made in preventing organ rejection (Calne *et al* 1978, Powles *et al* 1978). Since then, the clinical outcome of OLT has been improved dramatically with improvements in surgical technology, immunosuppression regimens and preservation of donor organs. These advances have led to significant improvements in survival rate. In the UK, patient survival rate is now 81% at 1 year, 68% at 5 years and 57% at 10 years (NHS Blood and Transplant 2015).

Whilst a number of studies have reported promising clinical outcomes with a measureable improvement in the liver function, OLT still requires complex surgery (total hepatectomy) and is costly procedure (Lee *et al* 2004). The NHS (National Health Service) undertook 842 liver transplants in the year 2014–2015 at an average cost of £70,000 each (Benenden National Health Report 2015). Furthermore, organ

donation has not kept up with the demand, leading to increased morbidity and mortality (Strom *et al* 2006, Jorns *et al* 2012, Bartlett and Newsome 2015). There were 566 adult and 45 paediatric patients registered on the UK active transplant list on 31 March 2015. On average, adult patients wait 152 days for a transplant while paediatric patients wait an average of 71 days. At six months-post registration on the active transplant list, 56% of patients had received a transplant, 33% were still waiting, 9% had died and 2% were removed from the list due to their condition deteriorating (NHS Blood and Transplant 2015). In the US, 16,000 patients were registered on the liver transplant waiting list in 2014. Only 35% of them received a transplant due to the organ shortage (Habka *et al* 2015).

2.2. Hepatocyte transplantation

Alternatives to OLT have been sought over the last three decades to overcome the shortage of donor organs, and cell therapy such as hepatocyte transplantation has emerged as a highly effective "bridging therapy" to OLT or even as a curative option in some reported experiments on ILDs (Stéphenne *et al* 2006, Dhawan *et al* 2010, Forbes and Rosenthal 2014, Bartlett and Newsome 2015). Most patients with metabolic liver diseases treated by OLT are caused by hepatocyte dysfunction, and it therefore seems unnecessary to replace the entire liver (Jorns *et al* 2012). The first attempt at hepatocyte transplantation was performed in Gunn rats in the context of liver enzyme replacement therapy in 1976 by Matas *et al* (1976). A sustained decrease of plasma bilirubin concentrations in the animals was observed after the treatment. Gunn rats have a congenital deficiency of uridine diphosphate glucuronyltransferase (UDPGT) enzyme activity and are unable to glucuronidate bilirubin in the bile, resulting in unconjugated hyperbilirubinemia. This animal model is clinically relevant to patients with Crigler–Najjar syndrome (CNS). High concentrations of bilirubin in the blood caused by the deficiency in the UDPGT enzyme can lead to fatal brain injury in infants. In 1990's, the first successful clinical hepatocyte transplantation as a bridge to OLT was performed by Strom *et al* (1997a) and Fox *et al* (1998). Transplanted cells survived more than 11 months and partially corrected genetic defects in liver function. Over the following decades,

more than eight patients with CNS have undergone hepatocyte transplantation to correct hyperbilirubinemia as part of clinical trials (Hughes *et al* 2012, Jorns *et al* 2012). The UDPGT enzyme activity was detected in a liver biopsy with significant reduction in serum bilirubin concentration in the blood over at least several months. All patients, however, underwent OLT four to 20 months later because of loss of the cell engraftment or insufficient improvement in quality of life.

Intra-portal injection is the preferred and most common route for hepatocyte transplantation (Bartlett and Newsome 2015) (see Figure 2.1). Initially, access to the portal vein or artery is accomplished through the liver by percutaneous puncture using a portal catheter. Isolated donor hepatocytes are then injected into the blood stream via this catheter and fill the terminal portal vein radicles. As the portal blood pressure increases transiently, hepatocytes leak into the hepatic sinusoids. Finally, infused hepatocytes are integrated into the recipient liver parenchyma. This integration process takes several weeks (Jorns *et al* 2012). To adequately restore the liver function, delivery of a large number of cells (approximately 5% to 10% of the liver mass or transplantation of 200 to 400 million cells/kg body weight) is necessary over a short period of time and often needs repetition (Grossman *et al* 1994, Strom *et al* 1997a,b, Fox *et al* 1998, Sokal *et al* 2003, Darwish *et al* 2004, Stéphenne *et al* 2006, Lee *et al* 2007, Ribes-Koninckx *et al* 2012, Pless *et al* 2012). It is challenging to effectively deliver such a large number of cells by the intra-portal approach (Baccarani *et al* 2005, Gramignoli *et al* 2015). When the cells are injected into the vascular compartments as shown in Figure 2.1, the liver engraftment efficiency ranges from 5% to 30% depending on the type and size of the cells and the majority of the cells end up in a different organ (Hoppo *et al* 2011, Puppi *et al* 2012). Cell engraftment and retention might increase when they are directly injected into the liver parenchyma (Turner *et al* 2013). A possible mismatch between the cell size and the sinusoidal endothelial pore size, resistance to uptake, integration of injected cells and occurrence of portal venous thrombosis are thought to be possible hurdles (Kocken *et al* 1997). Furthermore, it is difficult to induce extensive proliferation of transplanted cells in the recipient liver. This is due to the

fact that there are normal physiologic mechanisms which tend to keep the total hepatocyte mass constant (Yahya *et al* 2014).

As the liver has the ability to regenerate upon the loss of cell mass, massive repopulation of transplanted cells can be achieved when the recipient liver is damaged by iatrogenic methods. Liver irradiation, partial hepatectomy, reperfusion injury and types of noxious chemical agents have been used to increase the integration of transfused cells with excellent outcomes in reported experiments (Malhi *et al* 2002, Stéphenne *et al* 2006, Morán-Jiménez *et al* 2008, Turner *et al* 2011, Bartlett and Newsome 2015). Hepatic irradiation appears to damage hepatic sinusoidal endothelial cells and restrains the phagocytic function of Kupffer cells, leading to the enhancement of hepatocyte engraftment. Radiation-induced liver disease is, however, a major concern when whole-liver radiation at doses above 30 Gy is used (Malhi *et al* 2002, Dhawan *et al* 2010, Jorns *et al* 2012, Schlachterman *et al* 2015). The removal of large portions (two-thirds) of the recipient liver is a strong proliferation stimulus. Nevertheless, it has been reported that both the host and transplanted donor hepatocytes undergo proliferation to the same level after surgical resection (Sigal *et al* 1999, Gramignoli *et al* 2015). With portal vein embolization-mediated ischemia reperfusion injury, an increase in portal pressure and the risk of portal thrombosis are possible (Jorns *et al* 2012). Administration of noxious chemical agents such as carbon tetrachloride (CCl_4) can lead to liver fibrosis, cirrhosis and hepatocellular carcinoma (Fujii *et al* 2010).

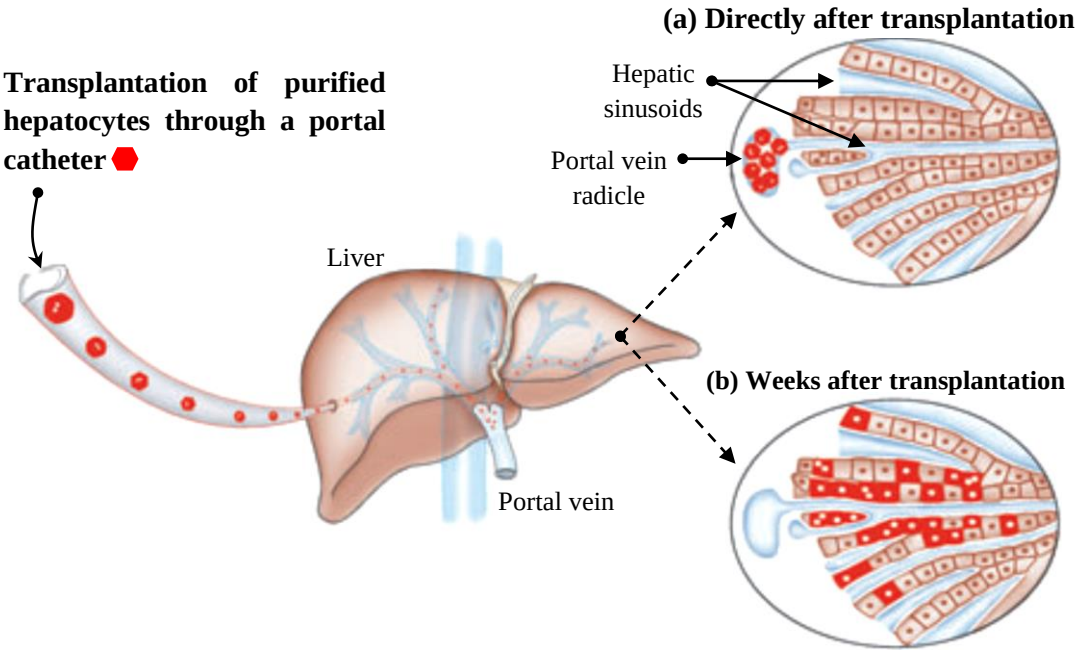

Figure 2.1. The process of intra-portal hepatocyte transplantation. (a) Hepatocytes travel in the blood stream; fill the terminal portal vein radicles, and leak into the hepatic sinusoids. Portal pressure transiently increases. (b) Colonies of hepatocytes have integrated into the liver parenchyma. Figure adapted from Jorns *et al* (2012).

2.3. High Intensity Focused Ultrasound (HIFU)

HIFU is a non-invasive ultrasound technique which has been used to thermally necrose tumours and cauterise blood vessels without disruption to surrounding tissue (Vaezy *et al* 2001, Yu *et al* 2006, ter Haar and Coussios 2007, Dubinsky *et al* 2008, Al-bataineh *et al* 2012, Zhou *et al* 2011, Aubry *et al* 2013). The basic principle behind the use of HIFU involves focusing an ultrasound beam and delivering acoustic energy into a small region of interest within body (see Figure 2.2). This leads to localised heating and protein denaturation, which causes irreversible tissue damage (Dubinsky *et al* 2008). The size and shape of the HIFU focal region is typically an ellipsoid with 2 to 3 mm in lateral width and 8 to 10 mm in axial length (Khokhlova and Hwang 2011).

Diagnostic ultrasound transducers generally deliver weakly focused ultrasound beam with time-averaged intensities of 0.1–100 $mW \cdot cm^{-2}$ and frequencies between

2 MHz and 12 MHz. In contrast, a typical HIFU transducer (spherical single element or multi-element phased-array transducer) operating in the range of 0.5 MHz to 7 MHz delivers a focusing ultrasound field with high local acoustic intensities much greater than 1 $kW \cdot cm^{-2}$ at the HIFU focal region (Dubinsky *et al* 2008, Miller *et al* 2012). Precise targeting and monitoring of HIFU treatments may be carried out with diagnostic ultrasound scanning and magnetic resonance imaging (MRI) systems (Vaezy *et al* 2001, Dubinsky *et al* 2008, Kim *et al* 2008). For instance, a HIFU treatment site generally appears as a bright (echogenic) region on a B-mode ultrasound image during HIFU exposure (Khokhlova *et al* 2006).

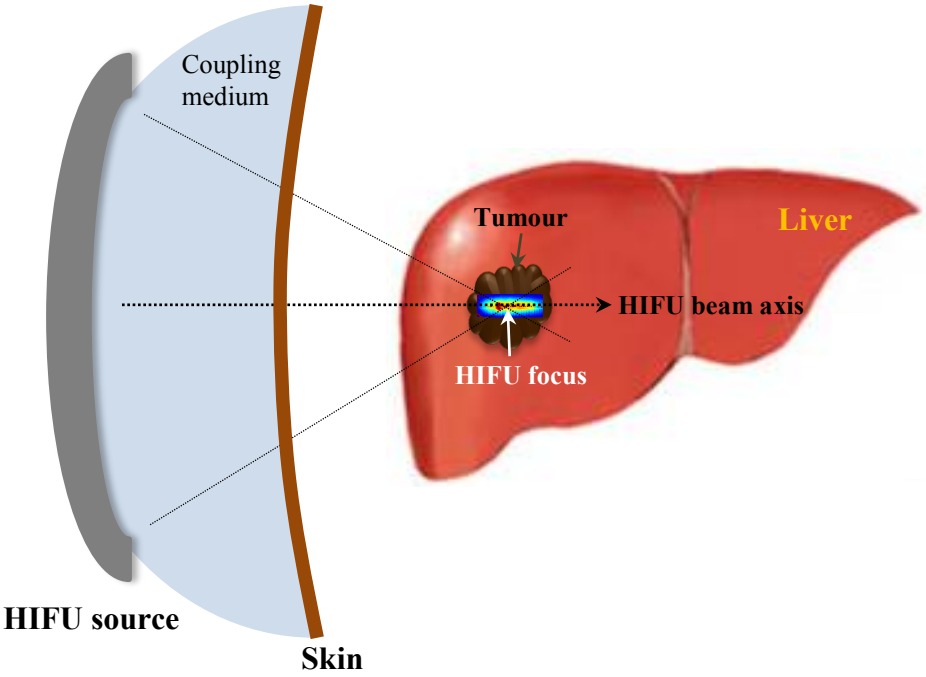

Figure 2.2. A schematic diagram of the principle of HIFU in the liver.

2.3.1. History

Early HIFU studies were performed in animal models in the context of neurosurgery in the 1940s by Lynn *et al* (1942, 1944). These works involved targeting areas in the brain with ultrasound and producing lesions through the intact skull bone. Small lesions were successfully generated in the brain; however, there was severe injury to the scalp due to a high degree of absorption in and reflection

from the skull. Subsequent work carried out by Fry *et al* (1954, 1955) involved concentrating intense ultrasound energy into a target volume through an acoustic window introduced in the skull and demonstrated the feasibility to create discrete lesions deep within the brain. The first HIFU study on humans was reported in 1960 by Fry and Fry (1960). Patients with Parkinson's disease (PD) were treated with HIFU under local anaesthetic. The substantia nigra and ansa lenticularis were exposed to HIFU through the dura mater. After the treatment, it was reported that the symptoms of Parkinsonism were reduced or even eliminated. However, no further work on PD using this technique was performed, probably because of the requirement to surgically remove a part of the skull bone (i.e. a craniotomy) to obtain an acoustic window and also because of the successful clinical trial for the use of the drug Levodopa for PD reported in 1961 (Birkmayer and Hornykiewicz 1961).

Despite some success with ophthalmological HIFU treatments reported by Lizzi *et al* (1978, 1981), the use of HIFU did not gain significant clinical acceptance until the 1990's. This was mainly because of the impracticality of the early HIFU equipment (which was heavy and unwieldy) and because of the lack of technology for monitoring treatment in real-time (ter Haar 1995, ter Haar and Coussios 2007). Development in transducer technology such as the introduction of piezoceramic and piezocomposite transducers has led to the ability to produce high-intensity focused ultrasound beams. Furthermore, advanced phase correction techniques can allow the HIFU focus to be reconstructed following ultrasound beam transmission through the skull (Clement *et al* 2000, Aubry *et al* 2003). The use of a multi-element transducer with independent phase control for each element has shown great promise in overcoming the limitations associated with a single-element transducer such as side lobe production, lack of electronic steering and lack of beam shaping (Gavrilov and Hand 2000, Pernot *et al* 2003). These in conjunction with high spatial and temporal resolution imaging modalities such as MR, have led to the efficacy of HIFU being demonstrated for the treatment of soft tissue tumours in organs. These organs include the liver (Wu *et al* 2004, Illing *et al* 2005, Leslie *et al* 2012), prostate (Sanghvi *et al* 1996, Uddin Ahmed *et al* 2012), kidney (Illing *et al* 2005, Ritchie *et*

al 2010) and breast (ter Haar and Coussios 2007). HIFU has received FDA (Food and Drug Administration) approval for the treatment of uterine fibroids, pain palliation of bone metastases and prostate cancer (Voogt *et al* 2012, Zhou 2015, Food and Drug Administration 2015).

2.3.2. HIFU thermal effects

The primary effect of HIFU in soft tissue is the generation of heat due to absorption of acoustic wave energy when propagating in tissue. Two main mechanisms contribute to the absorption, the viscous friction and the molecular relaxation processes (Pauly and Schwan 1971, Vaezy and Zderic 2009). When an incident acoustic wave propagates through tissue, the pressure fluctuations cause directional motion of tissue, which results in frictional heating. Part of the mechanical energy in the incident ultrasound waves is, therefore, converted into heat (ter Haar and Coussios 2007). Relaxation refers to the finite time required for a medium to reach equilibrium in a new thermodynamic state produced by a change in one or more of the state variables (Landau and Lifshitz 2011). A number of internal processes may contribute to the time required to establish equilibrium. This, for example, includes chemical reaction, phase transition and molecular vibration. Relaxation is accompanied by energy dissipation (Hamilton and Blackstock 2008, Solovchuk *et al* 2015). If the energy stored within the medium is suddenly changed by the propagation of an ultrasonic wave, the excess energy is subsequently redistributed to equilibrium by the relaxation process. This redistribution process is, however, associated with time delays which give rise to changes in the phase of the returned energy. This out-of-phase (phase lag) energy interferes with the acoustic waves, and an additional absorption occurs (Wells 1975).

Pauly and Schwan (1971) showed that the absorption of an ultrasound wave in soft tissue is dominated by the relaxation processes. For example, in the frequency range of 1–10 MHz, about two-thirds of the total absorption arises at the macromolecular level with the remainder caused by thermoviscous effect.

HIFU-induced thermal damage can be achieved by raising and maintaining tissue temperature to or above 55ºC for one second or longer, which can lead to irreversible cell death through coagulative necrosis (Sapareto and Dewey 1984). The majority of heat deposition appears in the HIFU focal volume (Khokhlova and Hwang 2011) with temperatures outside this focus being kept at noncytotoxic levels (ter Haar and Coussios 2007). The volume of necrotised tissue is, thus, spatially confined to the HIFU focus while sparing the overlying and surrounding tissue.

2.3.2.1. Nonlinear heating

In soft tissue, the distortion of an initially harmonic acoustic waveform due to tissue nonlinearity causes enhanced heating. This is because the absorption of ultrasound energy in tissue increases with frequency (Bailey *et al* 2003, ter Haar and Coussios 2007). Nonlinearity arises due to the variation in local particle velocity and nonlinearity of the pressure-density relation. These cause different parts of an acoustic wavefront to propagate at different speeds. The speed of sound c is given by (Hamilton and Blackstock 2008)

$$c = c_0 + \beta u \tag{2.1}$$

c_0 is the small signal sound speed, u is the particle velocity and β is the coefficient of nonlinearity. Higher β leads to stronger nonlinear wave propagation effects (Canney *et al* 2010a). Equation (2.1) implies that the speed of sound under compressive pressure (peak positive pressure) is faster than that for rarefactional pressure phase (peak negative pressure). This leads to the distortion of an acoustic wavefront and transfer of energy from the fundamental frequency towards higher order harmonic components (Wu *et al* 2004) (see Figure 2.3).

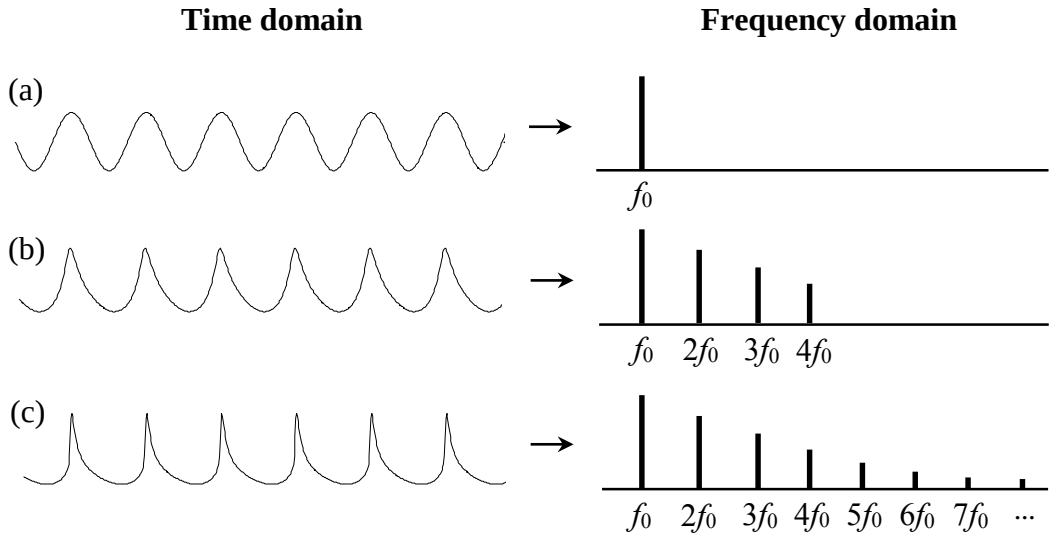

Figure 2.3. Illustration of an example of the distortion of acoustic waves due to the nonlinear wave propagation effects. (a) sinusoidal, (b) slightly distorted and (c) shocked waves in time domain are plotted in left column. The corresponding frequency spectra are shown in right column. f_0 is the fundamental frequency.

Nonlinearity accumulates over the propagation distance and results in the generation of a shocked wavefront which contains multiple higher harmonics in the frequency domain (see Figure 2.3(c)). For an initially harmonic acoustic wave (sinusoidal waveform) with pressure amplitude p, the distance x_{sh} at which shockwaves form is (Maxwell *et al* 2012)

$$x_{\mathrm{sh}} = \frac{\rho_0 c_0^3}{p\beta 2\pi f_0} \tag{2.2}$$

For a sound wave with low pressure amplitude, the x_{sh} is, however, so long that the wave has been absorbed before it can form a shock (Cleveland and McAteer 2007). This is because of a loss of acoustic intensity in the direction of ultrasound propagation due to attenuation (ter Haar and Coussios 2007). Attenuation of ultrasonic waves in soft tissue arises from acoustic absorption and scattering in all directions in the medium. Acoustic scattering refers to that part of an incident acoustic wave which is reflected and/or refracted from interfaces between different tissues due to inhomogeneities in their density and compressibility (Shung and

Thieme 1992, McLaughlan 2008). In the low megahertz frequency range, attenuation in tissue is known to be predominated by absorption whilst the scattering only accounts for 10%–15% of the total attenuation (Duck 1990). For most soft tissue types, the attenuation coefficient α has a power law dependence on frequency f of form (Duck 1990)

$$\alpha = a_{\mathrm{a}} f^{\,b_{\mathrm{a}}} \tag{2.3}$$

a_{a} and b_{a} are medium-dependent constants determined experimentally. The power law exponent b_{a} lies in the range from 1 to 1.5 (Cobbold 2007).

If sufficiently high acoustic pressures are employed, shockwaves can be developed at the HIFU focus where the nonlinear propagation effects are the strongest. In the case of plane harmonic waves for example, heat deposition H_{linear} is proportional to the acoustic pressure amplitude squared (Khokhlova and Hwang 2011), whereas for shockwaves the heating rate H_{shock} is proportional to the shock pressure amplitude cubed using weak shock theory (Hamilton and Blackstock 2008, Canney *et al* 2010a)

$$H_{\mathrm{linear}} = 2\alpha_a I \text{ with } I = \frac{p^2}{2c_0\rho_0} \tag{2.4}$$

$$H_{\mathrm{shock}} = \frac{\beta f_0 A_{\mathrm{s}}^3}{6c_0^4\rho_0^2} \tag{2.5}$$

where α_a is the absorption coefficient in tissue, I is the ultrasonic intensity and A_{s} is the shock pressure amplitude at the HIFU focus. According to the definition in Canney *et al* (2010a), Maxwell *et al* (2012) and Khokhlova *et al* (2015a), the shock amplitude is the pressure amplitude formed between negative and following positive pressure phase with the pressure change within 10 ns at the steepest part in the acoustic waveform (see Figure 2.4).

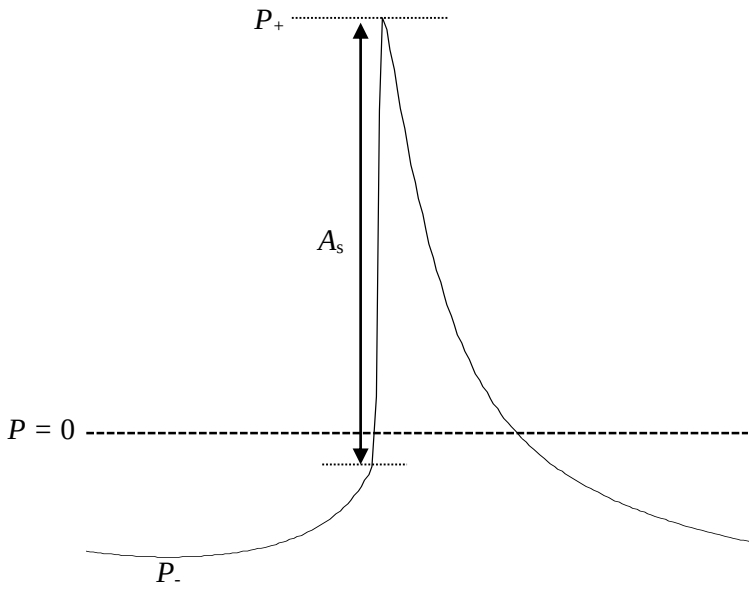

Figure 2.4. Illustration of a shockwave amplitude A_s. P_+ = peak positive pressure, P_- = peak negative pressure at the HIFU focus.

2.3.3. HIFU mechanical effects

Another biological effect, in addition to the production of heat, is HIFU-induced mechanical damage due to acoustic cavitation (Bailey *et al* 2003). When an acoustic wave propagates through tissue with a strong tensile phase (negative pressure), vapour and/or gas that originally dissolved in the medium can be drawn out to form small bubbles. Vapour bubbles may also form from boiling of fluid in blood or tissue due to HIFU-induced temperature rise (Bailey *et al* 2003, Khokhlova *et al* 2006). These bubbles will then oscillate, expand and collapse when they are subjected to sufficiently large acoustic pressures. This is known as acoustic cavitation, and is a threshold effect which depends acoustic pressure, temperature and ultrasound frequency (Neppiras 1984, Leighton 1994, Bailey *et al* 2003).

Acoustic cavitation can generally be divided into two types, stable and inertial. The type of cavitation activity depends on the bubble size compared to the linear resonance size at the insonation frequency f_0 and acoustic pressure amplitudes (Leighton 1994, ter Haar and Coussios 2007). In water, the resonant bubble radius is approximately $3/f_0$ (Akulichev 1971). In the first, a bubble oscillates stably

around its resonant size for the insonation frequency caused by the acoustic pressure fluctuation. This bubble behaviour is referred to as stable cavitation, which consists of both linear and nonlinear radial bubble oscillations (Leighton 1994, Labelle *et al* 2012) (see Figure 2.5(a)). Shear forces produced around this oscillating bubble can mechanically disrupt the cell membrane (Holt and Roy 2001). In the second, inertial cavitation is likely to occur when a bubble whose initial size is about a third of resonant size is exposed to higher acoustic pressure amplitudes (ter Haar and Coussios 2007). A bubble grows rapidly for a few acoustic cycles. This is, however, short-lived: the bubble eventually becomes too large to reverse the direction when the next rarefaction half cycle arrives, eventually leading to bubble collapse (inertial collapse) (see Figure 2.5(b)). This collapse is often due to the loss of sphericity of the bubble as well as the inertia of the inrushing fluid resulting from the change from the negative pressure to the positive pressure (Bailey *et al* 2003). This violent bubble collapse results in high velocity micro jetting emissions (~100 ms^{-1}) and shockwaves around the bubble, which can also destroy the cell membrane (Tezel and Mitragotri 2003, Schlicher *et al* 2010).

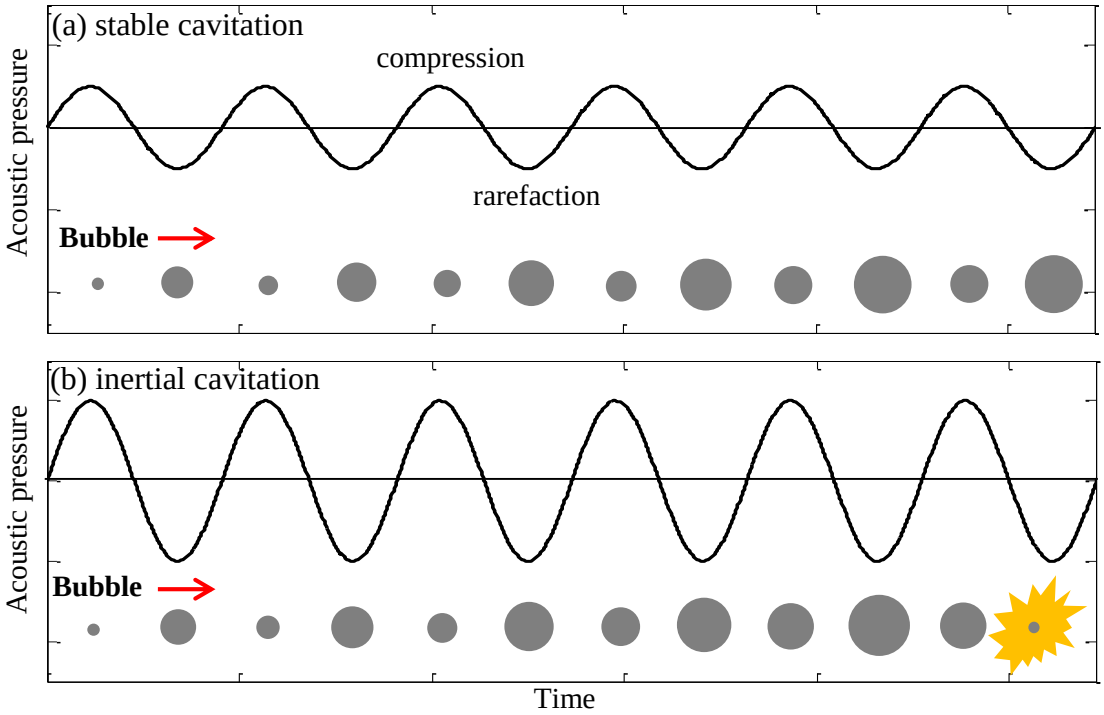

Figure 2.5. Illustration of (a) stable and (b) inertial cavitation.

In the context of HIFU thermal ablation, the presence of cavitation, especially boiling bubbles, in the HIFU focal region is highly undesirable because strong scattering and reflections of incident HIFU waves from the bubbles can promote prefocal (near-field) heating. This eventually leads to the growth of a thermally ablated lesion towards a HIFU transducer, resulting in the lesion shape distortion from a symmetric "cigar" shape to a "tadpole" shape (Watkin *et al* 1996, Bailey *et al* 2003, Chen *et al* 2003a, Khokhlova *et al* 2006, Coussios and Roy 2008).

2.4. HIFU Histotripsy

Recent studies have shown significant interest in exploring the use of HIFU to produce a mechanically fractionated lesion without causing coagulative necrosis. This technique is known as histotripsy and is highlighted in Chapter 1. In histotripsy, there are two different methods of creating purely mechanical damage of soft tissue by (a) pulsed ultrasound cavitation or (b) shock wave heating and millisecond boiling (Parsons *et al* 2006, Canney *et al* 2010a,b, Maxwell *et al* 2011, Khokhlova *et al* 2011, 2014, Khokhlova *et al* 2015a). In both methods, acoustic cavitation is believed to be one of the main mechanisms for inducing mechanical tissue fractionation (Khokhlova *et al* 2015a).

2.4.1. Cavitation cloud histotripsy

The periodical formation of an inertial cavitation cloud at the HIFU focus can mechanically fractionate tissue to a subcellular level (Allen and Hall 2015). This is known as cavitation cloud histotripsy. A number of *in vivo* studies on kidney, prostate, heart and liver (Lake *et al* 2008a, Hall *et al* 2009, Schade *et al* 2012a,b, Vlaisavljevich *et al* 2013) have shown that the boundary of a lesion created by cavitation cloud histotripsy is sharply demarcated between treated and untreated regions. This technique uses microsecond-long HIFU pulses with driving frequencies of 0.75 MHz to 1.0 MHz and high peak positive ($P_+ > 80$ MPa) and negative ($P_- = 15–25$ MPa) pressures at the HIFU focus (Parsons *et al* 2006). Three

to twenty acoustic cycles are delivered in a single HIFU pulse with the pulse repetition frequency (PRF) of 10 Hz to 1 kHz. A low duty cycle (less than 1%) is used to prevent an accumulation of heat at the HIFU focus (Maxwell *et al* 2012, Khokhlova *et al* 2015a).

One of the possible mechanisms for the production of bubble clouds at the HIFU focus is thought to be the reflection and inversion of shockwaves from a single cavitating bubble (Maxwell *et al* 2011). This is known as the shock scattering effect, which is illustrated in Figure 2.6. Maxwell *et al* (2011) used high speed photography to investigate the effects of shockwaves on the production of cavitation clouds in a gelatine based tissue mimicking phantom. The authors observed two distinct types of acoustic cavitation activity. During the initial acoustic cycles, a single bubble was produced and grown; later, cavitation clouds were generated in front of this bubble towards the HIFU transducer. They speculated that the reflection and inversion of the peak positive pressure from the surface of the bubble interfaced with the incoming incident rarefactional phase, and eventually produced a greater peak negative pressure field. As a result, it induced a cavitation cluster. Likewise, the next incident acoustic waves were backscattered from the first cavitation clouds and this process was repeated. Because a pressure threshold for cavitation clouds (i.e. the lowest rarefaction pressure at which a cavitation cluster is almost certain to occur) is –28 MPa for most soft tissues (Maxwell *et al* 2013, Lin *et al* 2014), the site of bubble clouds is spatially confined to the HIFU focus. This is a distinct advantage of cavitation cloud histotripsy as the HIFU focal volume is the only region which is mechanically ablated (Maxwell *et al* 2012).

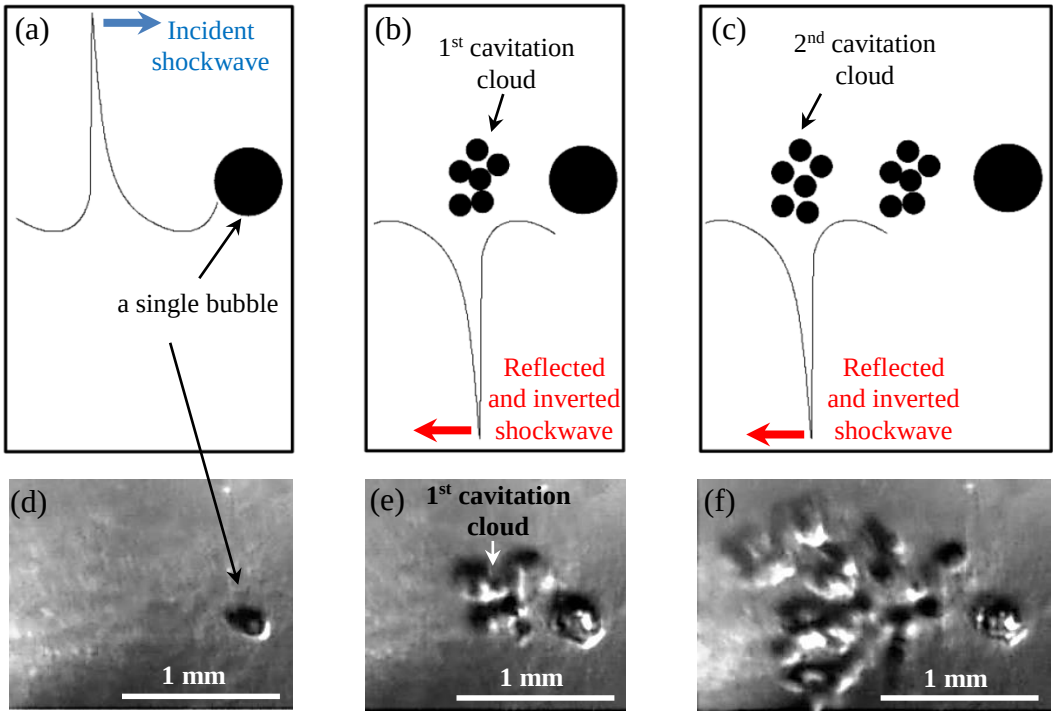

Figure 2.6. Illustration of the production of a bubble cloud during cavitation cloud histotripsy. (a) The interaction of an incident shockwave with a single cavitating bubble. (b) The reflected and inverted shockwave from the bubble producing a cavitation cluster. (c) The backscattered shockwave from the first cloud inducing another bubble clouds. (d)–(f) are a series of high speed images taken in an optically transparent tissue phantom showing an example for the production of bubble clouds towards the HIFU source. The HIFU beam propagates from left to right.

For trans-costal HIFU treatments, the presence of ribs presents additional challenges. In addition to reducing the acoustic window, ribs highly absorb and reflect ultrasound strongly. This can result in significant reduction of acoustic peak pressures at the HIFU focus and can also increase the magnitude of side lobes (Bobkova *et al* 2010, Khokhlova *et al* 2010, Gélat *et al* 2011, 2012). Furthermore, the overheating of bone and surrounding tissue can lead to skin burns and subcostal oedema (Wu *et al* 2004, Illing *et al* 2005, Jung *et al* 2011). Vlaisavljevich *et al* (2013) and Kim *et al* (2011, 2014) demonstrated the feasibility to produce a number of histotripsy lesions in an *in vivo* porcine liver through the intact ribs with no damage to the ribcage or other overlying tissues. This was achieved by generating appropriate acoustic pressure amplitudes where the focal peak negative pressure amplitude was above the cavitation clouds' threshold whilst the side lobes pressures

were not (Kim *et al* 2011, 2014). Additionally, potential thermal damage to the overlying and surrounding tissue or ribs was prevented by employing a low duty cycle of 0.13%. During their experiments, the maximum temperature measured on the ribs with needle thermocouples was 35.3^{o}C, which was below the body temperature (36–37^{o}C).

2.4.1.1. Limitations

Although cavitation cloud histotripsy has been shown to be a promising HIFU technique to mechanically fractionate tissue, one of its drawbacks is that the formation of cavitation clouds is a probabilistic event, due to the stochastic nature of cavitation activity which depends upon the location and number of pre-existing bubble nuclei within soft tissue (Khokhlova *et al* 2011, Maxwell *et al* 2011). Therefore, cavitation activity can stop unexpectedly during HIFU exposure (Khokhlova *et al* 2011). Moreover, very large and highly focused HIFU transducers (*f*-number < 0.8) driven by an extremely high radio frequency power amplifier (of the order of several kilowatts) are generally required to achieve high focal peak negative pressures for producing and maintaining the bubble clouds (Khokhlova *et al* 2014).

2.4.2. Boiling histotripsy

An alternative to cavitation cloud histotripsy has been proposed and its efficacy demonstrated (Canney *et al* 2010a, Khokhlova *et al* 2011). This is known as boiling histotripsy, which utilises shock wave heating to produce a boiling vapour bubble (as opposed to cavitation clouds) and fractionate bulk tissue with a number of millisecond HIFU pulses. In this method, peak positive and negative pressures of $P_+ > 40$ MPa and $P_- < 10$–15 MPa are produced at the HIFU focus with driving frequencies between 1 MHz and 3 MHz and a PRF of 0.5–1 Hz.

In contrast to cavitation cloud histotripsy, boiling histotripsy requires significantly less power (of the order of hundreds of watts) and the requirements on the size,

focusing gain (*f*-number ~ 1) and frequency of the HIFU source are less restrictive. Therefore, commercially available HIFU systems can be implemented to perform boiling histotripsy (Maxwell *et al* 2012, Kreider *et al* 2013, Khokhlova *et al* 2014).

Boiling histotripsy has been demonstrated in *ex vivo* bovine liver (Khokhlova *et al* 2011, Wang *et al* 2013), heart (Wang *et al* 2013), kidney (Schade *et al* 2014) and *in vivo* porcine and rat liver (Khokhlova *et al* 2014, Pahk *et al* 2015). These studies have shown that boiling histotripsy can induce similar lesions to those generated by cavitation cloud histotripsy with no evidence of coagulative necrosis. Although transcutaneous application of boiling histotripsy in liver has yet to be achieved (Khokhlova *et al* 2015a), overheating of the ribs and skin burns can also be prevented by applying a low duty cycle (Khokhlova *et al* 2011, 2014).

In general, the shape of a lesion produced by boiling histotripsy is tadpole like, consisting of a "head" and a "tail" with the "head" closest to the HIFU source (Khokhlova and Hwang 2011). An example of a lesion induced by boiling histotripsy is shown in Figure 2.7. Mechanisms involved in boiling histotripsy are currently being investigated by workers such as Canney *et al* (2010a), Kreider *et al* (2011a), Khokhlova *et al* (2011), Simon *et al* (2012) and Wang *et al* (2013). A schematic diagram of the possible mechanism is shown in Figure 2.8. Canney *et al* (2010a) demonstrated that localised super-heating by shockwaves at the HIFU focus can raise tissue temperature to 100^{o}C in a few milliseconds followed by the formation of a boiling vapour bubble. This bubble then grows to millimetre size, which may tear off tissue due to shear stress produced around the oscillating bubble (Khokhlova *et al* 2011). The growth of this millimetre-sized bubble is likely to be due to the combination of the asymmetry in the compressional and rarefactional pressure phases in the shock waveforms and water vapour transport (Kreider *et al* 2011a). As the peak positive pressure phase has a shorter duration than the negative pressure part in the shockwaves, the bubble has a relatively longer time to undergo expansion rather than collapsing, leading to rectified bubble growth within a few acoustic cycles. After the formation and explosive growth of a boiling bubble, it further interacts with incoming incident shockwaves to promote a mechanical tissue

fractionation process (Maxwell *et al* 2012). A miniature acoustic fountain and atomisation may occur at the tissue-bubble interface to emit jetting with sub-micrometre sized tissue fragments into the bubble (Simon *et al* 2012).

Ultrasonic atomisation or the emission of droplets from an acoustically vibrated thin liquid film exposed to air is a well-known phenomenon which has been the basis for commercial products such as ultrasonic air humidifiers and medical nebulisers. Although the mechanism for the atomisation is not fully understood yet, it is thought to be the combination of cavitation activity and capillary waves (i.e. standing waves) on the liquid surface (Simon 2013). A bulge on the liquid surface is initially formed due to the radiation force produced by a focused ultrasound wave. Cavitating bubbles are then subsequently produced within the bulging area caused by the reflected and inverted ultrasound waves at the bulge-air interface. This cavitation activity may further increase the amplitude of the capillary waves on the liquid surface until they become unstable at which the fountain as well as the atomisation are initiated. Simon *et al* (2012) observed this fountain and atomisation mediated by HIFU at the tissue-air interface using high speed photography. In their experiments, a cylindrical tunnel of 1–3 mm in diameter was introduced in an *ex vivo* bovine liver tissue prior to HIFU exposure. The tunnel filled with air was considered as a boiling bubble and a 2.0 MHz HIFU transducer was focused at the surface of the tunnel with P_+ = 65 MPa and P_- = –16 MPa.

Khokhlova *et al* (2011) and Simon *et al* (2012) suggested that the production of a "head" shaped lesion is likely to be due to the formation of a boiling bubble at the HIFU focus and the HIFU atomisation at the tissue-bubble interface. Besides this, the "tail" of a lesion may be formed by streaming of the liquefied tissue within the forming "head" (Wang *et al* 2013). This hypothesis is, however, somewhat contradictory to what they observed from their experiments. If the HIFU atomisation and the streaming are the major mechanisms for creating a "head" and a "tail", respectively, one would expect that the position of a "head" would be at the HIFU focus and a "tail" would subsequently form later. However, Canney *et al* (2010b) and Khokhlova *et al* (2011) observed that the HIFU focus was at the "tail",

and the "head" migrated towards the HIFU transducer during the course of boiling histotripsy. This discrepancy between the hypothesis and the experimental observations warrants further investigation into the mechanisms of HIFU boiling histotripsy. As mentioned in sections 2.3.3 and 2.4.1, scattering and reflections of incident HIFU beams from a boiling bubble in the HIFU focal volume can lead to the growth of a thermally ablated lesion towards the HIFU source. This results in the lesion shape distortion from an ellipsoid shape to a "tadpole" shape. Furthermore, the shock scattering effect is known to be the dominant mechanism for producing a cavitation cluster in the course of cavitation cloud histotripsy. This shock scattering has also been observed during boiling histotripsy. Canney *et al* (2010a) experimentally observed a significant increase in amplitude in the PCD voltage output and a sudden appearance of higher order multiple harmonic components of the fundamental frequency in the spectrogram when a boiling bubble formed at the HIFU focus. They speculated that these changes were because of the reflection and inversion of the incident shockwave from the boiling bubble. These experimental findings can indicate that there may be other mechanisms involved in boiling histotripsy besides the HIFU atomisation and the streaming effects. In this thesis, it was observed that a boiling bubble appeared in a localised super-heated region and cavitation clouds were subsequently produced in front of the boiling bubble towards the HIFU transducer in an optically transparent tissue phantom. This process was repeated and eventually resulted in a "tadpole" shaped lesion. This is discussed in Chapter 5 for more detail.

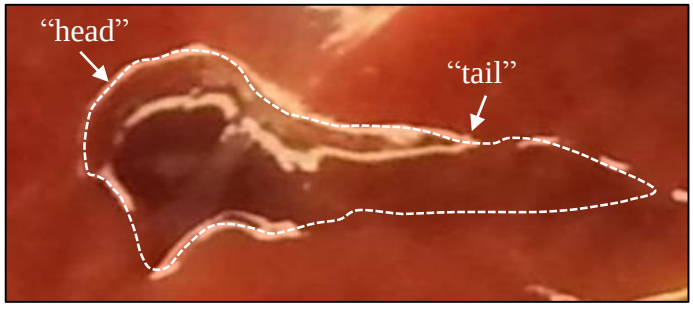

Figure 2.7. An example of a "tadpole" shaped lesion produced by HIFU boiling histotripsy in an *ex vivo* liver. The HIFU beam propagates from left to right.

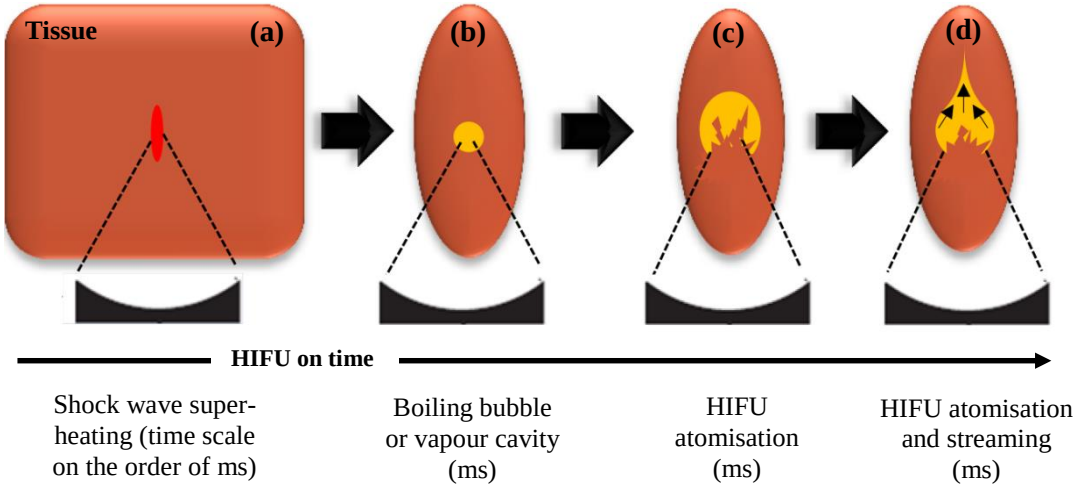

Figure 2.8. Mechanisms of tissue fractionation involved in boiling histotripsy proposed by Canney *et al* (2010a), Khokhlova *et al* (2011), Simon *et al* (2012) and Wang *et al* (2013). (a) A localised super-heated region by shocks. (b) Formation of a boiling vapour bubble or a vapour cavity at the HIFU focus. (c) Ultrasonic micro-fountains and tissue atomisation. (d) Tissue atomisation together with the streaming of the liquefied tissue within the forming "head".

2.4.2.1. Analytical estimation of time to reach a boiling temperature

Canney *et al* (2010a) demonstrated numerically that heat diffusion from a super-heated region by shocks at the HIFU focus is almost negligible if boiling appears within several milliseconds. The characteristic heat diffusion time t_d (i.e. the reaction time scale) can be estimated by

$$t_d = \frac{a_h^2}{4k} \tag{2.6}$$

where a_h is the initial radius of the heated region and k is the thermal diffusivity. In the case of shock wave heating at the HIFU focus in a tissue mimicking phantom, it takes 19 ms for heat to be transported over a_h = 0.1 mm with $k = 1.3 \times 10^{-7}$ $m^2 \cdot s^{-1}$ (Canney *et al* 2010a). This implies that heat diffusion has little effect if the heating rate is so high (e.g., H_{shock}) that boiling appears in times much shorter than t_d. The

time t_b to initiate boiling can therefore be predicted analytically by (Canney *et al* 2010a, Khokhlova *et al* 2011)

$$t_b = \frac{\Delta T c_v}{H_{\text{shock}}} \tag{2.7}$$

where ΔT is the difference between the ambient temperature and boiling temperature (100°C). c_v is the specific heat capacity at constant volume. Canney *et al* (2010a) and Khokhlova *et al* (2011) experimentally showed that the calculated value of t_b is in excellent agreement with the onset of the formation of a boiling vapour bubble at the HIFU focus in a tissue phantom.

If the duration of a single HIFU pulse is not much longer than t_b, thermal damage in the resulting lesion is negligible. This is likely because the extent of thermal injury at the HIFU focus prior to the formation of a boiling bubble, is much smaller than the region that will be mechanically fractionated by the exploding boiling bubble and its further interaction with incoming shockwaves (Maxwell *et al* 2012, Wang *et al* 2013).

2.4.3. Monitoring histotripsy treatments

Ultrasound imaging can be used for targeting and monitoring histotripsy treatments in real-time. The production of either cavitation clouds or a boiling bubble at the HIFU focus is visible as a hyperechoic region (increased echogenicity) on B-mode images, because bubbles are highly reflective to ultrasound (Khokhlova *et al* 2014). In addition, the appearance of a hypoechoic area (decreased echogenicity) is an indicator for treatment progression due to the loss of tissue echo texture in a mechanically fractionated tissue region (Maxwell *et al* 2012, Khokhlova *et al* 2015a). Khokhlova *et al* (2015b) recently demonstrated that the generation of lesions in *ex vivo* bovine liver by boiling histotripsy are clearly visible on MR imaging both in real-time and after the HIFU exposure.

2.5. Summary

At present, liver transplantation is the only effective treatment for end-stage liver diseases (Jorns *et al* 2012, Bartlett and Newsome 2015). The number of suitable donor organs is, however, limited, and a whole liver transplant requires complex surgery. Cell therapy, such as intra-portal hepatocytes transplantation, has been considered as a bridging therapy to liver transplantation but has shown a mixed clinical outcome with limited success including low level of engraftment of transplanted cells (Baccarani *et al* 2005, Stéphenne *et al* 2006, Dhawan *et al* 2010, Forbes and Rosenthal 2014, Gramignoli *et al* 2015). Iatrogenic methods such as liver irradiation, partial hepatectomy, reperfusion injury and noxious chemical agents have been used to induce extensive repopulation of the transplanted cells. Despite the excellent outcomes reported in *in vivo* experiments (Malhi *et al* 2002, Stéphenne *et al* 2006, Morán-Jiménez *et al* 2008, Turner *et al* 2011), radiation-induced liver disease, host hepatocyte proliferation, the risk of portal thrombosis and the development of hepatocellular carcinoma are major concerns (Malhi *et al* 2002, Dhawan *et al* 2010, Fujii *et al* 2010, Jorns *et al* 2012, Schlachterman *et al* 2015). A new approach of hepatocyte transplantation is, therefore, required in order to effectively deliver a large number of cells into the recipient liver and promote the integration and proliferation of the transplanted cells.

There has been a growing interest in HIFU-induced mechanical tissue fractionation or histotripsy. Histotripsy has been demonstrated using both cavitation clouds with microsecond HIFU pulses and boiling bubbles for milliseconds of HIFU excitation. Whilst the mechanisms involved in cavitation cloud histotripsy and boiling histotripsy are different, both can create similar lesions which contain complete fragmentation of tissue with no evidence of coagulative necrosis around the lesion (Lake *et al* 2008a, Hall *et al* 2009, Khokhlova *et al* 2011, Schade *et al* 2012a,b, Vlaisavljevich *et al* 2013, Wang *et al* 2013, Schade *et al* 2014, Khokhlova *et al* 2014, Pahk *et al* 2015). Contrary to the cavitation inception associated in cavitation cloud histotripsy, boiling histotripsy uses localised shockwave heating, which is more predictable and repeatable (Canney *et al* 2010a, Khokhlova *et al* 2011). This

boiling creates a vapour bubble which initiates the tissue fractionation process at the HIFU focus. Due to the repeatability and controllability of boiling histotripsy and its implementation with commercially available HIFU systems (Maxwell *et al* 2012, Kreider *et al* 2013, Khokhlova *et al* 2014), boiling histotripsy will be applied in this thesis to demonstrate the feasibility of the proposed hepatocyte transplantation.

A replacement of 5% to 10% of the liver mass with donor hepatocytes is necessary to adequately restore the liver function (Grossman *et al* 1994, Strom *et al* 1997a,b, Fox *et al* 1998, Sokal *et al* 2003, Darwish *et al* 2004, Stéphenne *et al* 2006, Lee *et al* 2007, Ribes-Koninckx *et al* 2012, Pless *et al* 2012). With the proposed cell therapy approach, 5%–10% of the liver mass will therefore be needed to be removed by boiling histotripsy prior to cell injection. Hence, it is important to have a thorough understanding of the physics behind HIFU boiling histotripsy in order to optimise the creation of a cavity. While a number of studies have demonstrated the efficacy of boiling histotripsy for fractionating tumours, the exact mechanisms underpinning this phenomenon are poorly understood, particularly after the formation of a boiling bubble. Further interaction of incident shockwaves with the bubble is believed to facilitate a mechanical tissue fractionation (Maxwell *et al* 2013). Yet the question of how this interaction eventually creates a "tadpole" shaped lesion remains.

Chapter 3. Numerical methods for modelling bubble dynamics in HIFU fields

HIFU histotripsy, the violent cavitation activity driven by nonlinear-shocked waves is considered to be the dominant mechanism for mechanical tissue fractionation (Kreider *et al* 2011a, Khokhlova *et al* 2015a). Under a nonlinear-shocked wave excitation, a bubble grows to a large size and collapses violently. Furthermore, water vapour and non-condensable gas diffuse into and out of the bubble as it oscillates (Kreider *et al* 2011a). It is known that tissue temperature rapidly increases in the course of boiling histotripsy. This eventually results in the variation of the physical properties of the surrounding medium and of water vapour and gas contents. To better understand the dynamics of bubbles exposed to boiling histotripsy insonation (nonlinear-shocked waves), an accurate and reliable bubble model accounting for the liquid compressibility, heat and mass (water vapour and gas) transfer and temperature variation is needed.

This Chapter describes numerical approaches to modelling the response of a single spherical gas-vapour bubble in the liver excited by histotripsy insonation as a function of temperature variation in the fluid. The underlying assumptions of the present numerical bubble model described in this Chapter are that (a) the single spherical bubble is initially at rest, (b) the bubble remains spherical during its oscillations, (c) there is no bubble fragmentation process after the bubble collapses, (d) the internal pressure and temperature inside the bubble are spatially uniform, (e) there is no bubble coalescence process, (f) the initial bubble radius is much smaller than the wavelength of an acoustic excitation, (g) the bubble is initially filled with gas and water vapour, (h) the gas in the bubble follows the ideal gas law and (i) there is no gravity acting on the bubble.

The present model will be compared against other published numerical and experimental observations for validation purposes.

3.1. Dynamics of a single spherical bubble

3.1.1. Radial bubble motion

The three most commonly used numerical models describing a single spherical bubble in a liquid are the Rayleigh-Plesset (Plesset 1949), the Herring-Trilling (Herring 1941, Trilling 1952) and the Gilmore (Gilmore 1952) equations. It is extremely important to choose a suitable bubble model to study bubble dynamics since all the models have slightly different assumptions. Although these models essentially behave in the same way for moderate bubble oscillations amplitudes, the Gilmore equation can provide satisfactory results in the region of violent radial oscillations where the bubble wall velocity is comparable to, or even greater than, the speed of sound in the liquid (Vokurka 1986). Because the Gilmore equation is particularly well suited to conditions of high acoustic pressures in which the liquid compressibility plays an important role upon bubble dynamics (Vokurka 1986, Church 1989), this bubble model is implemented in this thesis to describe the dynamic behaviour of a single bubble excited by a non-linear shocked wave.

3.1.1.1. The Rayleigh-Plesset bubble model

The Rayleigh-Plesset (RP) equation is one of the simplest models to describe radial bubble motions. This model assumes that the sound velocity is infinite in an incompressible fluid of constant density. The RP equation provides satisfactory numerical results only for small bubble oscillation amplitudes with relatively low flow velocity. Neppiras (1980) showed numerically that the RP equation gives validated results for stable cavitation over limited acoustic cycles and for inertial cavitation only where the bubble wall velocity is below one fifth of the speed of sound in the liquid. The RP equation is given by (Lauterborn 1976)

$$R\ddot{R}+\frac{3}{2}\dot{R}^2=\frac{1}{\rho_L}\left[\left(p_0+\frac{2\sigma}{R_0}-p_v\right)\left(\frac{R_0}{R}\right)^{3\gamma}+p_v-\frac{2\sigma}{R}-\frac{4\mu_L\dot{R}}{R}-p_\infty\right] \qquad (3.1)$$

where R is the instantaneous bubble radius, R_0 is the initial bubble radius, $\dot{R}$ and $\ddot{R}$ are the velocity and acceleration of the bubble wall, respectively. The dots denote differentiation with respect to time. ρ_L is the density of the liquid surrounding the bubble, p_0 is the ambient pressure of the surrounding liquid, $p_\infty = p_0 + p_a$ is the pressure far from the bubble, p_a is the applied acoustic pressure and p_v is the vapour pressure inside the bubble. σ is the surface tension at the bubble wall, γ is the polytropic index for the gas in the bubble and μ_L is the viscosity of the surrounding medium.

3.1.1.2. The Herring-Trilling bubble model

The derivation of the RP equation (3.1) ignores the compressibility of the surrounding liquid and its influence upon bubble dynamics. The effects of the compressibility on radial bubble oscillations, however, become significant for cases in which the bubble wall velocity is comparable with the acoustic velocity in the surrounding medium. Herring (1941) and Trilling (1952) rederived and modified equation (3.1) to take into account both the energy stored in the liquid during radial bubble oscillations and the damping effect introduced by the re-radiation of sound fields from bubble oscillations. The Herring-Trilling (HT) bubble model equation is given by

$$\left(1-\frac{2\dot{R}}{c_L}\right)R\ddot{R}+\frac{3}{2}\left(1-\frac{4\dot{R}}{3c_L}\right)\dot{R}^2=\frac{1}{\rho_L}\left[p_L+\frac{R}{c_L}\left(1-\frac{\dot{R}}{c_L}\right)\dot{p}_L-p_\infty\right] \qquad (3.2)$$

p_L is the pressure in the liquid at the bubble wall. Because the speed of sound c_L in the surrounding liquid is assumed constant, equation (3.2) is only valid when the bubble wall velocity is small compared to the speed of sound in the liquid. The Herring-Trilling bubble equation is, therefore, suitable for small to medium bubble radial oscillations with relatively moderate flow velocity, and violent bubble oscillations (i.e. $\dot{R}/c_L \geq 1$) cannot be studied.

3.1.1.3. The Gilmore bubble model

Gilmore (1952) improved the HT model (3.2) using the Kirkwood-Bethe hypothesis (1942) to take into account the compressibility of the liquid and the variation of sound velocity in the liquid as a function of the radial bubble motion. The Kirkwood-Bethe hypothesis (1942) states that the sound velocity is equal to the sum of the velocity of the surrounding liquid and the local velocity of sound at the bubble wall. The assumptions behind this model make it suitable for studying the dynamics of a single spherical bubble subjected to high acoustic pressure amplitudes (up to $\dot{R}/c_L$ = 2.2) such as those encountered in lithotripter shockwave pulses (Vokurka 1986, Church 1989, Phelps and Leighton 1997, Sboros *et al* 2002). The Gilmore bubble model is, therefore, considered in this thesis as the governing equation since acoustic peak and negative pressures at the HIFU focus used in boiling histotripsy are comparable to those in the shockwaves applied in lithotripsy (Zhu *et al* 2002, Pishchalnikov *et al* 2003). The Gilmore equation is a nonlinear second order differential equation, and is given by (Gilmore 1952)

$$\left(1-\frac{\dot{R}}{c_L}\right)R\ddot{R}+\frac{3}{2}\left(1-\frac{\dot{R}}{3c_L}\right)\dot{R}^2=\left(1+\frac{\dot{R}}{c_L}\right)H+\frac{\dot{R}}{c_L}\left(1-\frac{\dot{R}}{c_L}\right)R\frac{dH}{dR} \qquad (3.30)$$

In equation (3.30), H is the difference in liquid enthalpy between the bubble wall and infinity. The modified Tait equation, an empirical pressure-density relation for isentropic compression depending upon the liquid, is taken as the equation of state for the liquid (Sullivan 1981)

$$p=A_{\mathrm{m}}\left(\frac{\rho}{\rho_L}\right)^m-B_{\mathrm{m}} \qquad (3.31)$$

where A_{m}, $B_{\mathrm{m}} = A_{\mathrm{m}} - p_0$ and m are the medium-dependent empirical constants (Chavrier *et al* 2000). This modified Tait equation is valid when pressure in the liquid does not exceed 10 GPa (Church 1989). With the help of equation (3.31), the liquid enthalpy H can be obtained by (Minsier and Proost 2008)

$$H = \int_{p_\infty}^{p_w} \frac{dp}{\rho} = \frac{m}{m-1} A_{\mathrm{m}}^{1/m} \rho_0^{-1} \left[\left(p_w + B_{\mathrm{m}} \right)^{(m-1)/m} - \left(p_\infty + B_{\mathrm{m}} \right)^{(m-1)/m} \right] \tag{3.32a}$$

$$\frac{dH}{dR} = \frac{A_{\mathrm{m}}^{1/m}}{\rho_0} \left(p_w + B_{\mathrm{m}} \right)^{-1/m} \frac{dp_w}{dR} \tag{3.32b}$$

and the speed of sound at the bubble wall is

$$c_L = \sqrt{\frac{dp}{d\rho}} = \left[c_0^2 + (m-1)H \right]^{1/2} \tag{3.33}$$

In equation (3.32), the pressure at the bubble wall p_w can be calculated by balancing the forces acting on the wall

$$p_w = p_i - \frac{2\sigma}{R} - \frac{4\mu_L \dot{R}}{R} \tag{3.34a}$$

$$\frac{dp_w}{dR} = \frac{dp_i}{dR} + \frac{2\sigma}{R^2} + \frac{4\mu_L}{R^2} \dot{R} \tag{3.34b}$$

The pressure inside the bubble p_i can be described either using a polytropic law of compression with the absence of any heat or mass transfer at the bubble wall (Aymé-Bellegarda 1990)

$$p_i = \left(p_0 + \frac{2\sigma}{R_0} \right) \left(\frac{R_0}{R} \right)^{3\gamma} \tag{3.35a}$$

$$\frac{dp_i}{dR} = -3\gamma \left(p_0 + \frac{2\sigma}{R^2} \right) R_0^{3\gamma} R^{-3\gamma-1} \tag{3.35b}$$

or the van der Waals equation of state in the case of the inclusion of both heat and mass transfer at the bubble wall (Yasui 1995)

$$p_i = \frac{R_{\mathrm{gas}} T_b}{v - b_{\mathrm{v}}} - \frac{a_{\mathrm{v}}}{v^2} \text{ with } v = \frac{N_{\mathrm{A}} \frac{4}{3} \pi R^3}{N_{\mathrm{tot}}} \tag{3.36a}$$

$$\frac{dp_i}{dR} = 4\pi R^2 \left[\frac{-R_{\mathrm{gas}} T_b}{\left(v - b_{\mathrm{v}} \right)^2} + \frac{2a_{\mathrm{v}}}{v^3} \right] \frac{N_{\mathrm{A}}}{N_{\mathrm{tot}}} \tag{3.36b}$$

The van der Waals equation is a modification to and improvement of the ideal gas law taking into account (a) the finite volumes occupied by the gas molecules and (b) the attractive forces (i.e. the van der Waals forces) between the molecules (Berberan-Santos *et al* 2008). In equation (3.36), R_{gas} is the universal gas constant, T_b is the temperature inside the bubble, v is the mixture molar volume in the bubble, N_{A} is the Avogadro's number and $N_{\text{tot}} = N_{\text{air}} + N_{\text{vap}}$ is the total number of molecules in the bubble. N_{air} and N_{vap} are the number of air and water vapour molecules, respectively. The van der Waals constants a_{v} and b_{v} for the van der Waals forces and the volume occupied by the molecules are determined by (Yasui 1995)

$$a_{\text{v}} = a_{\text{air}}\left(\frac{N_{\text{air}}}{N_{\text{tot}}}\right)^2 + a_{\text{vap}}\left(\frac{N_{\text{vap}}}{N_{\text{tot}}}\right)^2 + 2\sqrt{a_{\text{air}}a_{\text{vap}}}\left(\frac{N_{\text{air}}}{N_{\text{tot}}}\right)\left(\frac{N_{\text{vap}}}{N_{\text{tot}}}\right) \tag{3.37}$$

$$b_{\text{v}} = b_{\text{air}}\left(\frac{N_{\text{air}}}{N_{\text{tot}}}\right)^2 + b_{\text{vap}}\left(\frac{N_{\text{vap}}}{N_{\text{tot}}}\right)^2 + 2\left\{\left[\frac{1}{2}\left(b_{\text{air}}^{1/3} + b_{\text{vap}}^{1/3}\right)\right]\right\}^{1/3}\left(\frac{N_{\text{air}}}{N_{\text{tot}}}\right)\left(\frac{N_{\text{vap}}}{N_{\text{tot}}}\right) \tag{3.38}$$

a_{air} and b_{air}, and a_{vap} and b_{vap} are the van der Waals constants of air and water vapour, respectively. The constant values are: $a_{\text{air}} = 1.402 \times 10^{-1}$, $a_{\text{vap}} = 5.536 \times 10^{-1}$ [J m^3·mol^{-2}], $b_{\text{air}} = 3.753 \times 10^{-5}$, $b_{\text{vap}} = 3.049 \times 10^{-5}$ [m^3·mol^{-1}].

Lastly, the time-varying pressure p_{rad} radiated by the radial bubble motions in the form of an outward travelling spherical wave in the liquid is calculated by (Akulichev 1971, Church 1989)

$$p_{rad} = A_{\text{m}}\left[\frac{2}{m+1} + \frac{m-1}{m+1}\left(1 + \frac{m+1}{r_d c_0^2}G\right)^{1/2}\right]^{2m/(m-1)} - B_{\text{m}} \tag{3.39}$$

where $G = R\left(H + \dot{R}^2/2\right)$ is an invariant of the bubble motion and r_d ($\geq R$) is the distance away from the centre of a bubble.

3.1.2. Mass transport across the bubble wall

Church (1989) suggested that non-condensable gas diffusion plays an important role in the radial bubble motions driven by a shockwave. The effects of gas flux caused by the relatively longer duration of negative pressure cycle in a shockwave, for example, can increase the time of the bubble growth phase, reduce the violence of the primary collapse and prolong the afterbounces. The afterbounces refer to as a series of bubble collapses following the primary collapse (Hilgenfeldt *et al* 1998). In addition to incondensable gas diffusion, the importance of the presence of water vapour (H_2O) inside a bubble has been confirmed both numerically and experimentally (Kamath *et al* 1993, Yasui 1997, Colussi and Hoffmann 1999, Storey and Szeri 2000). During the bubble expansion phase, water vapour transports into the bubble. Once the bubble collapses, the vapour in the bubble cannot completely diffuse out because the time scale of the collapse becomes much faster than the time scale of the diffusion of vapour out of the bubble. Water vapour is, therefore, trapped inside the bubble. This results in an increased heat capacity due to the additional number of water vapour particles limiting both the maximum temperature and pressure in the bubble (Brenner *et al* 2002).

In boiling histotripsy, the effect of water vapour on radial bubble motions is significant because the surrounding temperature reaches a boiling temperature of 100^{o}C (Kreider *et al* 2011a). To include the effects of mass transport in the present numerical model, rates of change of water vapour (H_2O) and non-condensable gas (air) with respect to time are modelled separately at the bubble wall (Kreider *et al* 2011b).

3.1.2.1. Water vapour transport: evaporation and condensation

To model the evaporation and condensation of vapour (i.e. the phase change between liquid and gas), the Hertz-Knudsen equation derived from the classical kinetic theory of gasses is employed, which estimates the change of molar rate of

water vapour $\dot{n}_{\mathrm{vap}}$ [mol·s^{-1}] at the bubble interface (Hertz 1882, Knudsen 1915, Holzfuss 2005)

$$\dot{n}_{\mathrm{vap}} = \dot{n}_{\mathrm{vap}}^{\mathrm{evap}} - \dot{n}_{\mathrm{vap}}^{\mathrm{cond}} = \frac{4\pi R^2}{M_{\mathrm{vap}}} \frac{\alpha_m \bar{c}(T_s)}{4} \left[\rho_{\mathrm{vap}}^{\mathrm{sat}} - \rho_{\mathrm{vap}}(R,t)\right]$$
$$\text{with } \bar{c}(T_s) = \sqrt{\frac{8R_{\mathrm{gas}}T_s}{\pi M_{\mathrm{vap}}}} \tag{3.40}$$

This Hertz-Knudsen model assumes the liquid-vapour interface is planar and takes the temperature distributions in the bubble and liquid as fixed (Ward and Fang 1999, Rahimi and Ward 2005, Holzfuss 2008). In equation (3.40), $\dot{n}_{\mathrm{vap}}^{\mathrm{evap}}$ and $\dot{n}_{\mathrm{vap}}^{\mathrm{cond}}$ are the molar rates of evaporation and condensation of water vapour and M_{vap} is the molar mass of vapour. α_m is the accommodation coefficient for evaporation or condensation (i.e. the diffusive behaviour of water vapour) and $\bar{c}$ is the average velocity of molecules. Because it is known that the surface temperature T_s of the bubble exceeds the surrounding liquid temperature T_0 only a very short time during collapse (Kamath *et al* 1993), the bubble surface temperature is taken as $T_s = T_0$. The saturated density of water vapour $\rho_{\mathrm{vap}}^{\mathrm{sat}}$ is estimated by (Wagner and Pruß 2002)

$$\rho_{\mathrm{vap}}^{\mathrm{sat}} = 322 \exp\left(b_1\vartheta^{2/6} + b_2\vartheta^{4/6} + b_3\vartheta^{8/6} + b_4\vartheta^{18/6} + b_5\vartheta^{37/6} + b_6\vartheta^{71/6}\right)$$
$$\text{with } \vartheta = 1 - T_0/647.096 \tag{3.41}$$

where the constants are: $b_1 = -2.0315024$, $b_2 = -2.6830294$, $b_3 = -5.38626492$, $b_4 = -17.2991605$, $b_5 = -44.7586581$ and $b_6 = -63.9201063$. The time-varying density of water vapour ρ_{vap} depends on the bubble dynamics and is calculated using the following equation (Yasui 1995)

$$\rho_{\mathrm{vap}} = \frac{M_{\mathrm{vap}}\left(\frac{N_{\mathrm{vap}}}{N_{\mathrm{tot}}}\right)}{v} \tag{3.42}$$

3.1.2.2. Non-condensable gas transport

The instantaneous rate of change of non-condensable gas $\dot{n}_{\mathrm{g}}$ [mol·s^{-1}] is estimated using Fick's law with the boundary layer approximation developed by Toegel *et al* (2000) and Toegel and Lohse (2003) and validated in Stricker *et al* (2011)

$$\dot{n}_{\mathrm{g,i}} = 4\pi R^2 D_{\mathrm{i}} \frac{c_{\infty,\mathrm{i}} - c_{s,\mathrm{i}}}{L_{\mathrm{g,i}}} \tag{3.43}$$

$$L_{\mathrm{g,i}} = \min\left(\sqrt{\frac{RD_{\mathrm{i}}}{|\dot{R}|}}, \frac{R}{\pi} \right) \tag{3.44}$$

The subscript i denotes different gas species (Nitrogen N_2, Oxygen O_2, Argon Ar), L_{g} is the instantaneous characteristic diffusion length and $c_s = p_i\left(n_{\mathrm{g}}/n_{\mathrm{tot}}\right)K_{\mathrm{H}}^{-1}$ is the instantaneous concentration of molecules per unit volume [mol·m^{-3}] at the bubble wall. $c_\infty = p_0 K_{\mathrm{H}}^{-1}$ is the concentration of dissolved gas far from the bubble, and is used as the initial concentration everywhere in the liquid. Henry's constant K_{H} [Pa·m^3·mol^{-1}] for different gas species i as function of temperature can be obtained by (Battino *et al* 1984)

$$K_{\mathrm{H,i}}(T_0) = \left[\frac{\rho_0}{p_0 M_{\mathrm{i}}} \exp\left(A_h + \frac{B_h}{\tau_h} + C_h \ln \tau_h \right) \right]^{-1}, \tau_h = \frac{T_0}{100} \tag{3.45}$$

where M_{i} is the molar mass for gas species i. The alphabetical constants for N_2, O_2 and Ar are given in Table 3.1.

The diffusivity of gas in liquids D_{i} [m^2·s^{-1}] in equation (3.43) is generally correlated with the viscosity of the liquid, which can be calculated empirically by (Othmer and Thakar 1953)

$$D_{\mathrm{i}} = \frac{1.4\times10^{-8}}{\left[1000\mu_L(T_0)\right]^{1.1} V_{m,\mathrm{i}}^{0.6}} \tag{3.46}$$

where $V_{m,\mathrm{i}}$ [mL·g^{-1}mol^{-1}] is the diffusion volume of gas.

Gases	A_h	B_h	C_h	V_m (Poling *et al* 2004)
N_2 (Battino 1982)	–67.4	86.3	24.8	18.5
O_2 (Battino 1981)	–66.7	87.5	24.5	16.3
Ar (Clever 1980)	–57.7	74.8	20.1	16.2

Table 3.1. The alphabetical constants in Henry's law and the diffusion volumes for N_2, O_2 and Ar.

3.1.3. Heat transfer and bubble temperature

3.1.3.1. Heat transfer at the bubble wall

Analogously to equations (3.43) and (3.44), the rate of heat transferred to the bubble $\dot{Q}$ and the thermal boundary layer thickness L_{th} can be approximated by (Toegel and Lohse 2003)

$$\dot{Q} = 4\pi R^2 \lambda_{\text{mix}} \frac{T_0 - T_b}{L_{\text{th}}} \tag{3.47}$$

$$L_{\text{th}} = \min\left(\sqrt{\frac{RK_{\text{mix}}}{|\dot{R}|}}, \frac{R}{\pi} \right) \tag{3.48}$$

The thermal conductivity of an air-vapour mixture λ_{mix} [W·m^{-1}K^{-1}] depends on temperature and density of the gas and vapour. The temperature dependence of the thermal conductivities of air λ'_{air} and of water vapour λ'_{vap} are assumed to be linear and calculated as (Yasui 1995)

$$\lambda'_{\text{air}} = \alpha_{\text{air}} T_b + \beta_{\text{air}} \tag{3.49}$$

$$\lambda'_{\text{vap}} = \alpha_{\text{vap}} T_b + \beta_{\text{vap}} \tag{3.50}$$

where $\alpha_{\text{air}} = 5.39 \times 10^{-5}$ [W·m^{-1}K^{-2}], $\beta_{\text{air}} = 0.0108$ [W·m^{-1}K^{-1}] for air and $\alpha_{\text{vap}} = 9.98 \times 10^{-5}$ [W·m^{-1}K^{-2}], $\beta_{\text{vap}} = -0.0119$ [W·m^{-1}K^{-1}] for water vapour. The temperature dependence of the thermal conductivity of the mixture (air and vapour) λ'_{mix} is then obtained by (Poling *et al* 2004)

$$\lambda'_{\mathrm{mix}} = \left(\frac{n_{\mathrm{vap}}}{n_{\mathrm{tot}}} \sqrt{\lambda'_{\mathrm{vap}}} + \frac{n_{\mathrm{air}}}{n_{\mathrm{tot}}} \sqrt{\lambda'_{\mathrm{air}}} \right)^2 \tag{3.51}$$

The density dependence of the thermal conductivity of the mixture λ_{mix} is calculated by (Hirschfelder *et al* 1964)

$$\lambda_{\mathrm{mix}} = \frac{b_{\mathrm{v}}}{v} \left(\frac{1}{y_a} + 1.2 + 0.755 y_a \right) \lambda'_{\mathrm{mix}} \tag{3.52}$$

$$y_a = \frac{b_{\mathrm{v}}}{v} + 0.6250 \left(\frac{b_{\mathrm{v}}}{v} \right)^2 + 0.2896 \left(\frac{b_{\mathrm{v}}}{v} \right)^3 + 0.1150 \left(\frac{b_{\mathrm{v}}}{v} \right)^4 \tag{3.53}$$

The thermal diffusivity K_{mix} [$\mathrm{m^2 \cdot s^{-1}}$] of the air-vapour mixture in equation (3.48) can be expressed by (Toegel and Lohse 2003)

$$K_{\mathrm{mix}} = \frac{\lambda_{\mathrm{mix}}}{c_p} \tag{3.54}$$

$$c_p = \sum_1^4 \frac{f_{\mathrm{i}} + 2}{2} K_{\mathrm{B}} \frac{N_{\mathrm{i}}}{V} \tag{3.55}$$

where c_p is the specific heat capacity per unit volume at constant pressure [$\mathrm{J \cdot m^{-3} K^{-1}}$], N_{i}/V is the molecular concentration [$\mathrm{m^{-3}}$] at the bubble wall, $V = 4\pi R^3/3$ is the bubble volume, and f_{i} is the number of translational and rotational degrees of freedom of gas species i. K_{B} is the Boltzmann constant.

3.1.3.2. Temperature change of the bubble

The first law of thermodynamics is employed for calculating the internal energy change inside the bubble (Toegel *et al* 2000, Samiei *et al* 2011, Chakma and Moholkar 2013)

$$\dot{E} = \sum_{\mathrm{i}=1}^{4} \left(h_{\mathrm{i}} - u_{\mathrm{i}} \right) \dot{N}_{\mathrm{i}} + \dot{Q} - \dot{W} \tag{3.56}$$

$$h_{\mathrm{i}} = \frac{f_{\mathrm{i}} + 2}{2} K_{\mathrm{B}} T_0 \tag{3.57}$$

$$u_{\mathrm{i}} = \left[\frac{f_{\mathrm{i}}}{2} + \sum_{1}^{n} \frac{\theta_n / T_b}{\exp\left(\theta_n / T_b\right) - 1} \right] K_{\mathrm{B}} T_b \tag{3.58}$$

where $\dot{E}$ is the rate of total energy change, $\left(h_{\mathrm{i}} - u_{\mathrm{i}}\right)\dot{N}_{\mathrm{i}}$ is the energy loss due to mass diffusion, $\dot{W} = p_i \dot{V}$ is the work done by the bubble expansion and $\dot{V} = 4\pi R^2 \dot{R}$ is the rate of bubble volume change. h_{i} is the molecular enthalpy and u_{i} is the internal energy. θ_n represents the characteristic vibrational temperatures in kelvin units. n is the number of the characteristic vibrational temperatures. Because of the constant temperature condition at the bubble wall (see section 3.1.2.1), the latent heat of evaporation and condensation (i.e. the heat energy which is taken in or given out by a substance when it changes state) is neglected and does not contribute to the energy balance in equation (3.56). The values f_{i}, θ_n and n for air (N_2, O_2, Ar) and water vapour H_2O are given in Table 3.2.

Combining equations (3.47)–(3.58) together, the rate of temperature change inside the bubble $\dot{T}_b$ [K·s^{-1}] can be obtained algebraically

$$\dot{T}_b = \frac{\dot{E}}{C_{v,\mathrm{mix}}} = \frac{\sum_{\mathrm{i}=1}^{4} \left(h_{\mathrm{i}} - u_{\mathrm{i}}\right)\dot{N}_{\mathrm{i}}}{C_{v,\mathrm{mix}}} + \frac{\dot{Q}}{C_{v,\mathrm{mix}}} - \frac{\dot{W}}{C_{v,\mathrm{mix}}} \tag{3.59}$$

$$= \frac{K_{\mathrm{B}}}{C_{v,\mathrm{mix}}} \left(\begin{array}{l} \left(\frac{5}{2} T_0 - \frac{3}{2} T_b \right) \dot{N}_{\mathrm{Ar}} + \left(\frac{7}{2} T_0 - \frac{5}{2} T_b - T_b \left(\frac{3350/T_b}{\exp\left(3350/T_b - 1\right)} \right) \right) \dot{N}_{\mathrm{N_2}} \\ + \left(\frac{7}{2} T_0 - \frac{5}{2} T_b - T_b \left(\frac{2273/T_b}{\exp\left(2273/T_b - 1\right)} \right) \right) \dot{N}_{\mathrm{O_2}} \\ + \left(\frac{8}{2} T_0 - \frac{6}{2} T_b - T_b \left(\frac{2295/T_b}{\exp\left(2295/T_b - 1\right)} + \frac{5255/T_b}{\exp\left(5255/T_b - 1\right)} + \frac{5400/T_b}{\exp\left(5400/T_b - 1\right)} \right) \right) \dot{N}_{\mathrm{vap}} \end{array} \right)$$

$$+ 4\pi R^2 \lambda_{\mathrm{mix}} \frac{T_0 - T_b}{L_{\mathrm{th}} C_{v,\mathrm{mix}}} - \frac{p_i 4\pi R^2 \dot{R}}{C_{v,\mathrm{mix}}}$$

In equation (3.59), $C_{v,\mathrm{mix}}$ is the heat capacity of the gas mixture (air and vapour) at constant volume [J·K^{-1}] and is given by (Toegel *et al* 2000, Kreider 2008, Samiei *et al* 2011, Chakma and Moholkar 2013)

$$C_{v,\mathrm{mix}} = K_{\mathrm{B}} \sum_{\mathrm{i}=1}^{4} \left(\frac{f_i}{2} + \sum_{1}^{n} \left(\frac{(\theta_n/T_b)^2 \exp(\theta_n/T_b)}{(\exp(\theta_n/T_b)-1)^2} \right) \right) N_{\mathrm{i}} \tag{3.60}$$

$$= K_{\mathrm{B}} \left(\begin{array}{l} \left(\frac{3}{2} N_{\mathrm{Ar}} + \left(\frac{5}{2} + \frac{(3350/T_b)^2 \exp(3350/T_b)}{(\exp(3350/T_b)-1)^2} \right) N_{\mathrm{N_2}} \right. \\ + \left(\frac{5}{2} + \frac{(2273/T_b)^2 \exp(2273/T_b)}{(\exp(2273/T_b)-1)^2} \right) N_{\mathrm{O_2}} + \\ \left. \left(\frac{6}{2} + \frac{(2295/T_b)^2 \exp(2295/T_b)}{(\exp(2295/T_b)-1)^2} + \frac{(5255/T_b)^2 \exp(5255/T_b)}{(\exp(5255/T_b)-1)^2} + \frac{(5400/T_b)^2 \exp(5400/T_b)}{(\exp(5400/T_b)-1)^2} \right) N_{\mathrm{vap}} \right) \end{array} \right)$$

The physical constants for the gas dynamics used in the model are displayed in Table 3.3.

Gases	f_{i}	θ_n	n
N_2	5	3350	1
O_2	5	2273	1
Ar	3	-	-
H_2O	6	2295, 5255, 5400	3

Table 3.2. The number of translational and rotational degrees of freedom f_{i}, the characteristic vibrational temperatures θ_n and the number of the characteristic vibrational temperatures n for N_2, O_2, Ar and H_2O (Toegel and Lohse 2003).

Symbol	**Definition**	**Value**	**Units**
R_{gas}	Universal gas constant	8.314472	J·mol^{-1}K^{-1}
K_{B}	Boltzmann constant	$1.3806503 \times 10^{-23}$	J·K^{-1}
N_{A}	Avogadro's constant	$6.02214179 \times 10^{23}$	mol^{-1}
M_{air}	Molar mass of air	28.97×10^{-3}	kg·mol^{-1}
M_{vap}	Molar mass of water vapour	18.015268×10^{-3}	kg·mol^{-1}
M_{N2}	Molar mass of nitrogen	28×10^{-3}	kg·mol^{-1}
M_{O2}	Molar mass of oxygen	31.9988×10^{-3}	kg·mol^{-1}
M_{Ar}	Molar mass of argon	39.95×10^{-3}	kg·mol^{-1}

Table 3.3. Physical constants for the gas dynamics used in the model (Wagner and Pruß 2002, Poling *et al* 2004).

3.1.4. Model assumptions, Initial boundary conditions and Nondimensionalisation

3.1.4.1. Assumptions

During the numerical computation, it is assumed that:

- a single spherical bubble is initially at rest;
- the bubble remains spherical during its oscillations;
- there is no bubble fragmentation process after the bubble collapses;
- the internal pressure and temperature inside the bubble are spatially uniform;
- the initial bubble radius is much smaller than the wavelength of an acoustic excitation;
- the bubble is initially filled with air (78% N_2, 21% O_2, 1% Ar) (Lemmon *et al* 2000) and water vapour (H_2O);
- the gas in the bubble follows the ideal gas law, and
- there is no gravity acting on the bubble.

3.1.4.2. Initial boundary conditions

The initial boundary conditions (at $t = 0$) were taken as

$$\begin{aligned} R = R_0; \quad \dot{R} = 0; \quad n_{\text{vap}} = \frac{p_v(T_0)}{K_{\text{B}}T_0}\frac{4\pi}{3}R_0^3; \quad n_{\text{N}_2} = 0.78\frac{p_0}{K_{\text{B}}T_0}\frac{4\pi}{3}R_0^3; \\ n_{\text{O}_2} = 0.21\frac{p_0}{K_{\text{B}}T_0}\frac{4\pi}{3}R_0^3; \quad n_{\text{Ar}} = 0.01\frac{p_0}{K_{\text{B}}T_0}\frac{4\pi}{3}R_0^3; \quad T_b = T_0 \end{aligned} \tag{3.61}$$

where p_v is the water vapour pressure at a given ambient temperature, and is given by (Webb *et al* 2011)

$$p_v = 610\exp\left[\left(\frac{T_0(\text{K})}{273.16}-1\right)\left(22.486\frac{273.16}{T_0(\text{K})}+0.3182\frac{T_0(\text{K})}{273.16}-2.9558\right)\right] \tag{3.62}$$

3.1.4.3. Nondimensionalisation

The physical parameters used in the present numerical model are nondimensionalised according to the following schemes:

- In the absence of any heat or mass transfer (see equation 3.35)

$$\text{Length (L)} = R_0; \quad \text{Time (T)} = (2\pi f_0)^{-1}; \quad \text{Mass (M)} = p_0 \text{LT}^2 \tag{3.63}$$

- In the presence of heat and mass transfer (see equation 3.36)

$$\text{Length (L)} = R_0; \quad \text{Temperature } (\theta) = T_0; \quad \text{Time (T)} = (2\pi f_0)^{-1}; \tag{3.64}$$
$$\text{Mole (MOL)} = n_{0,\text{total}}; \quad \text{Mass (M)} = \text{R}_{\text{gas}}\theta\text{MOLT}^2\text{L}^{-2}$$

**Nondimensionalised parameters are provided in Appendix A.*

The sets of five coupled ordinary differential equations, ODEs, (3.30), (3.40), (3.43), (3.47) and (3.59) were numerically integrated in MATLAB® (MathWorks Inc., R2013a). MATLAB scripts for solving the ODEs can be found in Appendix B.

3.1.5. Temperature-dependent physical properties of liver

In the present bubble model, the surrounding liquid is modelled as fluid whose properties are representative of those of human liver (Pahk *et al* 2015). The liver properties (density, speed of sound, viscosity and surface tension) as a function of temperature (independent of acoustic pressure fields) are assumed to follow similar trends to those of water, as it is acknowledged that information regarding this is not readily available (Choi *et al* 2011). The temperature dependences of the physical properties of water were initially calculated using the empirical equations (3.65)–(3.68)

$$\rho_{0,\text{water}} = 1000\left[1 - \frac{(T_\text{c} - 4)^2}{119000 + 1365T_\text{c} - 4T_\text{c}^2}\right] \text{with} \, T_\text{c} = T_0(^\circ\text{C}) \tag{3.65}$$

$$c_{0,\text{water}} = 1402.4 + 5.0384\tau - 5.8117\times10^{-2}\tau^2 + 3.3464\times10^{-4}\tau^3 - 1.4826\times10^{-6}\tau^4 + 3.1659\times10^{-9}\tau^5, \text{with} \, \tau = T_0(\text{K}) - 273.16 \tag{3.66}$$

$$\mu_{0,\text{water}} = \frac{1.779\mu(T_0 = 20^\circ\text{C})}{1 + 0.03367T_\text{c} + 2.2099\times10^{-4}T_\text{c}^2} \tag{3.67}$$

$$\sigma_{0,\text{water}} = 0.2358\,\vartheta^{1.256}(1 - 0.625\,\vartheta) \text{ with } \vartheta = 1 - T_0(\text{K})/647.1 \tag{3.68}$$

Equations (3.65)–(3.68) respectively give the variation of water density ρ_0 (Kravchenko 1966), speed of sound c_0 (Bilaniuk and Wong 1993), dynamic viscosity μ_0 (Joseph 1964) and surface tension σ_0 (Webb *et al* 2011) with temperature. To estimate the liver properties, the calculated water properties at a given ambient temperature were multiplied by the ratio of the liver and water properties measured at $T_0 = 20^\text{o}$C

$$\text{Ratio} = \text{Liver } (T_0 = 20^\text{o}\text{C})/\text{Water } (T_0 = 20^\text{o}\text{C}) \tag{3.69}$$

$$\text{Liver } (T_0) = \text{Water}_{\text{calculated}}(T_0) \times \text{Ratio} \tag{3.70}$$

Table 3.4 shows the properties of water and of liver at $T_0 = 20^\text{o}$C.

The temperature dependent parameters of water and of liver over a range of 20ºC to 100ºC are shown in Figure 3.1.

Symbol	Definition	Values measured at 20ºC		
		Water	Liver	Ratio
ρ_0	density [kg·m^{-3}]	998.2	1060	1.06
c_0	speed of sound [m·s^{-1}]	1482	1575	1.06
μ_0	viscosity [kg·m^{-1}s^{-1}]	1.0019×10^{-3}	9×10^{-3}	8.98
σ_0	surface tension [N·m^{-1}]	0.073	0.056	0.77

Table 3.4. Physical properties of water and of liver at 20ºC. These values were obtained from Duck (1990), Choi *et al* (2011) and Church *et al* (2012).

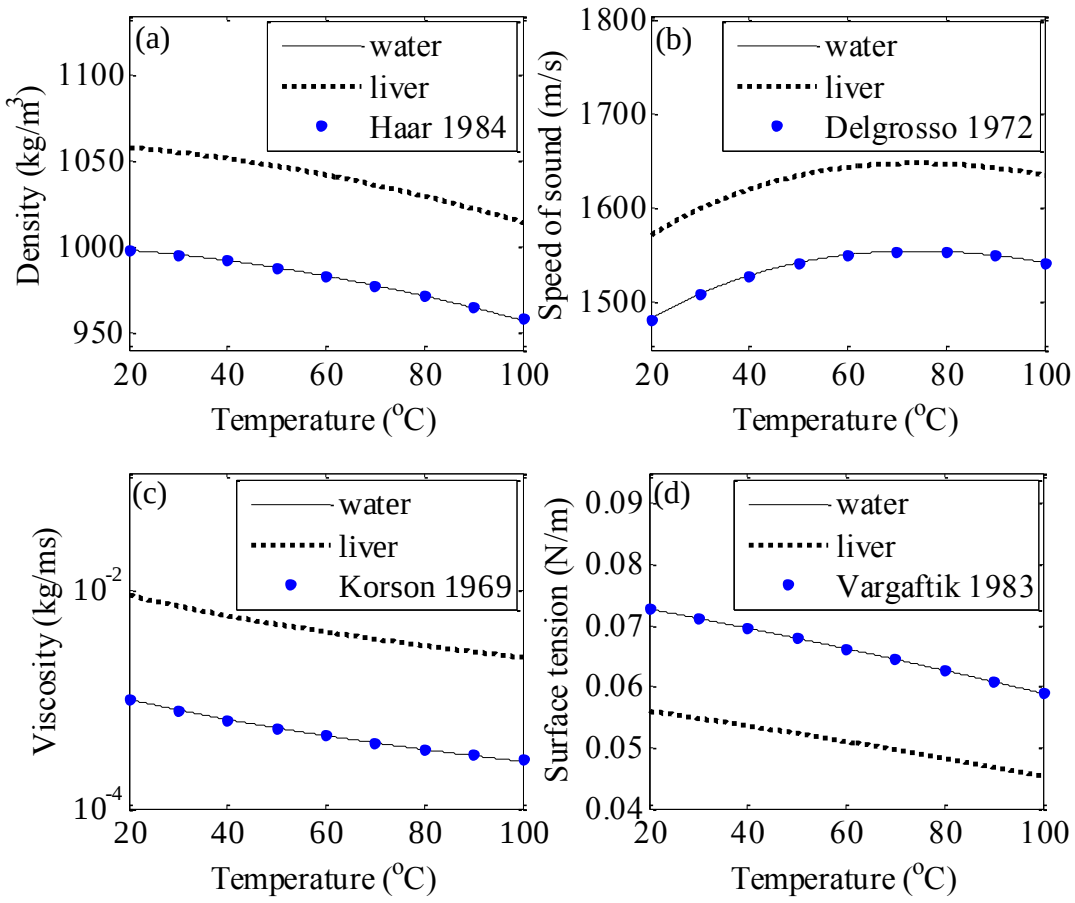

Figure 3.1. Calculated properties of water (solid line) and of liver (dashed line) as a function of temperature from 20ºC to 100ºC. (a) density, (b) speed of sound, (c) viscosity and (d) surface tension. The blue circles indicate experimental measurements of properties of water as a function of temperature variation. These values were obtained from Haar *et al* (1984) for density, Delgrosso *et al* (1972) for speed of sound, Korson *et al* (1969) for viscosity and Vargaftik *et al* (1983) for surface tension.

3.1.6. Model validation

For validation purposes, the present bubble model was compared with other published numerical and experimental observations. An in-depth comparison between these is beyond the scope of this Chapter. Instead, two cases including a single-bubble sonoluminescence (SBSL) (Storey and Szeri 2000) and a lithotripsy bubble (Matula *et al* 2002) were considered. These situations were chosen because:

- numerical models for SBSL in the literature address essential features of both heat and mass transfer;

- histotripsy uses high acoustic peak pressures which are comparable to those in the shockwaves used in lithotripsy.

3.1.6.1. Single bubble sonoluminescence (SBSL)

Sonoluminescence is characterised by the emission of a brief flash of light during collapse of a single bubble excited by ultrasonic waves in water (Gaitan *et al* 1992, Brenner *et al* 2002). For SBSL comparison, $R(t)$ and $N_{vap}(t)$ were calculated with the same parameters f_0 = 26.5 kHz, R_0 = 4.5 μm and p_a = 120 kPa as used by Storey and Szeri (2000), who implemented one of the most complete models in the literature for violent spherical collapses (Kreider 2008).

Simulation results for the variation of the bubble radius and molecular content inside the bubble with respect to time are plotted in Figure 3.2. Figure 3.2(a) and (c) are reproduced from Storey and Szeri (2000) while (b) and (d) are obtained from the present model. The present bubble model predicts essentially similar radial bubble motions and vapour trapping effects to within an order of magnitude. When comparing the maximum and the minimum bubble sizes attained and the amount of water vapour trapped during the primary collapse over one acoustic cycle, the present model shows R_{max} = 30.3 μm, R_{min} = 0.79 μm and 14.7% of the vapour

content while Storey and Szeri (2000) predicted 31.3 μm, 0.70 μm and 14%, respectively.

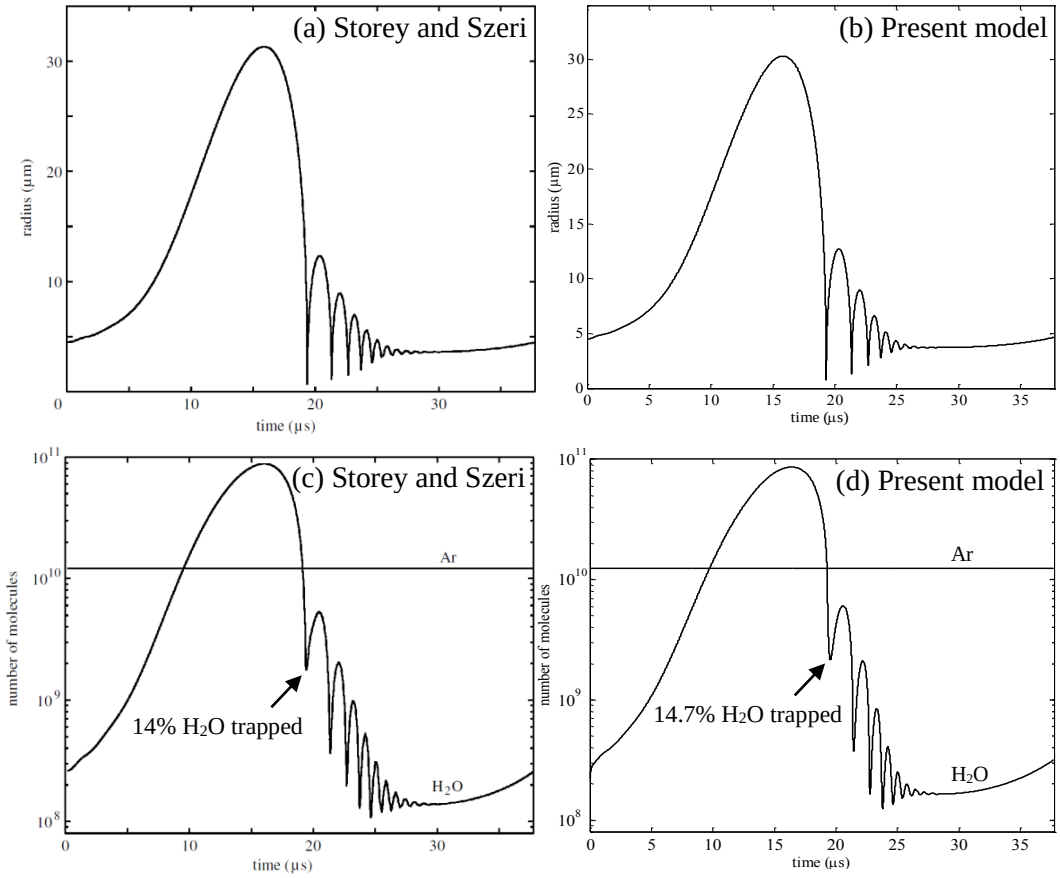

Figure 3.2. Comparisons of radius vs time (a,b) and number of vapour molecules (c,d) for SBSL. A single argon-vapour bubble in water was excited by a sinusoidal wave over one acoustic cycle with parameters f_0 = 26.5 kHz, R_0 = 4.5 μm, p_a = 120 kPa and T_0 = 298K as used by Storey and Szeri (2000). (a) and (c) are taken from Storey and Szeri (2000), whereas (b) and (d) are obtained from the present model. The vapour trapping was controlled by setting α_m = 0.1.

3.1.6.2. Lithotripsy bubble

In lithotripsy bubbles, as noted by Church (1989), the negative pressure component of a lithotripter shockwave causes a bubble to expand over 100 times its initial size and the gas diffusion increases the duration of afterbounces following primary collapse. The present numerical model was compared with the experimental and numerical results obtained by Matula *et al* (2002). The authors experimentally

measured single bubble oscillations in lithotripsy fields in water using light-scattering techniques, and considered heat and vapour transport in a bubble model to simulate spherical bubble dynamics.

In the present bubble model, the same lithotripter waveform used in Matula *et al* (2002) was applied to excite a single bubble. An analytical approximation for the lithotripter waveform as a function of time was obtained by (Church 1989, Matula *et al* 2002)

$$p(t) = 2p_a \exp(-at)\cos(2\pi ft + \pi/3) \tag{3.71}$$

where p_a = 33 MPa is the peak positive pressure, $a = 3.5 \times 10^5$ rad·s^{-1} is the decay constant and f = 50 kHz. The lithotripter pulse is shown in Figure 3.3.

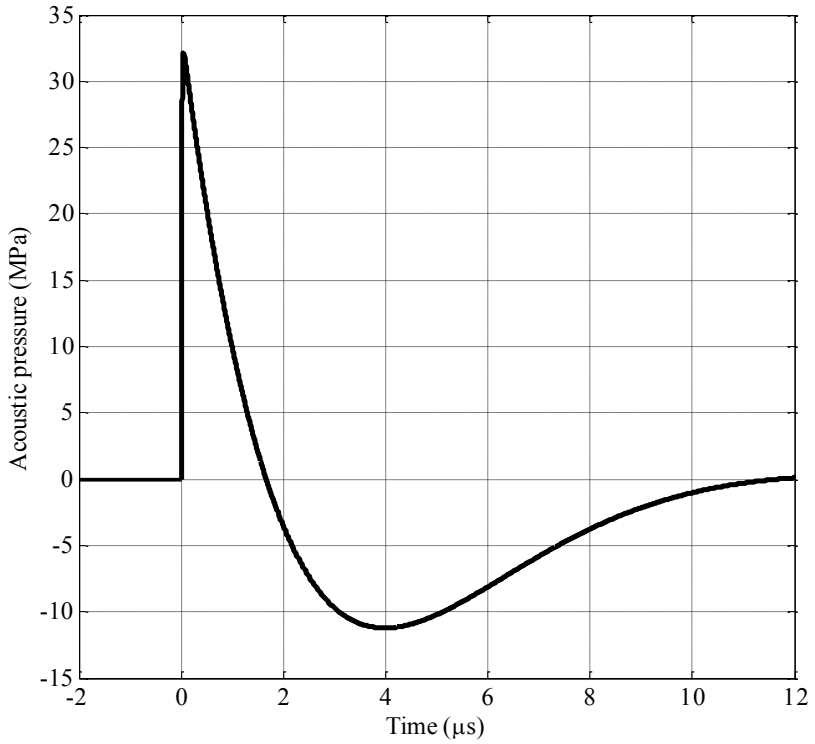

Figure 3.3. The analytical approximation for the lithotripter pulse with P_+ of 33 MPa and P_- of –11 MPa.

Simulated values of R, N_{vap}, and N_{air} as a function of time, obtained with equations (3.30)–(3.60), are plotted in Figure 3.4(b) and (d), whilst Figure 3.4(a) and (c) show the results obtained by Matula *et al* (2002) for the equivalent case, i.e. for a 4.5 μm air-vapour bubble in water at 298K. When comparing the bubble radius vs time curves and the molecular contents, it can be noticed that both the $R(t)$ curves agree well (e.g. the bubble grows to almost 2 mm before the first collapse at around 400 μs). However, N_{vap} and N_{air} behave differently. The discrepancy in the non-condensable gas diffusion with an order of magnitude is most probably due to the use of a different value for Henry's constant because both the present and the referenced models used Fick's law to describe gas diffusion at the bubble wall. For the water vapour curves, the amount of vapour inside the bubble "bounced" during the afterbounces in the present model, whereas it appears to decrease according to a "stair casing" pattern in Matula *et al* (2002). Matula *et al* (2002) considered chemical effects by adding the additional thermal damping from endothermic chemical reactions: $H_2O \rightarrow OH + H$, which acts as an energy sink and eats up the heat. This could possibly explain the reduction in the water vapour curve along a "staircase" pattern plotted in Figure 3.4(c).

Matula *et al* (2002) numerically demonstrated that the majority of the bubble contents throughout the growth phase consists of water vapour, and that the afterbounces were dominated by vapour transport, not non-condensable gas diffusion. These features can also be observed from the present model as shown in Figure 3.4(b) and (d).

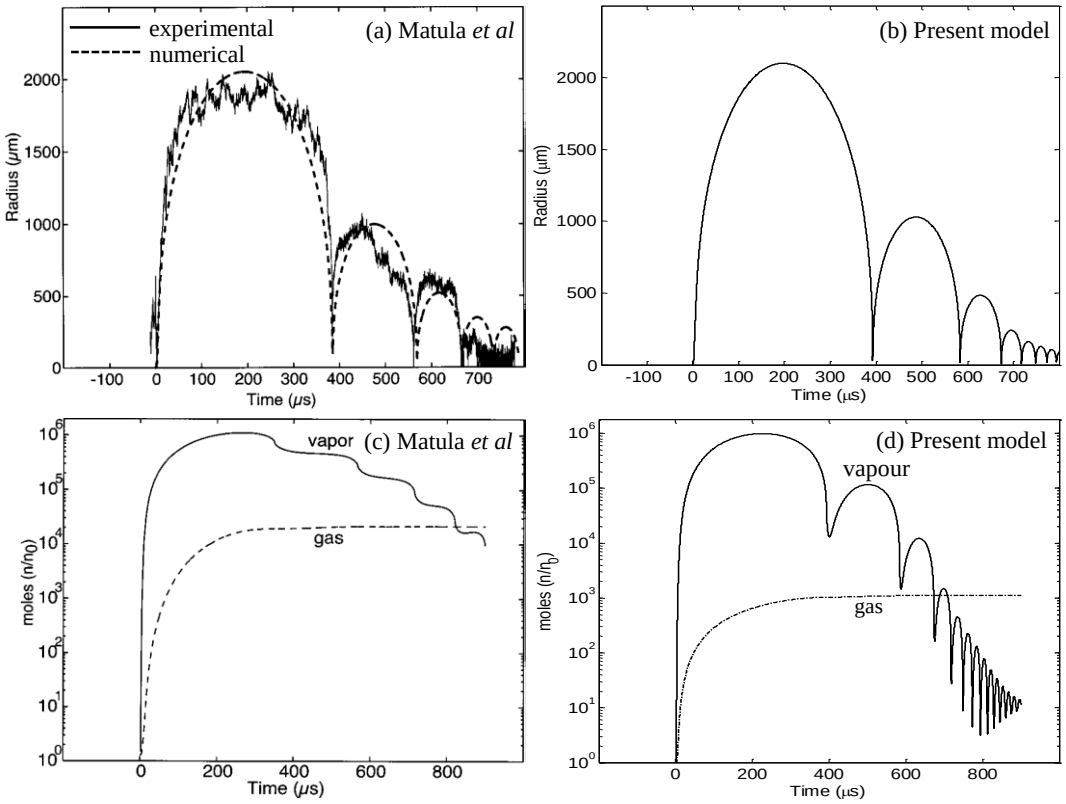

Figure 3.4. Comparison of radius vs time (a,b) and molecular contents (c,d) for a lithotripsy bubble. (a) and (c) are taken from Matula *et al* (2002); while (b) and (d) are obtained with the present model. The present calculations included the same parameters used by Matula *et al* (2002) i.e. a 4.5 μm air-vapour bubble in water at 298K. The peak positive and negative acoustic pressures used in the lithotripter shockwave were $P_+ = 33$ MPa and $P_- = -11$ MPa, respectively (see Figure 3.3). The vapour trapping was controlled by setting $\alpha_m = 0.15$.

3.2. HIFU pressure fields

In HIFU applications, a commonly used equation for simulating acoustic fields is the Khokhlov-Zabolotskaya-Kuznetsov (KZK) parabolic nonlinear wave propagation equation. It is an augmented form of Burgers' equation (Burgers 1948) and a parabolic approximation to the Westervelt equation. This latter accounts for the full effects of diffraction, absorption and nonlinearity (Hamilton and Blackstock 2008). The KZK equation is derived from the Westervelt equation by assuming that $k_w a_s \gg 1$, where k_w is the acoustic wave number and a_s is the source radius. This implies that the sound beam is reasonably directional and located in the vicinity of the axis of the wave propagation (Averkiou and Hamilton 1997). These assumptions ensure that the KZK equation is suitable for modelling HIFU fields, owing mainly to the ease with which it can be implemented compared with full wave equations. This is described in more detail by Hamilton and Blackstock (2008).

If the *z* axis is in the direction of the sound beam propagation, and the HIFU source lies in the (*x*,*y*) plane perpendicular to the *z* axis, the axisymmetric form of the KZK equation in terms of acoustic pressure *p* is given by (Kuznetsov 1971)

$$\frac{\partial^2 p}{\partial z \partial \tau} = \frac{c_0}{2}\nabla_\perp^2 p + \frac{\delta}{2c_0^3}\frac{\partial^3 p}{\partial \tau^3} + \frac{\beta}{2\rho_0 c_0^3}\frac{\partial^2 p^2}{\partial \tau^2} \tag{3.72}$$

where δ is the diffusivity of sound for a thermoviscous fluid, $\tau = t - z/c_0$ is the retarded time variable associated with propagation in the + *z* direction at c_0 and $\nabla_\perp^2 = \partial^2/\partial x^2 + \partial^2/\partial y^2$ is the Laplacian operator with transverse Cartesian coordinates (*x*,*y*). In the KZK equation (3.72), the first and the second terms on the right hand side describe the diffraction and absorption and the last term accounts for tissue nonlinearity. For plane sound waves, $\nabla_\perp^2 p$ = 0, and the KZK equation (3.72) reduces to Burgers' equation. The sound diffusivity δ and the coefficient of nonlinearity β are expressed by

$$\delta = \frac{1}{\rho_0}\left[\left(\mu_B + \frac{4\mu_s}{3}\right) + \kappa\left(\frac{1}{c_v} - \frac{1}{c_p}\right)\right] \tag{3.73a}$$

$$\beta = 1 + \frac{B}{2A} \tag{3.73b}$$

where μ_B and μ_s are bulk and shear viscosity, κ is the thermal conductivity, c_v and c_p are the specific heat capacities at constant volume and at constant pressure, respectively. *B/A* is the nonlinear parameter of the medium where *A* and *B* are the coefficients of the first and second order terms of the Taylor series expansion of the pressure-density relation. This is given by (Hamilton and Blackstock 2008)

$$p = A\left(\frac{\rho - \rho_0}{\rho_0}\right) + \frac{B}{2!}\left(\frac{\rho - \rho_0}{\rho_0}\right)^2 + \frac{C}{3!}\left(\frac{\rho - \rho_0}{\rho_0}\right)^3 + \cdots \tag{3.74a}$$

$$A = \rho_0\left(\frac{\partial P}{\partial \rho}\right)_{s,0} \equiv \rho_0 c_0^2; B = \rho_0^2\left(\frac{\partial^2 P}{\partial \rho^2}\right)_{s,0}; C = \rho_0^3\left(\frac{\partial^3 P}{\partial \rho^3}\right)_{s,0} \tag{3.74b}$$

The parameter *B/A* can then be written as

$$\frac{B}{A} = \frac{\rho_0}{c_0^2}\left(\frac{\partial^2 P}{\partial \rho^2}\right)_{s,0} \tag{3.74c}$$

$P = p + p_0$ is the total pressure, ρ is the mass density and *s* is the specific entropy.

Many efficient numerical algorithms which solve the KZK equation exist in the time domain (Lee and Hamilton 1995) and the frequency domain (Korpel 1980) using finite differences and operator splitting methods. Diffraction, absorption and nonlinearity are numerically solved independently over a small propagation step size Δz, and the total change in acoustic pressure can be approximated by their sum (Lee and Hamilton 1995). A numerical approach to solving the KZK equation is described in detail by Lee and Hamilton (1995), Pinton (2007) and Hamilton and Blackstock (2008).

3.3. HIFU temperature fields

As explained in Chapter 2, a localised super-heating by shockwaves at the HIFU focus during boiling histotripsy can raise tissue temperature to 100°C in a few milliseconds, which is then followed by the formation of a boiling vapour bubble. It has been shown that the time to initiate boiling at the HIFU focus can be reliably predicted theoretically (Canney *et al* 2010a, Khokhlova *et al* 2011, Wang *et al* 2013). A commonly used equation for calculating temperature distribution in soft tissue is the Bioheat transfer (BHT) equation in which the effects of heat diffusion, blood perfusion and heat deposition are taken into account (Pennes 1948). The BHT equation is an augmented form of the classical Fourier law of heat conduction, and is given by

$$\rho_{\mathrm{T}} C_{\mathrm{T}} \frac{\partial T_{\mathrm{T}}}{\partial t} = \kappa_{\mathrm{T}} \nabla^2 T_{\mathrm{T}} - w_{\mathrm{B}} C_{\mathrm{B}} \left(T_{\mathrm{T}} - T_{\mathrm{B}} \right) + H_{\mathrm{heat}} \tag{3.75}$$

where ρ, C, T and κ are the density, specific heat capacity [$\mathrm{J \cdot kg^{-1} K^{-1}}$], temperature and the thermal conductivity [$\mathrm{W \cdot m^{-1} K^{-1}}$], respectively, with the subscripts T and B referring to tissue and blood. w_{B} is the perfusion rate of blood [$\mathrm{kg \cdot m^{-3} s^{-1}}$]. Spatial distributions of acoustic pressure amplitudes p obtained from the KZK equation (3.72) can be used to calculate the heat source term H_{heat} [$\mathrm{W \cdot m^{-3}}$]. In the linear wave propagation case, the ultrasonic intensity is equal to $I_L = p^2 / 2\rho c_0$. For the nonlinear case, the total intensity is

$$I_{\mathrm{tot}} = \sum_{n=1}^{\infty} I_N \tag{3.76a}$$

where I_N are the intensities for the respective harmonics nf_0 (n is a positive integer). The heat source term H_{heat} can then be calculated as (Khokhlova *et al* 2006, Solovchuk *et al* 2015)

$$H_{\mathrm{heat}} = 2 \sum_{n=1}^{\infty} \alpha_a (n f_0) I_N \text{ with } \alpha_a (f) = \alpha_0 \left(\frac{f}{f_0} \right)^{\mathrm{b_a}} \tag{3.76b}$$

$\alpha_a(f)$ is the absorption coefficient at a frequency f and α_0 is the medium dependent absorption coefficient [dB·m^{-1}] at the fundamental ultrasonic frequency f_0.

As mentioned in Chapter 2, the heating resulting from absorption at the shockwaves can be estimated analytically when shockwaves are present in the focal acoustic waveform (Hamilton and Blackstock 2008)

$$H_{\text{shock}} = \frac{\beta f_0 A_s^3}{6 c_0^4 \rho_0^2} \tag{3.77}$$

The shockwave amplitude at the HIFU focus A_s can be obtained by either numerically solving the KZK equation (3.72) or by experimentally measuring the acoustic pressure using a calibrated hydrophone (Canney *et al* 2010a, Khokhlova *et al* 2011). Canney *et al* (2008) showed that, owning to a limited bandwidth of a fibre-optic probe hydrophone, modelled waveforms using the KZK equation were more accurate than measurements when shocks were present at the HIFU focal region.

As highlighted in the previous chapter, the amount of heat loss by diffusion is generally negligible if boiling occurs faster than the characteristic heat diffusion time t_d. The thermal diffusion term in the BHT equation (3.75) can be therefore be neglected. The time to initiate boiling can be expressed using H_{shock} (Canney *et al* 2010a, Khokhlova *et al* 2011)

$$t_b = \frac{\Delta T c_v}{H_{\text{shock}}} \tag{3.78}$$

where ΔT is the temperature difference between the ambient and boiling temperature (100^{o}C) and c_v is the specific heat capacity at constant volume. Canney *et al* (2010a) demonstrated that the experimentally measured time taken to form a boiling bubble at the HIFU focus in an optically transparent tissue phantom is in agreement with the calculated temperature fields obtained by solving either equation (3.75) or (3.78) to within experimental error.

The HIFU Simulator 1.2 (Soneson 2009) was used in this thesis to solve the KZK (3.72) and the BHT (3.75) equations to obtain acoustic pressure and temperature fields at the HIFU focus as a function of electrical power supplied to a HIFU source. This open KZK-BHT source software written in MATLAB® (MathWorks Inc., R2013a) has been widely used and validated experimentally by other HIFU studies on cavitation cloud histotripsy (Xu *et al* 2013), cavitation enhanced heating in liver (Chen *et al* 2012), HIFU beam profile (Soneson and Myers 2007), temperature measurements in *ex vivo* muscle (Maruvada *et al* 2012) and the formation of HIFU thermal lesions in *ex vivo* tissues (Xu *et al* 2012).

Simulated acoustic pressure waveforms and temperature fields at the HIFU focus were used (a) as input acoustic pressure p_a in the Gilmore bubble model (3.30) to excite a single bubble and (b) to predict the time to reach boiling. In this thesis, boiling is assumed to be 100ºC for aqueous media.

3.4. A piecewise constant approximation for the dynamics of a bubble

It is known that tissue temperature rapidly increases in the course of boiling histotripsy. This eventually results in the variation of:

- the physical properties of the surrounding medium;
- the saturated water vapour density and Henry's constants for different gas species.

One simple approach to take into account the effects of the temperature-dependent parameters on the bubble dynamics is to apply a piecewise constant approximation. The change of tissue temperature with time at the HIFU focus was initially obtained from the BHT simulation. The saturated water vapour density, Henry's constants for incondensable gases and the physical properties of liver were then calculated using equations (3.41), (3.45) and (3.65)–(3.70) for each simulated temperature step $T_{0,n}$. Additionally, the initial bubble boundary conditions BCs (i.e. bubble radius R_0, bubble wall velocity $\dot{R}_0$, temperature inside the bubble T_{b0} and molecular contents

$N_{vap,0}$, $N_{O2,0}$, $N_{N2,0}$, $N_{Ar,0}$) at $T_{0,n}$ were updated from the previous numerical results simulated at $T_{0,n-1}$. Figure 3.5 shows an example of the piecewise constant approach used in this thesis. With the help of this approach, the dynamics of a single bubble in the liver can be investigated as a function of temperature variation from 20°C to 100°C.

The effects of the temperature-dependent parameters on acoustic and temperature fields were neglected in the KZK and the BHT simulations.

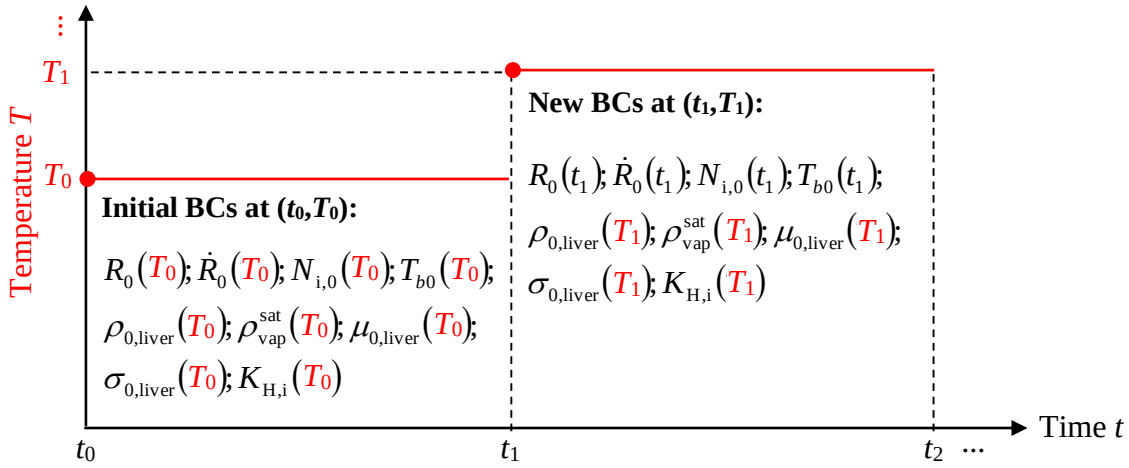

Figure 3.5. An example of the piecewise constant approach used in the thesis. R_0, $\dot{R}_0$, $N_{i,0}$ at t_0 are obtained from equation (3.61). Saturated water vapour density, Henry's constants for incondensable gases and the physical properties of liver are calculated using equations (3.41), (3.45) and (3.65)–(3.70), respectively.

3.5. Quantification method of stable and inertial cavitation

As described in Chapter 2, acoustic cavitation activity can be categorised into two types: stable and inertial cavitation. When a pre-existing bubble nucleus in liquids is excited by an incident acoustic wave, it will oscillate and emit acoustic pressure waves in all directions. These emitted waves are referred to as acoustic emissions (Neppiras 1980). The two distinct types of cavitation activity can be identified by the frequency spectrum of the acoustic emissions. The spectrum induced by bubble oscillations and collapses contains broadband emissions and subharmonics (of the

form f_0/m, where m is a positive integer), superharmonics (mf_0) and ultraharmonics (nf_0/p, p is a positive integer and $n > p$) of the insonation ultrasound frequency f_0 (Leighton 1994). Stable cavitation consisting of both linear and nonlinear radial bubble oscillations can be detected using the specific spectrum components at subharmonics and superharmonics (Nepirras 1980, Miller 1981), whereas both ultraharmonics and broadband emissions are indicators for inertial cavitation (Leighton 1994, Basude and Wheatley 2001). The broadband component is the result of the short-duration pressure spikes (shockwaves) caused by collapsing bubbles (i.e. the violent collapse of the bubble re-radiates energy across a broad spectrum of frequencies) (Leighton 1994).

When analysing cavitation activity for a given HIFU exposure condition in this thesis, the Akulichev equation (3.39) is employed to calculate the time-varying radiated acoustic pressure resulting from radial bubble motions in the form of an outward travelling spherical wave. This simulated radiated pressure is then converted to the frequency domain for characterising and quantifying cavitation activity, using a fast Fourier transform (FFT). The quantification process used in this thesis is similar to the methods described by Chen *et al* (2003b), Tu *et al* (2006a,b), Farny *et al* (2009) and Zhou and Gao (2013). In an FFT plot, specific narrow frequency windows with a fixed bandwidth of 0.1 MHz, whose central frequencies are the mean values of each harmonic component of the fundamental frequency, are chosen to investigate broadband emissions resulting from inertial cavitation (IC). Meanwhile, multiple harmonics, excluding the fundamental frequency, are used to indicate stable cavitation (SC). Cavitation activity is quantified by integrating the areas under the specified frequency windows and these are cumulated to obtain the "amount" or "dose" of SC and IC. The width of 0.1 MHz was chosen in order to have sufficient number of data points within the specified frequency windows for the integration. As there is no "absolute" basis by which to quantify the "amount" of cavitation that has occurred (Chen *et al* 2003b), these values provide relative measures of cavitation under a given HIFU insonation condition. Figure 3.6 shows an example for characterising and quantifying IC and SC.

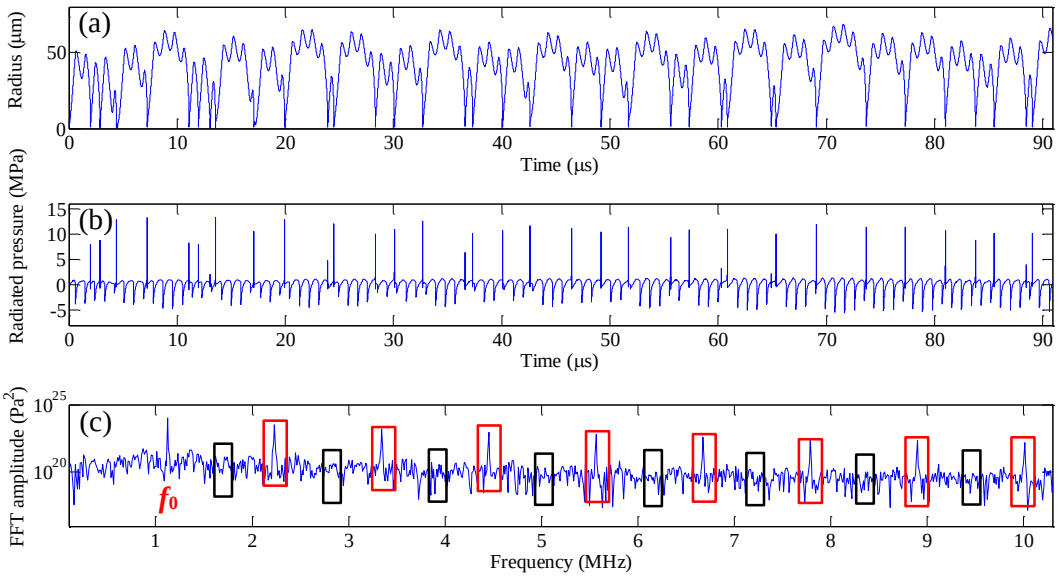

Figure 3.6. Illustrating the methods for quantifying IC and SC. (a) Radius vs time curve. (b) Corresponding simulated radiated pressures. The large amplitude short-duration pressure spikes are due to the collapses of bubble. (c) Corresponding FFT plot with the specified windows for IC (within the black solid line) and SC (within the red solid line). Cavitation activity is quantified by integrating the areas under the specified frequency windows and these are cumulated to obtain the "amount" of SC and IC.

3.6. Summary

The main objective of this Chapter was to develop a model for the dynamics of a single spherical gas-vapour bubble in the liver exposed to HIFU fields. The present model accounted for the compressibility and heat and mass transport (gas and water vapour) across the bubble wall. The main components of the bubble model were the Gilmore model (equation 3.30) for describing radial bubble motions, the Hertz-Knudsen model (equation 3.40) for water vapour transport (evaporation and condensation), Fick's law (equation 3.43) for non-condensable gas diffusion, heat conduction (equation 3.47) through a bubble wall and the first law of thermodynamics (equation 3.59) for calculating the temperature inside the bubble. The latent heat of evaporation and condensation was neglected. The numerical model was compared and validated against the results produced by Storey and Szeri (2000) and Matula *et al* (2002) for the cases of a single-bubble sonoluminescence (SBSL) and a lithotripsy bubble in water.

Furthermore, a piecewise constant approximation method (see Figure 3.5) was introduced and adopted into the bubble model in order to describe the dynamics of a single bubble as a function of temperature variation. This approach is important for investigating the bubble dynamics induced by boiling histotripsy because the surrounding tissue temperature rapidly increases to 100^{o}C in the course of HIFU exposure. The temperature-dependent liver properties were assumed to follow similar trends to those of water. The BHT equation (3.75) was initially used to obtain the change of tissue temperature with time at the HIFU focus. The saturated water vapour density, Henry's constants and the physical properties of liver were then calculated using the empirical equations (3.41), (3.45) and (3.65–3.70) for each temperature step $T_{0,n}$. In addition, the initial bubble boundary conditions for bubble radius, bubble wall velocity, temperature inside the bubble and molecular contents (gas and water vapour) at $T_{0,n}$ were obtained from the numerical results simulated at $T_{0,n\text{-}1}$.

Numerical simulations of the bubble dynamics resulting from exposure of the bubble to HIFU boiling histotripsy, will be presented and discussed in the following chapter.

Chapter 4. Numerical observations of boiling histotripsy bubble dynamics in liver

A suitable numerical model describing the bubble dynamics excited by an ultrasound field was formulated and validated in Chapter 3. The compressibility and heat and mass transport of gas and water vapour were included in the model.

As mentioned in Chapter 2, a HIFU treatment site appears as a bright hyperechoic region on B-mode ultrasound images during the course of either HIFU thermal ablation or boiling histotripsy. In the case of a HIFU thermal ablation process, the appearance of a boiling bubble in the HIFU focal region can be highly undesirable because increased scattering by the bubble can help promote near-field heating. This creates a tadpole shaped thermally ablated lesion, which is unpredictable in size and shape. On the contrary, the formation of a boiling bubble at the HIFU focal zone is essentially required to initiate the mechanical tissue fractionation process during boiling histotripsy. Additional information to echogenicity is, therefore, needed to help monitor (a) HIFU treatment under different exposure conditions (thermal ablation and boiling histotripsy) and (b) the presence of a boiling bubble at the HIFU focus.

In this Chapter, the numerical bubble model described in the previous chapter will be implemented to:

- Investigate the dynamics of a single spherical gas-vapour bubble in the liver exposed to different HIFU fields;

- Evaluate and distinguish between the different types of acoustic cavitation activity which occur as a result of (a) thermally induced HIFU ablation and (b) mechanically induced lesions caused by HIFU boiling histotripsy.

4.1. Dynamics of a single bubble in the liver at constant temperature

4.1.1. Effects of the shapes of acoustic waveforms on an oscillating bubble in the absence of any heat or mass transfer

The effect of different shapes of acoustic pressure waveforms on the dynamics of a single bubble, was investigated in the absence of any heat or mass transfer. Three acoustic pressure waveforms with the variation in the shock parameter σ_{sh} (the degree of nonlinear distortion of the wave) were considered: purely sinusoidal (WF1, σ_{sh} = 0), slightly distorted with harmonic components up to the third harmonic (WF2, σ_{sh} = 4.5) and nonlinear shocked (WF3, σ_{sh} = 10.8). The KZK equation (3.72) was used to calculate the acoustic pressure waveform at the focus, from which the peak positive (P_+) and peak negative (P_-) pressures and the shock parameter (σ_{sh}) were obtained. The waveforms were computed in liver tissue as a function of the electrical power (P_{elect}) supplied to a 1.1 MHz HIFU transducer (H102, Sonic Concepts, Bothell, WA, USA). This HIFU source will be used for *ex vivo* experiments performed in Chapter 6. Simulated slightly distorted nonlinear waves (P_{elect} = 60 W, P_+ = 13.4 MPa, P_- = –7.5 MPa, hereafter referred to as thermal ablation) and nonlinear-shocked waves (P_{elect} = 350 W, P_+ = 82 MPa, P_- = –15 MPa, boiling histotripsy) are shown in Figure 4.1. These acoustic pressure waveforms were used as input acoustic pressure p_a in the bubble model (see equation 3.32) to excite a single bubble. The simulated *in situ* peak pressure values for thermal ablation and boiling histotripsy exposure conditions were chosen, because (a) Pahk *et al* (2015) produced a well-defined thermally ablated lesion in an *ex vivo* liver with P_+ of 13.4 MPa, P_- of –7.5 MPa and (b) P_+ = 82 MPa and P_- = –15 MPa were within the range of required pressure values reported by other boiling histotripsy studies (Khokhlova *et al* 2011, Wang *et al* 2013). The physical parameters used in the acoustic field simulation are listed in Table 4.1. For a focused Gaussian beam, the shock parameter σ_{sh} can be obtained using (Hamilton and Blackstock, 2008)

$$\sigma_{\mathrm{sh}} = \frac{\beta \varepsilon k_{\mathrm{w}} d_{\mathrm{rc}}}{\sqrt{1-G_f^{-2}}} \ln\left[\left(G_f + \sqrt{G_f^2 - 1}\right)\left(R_c + \sqrt{R_c^2 + 1}\right)\right] \text{ with } R_c = -\left(1 - z_l / d_{\mathrm{rc}}\right)\left(G_f^2 - 1\right)^{1/2} \qquad (4.1)$$

In equation (4.1), ε is the ratio of the particle velocity amplitude at the sound source to the small-signal sound speed c_0, k_w is the acoustic wave number, d_{rc} is the radius of curvature of the source (i.e. focal length), G_f is the focal gain and z_l is the distance from the sound source.

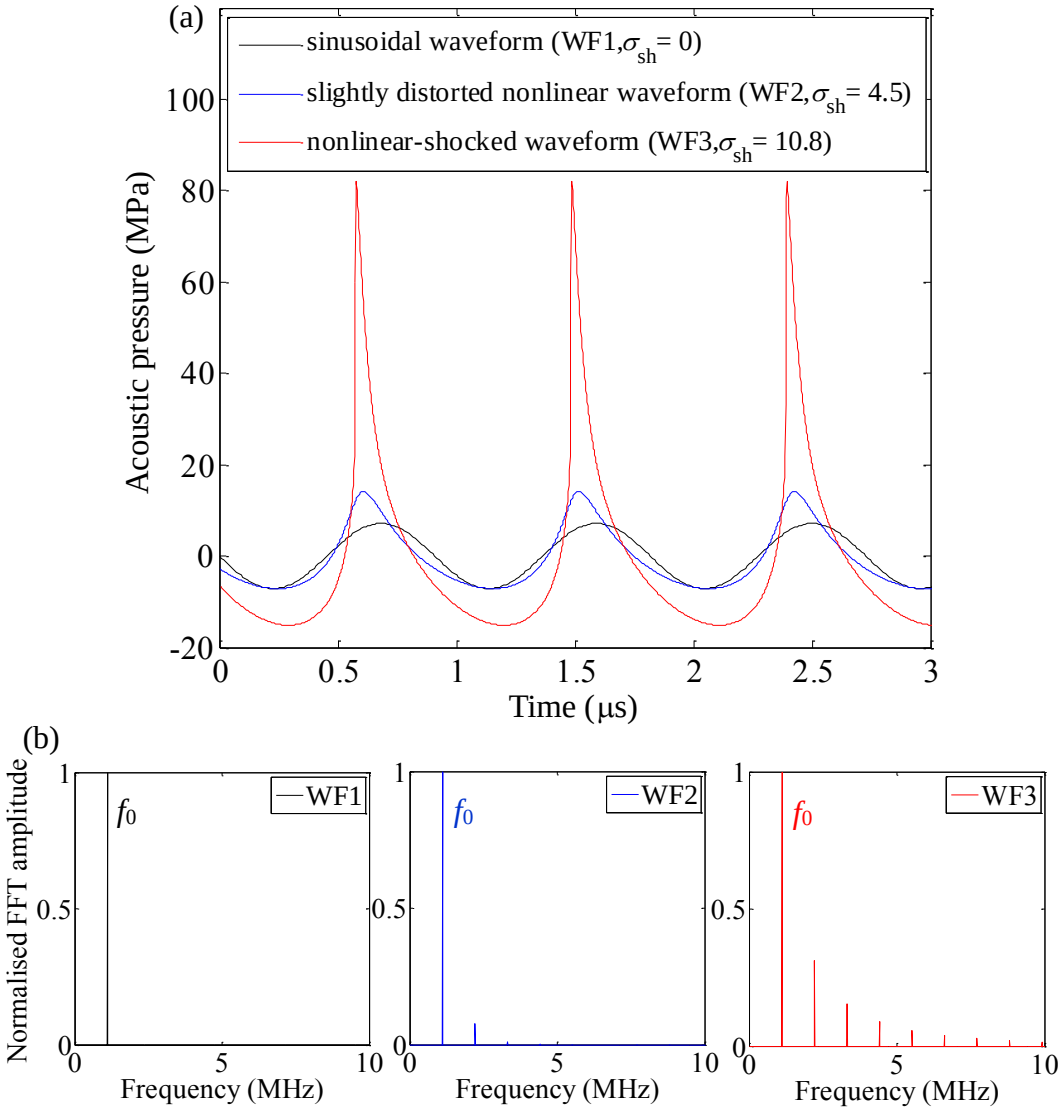

Figure 4.1. (a) Sinusoidal (WF1, black solid line, P_+ = 7.5 MPa), slightly distorted nonlinear (WF2, blue solid line, thermal ablation, P_+ = 13.4 MPa, P_- = –7.5 MPa) and nonlinear-shocked (WF3, red solid line, boiling histotripsy, P_+ = 82 MPa, P_- = –15 MPa) waveforms at the HIFU focus with a driving frequency of 1.1 MHz. P_+ and P_- are within the range of required pressure values reported by other boiling histotripsy studies (Khokhlova *et al* 2011, Wang *et al* 2013). (b) Corresponding frequency spectra over 100 acoustic cycles. f_0 is the fundamental frequency.

Parameter	HIFU transducer	
driving frequency	1.1 MHz	
outer radius of HIFU transducer	3.2 cm	
inner radius of HIFU transducer	1 cm	
geometric focal length	6.26 cm	
focal gain	35.8	
electrical power	60 W (thermal ablation) and 350 W (boiling histotripsy)	
efficiency of HIFU transducer	85%	
	Water	**Liver (Choi *et al* 2013)**
small-signal speed of sound	1482 $m \cdot s^{-1}$	1575 $m \cdot s^{-1}$
mass density	998.2 $kg \cdot m^{-3}$	1060 $kg \cdot m^{-3}$
absorption at 1 MHz	0.217 $dB \cdot m^{-1}$	52 $dB \cdot m^{-1}$
exponent of absorption vs frequency curve	2	1.1
coefficient of nonlinearity	3.5	4.4
number of harmonics used in the KZK equation	200	200

Table 4.1. Parameters used in the KZK equation (3.72) for simulating an acoustic field in the liver. The electrical powers supplied to a 1.1 MHz HIFU source were 60 W and 350 W for the slightly distorted nonlinear waveforms (WF2, thermal ablation) and the nonlinear-shocked waves (WF3, boiling histotripsy), respectively. The HIFU focus was set to 5 mm below the surface of the liver. The characteristics of the HIFU source were calibrated and provided by the manufacturer (Sonic Concepts, Bothell, WA, USA).

At first, the bubble dynamics in the liver exposed to both sinusoidal (WF1, $P_- = -15$ MPa, $\sigma_{sh} = 0$) and nonlinear-shocked (WF3, boiling histotripsy, $P_+ = 82$ MPa, $P_- = -15$ MPa, $\sigma_{sh} = 10.8$) waveforms were compared at a temperature of 20°C. Because acoustic cavitation threshold is dependent upon peak negative pressure at a given driving frequency (Kreider *et al* 2011a), the peak negative pressure amplitude of the sinusoidal wave was matched to that of the shockwave. The initial bubble radius was chosen as $R_0 = 15$ μm in the bubble simulations as this demonstrated the effect of the different shapes of the acoustic pressure waveforms after only a few acoustic cycles. The physical parameters of the liver at 20°C used in the bubble model are displayed in Table 4.2.

Figure 4.2 shows the responses of a single spherical gas bubble driven by the sinusoidal (WF1) and the nonlinear-shocked (WF3) waves. For the sinusoidal excitation case (see Figure 4.2(a)), the bubble continues to grow and collapse with time; whereas the nonlinear-shocked waveform leads the bubble to respond more to the negative pressure cycle and its radial motion is biased towards increase over

each acoustic cycle (indicated by an arrow in Figure 4.2(a)). This bubble behaviour is known as rectified bubble growth and is thought to be due to the asymmetry between compressive and tensile portions of shocked waveforms (Kreider *et al* 2011a).

In contrast with the explosive bubble growth caused by the nonlinear-shocked waves (WF3, σ_{sh} = 10.8), no rectified radial motion is observed under the slightly distorted nonlinear waveforms (WF2, σ_{sh} = 4.5) as shown in Figure 4.2(b). Nevertheless, the bubble growth is enhanced (maximum bubble radius R_{max} = 65 μm) compared with that of the sinusoidal excitation (R_{max} = 63 μm) since it has a slightly longer duration of negative pressure cycle than that of the sine wave.

Symbol	Definition	Liver at 20°C
ρ_0	density	1058 kg·m^{-3}
c_0	speed of sound	1575 m·s^{-1}
μ_0	viscosity	0.0087 kg·m^{-1} s^{-1}
σ_0	surface tension	0.056 N·m^{-1}
γ	polytrophic exponent of a diatomic gas (air)	1.4
p_0	ambient pressure	1.01325×10^5 Pa
T_0	ambient temperature	20 °C
m	empirical material dependent constant	5.527
A_m	empirical material dependent constant	614.6 MPa
B_m	empirical material dependent constant	$A - p_0$ MPa

Table 4.2. Parameters used in the Gilmore bubble model at T_0 = 20°C. The density, speed of sound, viscosity and the surface tension were calculated using equations (3.65)–(3.70) described in Chapter 3. The material dependent constants m and A_m for the liver were obtained from Pahk *et al* (2015).

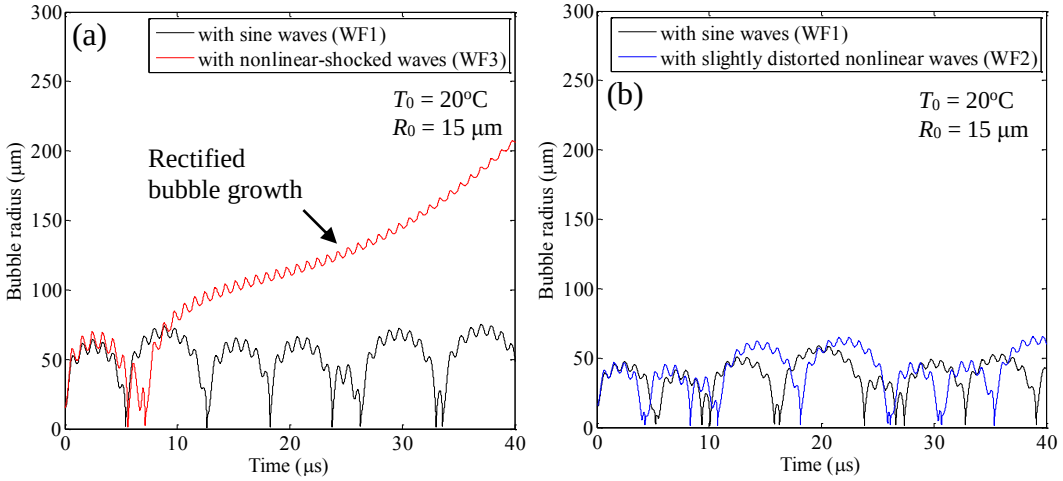

Figure 4.2. Radius vs time curves at T_0 = 20ºC in the absence of any heat or mass transfer at the bubble wall. (a) resulting from the sinusoidal waves (WF1, black solid line, P_- = –15 MPa) and the nonlinear-shocked waveforms (WF3, red solid line, boiling histotripsy, P_+ = 82 MPa, P_- = –15 MPa at the focus). (b) with the sinusoidal waves (WF1, black solid line, P_- = –7.5 MPa) and the slightly distorted nonlinear waves (WF2, blue solid line, thermal ablation, P_+ = 13.4 MPa, P_- = –7.5 MPa at the focus). The initial radii were 15 µm in the simulations.

Additional calculations were performed with the variation in the shock parameters σ_{sh} from 5 to 9. This was to investigate the effects of the nonlinear distortion of the waveform on the bubble growth. Acoustic waveforms used in the simulations are plotted in Figure 4.3(a). Figure 4.3(b) shows the dynamics of a single gas bubble as a function of the shock parameter σ_{sh} = 5, 7 and 9. As σ_{sh} increases, the maximum bubble radius R_{max} becomes larger. However, rectified bubble growth only appears when σ_{sh} = 9. This is summarised in Table 4.3.

Shock parameter σ_{sh}	**P_+ (MPa)**	**P_- (MPa)**	**R_{max} (µm)**	**Does rectified bubble growth appear?**
5	16.4	–8.7	69.9	No
6	22.2	–9.9	73.0	No
7	29.7	–11.1	75.4	No
8	39.9	–12.1	77.9	No
9	55.4	–13.4	124.1	***Yes***

Table 4.3. The effects of the degree of nonlinear distortion of the waveform on the bubble growth.

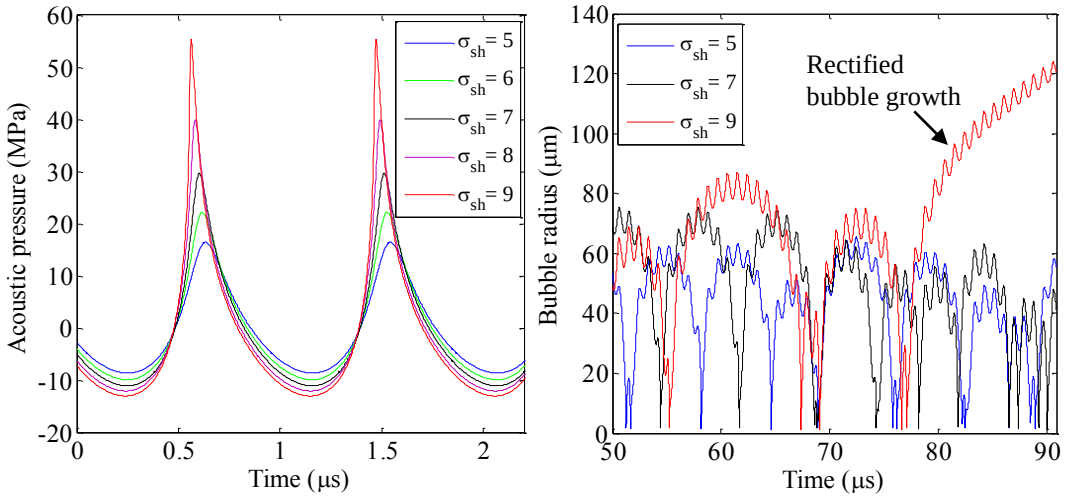

Figure 4.3. (a) Simulated acoustic waveforms with σ_{sh} = 5 to 9. (b) Radius vs time curves with σ_{sh} = 5, 7 and 9 over 100 acoustic cycles. The initial bubble radii were 15 μm in the simulations.

4.1.2. Effects of heat and mass transfer on an oscillating bubble

Khokhlova *et al* (2011) demonstrated that purely mechanical damage of soft tissue is only observed when both boiling and shockwaves are present at the HIFU focus. Figure 4.4 shows the responses of a 1 μm gas-vapour bubble in the liver excited by the nonlinear-shocked waves (WF3, P_+ = 82 MPa, P_- = –15 MPa, σ_{sh} = 10.8) at a boiling temperature of 100°C. Temperature-dependent physical properties of liver at 100°C (i.e. density, speed of sound, viscosity and surface tension) were used in the simulations and are given in Table 4.4.

Symbol	Definition	Liver at 100°C
ρ_0	density	1015 kg·m^{-3}
c_0	speed of sound	1640 m·s^{-1}
μ_0	viscosity	2.3×10^{-3} kg·m^{-1}s^{-1}
σ_0	surface tension	0.0453 N·m^{-1}

Table 4.4. Physical properties of liver at T_0 = 100°C used in the bubble model. These values were calculated using equations (3.65)–(3.70) described in Chapter 3. The material dependent constants m, A_m and B_m are shown in Table 4.2.

When accounting for both the heat and mass transport in the bubble model, rectified bubble growth is caused by the combination of the asymmetry in shockwaves and water vapour (H_2O) that transports into the bubble at 100^{o}C. Examining the molecular contents of H_2O and of the gas in the bubble (see Figure 4.4(b)), it is noticed that the number of gas molecules gradually increases over each acoustic cycle by rectified gas diffusion (Crum 1984); however H_2O behaves differently. The number of H_2O molecules in the bubble decreases at 30 μs, causing it to shrink. This amount is then biased towards increase by rectified heat transfer (Hao and Prosperetti 1999, 2002) at 40 μs, leading to the explosive bubble growth with an average growth rate of U = 7 m·s^{-1} (see Figure 4.4(a)). In addition, water vapour comprises the majority of the bubble contents during the growth phase (99.99% molar basis, see Figure 4.4(b)). Rectified bubble growth can also be observed without gas diffusion (i.e. accounting for vapour transfer only), as shown in Figure 4.4(c) and (d).

When neglecting the water vapour transport in the bubble model (i.e. accounting for gas diffusion only), rectified bubble growth does not occur (see Figure 4.4(e) and (f)). However, the maximum bubble radius R_{max} is 1.2 times larger than that which would occur with shockwaves only (R_{max} = 58 μm, the blue line in Figure 4.4(a)). The effects of vapour transport on the radial bubble motion at 100^{o}C are summarised in Table 4.5.

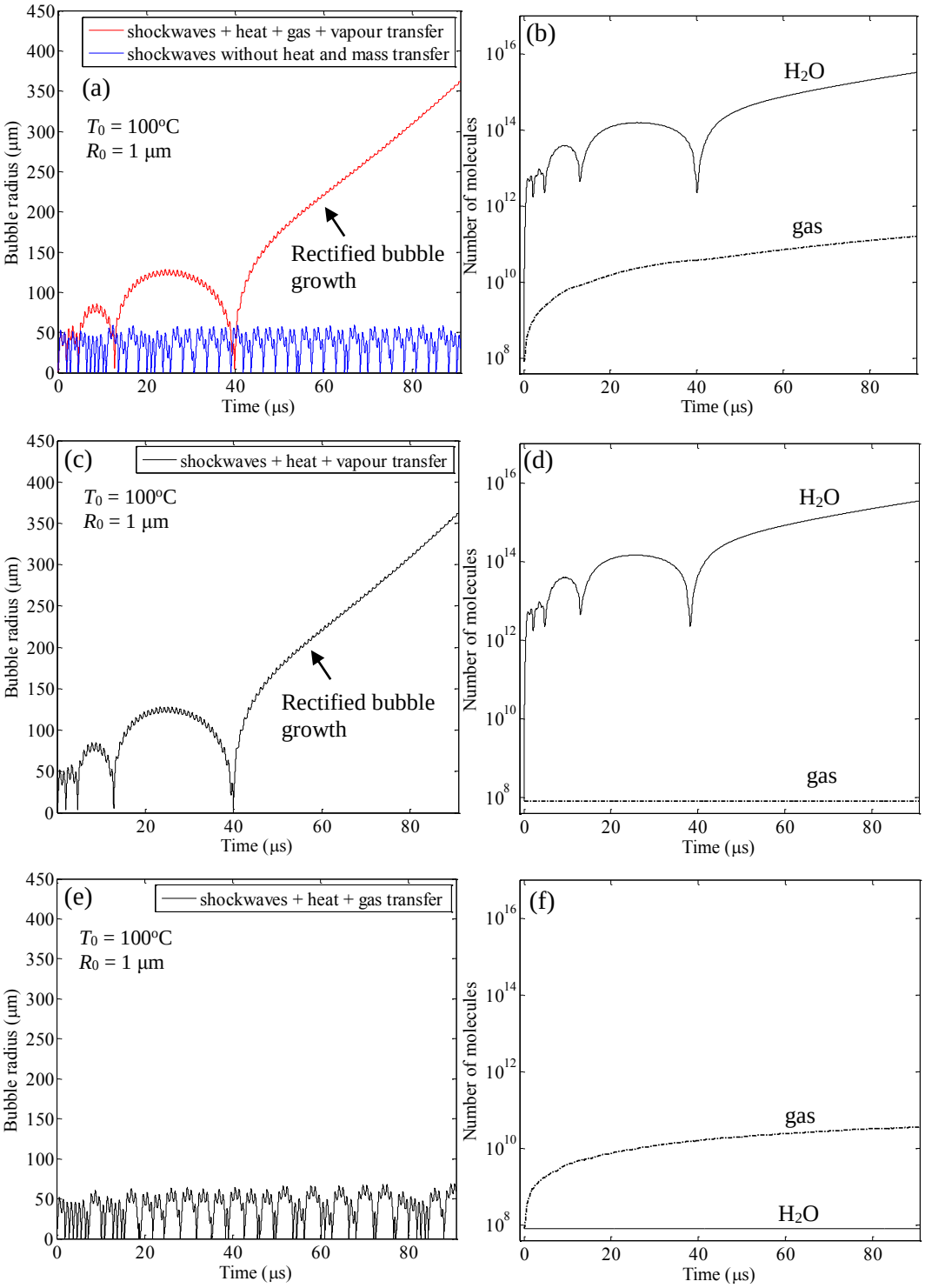

Figure 4.4. Dynamics of a 1 μm gas-vapour bubble in the liver at 100°C with the nonlinear-shocked waveforms (WF3, P_+ = 82 MPa, P_- = –15.1 MPa) over 100 acoustic cycles. (a) Radius vs time curves with (red solid line) and without (blue solid line) heat and mass transfer. (b) Corresponding molecular contents of water vapour and gas of (a). (c) Radius vs time curve without gas diffusion. (d) Corresponding molecular contents of (c). (e) Radius vs time curve without water vapour transport. (f) Corresponding molecular contents of (e).

Bubble simulation conditions at 100ºC	Does rectified bubble growth appear?	R_{max} (μm)
Shockwaves (SWs) only	No	58
SWs + heat + gas transfer	No	69
SWs + heat + vapour transfer	**Yes**	362
SWs + heat + gas + vapour transfer	**Yes**	370

Table 4.5. The effects of water vapour on the bubble dynamics at a boiling temperature of 100ºC.

Removing the impact of the asymmetry in the acoustic waveform shape on the bubble growth, a sinusoidal excitation (WF1) at P_- = –15 MPa can lead to rectified bubble growth with U = 2.2 m·s^{-1} by vapour transport when ambient temperature exceeds 100ºC, as shown in Figure 4.5.

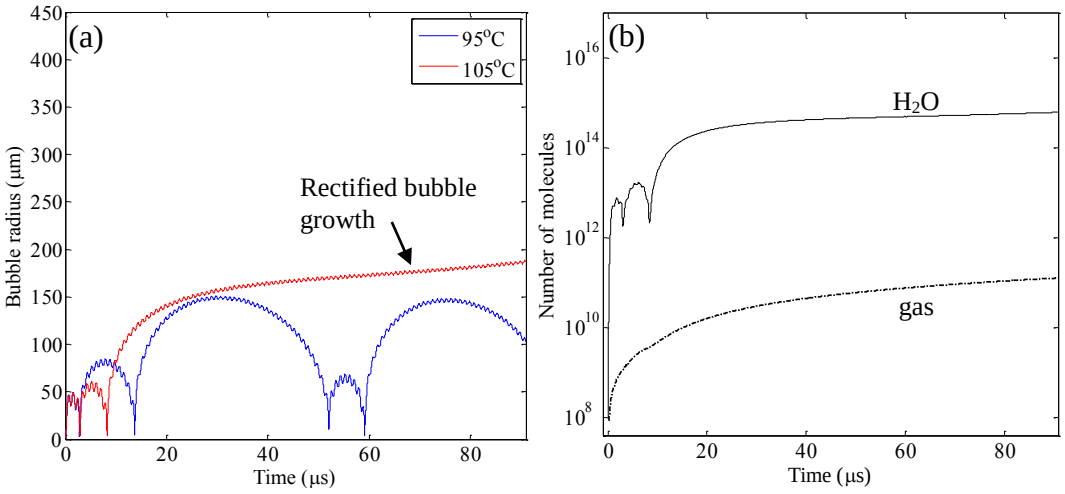

Figure 4.5. (a) Radius vs time curves with the sinusoidal waves (WF1, P_- = –15 MPa) at temperatures of 95ºC (blue solid line) and 105ºC (red solid line) over 100 acoustic cycles. (b) Corresponding molecular contents of (a) at 105ºC. The initial bubble radii were 1 μm.

4.2. Dynamics of boiling histotripsy bubbles and acoustic emissions in liver as a function of temperature variation

4.2.1. Radial bubble motion

The piecewise constant approximation method described in Chapter 3 (see section 3.4) was implemented to explore the bubble dynamics as a function of temperature variation. In the bubble simulations, the surrounding temperature T_0 was varied from 20°C to 100°C with ΔT_0 = 10°C/200 acoustic cycles. The initial bubble boundary conditions (bubble radius, bubble wall velocity, temperature inside the bubble and molecular contents) and the physical properties of the liver were updated at each temperature step. The responses of a 1 μm gas-vapour bubble in the liver exposed to both the slightly distorted nonlinear (WF2, thermal ablation, P_+ = 13.4 MPa, P_- = –7.5 MPa) and the nonlinear-shocked waves (WF3, boiling histotripsy, P_+ = 82 MPa, P_- = –15 MPa) are shown in Figure 4.6. For both HIFU excitations, the time of the bubble growth phase increases as the surrounding temperature increases. When the temperature reaches a boiling temperature of 100°C, rectified bubble growth occurs at 1.45 ms under the nonlinear-shocked waves (WF3) with an average bubble growth rate of U = 3.4 m·s^{-1} (see Figure 4.6(a)). This rectified radial motion can also be attained via exposure to the slightly distorted nonlinear waveform (WF2) with U = 2.3 m·s^{-1}, once the surrounding temperature exceeds 100°C (see Figure 4.6(b)).

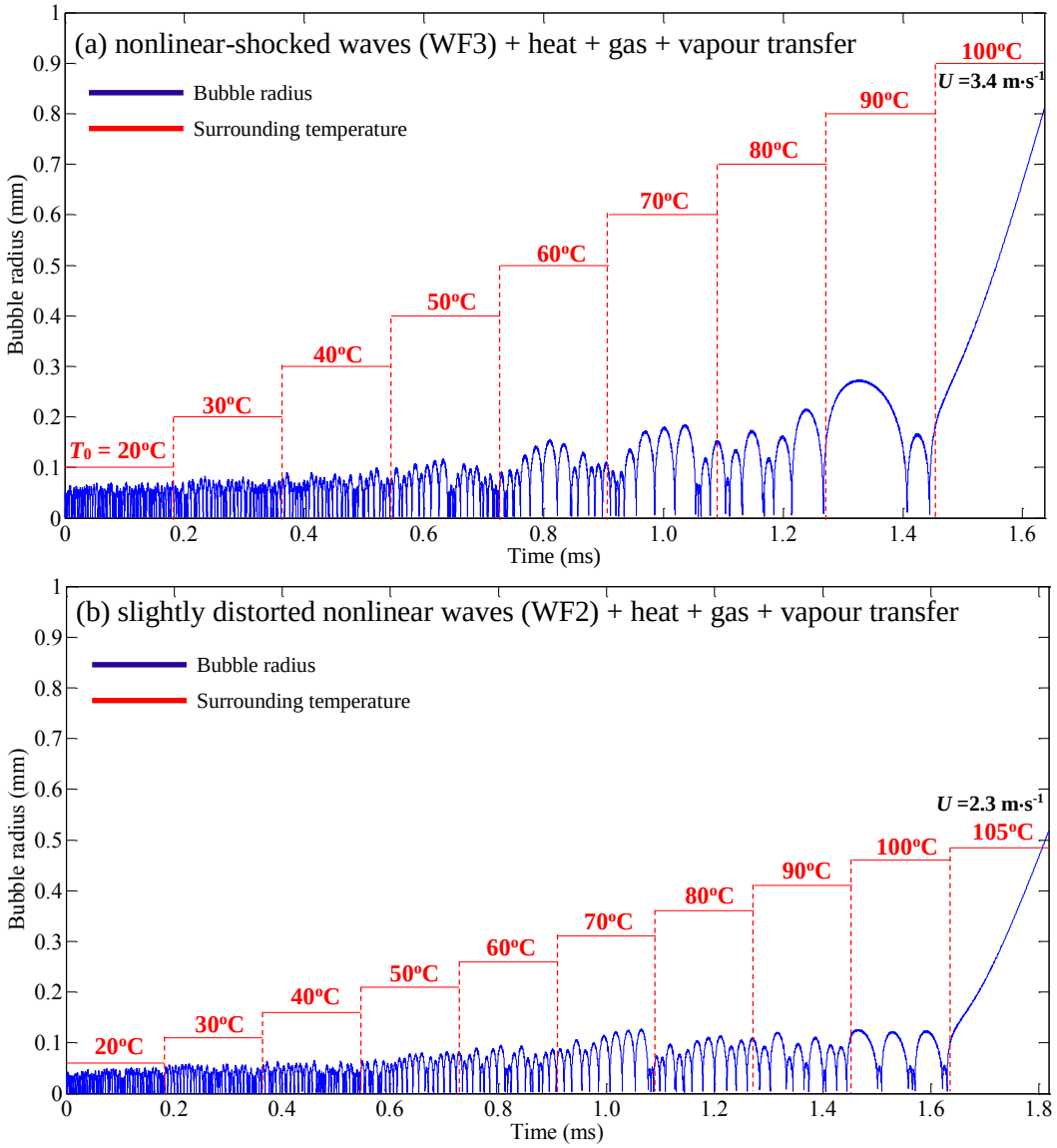

Figure 4.6. Dynamics of a 1 μm gas-vapour bubble as a function of temperature variation from 20ºC to 100ºC with ΔT_0 = 10ºC/200 acoustic cycles. Radius vs time curves with (a) the nonlinear-shocked waves (WF3, boiling histotripsy, P_+ = 82 MPa, P_- = –15 MPa) and (b) the slightly distorted nonlinear waveforms (WF2, thermal ablation, P_+ = 13.4 MPa, P_- = –7.5 MPa). The liver properties (density, speed of sound, viscosity and surface tension) that change with temperature were calculated using equations (3.65)–(3.70).

Additional simulations were performed with the reduction of the surrounding temperature from 100ºC to 70ºC under the nonlinear-shocked wave excitation case (WF3). This was to investigate whether a boiling vapour bubble continuously undergoes rectified growth when the size of the bubble becomes larger than that of a localised super-heated region (100ºC) at the HIFU focus (i.e. the surrounding

temperature becomes lower than 100ºC). It is observed in Figure 4.7 that the average bubble growth rate decreases to 2.9 m·s^{-1} (90ºC), 1.3 m·s^{-1} (80ºC) and –1.1 m·s^{-1} (70ºC).

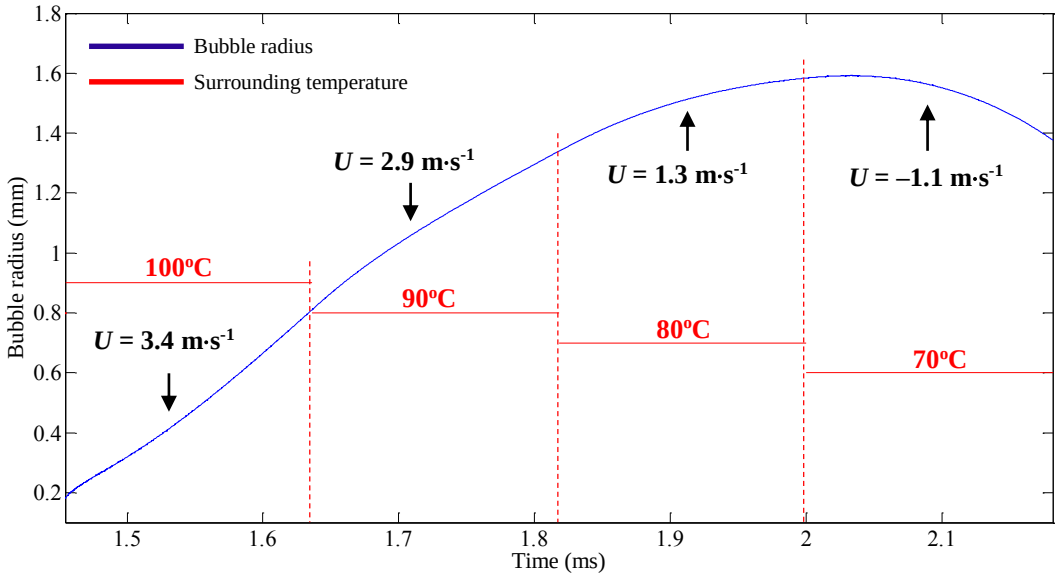

Figure 4.7. Radius vs time curve under the nonlinear-shocked waves (WF3, P_+ = 82 MPa, P_- = –15 MPa) at temperatures of 100ºC, 90ºC, 80ºC and 70ºC.

4.2.2. Acoustic emissions

Radiated acoustic pressures resulting from the bubble radial motions plotted in Figure 4.6 were calculated using the Akulichev equation (3.39) to investigate the changes in the emitted acoustic signal as a function of changes in the incident acoustic field. The simulated time-varying radiated pressures were converted to the frequency domain using a fast Fourier transform (FFT). Stable (SC) and inertial (IC) cavitation doses were quantified using the method described in Chapter 3 (see section 3.5). The passive cavitation detector (PCD) used as part of the *ex vivo* experiments carried out in this thesis (which will be detailed in Chapter 6), features a bandwidth of 10 kHz–20 MHz. It was, therefore, possible to consider multiple harmonic components of the fundamental frequency (f_0 = 1.1 MHz), up to 18th harmonic (19.8 MHz). In an FFT plot, multiple harmonics (of the form nf_0, where n is a positive integer) with a fixed bandwidth of 0.1 MHz were used to indicate SC. Specific narrow frequency windows, with a width of 0.1 MHz, were chosen for IC. The central frequency of each window (of the form $(2n+1)f_0/2$) was obtained from

the mean value of adjacent harmonics of the fundamental frequency. The areas under the specified frequency windows were integrated and these were cumulated to obtain SC and IC doses.

Figure 4.8 shows the radiated acoustic pressures and the corresponding spectrograms (frequency vs time) during boiling histotripsy (WF3, nonlinear-shocked waves) and thermal ablation (WF2, slightly distorted nonlinear waves) exposures. For the boiling histotripsy insonation, there are noticeable differences in the acoustic emissions before and after t = 1.45 ms. In the radiated pressure vs time plot (see Figure 4.8(a)), the pressure amplitude is fairly uniform; it, however, increases significantly at t = 1.45 ms. The corresponding spectrogram also indicates these changes (see Figure 4.8(b)). Multiple harmonic components from 1.1 MHz to 8.8 MHz (first to eighth harmonic) can be observed before t = 1.45 ms followed by the significant occurrence of higher harmonics up to 19.8 MHz (18^{th} harmonic) at t = 1.45 ms. The presence of these multiple harmonics in the spectrogram is due to strongly nonlinear radial bubble oscillations and is the indication of stable cavitation (Pahk *et al* 2015). The time of occurrence of a local maximum in the radiated pressure vs time curve, as well as in the spectrogram, matches the onset of the rectified bubble growth plotted in Figure 4.6(a).

Prior to the inception of rectified radial motions at t = 1.45 ms, higher order multiple harmonic components with larger amplitudes gradually appear in the spectrogram whilst the magnitude of the levels of broadband emissions reduces with time (see Figure 4.8(b)). The broadband component is the result of the short-duration pressure spikes caused by violent bubble collapses (Leighton 1994). The corresponding quantified SC and IC doses plotted in Figure 4.9 also indicate the inverse relationship between SC and IC with time.

In contrast to the acoustic emissions which occur during the boiling histotripsy exposure, a lower peak-to-peak radiated pressure amplitude and lower multiple harmonics with lower levels of broadband emissions are observed under the thermal ablation exposure (see Figure 4.8(a),(c) and Figure 4.10). Indeed, the amount of

quantified cavitation dose (both SC and IC) is less than that produced by the boiling histotripsy insonation (see Figure 4.9).

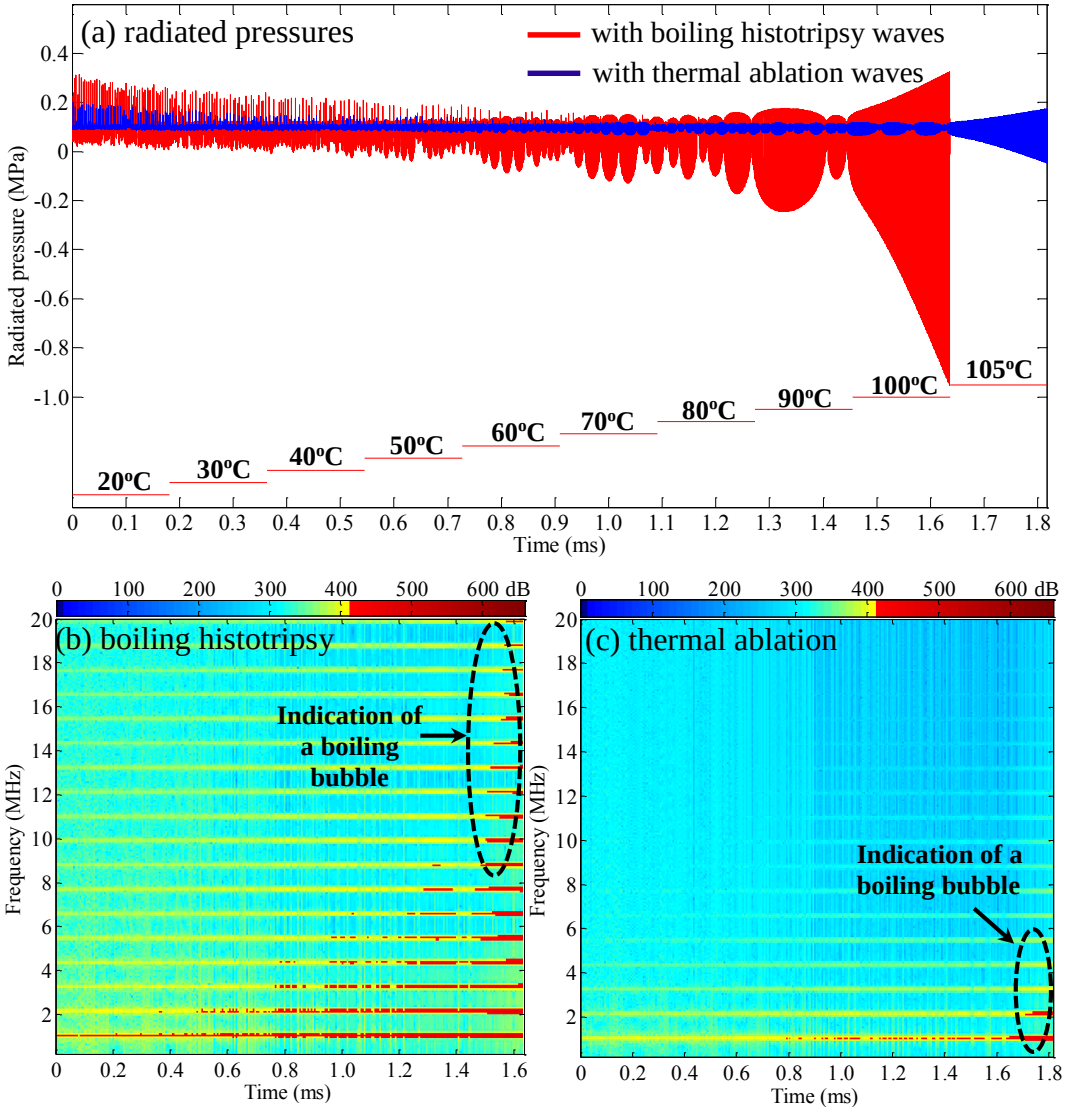

Figure 4.8. Simulated radiated pressures and spectrograms with the thermal ablation (WF2, slightly distorted nonlinear waveforms, P_+ = 13.4 MPa, P_- = –7.5 MPa) and the boiling histotripsy (WF3, nonlinear-shocked waves, P_+ = 82 MPa, P_- = –15 MPa) exposures. (a) Radiated acoustic pressures during the boiling histotripsy (WF3, red solid line) and the thermal ablation (WF2, blue solid line) insonations. (b) and (c) are the corresponding spectrograms for the boiling histotripsy and the thermal ablation exposures, respectively. A sampling frequency of 22 GHz was used in the simulations.

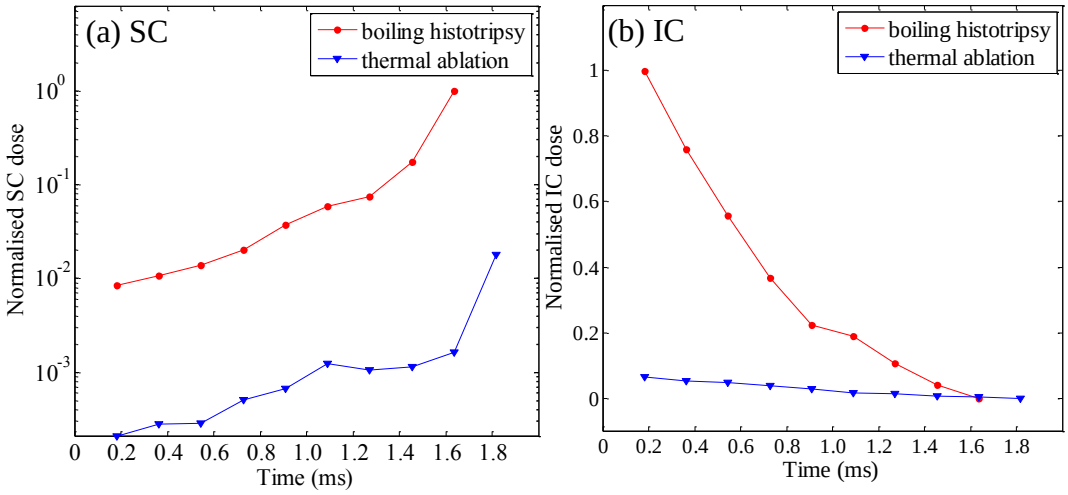

Figure 4.9. Corresponding amounts of (a) SC and (b) IC during the boiling histotripsy (red solid line, P_+ = 82 MPa, P_- = –15 MPa) and the thermal ablation (blue solid line, P_+ = 13.4 MPa, P_- = –7.5 MPa) exposures.

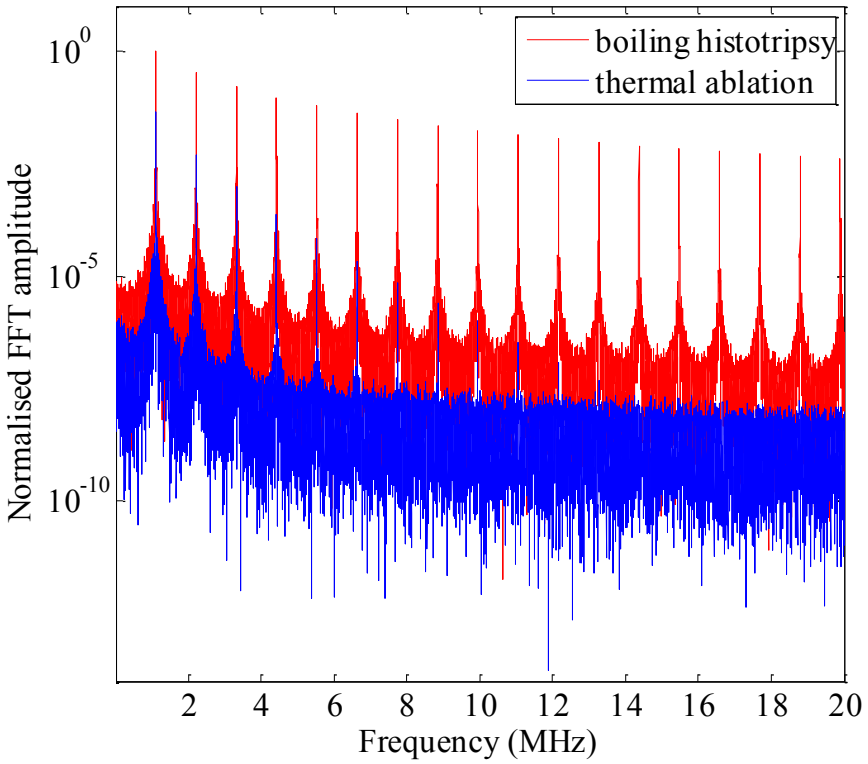

Figure 4.10. Corresponding simulated frequency spectra of the radiated pressures plotted in Figure 4.8(a) during the boiling histotripsy (red solid line, P_+ = 82 MPa, P_- = –15 MPa) and the thermal ablation (blue solid line, P_+ = 13.4 MPa, P_- = –7.5 MPa) exposures.

4.3. Discussion

In this Chapter, the numerical bubble model described in Chapter 3 was implemented to study the dynamics of a single bubble in the liver exposed to different HIFU waveforms. Three different acoustic pressure waveforms were considered to excite bubble motions: (a) sinusoidal WF1, (b) slightly distorted nonlinear WF2 and (c) nonlinear-shocked WF3 waves (see Figure 4.1).

4.3.1. Effects of the shapes of acoustic waveforms

With the absence of any heat or mass transfer, the bubble continued to grow and collapse with time when excited by the sinusoidal waves (WF1, P_- = –15 MPa), whereas the nonlinear-shocked waves (WF3, boiling histotripsy, P_+ = 82 MPa, P_- = –15 MPa) caused the bubble to undergo rectified growth after 10 acoustic cycles (see Figure 4.2(a)). Because these calculations did not take heat and mass transport at the bubble wall into account, this qualitative difference in the radial motions must be attributable to the shape of the acoustic excitation waveforms. As the peak positive pressure phase has a shorter duration than the negative pressure part in the shockwaves (i.e. 0.27 μs vs 0.62 μs, see Figure 4.1(a)), the bubble has a relatively longer time to undergo expansion rather than collapsing, leading to rectified bubble growth. As the bubble gets larger over each acoustic cycle, its resonance frequency decreases, and thereby the bubble responds increasingly to the negative pressure part of the waveform (Kreider *et al* 2011a). This radial behaviour is clearly visible in Figure 4.2(a), where the bubble growth rate accelerates as the bubble grows.

On the other hand, no rectified bubble growth occurs under the excitation of slightly distorted nonlinear waves (WF2, P_+ = 13.4 MPa, P_- = –7.5 MPa). This is most probably because, due to the absence of shock, the duration and pressure magnitude of the negative pressure phase are not sufficient to lead to rectified radial motion (see Figure 4.3 and Table 4.3) (Pahk *et al* 2015).

4.3.2. Effects of heat and mass transfer

Nonlinear heat and mass diffusion can occur at a bubble wall in the presence of acoustic pressure fields (Crum 1984, Hao and Prosperetti 1999, 2002). When the bubble is compressed during the positive half cycle, the internal pressure p_i as well as the bubble temperature T_b increases and some vapour condenses. Heat is, therefore, conducted away from the bubble into the surrounding medium. Conversely, the opposite holds true during the bubble expansion phase: a decrease in p_i and T_b, and evaporation takes place. There is, however, a net flux of heat into the bubble (i.e. rectified heat diffusion) because the thermal diffusion boundary layer becomes thicker during the bubble compression phase than that during the expansion process. Furthermore, the bubble surface area available for the phase change between liquid and gas is larger during the expansion phase; thereby, more volatile species in the surrounding medium evaporate into the bubble (Hao and Prosperetti 1999, 2002). Rectified incondensable gas diffusion, in addition to a net flux of heat, can also appear where the bubble can grow further. The gas in the bubble diffuses out into the surrounding medium during the positive half cycle, and vice versa. As the bubble grows during the negative half cycle, the diffusion boundary layer and the surface area become thinner and larger, respectively, causing a net flux of gas into the bubble (Crum 1984). The presence of a shocked wavefront in an acoustic waveform can enhance both nonlinear heat transfer and incondensable gas diffusion due to the asymmetry in the waveform. Since this asymmetry increases the time of the bubble expansion process, more volatile species and gas molecules in the surrounding medium will evaporate and diffuse into the bubble, resulting in an enhanced bubble growth. When accounting for both the heat and mass transport in the bubble model, it was seen that excitation by WF1 (sinusoidal excitation, $P_- = -15$ MPa) led to rectified bubble growth at 105°C with the average growth rate of $U = 2.2$ m·s^{-1}. The maximum bubble radius and the total number of molecules (water vapour and gas) in the bubble at the end of the growth phase were 188 μm and 6.302×10^{14}, respectively (see Figure 4.5 (a) and (b)). On the other hand, an explosive rectified bubble growth occurred at 100°C in the case of excitation by WF3 (nonlinear-shocked excitation, $P_+ = 82$ MPa, $P_- = -15$ MPa)

(see Figure 4.4(a)). Relative to excitation by WF1 (sinusoidal excitation), the average growth rate was 3.2 times faster, R_{max} was twice as large and the molecular contents was 5.3 times greater (see Figure 4.4(b)). These results are summarised in Table 4.6.

Waveform types	**Maximum bubble radius (μm)**	**Average growth rate ($m \cdot s^{-1}$)**	**Number of molecules in the bubble**	
			Water vapour	**Gas**
Sine waves ($\sigma_{sh} = 0$)	188	2.2	6.301×10^{14}	1.286×10^{11}
Shock waves ($\sigma_{sh} = 10.8$)	370	7	3.318×10^{15}	1.633×10^{11}

Table 4.6. The maximum bubble radius, average bubble growth rate and the number of molecular contents attained by the sinusoidal (WF1, $P_- = -15$ MPa) and the nonlinear-shocked excitations (WF3, $P_+ = 82$ MPa, $P_- = -15$ MPa) over 100 acoustic cycles.

The increase of water vapour and gas molecules in the bubble due to the presence of asymmetry in the acoustic excitation waveform was examined (see Table 4.6). It was observed that the amount of water vapour was enhanced by a factor of 5.3 whereas that of gas was only increased by a factor of 1.3. This is most probably due to the fact that temperature significantly affects the number of available water vapour and gas molecules in the surrounding medium (i.e. the density of H_2O increases while that of gas decreases exponentially with temperature, see Figure 4.11). At a boiling temperature of 100°C, the molecular concentration of water vapour in the liver is, for example, 27 times higher than that of gas, as shown in Figure 4.11. Therefore, relatively greater amounts of water vapour in the surrounding medium diffuse into the bubble during the bubble expansion process over a given time.

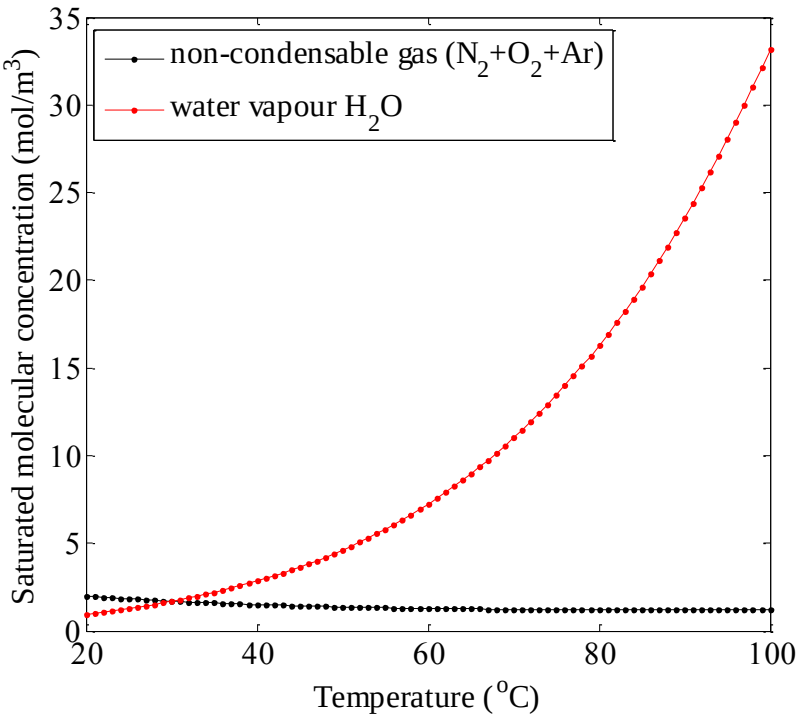

Figure 4.11. Saturated density of water vapour H_2O and gas (Nitrogen N_2 + Oxygen O_2 + Argon Ar) in the liver with temperature. Equations (3.41) and (3.45) were used to calculate the molecular concentrations for water vapour and gas, respectively.

4.3.3. Effects of temperature variation

The piecewise constant method described in Chapter 3 (see section 3.4) was adopted in the bubble model to investigate the bubble dynamics driven by the nonlinear-shocked waves (WF3) at elevated temperatures from 20^{o}C to 100^{o}C. It was observed that the radial bubble growth persisted for a longer period as the surrounding temperature increased with time (see Figure 4.6(a)). This is because of the combination of the vapour trapping effect and the increased vapour pressure in the bubble (Matula *et al* 2002, ter Haar and Coussios 2007). This combination softens the inertial bubble collapses and leads to the bubble oscillating more stably. As a result, higher order multiple harmonic components gradually appear (leading to a greater SC dose) whilst the levels of broadband emissions reduce (leading to a lesser IC dose) as a function of time. This can be visualised in the spectrogram (displayed in Figure 4.8), as well as in the quantified cavitation doses plotted in Figure 4.9.

Additional calculations for the radial bubble motions were performed under the nonlinear-shocked wave excitation case (WF3), this time reducing the surrounding temperature from 100°C to 70°C (see Figure 4.7). Interestingly, the average bubble growth rate gradually decreases with time (i.e. $U_{100^oC} = 3.4\ m{\cdot}s^{-1}$, $U_{90^oC} = 2.9\ m{\cdot}s^{-1}$, $U_{80^oC} = 1.3\ m{\cdot}s^{-1}$) and drops to $U = -1.1\ m{\cdot}s^{-1}$ at 70°C. These numerical observations suggest that the extent of an exploding bubble growth at the HIFU focus during boiling histotripsy is likely to be limited to the HIFU focal volume owing to the significant differences in tissue temperatures inside and outside of the focal region.

4.3.4. Acoustic emissions and cavitation activity

Canney *et al* (2010a) experimentally observed that there was a significant increase in amplitude in the PCD voltage output and a sudden occurrence of higher order multiple harmonic components of the fundamental frequency in the spectrogram when a millimetre-sized boiling bubble formed at the HIFU focus in a tissue phantom. The authors speculated that these significant changes were likely to be due to the reflection of the incident nonlinear-shocked waves from the boiling bubbles filled with gas and vapour because of the large acoustic impedance mismatch at their surface. Whilst the present bubble model does not take into account the shock scattering effect for simulating the acoustic emissions, the numerical results presented in this Chapter showed similar features to those described by Canney *et al* (2010a). The data shown in Figure 4.6(a) and Figure 4.8(a) and (b) demonstrates that the explosive rectified bubble growth at 100°C manifests itself as the significant increase of the amplitude in the radiated pressure vs time curve (see Figure 4.8(a)). Simultaneously, stronger and higher order multiple harmonics appear in the spectrogram (see Figure 4.8(b)). These observations together with the experimental results from Canney *et al* (2010a) suggest that the acoustic emissions resulting from the formation and the dynamic behaviour of a boiling bubble at the HIFU focus can be monitored, because the bubble acts as a strong scatterer and oscillates with a highly nonlinear radial behaviour.

Radiated acoustic pressures resulting from the bubble dynamics excited by both the thermal ablation (WF2, slightly distorted nonlinear waves) and the boiling histotripsy (WF3, nonlinear-shocked waves) waveforms were compared for monitoring purposes. The shockwave resulting from the boiling histotripsy exposure contains higher order multiple harmonics in the frequency domain and results in larger acoustic pressure amplitudes (see Figure 4.1). This essentially leads to (a) a high degree of nonlinearity in the radial bubble oscillations and (b) violent bubble collapses with larger amplitude short-duration pressure spikes (Pahk *et al* 2015). Hence, more noticeable higher order multiple harmonic components with larger amplitudes, as well as higher levels of broadband emissions, were observed in the spectrogram during boiling histotripsy excitation relative to those during thermal ablation exposure (Figure 4.8 and Figure 4.10). Indeed, the quantified amounts of both IC and SC were greater during boiling histotripsy (Figure 4.9). These unique frequency domain features enable the acoustic emissions to be distinguished between the thermal ablation and the boiling histotripsy insonations.

4.4. Summary

The bubble model formulated in Chapter 3 was successfully implemented in this Chapter to (a) explore the dynamics of a single spherical gas-vapour bubble in the liver induced by HIFU boiling histotripsy waves, and (b) distinguish between the different types of acoustic cavitation activity produced by the different HIFU exposure conditions (i.e. HIFU thermal ablation and HIFU boiling histotripsy).

The numerical results presented in this Chapter showed that the asymmetry in a shockwave and water vapour transport are the key parameters that lead the bubble to undergo rectified growth at a boiling temperature of 100^{o}C. The extent of this growing bubble process is, however, likely to be limited to the HIFU focal zone due to the significant differences in tissue temperatures inside and outside of the HIFU focus. The onset of rectified bubble growth manifested itself as (a) the significant increase in the radiated pressure vs time curve and (b) the sudden appearance of higher order multiple harmonics with larger amplitudes in the corresponding

spectrogram. Examining the frequency spectra produced by the thermal ablation (slightly distorted nonlinear waveforms) and the boiling histotripsy (nonlinear-shocked waves) exposures, it was clearly noticed that higher order multiple harmonics as well as higher levels of broadband emissions occurred during the boiling histotripsy insonation. These unique features in the emitted acoustic signals can, therefore, be used to monitor (a) the different types of cavitation activity for either a thermally or a mechanically induced lesion and (b) the onset of a boiling bubble at the HIFU focus in the course of HIFU exposure.

In the following chapter, experiments will be performed with a high-speed camera and a passive cavitation detection system to observe the bubble dynamics and record the corresponding acoustic emissions produced at the HIFU focus in a tissue phantom during HIFU boiling histotripsy.

Chapter 5. Mechanisms involved in the production of a tadpole shaped lesion during HIFU boiling histotripsy

As highlighted in Chapter 2, localised shockwave heating produces a millimetre-sized boiling bubble at the HIFU focus during boiling histotripsy. Further interaction of incident shockwaves with this boiling bubble leads to the creation of a tadpole shaped lesion. However, the question of how this interaction produces such a lesion remains unclear. In Chapter 4, the formation and dynamic behaviour of a boiling bubble in the liver exposed to HIFU boiling histotripsy was numerically investigated. The numerical results showed that the asymmetry in a shockwave together with vapour transport caused a bubble to undergo rectified radial motions, leading to an explosive bubble growth at a boiling temperature of 100^{o}C. This observation is, however, limited to the onset of a boiling bubble.

The aim of this Chapter is, therefore, to investigate the interaction of a boiling bubble with incoming shockwaves. A high-speed camera with a passive cavitation detection (PCD) system will be used to observe the dynamics of bubbles induced in tissue mimicking materials (TMM) consisting of optically transparent gels. The main purpose of using a PCD system is to monitor the formation of a boiling bubble at the focus in the course of boiling histotripsy. A detailed analysis of acoustic emissions resulting from cavitation activity at the HIFU focus is beyond the scope of this thesis.

5.1. Material and methods

5.1.1. HIFU experimental arrangement

A schematic diagram of the experimental set up used in the work described in this Chapter is shown in Figure 5.1. The experiment was performed in an acrylic water bath filled with degassed and de-ionised water at a temperature of 20^{o}C. A water treatment system (Precision Acoustics Ltd, Dorset, UK) was used for degassing. A 2.0 MHz single element bowl-shaped HIFU transducer (Sonic Concepts H106, Bothell, WA, USA) was used. This source was driven by a function generator (Agilent 33220A, Santa Clara, CA, USA) via a linear radiofrequency (RF) power amplifier (ENI 1040L, Rochester, NY, USA). To measure the level of an electrical power P_{elect} supplied to the transducer, a power meter (Sonic Concepts 22A, Bothell, WA, USA) was connected between the RF power amplifier and the HIFU source. A computer with waveform generation software (Agilent Waveform Builder, CA, USA) was used for driving the function generator with the desired HIFU pulsing protocol.

The position of the HIFU transducer was fixed at one end in the water bath and an acoustic absorber (Precision Acoustics Ltd AptFlex F28, Dorchester, UK) was placed on the opposite end to minimise ultrasonic reflections. A 10 MHz focused PCD (20 mm in diameter and 64 mm in geometric focal length, Sonic Concepts Y107, Bothell, WA, USA) featuring of a wide bandwidth (10 kHz–20 MHz) was connected to a digital oscilloscope (LeCroy HDO 6054, Berkshire, UK). This PCD was used to obtain acoustic emissions resulting from cavitation activity at the HIFU focus. A sampling frequency of 0.5 GHz was used.

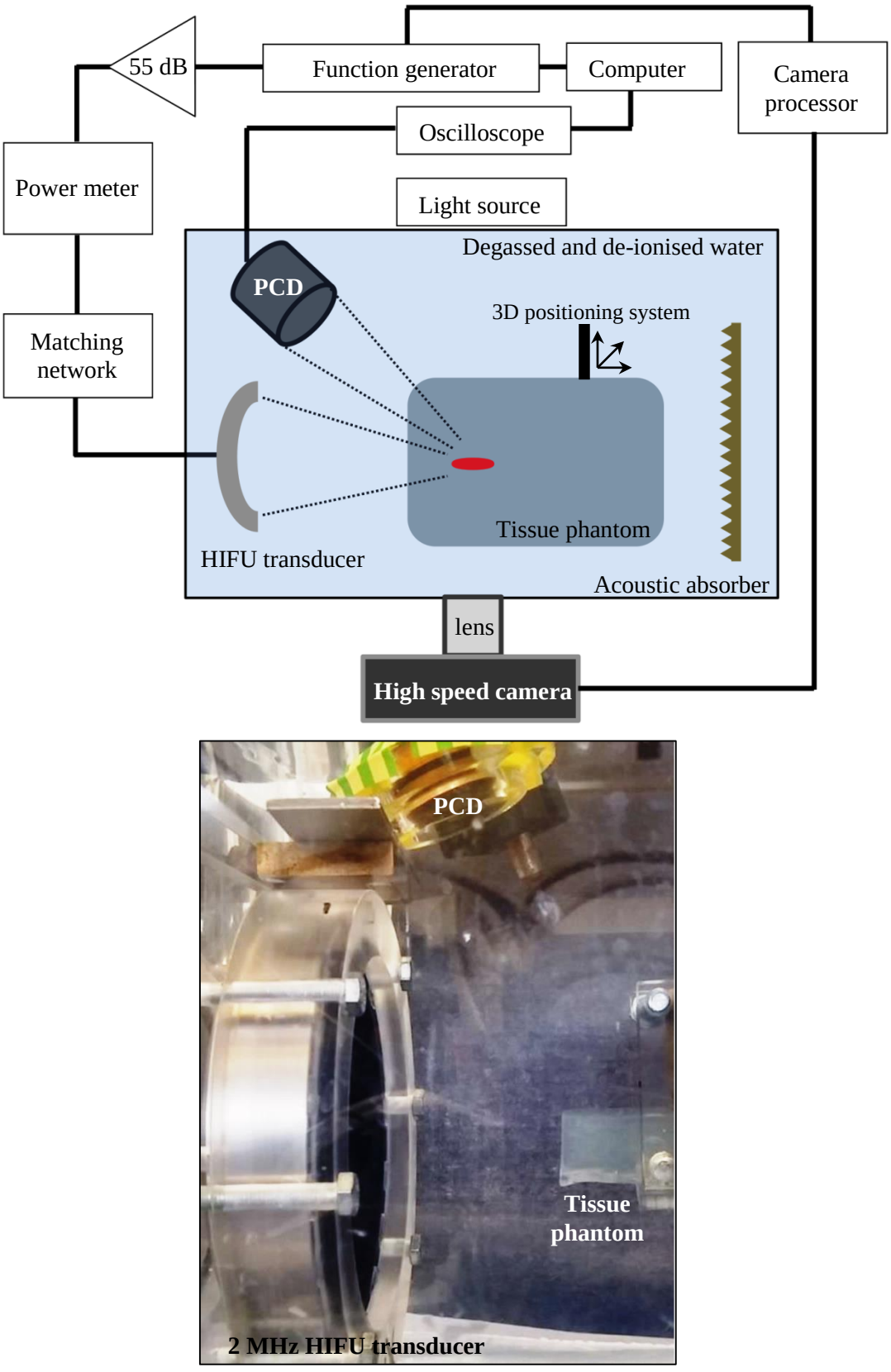

Figure 5.1. HIFU experimental set up used for investigating the generation of tadpole shaped lesions resulting from boiling histotripsy.

5.1.2. Acoustic characterisation of HIFU transducer

The HIFU transducer used in this Chapter was characterised using a calibrated needle hydrophone in water (free-field). Figure 5.2 shows the schematic diagram of the experimental setup used to characterise the device. The source was positioned and fixed at one end of a tank (60 × 60 × 100 cm) of degassed and de-ionised water (24.4 ± 0.1^{o}C), and was driven by a signal generator (Agilent 33522A, Santa Clara, CA, USA) via a 75 W power amplifier (ENI A075, Rochester, NY, USA). The driving input signal was a 2.0 MHz sinusoidal tone burst mode containing 68 cycles with a pulse repetition frequency of 100 Hz and an RMS voltage of 28 V. The drive voltage at the HIFU transducer was measured with a high-voltage probe (Tektronix TPP0850, Berkshire, UK) via an oscilloscope (Tektronix DPO5034B, Berkshire, UK).

The axial and lateral acoustic pressure fields under linear propagation conditions were measured with a calibrated 0.2 mm Polyvinylidene fluoride (PVDF) needle hydrophone (Precision Acoustics Ltd, Dorchester, UK) at a spatial step size of 0.2 mm. The hydrophone was connected to a software controlled three-axis positioning system (Precision Acoustics Ltd, Dorchester, UK) scanned a 22 × 22 mm *xy* planar field perpendicular to the HIFU beam axis over a distance between 31 mm to 131 mm (*z* direction) away from the centre of the transducer surface. The transducer to hydrophone distance was measured using the time-of-flight technique described by Canney *et al* (2008). The acquired analogue signals were then digitised via the oscilloscope at a sampling frequency of 0.8 GHz.

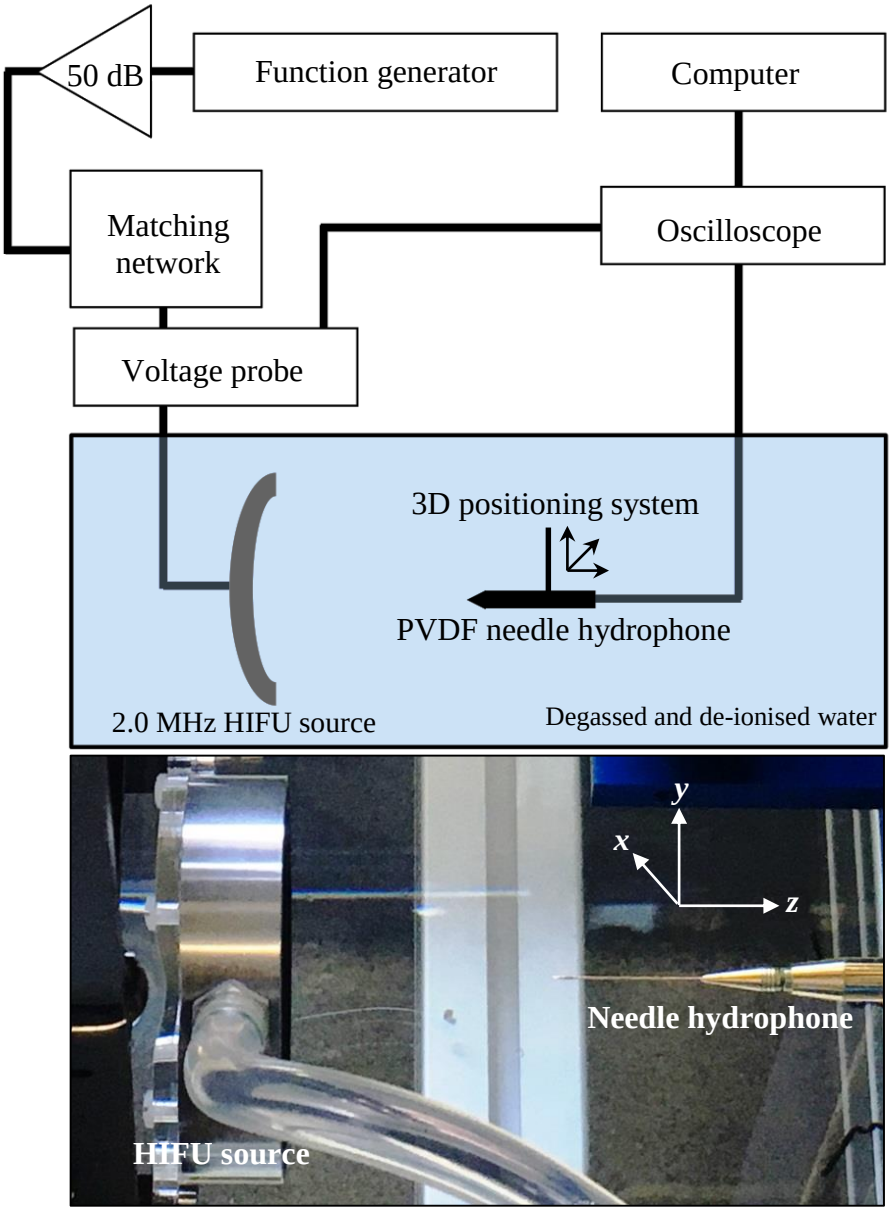

Figure 5.2. Experimental setup for the acoustic characterisation of the HIFU transducer.

5.1.2.1. Acoustic characterisation results

The measured one dimensional HIFU focal pressure beam profiles along the axial and lateral directions are shown in Figure 5.3. From the measurement, it was determined that the HIFU axial focal distance was at z = 62.6 mm and the lateral and axial full width half maximum (FWHM) dimensions were 1.05 mm and 6.67

mm, respectively. In addition, acoustic field simulations were carried out using the HIFU Simulator 1.2 (equation 3.72 in Chapter 3) for various values of the source aperture (active diameter) to obtain the "best-fit" with the measurement (Canney *et al* 2008). The active aperture size of the HIFU transducer was found to be 59.0 mm.

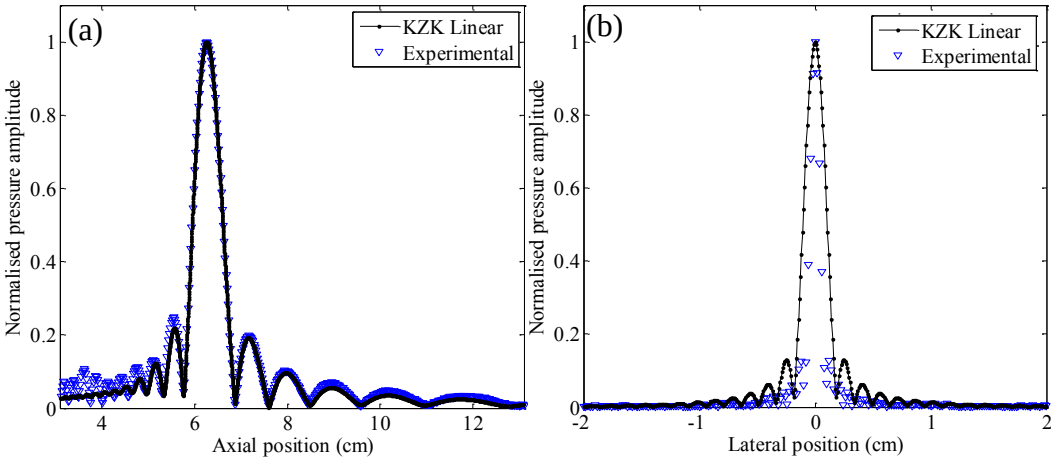

Figure 5.3. Comparison of (a) axial and (b) lateral focal pressure fields (under linear propagation conditions) measured in water by the needle hydrophone and calculated with the linearised KZK equation.

Although there was good agreement between the acoustic field measurement and the simulation under linear propagation conditions (see Figure 5.3), there were some discrepancies in the prefocal region of the axial beam profile (see Figure 5.3(a)) as well as in the pressure profile along the lateral direction (see Figure 5.3(b)). This was most probably due to a slight misalignment of the needle hydrophone in the experimental measurement.

5.1.3. Tissue mimicking gel phantoms

Optically transparent polyacrylamide gel phantoms containing bovine serum albumin (BSA) were used in the camera experiment. Temperatures above 60°C cause BSA to denature and form an opaque thermal lesion, which can be visualised (see Figure 5.4). Table 5.1 shows chemical composition of 50 mL gel with 7% BSA concentration. A tissue mimicking phantom consisting of the chemical substances listed in Table 5.1 has very similar acoustic and thermal properties to those of liver, except for the attenuation coefficient, which is 0.15 $dB \cdot cm^{-1}MHz^{-1}$ rather than 0.52 $dB \cdot cm^{-1}MHz^{-1}$ (Lafon *et al* 2005, Khokhlova *et al* 2011, Choi *et al* 2013). The cavitation threshold of degassed 7% BSA tissue phantom is P_- = –2 MPa (Khokhlova *et al* 2006). This value is slightly higher than that of perfused porcine liver tissue (P_- = –1.3 MPa, McLaughlan 2008).

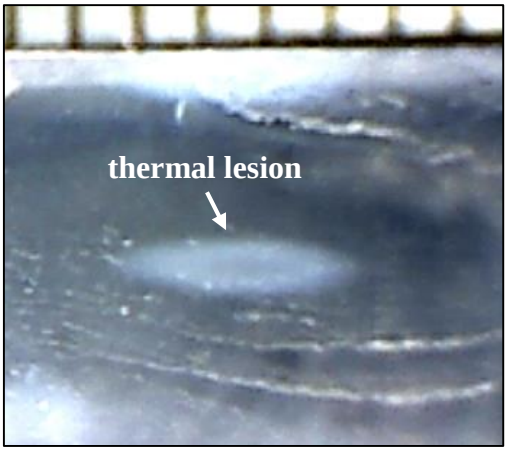

Figure 5.4. An example of a cross section of a HIFU-induced thermal lesion in the tissue phantom. The HIFU beam propagates from left to right.

Components	Quantity	Percent (%)
Degassed and de-ionised water	35.805 mL	71.61
BSA	3.5 g	7
1 M TRIS	5 mL	10
Acrylamide	8.75 mL	17.5
APS	0.42 mL	0.84
TEMED	0.025 mL	0.05

Table 5.1. Composition of 50 mL gel with 7% concentration of BSA. APS = ammonium persulfate. TEMED = tetramethylethylenediamine.

A tissue phantom was prepared by first mixing 3.5 g of BSA (Sigma-Aldrich A7906, Dorset, UK) in 35.805 mL of degassed and de-ionised water. The mixture was gently stirred to dissolve the BSA completely. The solution was then placed in a vacuum chamber (Edwards High Vacuum ISC30A, Sussex, UK) and held in a vacuum of 720 mm Hg for 30 minutes for additional degassing. 8.75 mL of acrylamide (Sigma-Aldrich A9926, Dorset, UK) was added to the mixture followed by a 1 mol·L^{-1} TRIS buffer (Sigma-Aldrich, Trizma hydrochloride and trizma base T2694, Dorset, UK) and a 0.42 mL of APS (Sigma-Aldrich, A7460, Dorset, UK) to initiate polymerisation. Because acrylamide is a neurotoxic substance, the mixing process was performed in a fume hood (Labcaire T400L, Somerset, UK) with appropriate safety goggles, gloves and laboratory coat. The entire solution was again stirred gently and placed in the vacuum chamber with a vacuum of 720 mm Hg for 1 hour. 0.025 mL of TEMED (Sigma-Aldrich, T9281, Dorset, UK) was finally added to the solution to accelerate the polymerisation process. The final solution was immediately poured into a customised mould (6 × 6 × 6 cm). Because the polymerised gel has a limited lifespan of several weeks (Khokhlova *et al* 2006), it was stored in an air-tight plastic bag at 8^{o}C and used the next day for experiments.

Prior to the experiments, the tissue phantom was kept at room temperature until its temperature reached 20^{o}C. The phantom was then cut into cuboid samples (1.5 × 3 × 6 cm) and clamped in a custom-built holder (4.5 × 5 × 7.5 cm). The holder coupled with the phantom was attached to a customised three-axis positioning system for alignment with the HIFU focus. The distance from the centre of the transducer surface to the phantom was z = 57.6 mm. Therefore, the HIFU focus was 5 mm below the surface of the phantom. 17 tissue phantoms in total (n_s = 17) were used in the camera experiments.

5.1.4. Camera set up

A high speed camera (FASTCAM-ultima APX, Photron, San Diego, CA, USA) with a 12X Navitar lens (Navitar, Rocester, NY, USA) connected to a three-axis-positioning system (Sherline Products 5430, Vista, CA, USA) was used to film the

bubble dynamics induced at the HIFU focus in the tissue phantom. The camera was operated at 1000, 15,000 and 100,000 frames per second (fps) with a pixel resolution of 512 × 128, 1028 × 128 and 128 × 32, respectively (24 μm/pixel). All experiments were backlit with an illuminating system (Solarc ELSV-60, General Electric Company, Connecticut, USA). Hence, captured optical images appeared as shadowgraphs where the tissue phantom appeared grey and HIFU-induced bubbles appeared black (see Figure 5.5). Optical images were post-processed with Photron FASTCAM Viewer (Photron, San Diego, CA, USA).

During the experiments, a camera processor (FASTCAM-ultima APX, Photron, San Diego, CA, USA) triggered the camera and the function generator at the same time to synchronise an image capturing process and HIFU exposure.

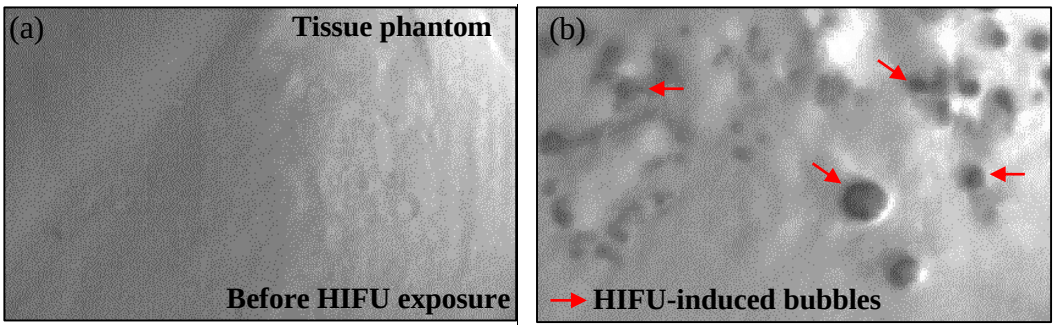

Figure 5.5. An example of captured optical images (a) before and (b) during HIFU exposure.

5.1.5. HIFU exposure condition

A 10 ms-long HIFU pulse with P_{elect} = 200 W (P_+ = 85.4 MPa and P_- = –15.6 MPa) was used to produce a mechanically induced lesion in the tissue phantom. The duty cycle (1%) and the pulse repetition frequency (1 Hz) were kept constant while changing the number of pulses, which was set to 1, 5 or 50. The KZK equation (3.72) was used to obtain acoustic peak positive (P_+) and negative (P_-) pressures *in situ* at the HIFU focus, which are plotted in Figure 5.6(a). Figure 5.6(b) shows the corresponding peak temperature rise at the HIFU focus. This was calculated using

the BHT equation (3.75) and the time t_b to reach a boiling temperature of 100ºC was predicted to be 3.66 ms. The physical properties of the tissue phantom used in the simulations are listed in Table 5.2. In the acoustic field simulation, the computational domain sizes were r = 2.95 cm radially and z = 9.39 cm axially with the grid steps of Δr = 0.036 mm and Δz = 0.023 mm. The temporal step size used in the temperature simulation was Δt = 0.05 ms.

The HIFU exposure parameters used in the camera experiment were similar to those used by Khokhlova *et al* (2011): 2.158 MHz HIFU frequency, 10 ms pulse length, 1 Hz pulse repetition frequency, 1% duty cycle, P_+ = 76 MPa and P_- = –13.5 MPa with 50 HIFU pulses and t_b = 3.8 ms.

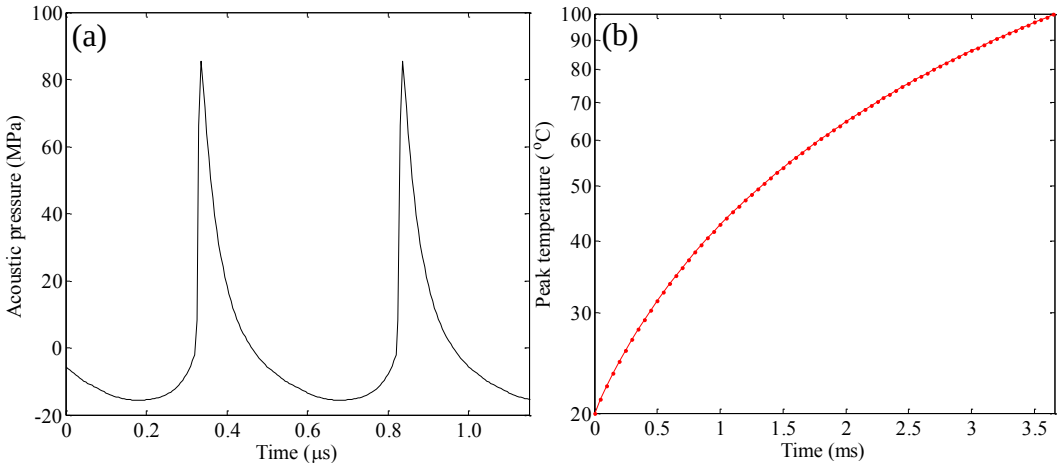

Figure 5.6. Simulated acoustic waveforms and peak temperatures at the HIFU focus in the tissue phantom. (a) Acoustic wavefronts with P_{elect} = 200 W (P_+ = 85.4 MPa, P_- = –15.6 MPa at focus). (b) Corresponding peak temperature. The time to reach a boiling temperature of 100ºC is predicted to be 3.66 ms.

Symbol	Definition	Value
c_0	speed of sound	1544 m·s^{-1}
ρ_0	mass density	1044 kg·m^{-3}
α_0	absorption coefficient at 1 MHz	15 dB·m^{-1}
β	coefficient of nonlinearity	4.0
c_v	specific heat capacity per unit volume	5.3×10^6 J·m^{-3}·ºC^{-1}
k	thermal diffusivity	1.3×10^{-7} m^2·s^{-1}
T_0	ambient temperature	20 ºC

Table 5.2. Properties of tissue phantom used in the acoustic and temperature fields simulations (Khokhlova *et al* 2011).

5.1.6. Scattered pressure fields

The presence of a vapour bubble close to the focus of the HIFU transducer is likely to have an effect on its incident ultrasonic field. Indeed, due to the difference in acoustic impedance between water vapour and the TMM material, the bubble is likely to scatter the incident ultrasonic field. This phenomenon may lead to constructive and destructive interactions of the scattered field with the incident field, potentially generating localised peak negative pressures, leading to additional cavitation nucleation sites. Furthermore, the presence of a vapour bubble close to the transducer focus may also lead to an aberration of the focus and generate a shadow zone.

It is well-known that the KZK equation (3.72) can only simulate one-way propagation (i.e. along the axis of the transducer). Producing a full-wave nonlinear acoustic propagation model capable of dealing with scattering by localised heterogeneities remains a challenge. This is particularly the case if the computational domain is large relative to the wavelength of the highest frequency present in the ultrasonic signal. On the basis of the KZK simulations, significant harmonic content is present at the focus up to 10 MHz. This is likely to result in a densely meshed computational grid. It is, therefore, likely that accurately modelling such a configuration will present substantial computational challenges. To get a qualitative appreciation of what the effects of scattering of the incident HIFU field by a vapour bubble may be, a linear scattering analysis was, therefore, opted for. Boundary element methods (BEM) are particularly well-suited to dealing with exterior scattering problems, and such analysis techniques will be opted for here. In BEM, the partial differential equation to be solved is reformulated into an integral equation that is defined on the boundary of the domain (in this case, on the surface of the vapour bubble) and an integral that relates the boundary solution to the solution at any point in the domain. The boundary integral equation may then be solved by discretising the surfaces defined by the domain boundaries into smaller regions known as boundary elements. A major advantage of BEM over other numerical schemes, such as finite difference time domain methods, is that the

discretisation occurs only over the surfaces rather than over the entire domain. More details on BEM are provided by Banerjee (1994).

The BEM implementation used in this chapter was described by Gélat *et al* (2014, 2015). The method is a colocation BEM implementation of the Kirchhoff-Helmholtz integral equation, which uses isoparametric elements with quadratic shape functions. The scatterer is assumed to be locally reacting so that $\partial p/\partial n = i\omega\rho_{\text{vap}}u_n$ on the surface of the vapour bubble, where u_n is the normal component of the particle velocity vector, ω is the angular frequency and $i^2 = -1$. Transmission of acoustic waves through the bubble was neglected, due to the large difference between the acoustic impedance of water vapour and that of the TMM gel (Canney *et al* 2010a).

The BEM scheme requires an incident acoustic pressure field on the surface of the scatterer as input data. This was derived using a Rayleigh integral method (Pierce 1989) by effectively discretising the surface of the HIFU source into smaller surfaces with a point source located at their centroid. By weighting each source with the appropriate surface area and by summing all their contributions, the incident field at any required location may be computed. This is achieved through a discretisation of the following integral

$$p(\vec{r},t) = \frac{i\rho c k_{\text{w}}}{2\pi}\exp(i\omega t)\iint_S \frac{\exp\left(-ik_{\text{w}}\|\vec{r}-\vec{r}_0\|\right)}{\|\vec{r}-\vec{r}_0\|}\vec{u}\cdot\vec{n}\,dS \qquad (5)$$

where $\vec{r}$ depicts a position vector in the acoustic domain and $\vec{r}_0$ a position on the surface of the source. $\vec{n}$ is the unit normal vector on the surface of the source (pointing towards to the focus) and $\vec{u}$ is the velocity. *S* is the radiating surface of the HIFU source, which is assumed to be moving uniformly in the radial direction.

The exterior domain was assumed to be homogeneous, possessing the properties of the TMM gel. In fact, this domain also comprises a region of water between the HIFU source and the TMM gel. This water region was not included here, and the

normal surface velocity of the transducer was adjusted to result in 22 MPa at the focus, in absence of the scatterer. The pressure value of 22 MPa was obtained from the simulated acoustic pressure for the first harmonic using the KZK simulation. The resulting acoustic pressure at focus is shown in Figure 5.7, which represents the sum of the incident and the scattered pressure magnitude from a vapour bubble. The BEM code which was used was the proprietary programme SCATTER provided by PACSYS Ltd (Nottingham, UK). This programme has been used in earlier studies on HIFU scattering by ribs (Gélat *et al* 2014, 2015).

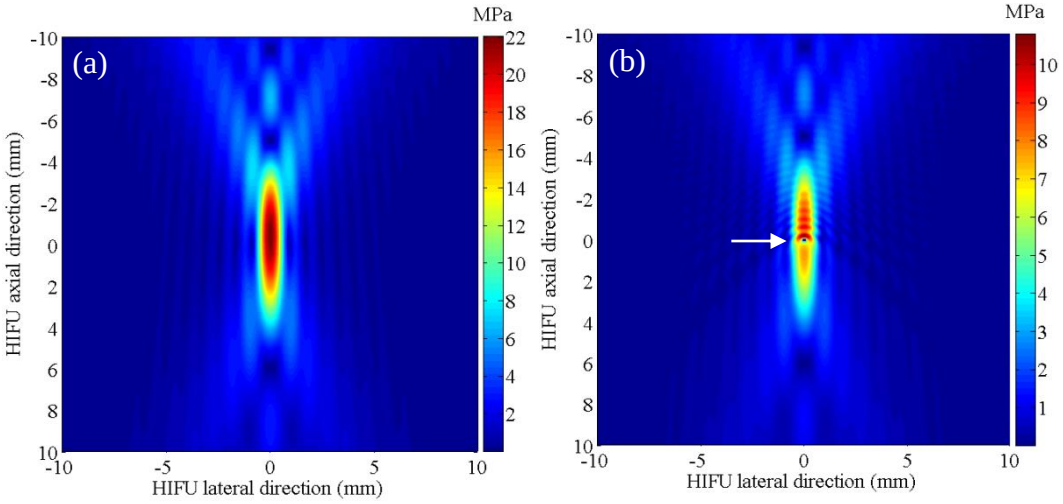

Figure 5.7. Simulated acoustic pressure magnitudes at the HIFU focus using BEM. The contour plots of the incident acoustic pressure (a) without and (b) with a scatterer. The presence of a vapour bubble is indicated by an arrow in (b). The HIFU beam propagates from top to bottom.

5.2. Results

5.2.1. The formation of a boiling bubble in the gel with a single HIFU pulse

Figure 5.8 shows a sequence of camera images obtained over the single 10 ms HIFU insonation in the tissue mimicking gel phantom with an electrical power of 200 W (P_+ = 85.4 MPa; P_- = –15.6 MPa at the HIFU focus). A localised heating in the HIFU focal region is observed as a dark elliptical shape at 3.4 ms (Figure 5.8(b)). This heated region corresponds well to the simulated temperature contour plot shown in Figure 5.8(c). A large bubble of 360 μm in diameter appears in this super-heated region after 3.6 ms of exposure to the HIFU field (indicated by an arrow in Figure 5.8(d)). This bubble is hereafter referred to as a boiling bubble because its onset time matches the calculated time to reach a boiling temperature of 100°C (t_b = 3.66 ms). A significant increase in the PCD voltage occurs as this large boiling bubble manifests itself. This can be seen in the PCD voltage vs time plot in Figure 5.9(a). Also coinciding with the appearance of this bubble is the manifestation of higher order multiple harmonic components of the fundamental frequency (2 MHz) in the spectrogram in Figure 5.9(b). As discussed in Chapter 4, these significant changes are indications of the formation of a boiling bubble due to the reflection of an incident nonlinear-shocked wave from this bubble and due to its highly nonlinear radial oscillation.

During the experiments, the boiling time of the single HIFU pulse in the gel was 3.78 ± 0.67 ms (mean ± standard deviation SD with n_s = 17) with differences of 0.12 ms between the PCD measurement and the temperature simulation.

Another set of high speed camera images obtained in the optically transparent tissue phantom during the single 10 ms HIFU exposure is shown in Figures C.1 and C.2 in Appendix C.

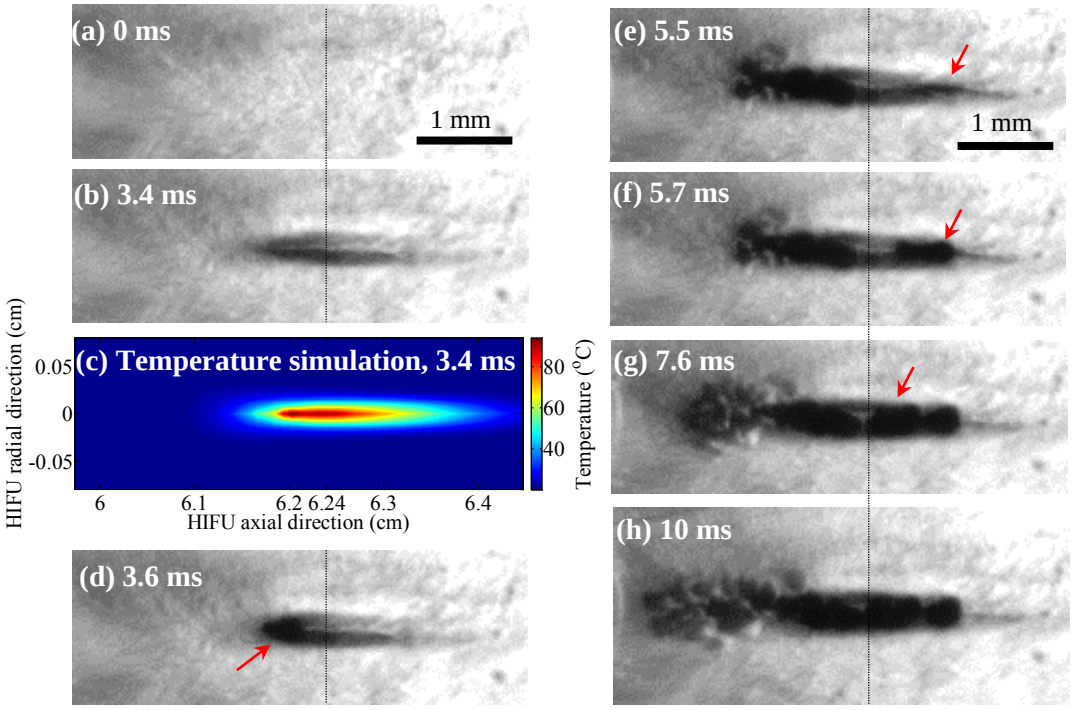

Figure 5.8. A sequence of high speed camera images (a), (b), (d)-(h) obtained in an optically transparent tissue phantom during the single 10 ms HIFU insonation with an electrical power of P_{elect} = 200W (P_+ = 85.4 MPa; P_- = –15.6 MPa at the HIFU focus). Images were captured at a 15,000 fps. (c) Simulated temperature contour plot at t = 3.4 ms. The HIFU beam propagates from left to right. The vertical dashed lines indicate the HIFU focus. The time at 0 ms corresponds to the start of the HIFU exposure.

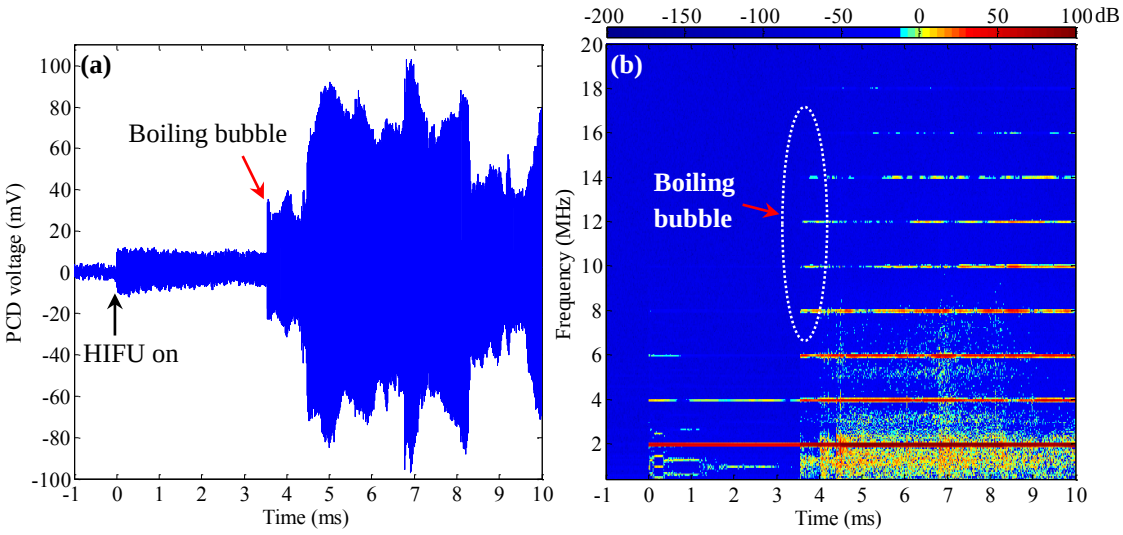

Figure 5.9. Acoustic emission emitted at the HIFU focus in the gel during the single 10 ms HIFU pulse. (a) shows the PCD voltage vs time plot and (b) is the corresponding spectrogram. Acoustic emissions were recorded at a sampling rate of 0.5 GHz. The time at 0 ms represents the start of the HIFU insonation.

After the formation of a boiling bubble at t = 3.6 ms, a cavitation cluster is subsequently produced in front of the boiling bubble, progressing towards the HIFU source until it is switched off (see Figure 5.8 (e) to (h)). Simultaneously with the generation of the bubble clouds, significant appearance of broadband emissions (an indicator of inertial cavitation) is noticed in the corresponding spectrogram plotted in Figure 5.9(b).

In addition to the generation of a cavitation cluster, a secondary localised heated region at ~1 mm away from the primary boiling bubble along the positive z-axis is observed. This event is indicated by an arrow in Figure 5.8(e) and is followed by the production of a secondary boiling bubble at t = 5.7 ms, also indicated by an arrow in Figure 5.8(f). A number of boiling bubbles then form in front of the secondary boiling bubble at t = 7.6 ms towards the primary boiling bubble. This event is denoted by an arrow in Figure 5.8(g). These boiling bubble motions are spatially confined to the localised super-heated region.

Figure 5.10 displays a number of high speed images showing rectified bubble growth. These images were obtained at the highest possible frame rate (100,000 fps, 1 frame per 20 acoustic cycles) prior to the production of a cavitation cluster. A localised super-heated region is visible at t = 4.69 ms (see Figure 5.10(a)) followed by the formation of a boiling bubble with a radius of 132 μm (see Figure 5.10(b)). This boiling bubble then grows to 270 μm in radius over 0.04 ms (i.e. 80 acoustic cycles, see Figure 5.10 (c)-(f)). The bubble growth rate gradually decreases with time and the extent of this growing bubble is confined to the volume defined by the super-heated region. The simulated radius vs time curve plotted in Figure 5.10(g) shows similar bubble growth.

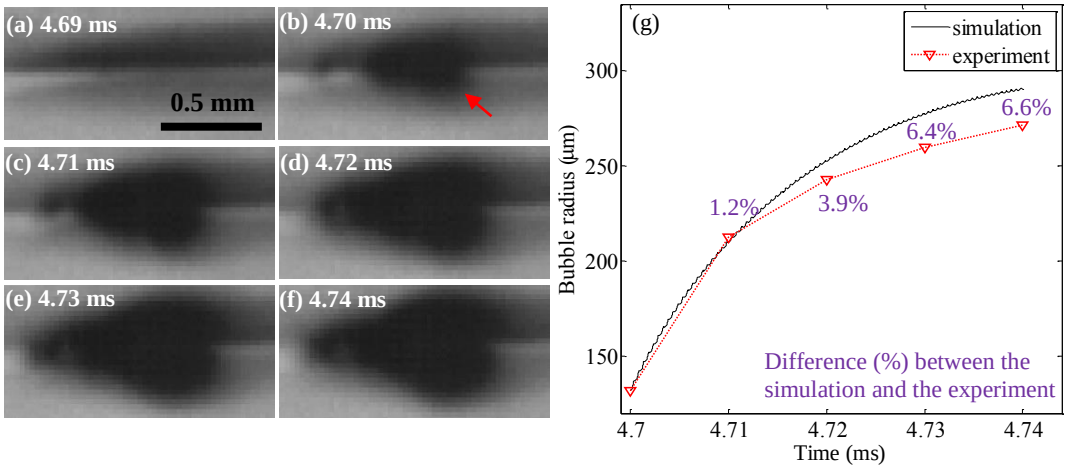

Figure 5.10. A series of camera images acquired at 100,000 fps during a single 10 ms HIFU exposure. (a)-(f) are captured high speed images over 4.69 to 4.74 ms (1 frame per 20 acoustic cycles). The HIFU beam propagates from left to right. The red arrow in (b) indicates the formation of a boiling bubble. (g) A comparison between the experimentally measured bubble radius and the simulated radius vs time curve. Photron FASTCAM Viewer (Photron, San Diego, CA, USA) was used to measure the size of the bubble (24 μm/pixel). The initial bubble radius was chosen as R_0 = 132 μm at a temperature of 100ºC in the bubble simulation.

5.2.2. The formation of a tadpole shaped lesion with multiple HIFU pulses

Figure 5.11 shows a series of high speed camera images taken during five 10 ms HIFU pulses. Images in the left column represent the formation of a boiling bubble at each HIFU pulse (see Figure 5.11(a)), whereas those in the middle column show bubble activities at the end of each HIFU pulse (see Figure 5.11(b)). In every HIFU pulse, a boiling bubble appears either at the HIFU focus or close to the focus within 1 mm (indicated by arrows in Figure 5.11(a)), but dissolves in the time interval between HIFU pulses (1% duty cycle). The time taken to form a boiling bubble decreases with HIFU pulses (i.e. 3.6, 3.1, 2.9, 2.5 and 2.3 ms with pulses). Besides this boiling bubble, a cavitation bubble clouds is always produced in front of a boiling bubble (see Figure 5.11(b)), persists throughout each HIFU exposure, and dissolves between HIFU pulses.

The corresponding induced mechanical damage in the gel prior to the subsequent arrival of HIFU pulse is shown in the right column in Figure 5.11(c). As mentioned

in Chapter 2, the shape of a lesion produced by boiling histotripsy is typically tadpole like, consisting of a "head" and a "tail" with the "head" closest to the HIFU source (Khokhlova and Hwang 2011). Examining the phantom morphology at the HIFU focus, residual mechanical damage of the gel is optically visible and the size of the lesion broadens with the number of HIFU pulses. During the first pulse, two major disrupted areas occur behind and in front of the HIFU focus. These areas gradually merge together as the number of HIFU pulses is increased. When comparing the location of the bubble motions (i.e. boiling bubbles and cavitation clouds) with the corresponding residual damage induced in the phantom (see Figure 5.11(b) and (c)), the position of the "head" shaped lesion corresponds well to that of the cavitation cloud, and the boiling bubbles generated in the super-heated region match the location of the "tail" shaped lesion. In addition, bubbles less than 200 μm in diameter are pushed away from the HIFU focus due to the HIFU radiation force (indicated by arrows in Figure 5.11(b)). This movement may also contribute to the formation of the "tail" together with the generation of boiling bubbles.

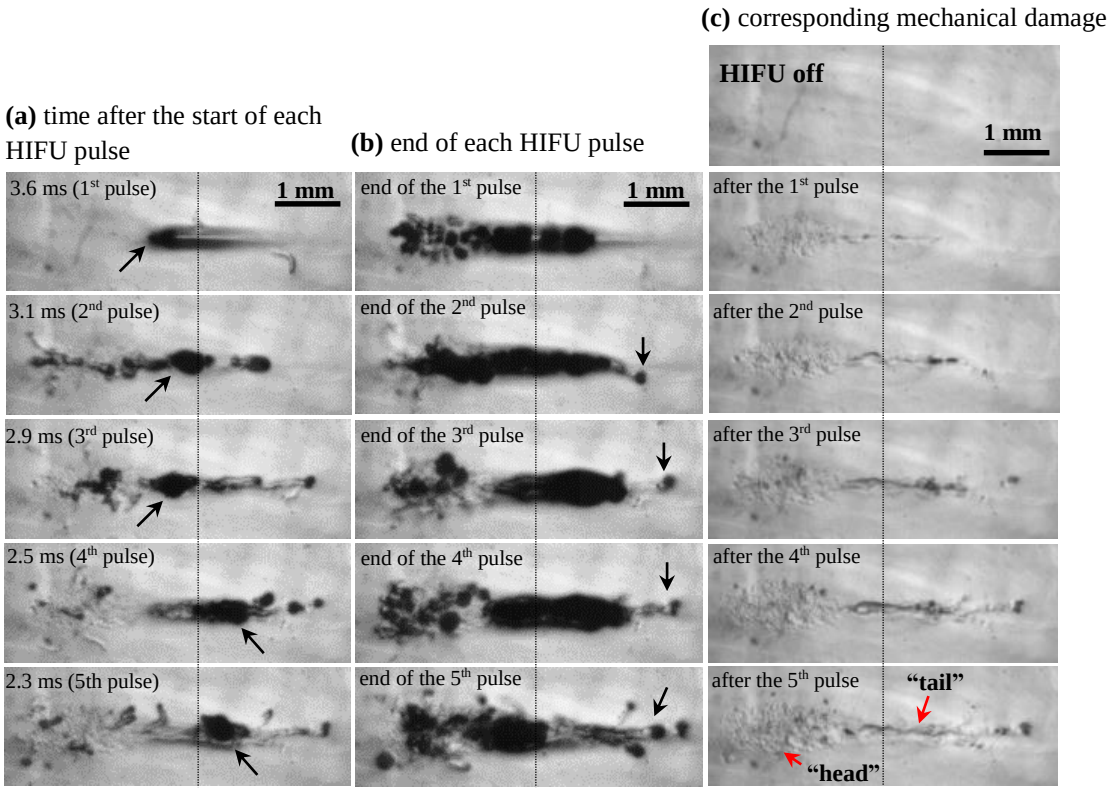

Figure 5.11. High speed images taken over the course of five HIFU pulses. (a) Images acquisition of the formation of a boiling bubble at the beginning of each

HIFU pulse (left column). (b) Images-captured at the end of each pulse (middle column). (c) Corresponding mechanical damage induced in the gel prior to the subsequent arrival of HIFU pulse (right column). The HIFU beam propagates from left to right. The images were captured at the frame rate of 15,000 fps. The vertical dashed lines indicate the HIFU focus.

In boiling histotripsy, 10 to 50 HIFU pulses are usually delivered to produce a well-defined mechanically fractionated lesion (Maxwell *et al* 2012). Figure 5.12 shows a number of high speed images captured during 50 HIFU pulses. The shape of a tadpole-like mechanical damage produced in the phantom corresponds well to the locations of a cavitation cloud and of boiling bubbles, in the "head" and in the "tail", respectively. This is further confirmed by cross sectioning the lesion immediately after exposure to the 50^{th} HIFU pulse, as shown in Figure 5.12 (f) and (g). No evidence of thermal damage, which would manifest itself as an opaque lesion (Khokhlova *et al* 2011) (see Figure 5.4), was present.

Figure 5.13 shows the length along the *z*-axis (the direction of wave propagation) and the width along the *y*-axis (the lateral direction) of the "head" and of the "tail" as a function of the HIFU pulse numbers. After the fifth HIFU pulse, the length of the "head" does not increase significantly, whereas the width of the "head" and both the width and length of the "tail" continue to grow. After the 30^{th} HIFU pulse, the overall lesion size does not change significantly.

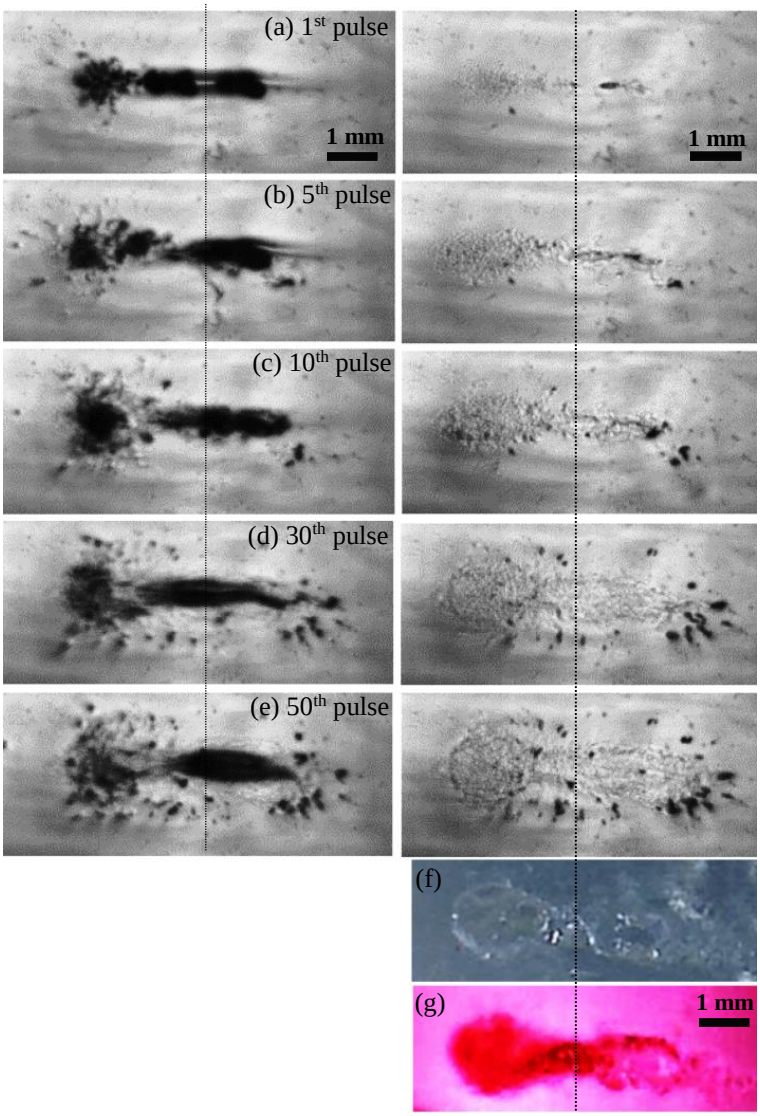

Figure 5.12. (a)-(e) high speed images taken over the course of 50 HIFU pulses. (f) is the cross-sectioned lesion after the 50th HIFU pulse and (g) is the same lesion as (f) but with an added dye. An acquisition rate of 1000 fps was used. Images on the left and right columns represent bubbles activities at the end of each 10 ms HIFU pulse and the corresponding mechanical damage induced in the gel, respectively. The HIFU beam propagates from left to right. The vertical dashed lines indicate the HIFU focus.

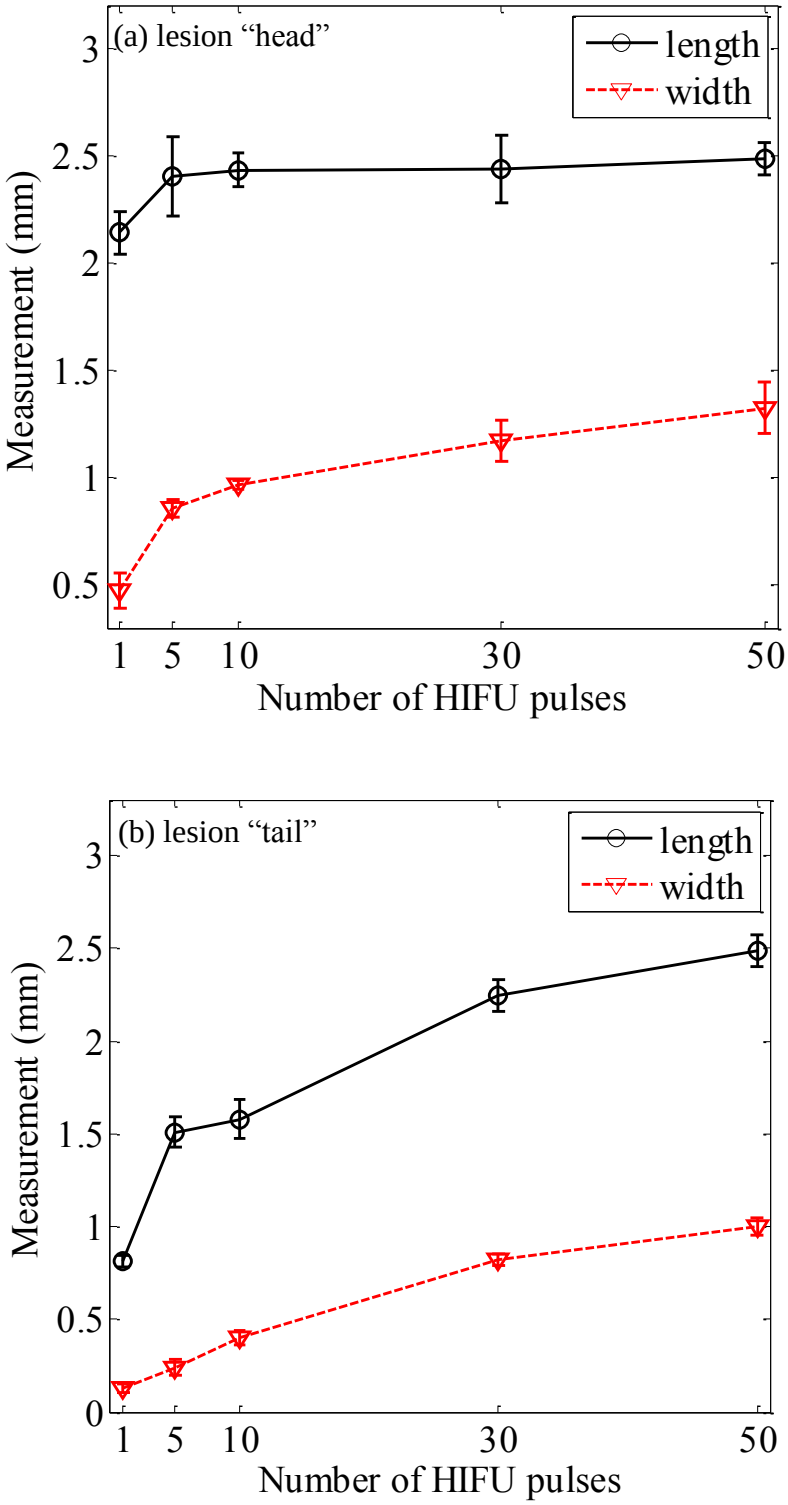

Figure 5.13. Length measurement (mean ± SD) along the *z*-axis (the direction of wave propagation) and the width along the *y*-axis (the lateral direction) of the "head" and of the "tail" as a function of the HIFU pulse exposure. The reference measurement point was at the HIFU focus. Photron FASTCAM Viewer software (Photron, San Diego, CA, USA) was used for the size measurement (24 μm/pixel). Each measurement was repeated five times.

5.3. Discussions

5.3.1. Formation of a boiling bubble

Canney *et al* (2010a) and Khokhlova *et al* (2011) showed that localised shock wave heating can increase temperature to 100°C in a few milliseconds followed by the formation of a boiling vapour bubble at the HIFU focus. The experimental results presented in this Chapter concur with theirs. A boiling bubble appeared in a localised super-heated region (see Figure 5.8). The boiling time resulting from a single 10 ms HIFU pulse in the gel (3.78 ± 0.67 ms, mean ± SD with $n_s = 17$) agreed well with that obtained from the temperature simulation, where the computed time to boil was predicted to be 3.66 ms. Furthermore, it was noticed that the onset time of a boiling bubble reduced with the number of HIFU pulses used (see Figure 5.11). This is most likely to be due to an accumulation of heat at the HIFU focus, where the peak temperature does not return to ambient temperature between pulses (Khokhlova *et al* 2011). Zhou and Gao (2013) measured the temperature variation at the HIFU focus in a tissue phantom with thermocouples during the first four 20 ms-long histotripsy pulses ($P_+ = 47$ MPa, $P_- = -16$ MPa, pulse repetition frequency of 1 Hz). They showed that the ambient temperature increased exponentially with the number of HIFU pulses.

During the course of HIFU exposure, the changes in temperature dependent acoustic properties, especially speed of sound, can lead to a shift of the HIFU focus in the axial direction towards the transducer (Connor and Hynynen 2002). In Figure 5.8(d) and Figure 5.11(a), it can be seen that a boiling bubble forms at the edge of the heated region during the first 10 ms HIFU pulse. This was also observed by Khokhlova *et al* (2011) although the authors did not interpret this phenomenon. In the presence of a localised region super-heated by shockwaves, there is a significant difference in temperatures between the inside and the outside of this region (see Figure 5.8(c)). This eventually leads the local speed of sound in the heated volume to be greater than that outside of this region (e.g. 1571 $m \cdot s^{-1}$ at 20°C; 1643 $m \cdot s^{-1}$ at

90°C, see Figure 3.1(b) in Chapter 3), causing an acoustic refraction effect at the interface (see Figure 5.14).

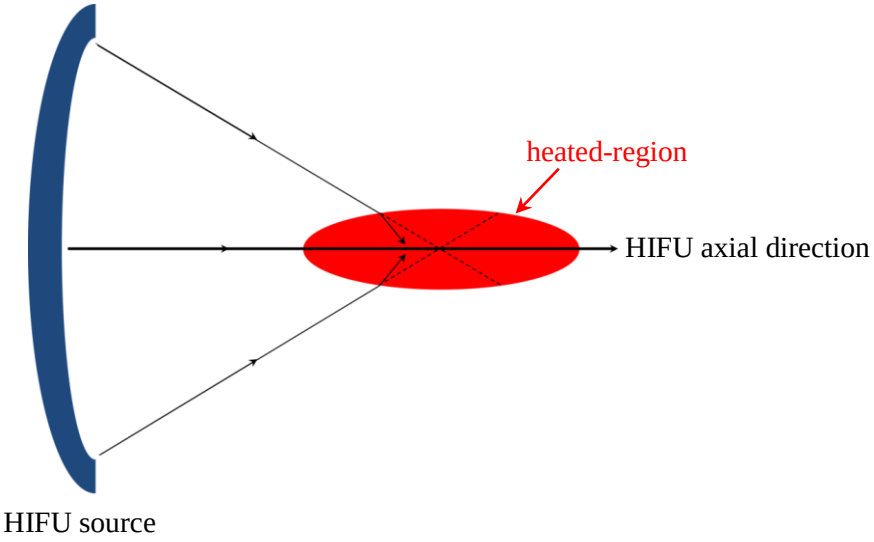

Figure 5.14. An illustration of a shift of the HIFU focus towards the transducer which can occur during boiling histotripsy.

In Chapter 4, it was shown that the combination of the asymmetry in a shockwave and water vapour transport causes a bubble to undergo rectified growth at 100°C; however, a lower surrounding temperature outside of the HIFU focal zone limits this growth process. Rectified growth of a boiling bubble can be clearly seen in Figure 5.10 and the extent of this bubble motion was spatially confined to the heated region.

5.3.2. Interaction of a boiling bubble with an incident shockwave

In HIFU cavitation cloud histotripsy, the reflection and inversion of incident shockwaves from the surface of a single cavitating bubble produces a greater peak negative pressure field, leading to additional bubble nucleation sites for cavitation clouds. This phenomenon is also known as the shock scattering effect (Maxwell *et al* 2011). This cavitation cluster was also observed during the course of boiling histotripsy, after the creation of a boiling bubble at the HIFU focus (see Figure 5.8(e)-(h)). Simultaneously with the bubble cloud formation in front of a boiling

bubble, a secondary localised heated region appears within the HIFU focal region followed by the secondary boiling bubble (see Figure 5.8(e),(f)). This is likely to be due to (a) the fact that the incident acoustic field is partially shielded by a cavitation cluster together with the boiling bubble and (b) the larger size of the HIFU focal width (FWHM of 1.05 mm, see Figure 5.3(b)) relative to that of the region super-heated by shocks (~0.2 mm, see Figure 5.8(c)). Indeed, as a result of the constructive and destructive interference between the incident field and that scattered by the secondary boiling bubble, local pressure minima as well as enhanced heating may be induced. This may lead to the generation of a number of boiling bubbles in front of the secondary boiling bubble towards the primary boiling bubble (see Figure 5.8 (f)-(h)). Figure 5.15 shows the simulated sum of the incident pressure and the pressure scattered by a boiling vapour bubble. The backscattered acoustic pressure field in front of the bubble and the reduced acoustic pressure in the shadow zone behind the bubble can be clearly observed, demonstrating good qualitative agreement with the experimental result in Figure 5.8(e).

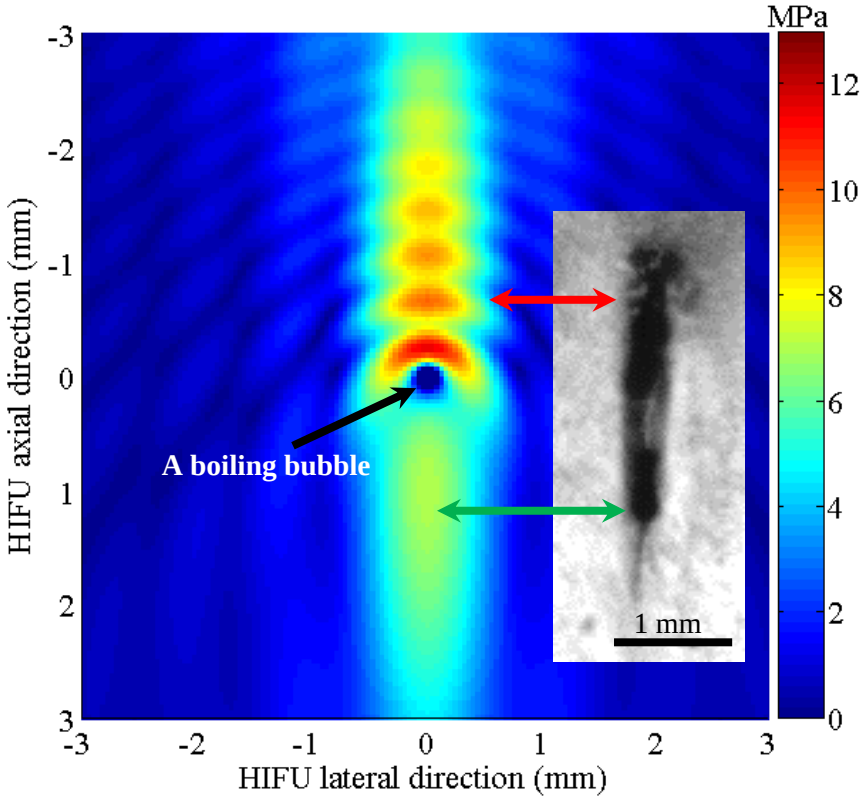

Figure 5.15. Calculated acoustic pressure magnitudes resulting from the scattering of the HIFU field by a boiling bubble. The green arrow indicates the presence of

partially shielded acoustic pressure field behind the vapour bubble. The red arrow shows the backscattered pressures. The HIFU beam propagates from top to bottom. Inset: a captured high speed image showing a cavitation cluster in front of and a secondary boiling bubble behind the primary boiling bubble. This acoustic pressure field was simulated using equation (5).

5.3.3. Mechanisms for the creation of a tadpole shaped lesion

As mentioned in Chapter 2, Khokhlova *et al* (2011), Simon *et al* (2012) and Wang *et al* (2013) proposed that the formation of a tadpole shaped lesion produced by HIFU boiling histotripsy is most likely to be due to the explosive growth of a boiling bubble together with the HIFU atomisation for a "head" shaped lesion and the streaming of a mechanically fractionated tissue within the forming "head" for a "tail" shaped lesion. The experimental results presented in this Chapter, however, support slightly different conclusions. Residual mechanical damage produced in the tissue phantom corresponded well to the locations of cavitation clouds and boiling bubbles for a "head" and a "tail", respectively (see Figure 5.11 and Figure 5.12). The shape of the lesion was further confirmed by cross sectioning it immediately after the HIFU insonation (see Figure 5.12 (f) and (g)).

Based upon the numerical and experimental results presented in this Chapter, another possible mechanism for boiling histotripsy is proposed. This is shown in Figure 5.16. After the formation and explosive growth of a boiling bubble at the HIFU focus, the shock scattering effect leads to the production of cavitation clouds in front of the boiling bubble. These bubble clouds enable the disruption of tissue (Lake *et al* 2008a, Hall *et al* 2009, Schade *et al* 2012a,b, Vlaisavljevich *et al* 2013) through the production of a "head" shaped lesion. In addition to this, the shear stresses produced around a number of boiling bubbles within a localised super-heated region create a "tail" shaped lesion.

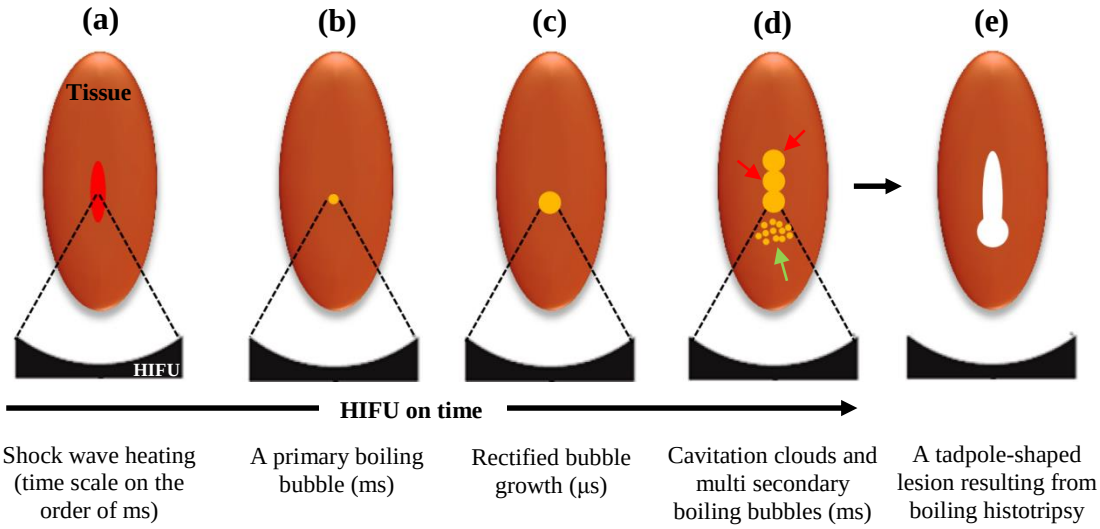

Figure 5.16. Proposed mechanisms for boiling histotripsy. (a) Shock wave heating. (b) Formation of a primary boiling bubble at the HIFU focus. (c) Rectified growth of a boiling bubble. (d) Production of cavitation clouds (indicated by the green arrow) and secondary boiling bubbles (indicated by the red arrows). (e) Creation of a tadpole-shaped lesion resulting from HIFU boiling histotripsy.

5.3.4. The variation of the size of a lesion with HIFU pulses

As shown in Figure 5.12 and Figure 5.13, the overall size of the lesion produced by boiling histotripsy increased gradually with the number of HIFU pulses, but did not change significantly starting from the 30th pulse. Khokhlova *et al* (2011) and Wang *et al* (2013) have also observed a similar trend in the growth of a lesion size with HIFU pulses. With the proposed mechanism described in Figure 5.16, it is suggested that the change of a lesion dimension is primarily dependent upon the extent of a localised super-heated region and the pressure amplitude of backscattered acoustic fields. As a heated region broadens with HIFU pulses due to an accumulation of heat, more boiling bubbles with larger sizes will form within this heated volume. These spatially confined boiling bubbles lead to a "tail" shaped lesion which grows in both axial and lateral directions with during exposure to ultrasonic pulses. Simultaneously, the enlarged boiling bubble with a larger surface area generates a wider backscattered acoustic field (see Figure 5.17). This results in the formation of a wider cavitation cluster in the lateral direction towards the HIFU source, producing a wider "head" shaped lesion. However, as heat transfer

processes reach equilibrium in between HIFU pulses, the volume over which the super-heating occurs reaches a maximum (Wang *et al* 2013). It is, therefore, reasonable to assume that beam width of the backscattered pressure field also reaches a maximum. As a result of this, the axial and lateral sizes of a "tail" do not change and neither does the lateral size of a "head". Furthermore, the reduction of pressure amplitudes of backscattered fields due to attenuation limits the axial growth of a "head" towards the HIFU source. Cavitation clouds, for example, stop progressing in the direction towards the HIFU transducer when the sum of incident and scattered acoustic pressures is below the cavitation clouds' threshold (i.e. –28 MPa).

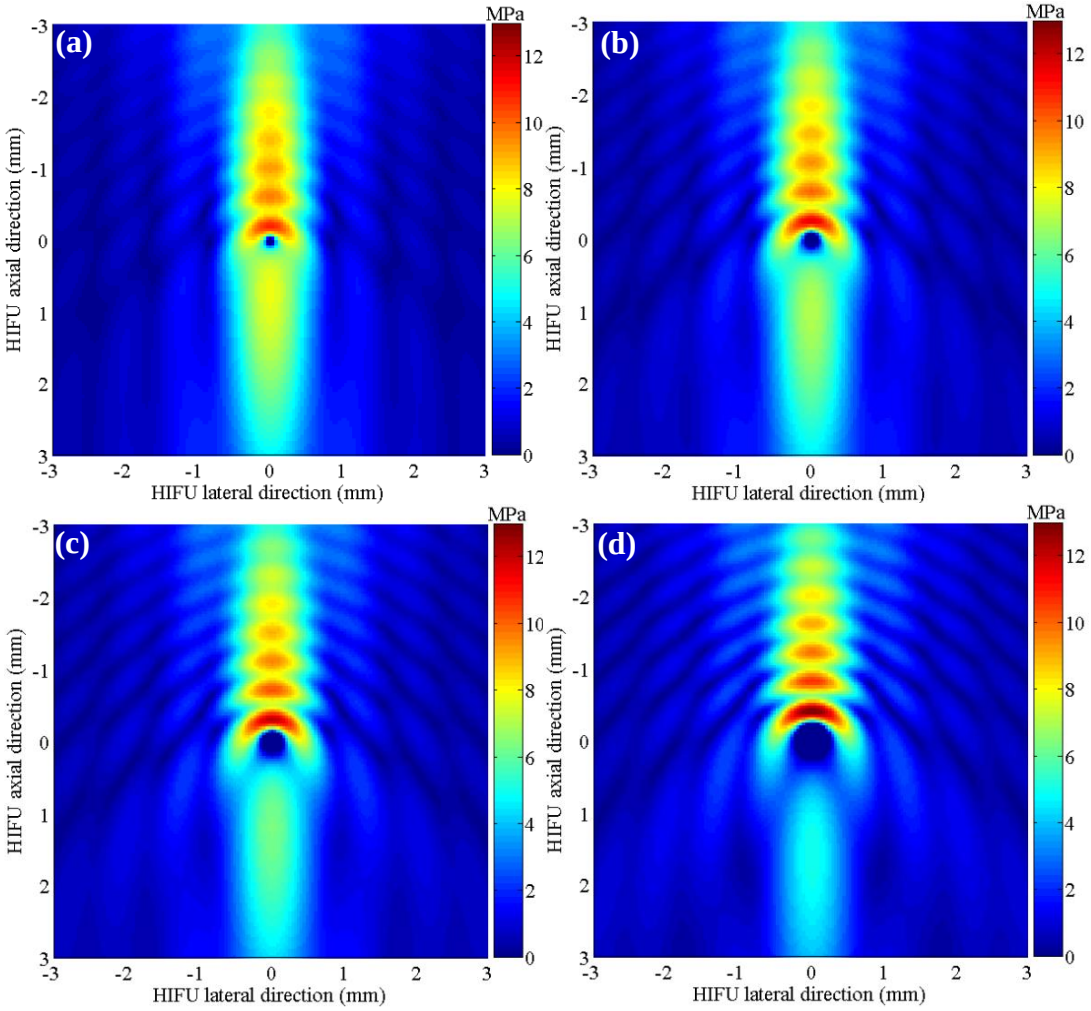

Figure 5.17. The sum of the incident and the backscattered acoustic pressure magnitudes from a vapour bubble with a diameter of (a) 100 μm, (b) 200 μm, (c) 300 μm and (d) 500 μm. The HIFU beam propagates from top to bottom.

5.4. Summary

The main objective of this Chapter was to gain an improved understanding of the mechanisms behind the production of a tadpole shaped lesion created by HIFU boiling histotripsy. A high speed camera with a PCD system was used to observe the bubble dynamics and record the corresponding acoustic emissions at the HIFU focus in optically transparent tissue phantoms during HIFU exposure. It was clearly observed that a number of boiling bubbles were induced and these were spatially confined to a localised super-heated region. Cavitation clouds were subsequently produced ahead of the expanding bubble. This process was repeated and eventually resulted in a tadpole shaped lesion. When comparing the location of the bubble motions with the corresponding mechanical damage produced at the HIFU focus, the position of the "head" shaped lesion matched that of the bubble clouds whereas the location of the "tail" lesion corresponded to that of the boiling bubbles. This was further confirmed by cross-sectioning the lesion after the HIFU exposure.

A simplified numerical model describing the scattering of the incident ultrasound wave by a vapour bubble was used to help interpret the experimental observations. Together with the numerical results, these observations suggest that the overall size of a lesion produced by boiling histotripsy is dependent upon the sizes of (a) the super-heated region at the HIFU focus and (b) the backscattered acoustic waves by the original vapour bubble.

Since there are two different types of cavitation activity (i.e. a boiling bubble and cavitation clouds) that contribute to the production of a tadpole shaped lesion, the nature of the damage in cellular structures around a "head" and a "tail" shaped lesions must be distinct from each other. This will be investigated in the following chapter with *in vivo* liver.

Chapter 6. *Ex*- and *in vivo* liver experiments: production of a mechanically fractionated lesion

Mechanisms involved in HIFU boiling histotripsy were investigated in the previous two chapters both numerically and experimentally. In Chapter 4, a significant difference in radiated acoustic pressures resulting from the bubble radial motions during thermal ablation and boiling histotripsy exposures was observed numerically. The distinction was made in terms of (a) the number of multiple harmonic components of the fundamental frequency and (b) the level of broadband emissions in the frequency domain. Higher order multiple harmonics with the elevation of broadband emissions appeared in the case of boiling histotripsy excitation (i.e. nonlinear-shocked wave excitation) relative to those under thermal ablation exposure conditions (i.e. a weakly distorted nonlinear waveform).

In Chapter 5, a high-speed camera with an optically transparent liver tissue phantom was used to explore mechanisms underpinning the production of a tadpole shaped lesion during HIFU boiling histotripsy. Boiling bubbles together with a cavitation cluster were found to be the major mechanisms that create a "head" and a "tail" shaped lesions, respectively. It was suggested that the nature of the damage in cellular structures around a "head" and a "tail" should be different from each other because of two different types of acoustic cavitation activity (inertial and stable cavitation) involved in the lesion creation.

The objective of this Chapter is to (a) produce a thermally and a mechanically induced lesion in *ex*- and *in vivo* livers and (b) obtain corresponding acoustic emissions for monitoring purposes. HIFU exposed *in vivo* liver tissue will be collected for histological analysis. The feasibility of a histotripsy lesion to serve as a potential site for cell injection will also be examined based on histological observations. Intra-hepatic cell transplantation mediated by HIFU, which was proposed in Chapter 1, will be performed in Chapter 7.

6.1. Materials and methods

Both *ex*- and *in vivo* experimental methods used in this Chapter are described in this section.

6.1.1. *Ex vivo* liver experiments

6.1.1.1. HIFU experimental set up

A schematic diagram of the *ex vivo* experimental set up used in this Chapter is shown in Figure 6.1. The experiments were performed in a water bath filled with degassed and de-ionised water at a temperature of 20^{o}C. A 1.1 MHz HIFU source with a 20 mm central aperture (nominal active diameter: 64 mm, nominal lateral full width half maximum FWHM: 1.33 mm, nominal axial FWHM: 13.5 mm, Sonic Concepts H102, Bothell, WA, USA) and the 2.0 MHz HIFU transducer (Sonic Concepts H106, Bothell, WA, USA) employed in Chapter 5 were used. Both HIFU sources consisted of spherical single element bowl-shaped transducers with a geometric focal length of 62.6 mm (Sonic Concepts, WA, USA). Each of these transducers was used to produce thermally ablated and mechanically fractionated lesions.

The HIFU device was positioned at one end in the water bath and an acoustic absorber (Precision Acoustics Ltd AptFlex F28, Dorchester, UK) was put on the opposite side to minimise acoustic reflections from the wall. The same electronics used in the previous chapter were used to drive the HIFU transducer: a function generator (Agilent 33220A, Santa Clara, CA, USA), an RF power amplifier (ENI 1040L, Rochester, NY, USA), waveform generation software (Agilent Waveform Builder, Santa Clara, CA, USA) and a power meter (Sonic Concepts 22A, Bothell, WA, USA).

During the *ex vivo* experiments, a 10 MHz 15-element ultrasound imaging probe (Siemens Sonoline Versa Plus, USA) was in contact with a tissue sample to obtain ultrasound B-mode images before and after HIFU insonation.

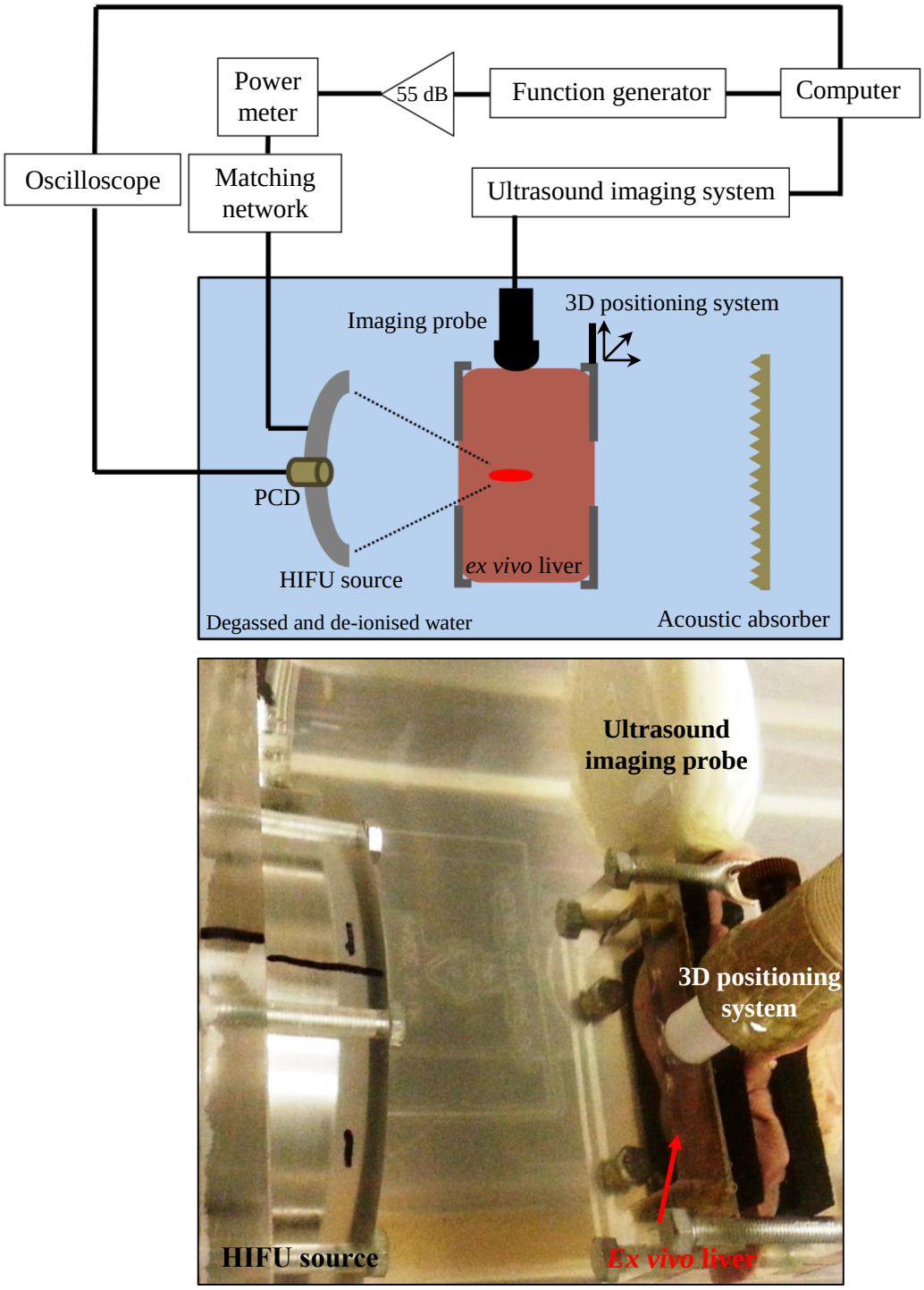

Figure 6.1. HIFU experimental set up used for producing thermally and mechanically induced lesions in an *ex vivo* liver.

6.1.1.2. HIFU exposure condition

The HIFU pulsing protocols used in the *ex vivo* experiments are shown in Table 6.1. Acoustic peak positive and negative pressures (P_+ and P_-) at the HIFU focus *in situ* and time t_b to reach a boiling temperature of 100°C were calculated using the KZK equation (3.72) and the BHT equation (3.75), respectively. The physical properties of the *ex vivo* liver used in the simulations are listed in Table 6.2.

1.1 MHz HIFU transducer								
Electrical power (W)	**Exposure type**	**P_+ (MPa)**	**P_- (MPa)**	**Time to boil**	**Duty cycle**	**Pulse length**	**Pulse repetition frequency**	**Number of pulses**
60	Thermal ablation	13.4	-7.5	2.2 s	100%	5 s		
350	Boiling histotripsy	82.1	-15.1	4.45 ms	1%	10 ms	1 Hz	50

2.0 MHz HIFU transducer								
Electrical power (W)	**Exposure type**	**P_+ (MPa)**	**P_- (MPa)**	**Time to boil**	**Duty cycle**	**Pulse length**	**Pulse repetition frequency**	**Number of pulses**
200	Boiling histotripsy	80	-15.6	2.66 ms	1%	10 ms	1 Hz	50

Table 6.1. HIFU exposure settings used in the *ex vivo* experiments. A continuous 5s HIFU insonation was used for the thermal ablation process whereas the duty cycle, pulse length, pulse repetition frequency and the number of HIFU pulses for the boiling histotripsy were 1%, 10 ms, 1 Hz and 50, respectively. Corresponding computed temperature fields are plotted in Figure 6.2.

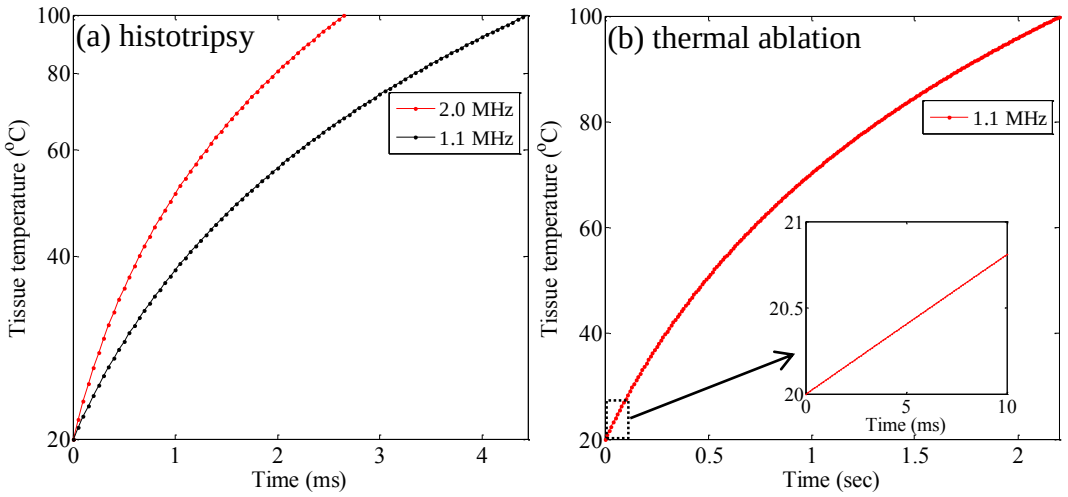

Figure 6.2. Simulated peak temperatures at the HIFU focus in *ex vivo* liver. (a) Boiling histotripsy exposure with a 1.1 MHz and a 2.0 MHz HIFU transducers. (b)

Thermal ablation insonation with a 1.1 MHz HIFU source. The inset in (b) represents the calculated temperature rise over 10 ms.

Symbol	Definition	**Values** (Choi *et al* 2013)	Units
C_T	specific heat capacity	3628	$J \cdot kg^{-1}K^{-1}$
κ_T	thermal conductivity	0.572	$W \cdot m^{-1}K^{-1}$
w_B	perfusion rate	0	$kg \cdot m^{-3}s^{-1}$
T_0	ambient temperature	20	^oC

Table 6.2. Properties of *ex vivo* liver used in the temperature field simulation. Acoustic properties listed in Table 4.1 in Chapter 4 were used in the acoustic field simulation.

6.1.1.3. Liver sample preparation and HIFU focus positioning

A cuboid tissue sample of dimensions 3 × 6 × 2 cm was obtained from an *ex vivo* chicken liver purchased from a local grocery store on the same day as the experiments. Prior to the experiments, the liver was kept at room temperature until its temperature reached 20^{o}C. The liver sample was then clamped by a custom-built tissue holder of dimensions 4.5 × 7.5 × 5 cm. The holder coupled with the sample was connected to a customised manual three-axis positioner. For consistency with the camera experiments performed in Chapter 5, the distance from the centre of the HIFU transducer surface to the liver surface was set to z = 57.6 mm. Hence, the HIFU focus was 5 mm below the surface of the liver sample.

To specify the lateral position of a HIFU-induced lesion within the liver sample, two thermal "marker" lesions were created laterally ± 7 mm away from the HIFU transducer axis on the liver surface (see Figure 6.3(a)). A continuous 2 s to 3 s HIFU insonation was applied until a well-defined thermally ablated lesion appeared on the surface. The HIFU exposed tissue sample was then cut along the line defined by these two thermal markers (see Figure 6.3(b)).

Ex vivo livers used in the experiments were not degassed prior to HIFU exposure although it is well known that gases released by autolysis can increase the probability of acoustic cavitation events (McLaughlan 2008, ter Haar 2015).

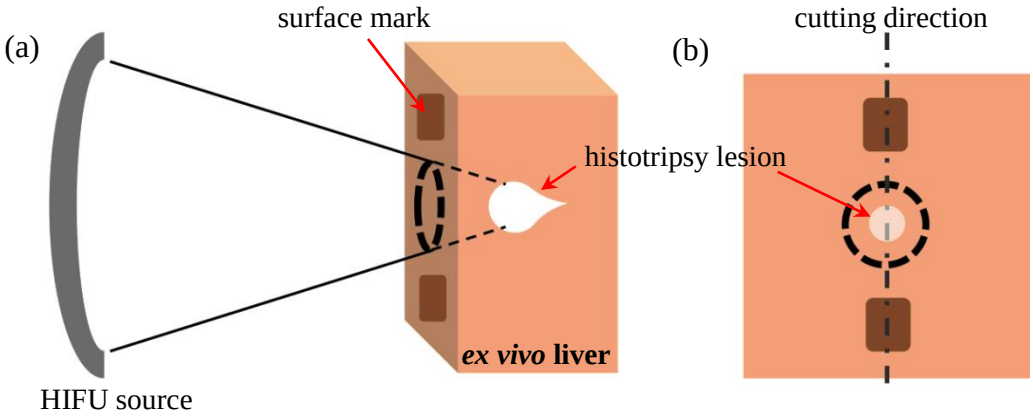

Figure 6.3. An illustration of a surface marking method used in this Chapter. (a) Two thermal "marker" lesions were produced on the liver surface facing the HIFU transducer in order to specify the lateral position of a histotripsy lesion produced within the sample. (b) After the HIFU experiments, the liver sample was cut along these two markers.

6.1.1.4. Experimental quantification of cavitation dose

A 10 MHz focused PCD with a diameter of 20 mm and a geometric focal length of 64 mm (Sonic Concepts Y107, Bothell, WA, USA) was used to monitor acoustic emissions produced at the HIFU focus. The PCD transducer was inserted into the central hole of the 1.1 MHz HIFU transducer and aligned confocally with the HIFU focus. Acoustic emissions emitted from either a thermally or a mechanically induced lesion were recorded via a digital oscilloscope (LeCroy HDO 6054, Berkshire, UK) at a sampling rate of 125 MHz over a period of 10 ms.

The PCD output signals (voltage vs time) were transferred to a computer for analysing cavitation activity using the quantification method described in Chapter 3 (see section 3.5). A 10 ms-long recorded raw PCD data window was initially divided into 50 segments, so that each of these represented a 0.2 ms-long acoustic emission. This PCD data was then converted to the frequency domain using an FFT. In an FFT plot, the areas under multiple harmonic components of the fundamental frequency (of the form nf_0, where n is a positive integer) and specified frequency windows (of the form $(2n+1)f_0/2$) with a fixed bandwidth of 0.1 MHz were

numerically integrated. These were then cumulated to obtain stable (SC) and inertial (IC) cavitation doses. Because of the limited bandwidth of the PCD transducer (10 kHz to 20 MHz) and the reflections of the driving frequency (1.1 MHz), frequencies in the range of the 2nd harmonic (2.2 MHz) to the 18th harmonic (19.8 MHz) were considered in the calculations. As an amount of acoustic cavitation dose was calculated over each 0.2 ms time segment, it was possible to investigate the temporal variation of both IC and SC doses. MATLAB® (MathWorks Inc., R2013a) was used for the signal processing.

During the *ex vivo* experiments, 13 PCD data sets in total (n_s = 9 for the boiling histotripsy and n_s = 4 for the thermal ablation exposures) were collected. Quantified IC and SC doses were presented as the means ± standard deviations (SD). Acoustic signals were not recorded during the experiments performed with the 2.0 MHz HIFU transducer as this device did not feature a central aperture.

6.1.1.5. Numerical simulations of radiated acoustic pressures

The numerical bubble model and the piecewise constant approximation method described in Chapter 3 (see sections 3.1 and 3.4) were used to simulate acoustic emissions at a given HIFU exposure setting listed in Table 6.1. The change of tissue temperature at the HIFU focus as a function of time was initially obtained from the temperature simulation (see Figure 6.2). The bubble model was then run at each temperature step with updated boundary conditions (i.e. temperature-dependent physical properties of liver, saturated water vapour density, Henry's constants, initial bubble radius, bubble wall velocity, temperature inside the bubble and molecular contents). The sampling frequency of 125 MHz and the quantification method used in the experiments were applied in the numerical simulations.

6.1.2. *In vivo* liver experiments

6.1.2.1. Animals

Male Sprague–Dawley rats, 6–8 week old and weighing 200–250g, were obtained from the Charles-River Laboratories UK Ltd (Margate, Kent, UK). The animals were housed in a temperature controlled room (23 ± 2^{o}C), with a relative humidity of 50 ± 10 % and alternate light/dark conditions. They were given standard laboratory rodent chow. All animal experiments were conducted according to the Home Office guidelines under the UK Animals and Scientific Procedures Act 1986. All experiments were performed under isoflurane general anesthesia.

6.1.2.2. *In vivo* HIFU experimental set-up

Figure 6.4 shows a schematic diagram of the *in vivo* experiment set up used in this Chapter. The experiments were conducted with a customised transducer-holder allowing circulation of degassed and de-ionised water using a peristaltic pump (Seko PR18, Harlow, UK) for cooling and coupling purposes. The pump was switched on immediately after each set of experiments to prevent possible transducer overheating. The 2.0 MHz HIFU transducer (Sonic Concepts H106, Bothell, WA, USA) was used with the same electronics employed in the *ex vivo* experiments. During the *in vivo* experiments, the transducer holder connected to a manual-three-axis-positioning system (Sherline Products 5430, Vista, CA, USA) was placed directly on the animal's exteriorised liver and the field coupled through a 12 μm-thick acoustically transparent polyethylene (Mylar) film (PMX 980, HiFi Industrial Film, Stevenage, UK). The holder was designed so that the distance from the end of the holder (in contact with the liver) to the centre of the transducer surface was z = 57.6 mm. Therefore, the HIFU focus was 5 mm below the surface of the exteriorised liver. An adjustable laser pointer aligned with the HIFU transducer axis was attached to the translation stage for targeting the HIFU beam on the liver surface laterally. The HIFU exposure settings used in the *in vivo* experiments are listed in Table 6.3.

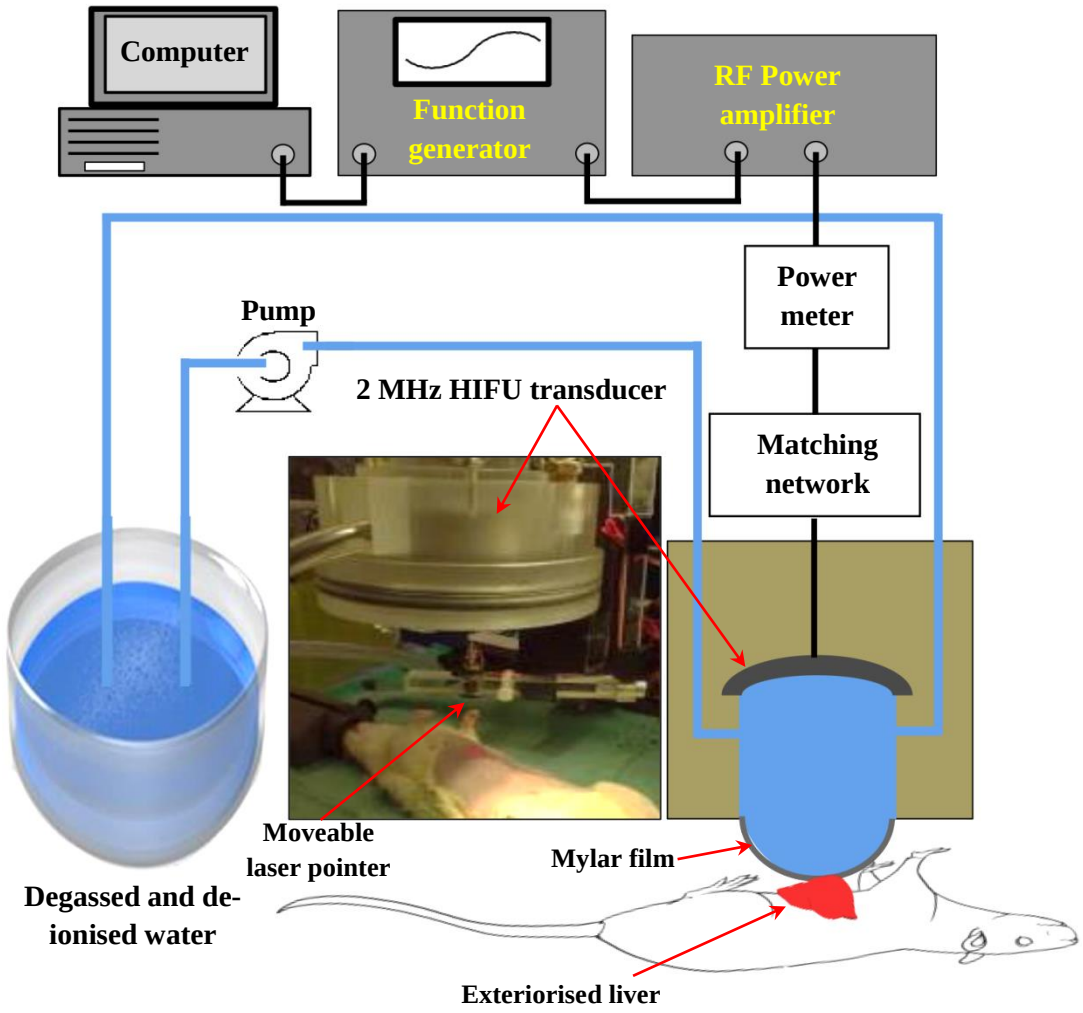

Figure 6.4. A schematic diagram of the *in vivo* HIFU experimental set up used in this Chapter.

Electrical power (W)	Peak pressures at focus *in situ* (MPa)	Time to boil (ms)	Duty cycle (%)	Pulse length (ms)	Pulse repetition frequency (Hz)	Number of HIFU pulses
150	$P_+ = 66$, $P_- = -14.1$	4.59	1	10	1	5,10,50
200	$P_+ = 80$, $P_- = -15.6$	2.05	1	10	1	5,10,50

Table 6.3. HIFU exposure conditions used in the *in vivo* experiments. Each HIFU pulse contains a continuous 10 ms HIFU insonation. The KZK equation (3.72) and the BHT equation (3.75) were used to simulate the peak positive and negative pressures at the HIFU focus and the time t_b to reach a boiling temperature of 100ºC with P_{elect} = 150 W and 200 W. The physical parameters of the *in vivo* liver used in the temperature simulation are displayed in Table 6.4.

Symbol	Definition	Values	Units
C_T	specific heat capacity	3628	$J{\cdot}kg^{-1}K^{-1}$
κ_T	thermal conductivity	0.572	$W{\cdot}m^{-1}K^{-1}$
w_B	perfusion rate	19.5 (Rijkhorst *et al* 2011)	$kg{\cdot}m^{-3}s^{-1}$
T_0	ambient temperature	37	^oC

Table 6.4. Physical properties of *in vivo* liver used in the temperature simulation. The acoustic properties displayed in Table 4.1 in Chapter 4 were used in the acoustic field simulation.

Prior to the *in vivo* experiments, the customised holder coupled with the HIFU transducer was tested with an unperfused *ex vivo* chicken liver. This is shown in Figure 6.5. A laser pointer was initially used to target the HIFU beam on the liver surface laterally (see Figure 6.5(a)). The end of the holder was then in contact with the liver surface for HIFU exposure. After the HIFU insonation, a "dimple" was observed on the liver surface (see Figure 6.5(b)) due to the formation of a cavity (see Figure 6.5(d)). Indeed, the lateral position of a laser point on the surface matched that of the "dimple" (see Figure 6.5(c)).

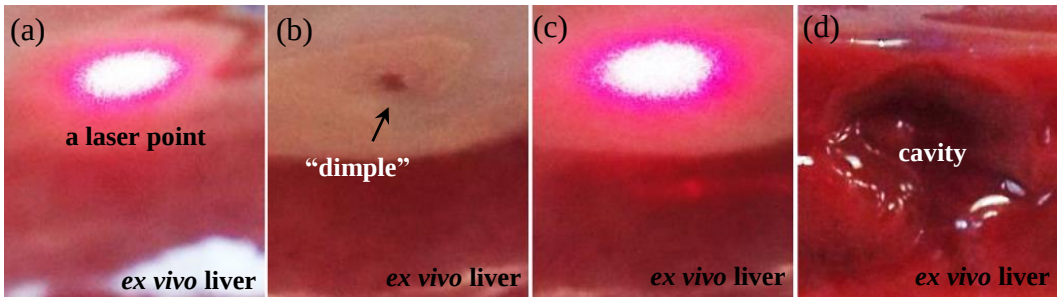

Figure 6.5. Testing the *in vivo* HIFU experimental set-up with an *ex vivo* liver sample. (a) Targeting the HIFU beam on the liver surface laterally using a laser pointer. (b) shows the appearance of a "dimple" on the liver surface after the HIFU exposure. (c) The lateral position of the "dimple" on the surface matches that of a laser point. (d) shows a cross-section of a cavity. An electrical power of 200 W, 10 ms pulse length, 1% duty cycle, 1 Hz pulse repetition frequency and 50 HIFU pulses were used.

6.1.2.3. HIFU animal experiments

Five Sprague–Dawley rats were used for the boiling histotripsy experiments. Isoflurane-induced general anesthesia was used during the operative procedure. A midline incision was made and the median and the left lateral liver lobes were taken outside the abdominal cavity. The transducer was coupled to the exteriorised liver targeting the median lobe immediately right of the falciform ligament. Animals were sacrificed immediately after the HIFU exposure. After euthanasia, sliced liver tissue containing a cavity was placed into formalin solution for preservation and formalin-fixed and paraffin-embedded for histological analysis. A longitudinally sectioned paraffin block was stained with haematoxylin and eosin (H&E) to make the various tissue components conspicuous but also to allow distinctions to be made between them. Haematoxylin stains cell nuclei as blue-purple colour, whereas eosin stains cytoplasm and collagen as pink colour.

Exteriorisation of the liver and the preparation of paraffin embedded samples were performed by Dr Dipok Kumar Dhar (Institute for Liver and Digestive Health, Royal Free Hospital, University College London, UK).

During the experiments, an acoustic absorber was not placed under the bottom surface of the exteriorised liver. Therefore, we could have had the acoustic reflection from the bottom surface of the exteriorised liver which might affect the simulated *in situ* peak pressure values at the HIFU focus.

6.2. Results

6.2.1. *Ex vivo* experimental results

Figure 6.6 shows cross-sections of *ex vivo* livers exposed to different HIFU insonation conditions. In the boiling histotripsy exposure case (P_{elect} = 200 W for the 2.0 MHz HIFU transducer and P_{elect} = 350 W for the 1.1 MHz source), a well-defined cavity is produced in the liver with no evidence of thermal damage at the boundary of the cavity such as blanching (see Figure 6.6(a) and (b)). For the thermal ablation insonation condition (P_{elect} = 60 W for the 1.1 MHz source), there is a cigar-shaped thermally ablated lesion which corresponds to the ellipsoidal shape of the HIFU focal region (see Figure 6.6(c)). Three pits (indicated by the black arrows in Figure 6.6(c)) are observed within the lesion, and these might be the results of inertial cavitation (Tezel and Mitragotri 2003) or boiling bubbles (McLaughlan 2008). Both mechanically and thermally induced lesions are identified as hyperechoic regions on the B-mode images (see Figure 6.6(a), (b), (c)-ii).

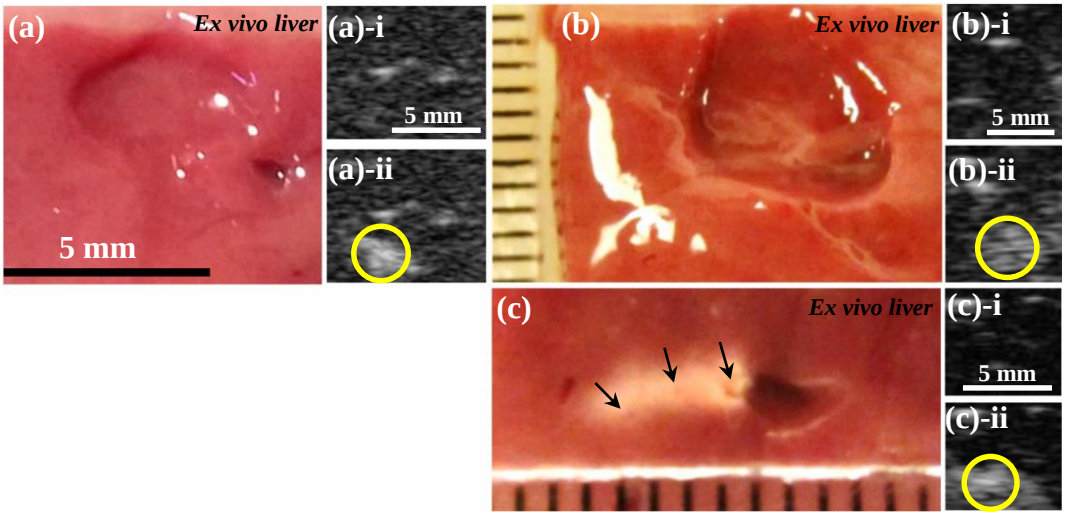

Figure 6.6. Photographs showing cross-sections of HIFU-induced lesions produced inside an *ex vivo* chicken liver. (a) A mechanically fractionated lesion (a cavity) with the 2.0 MHz HIFU transducer (P_{elect} = 200 W, P_+ = 80 MPa, P_- = –15.6 MPa at the HIFU focus). (b) A cavity produced by the 1.1 MHz HIFU source with P_{elect} = 350 W (P_+= 82.1 MPa, P_- = –15.1 MPa). The HIFU beam propagates from top to bottom. (c) A thermally ablated lesion induced by the 1.1 MHz HIFU source with P_{elect} = 60 W (P_+ = 13.4 MPa, P_- = –7.5 MPa). The HIFU beam propagates from left

to right. Images (a), (b), (c)-i and (a), (b), (c)-ii represent the corresponding ultrasound B-mode images before and after the HIFU exposure, respectively. The hyperechoic regions on the B-mode images indicated by the yellow circles in (a), (b), (c)-ii represent the HIFU-induced lesions.

Acoustic emissions recorded over a period of 10 ms under boiling histotripsy and thermal ablation exposures are shown in Figure 6.7. Variations of the peak-to-peak PCD voltage output present the amplitudes of acoustic cavitation during HIFU exposure (Everbach *et al* 1997, Zhou and Gao 2013). When comparing spectrograms resulting from the recorded acoustic signals, higher order multiple harmonic components of the fundamental frequency (f_0 = 1.1 MHz) up to the 17th harmonic (18.7 MHz) with larger amplitudes, as well as higher levels of broadband emissions, can be seen under the boiling histotripsy insonation relative to those during thermal ablation exposure (see Figure 6.7(b) and (d)). These frequency domain features are in agreement with the numerically obtained spectrograms in Figure 6.8(e) and (f).

As discussed in Chapters 4 and 5, a significant appearance of higher order multiple harmonics in the frequency domain is an indicator of the presence of a boiling bubble at the HIFU focus during the course of HIFU exposure. In the case of the boiling histotripsy excitation, the manifestation of a boiling bubble appears at t = 4.72 ms (see Figure 6.7(b)), whilst this is not observed under the thermal ablation exposure (see Figure 6.7(d)). This is due to the fact that the acoustic absorption of weakly distorted nonlinear waves in tissue does not increase tissue temperature to a boiling temperature of 100^{o}C within 10 ms (i.e. the computed time to boil was predicted to be 2.2 s, see Figure 6.2(b)). Nevertheless, the recorded acoustic emissions suggest that acoustic cavitation may be occurring (see Figure 6.7(d)), but that this is not due to the large bubble formed by boiling.

During the experiments, the boiling time of the first 10 ms-boiling histotripsy pulse in the *ex vivo* liver was 4.56 ± 1.15 ms (mean ± SD with n_s = 9), which was similar to the temperature simulation (t_b = 4.45 ms, see Figure 6.2(a)) with differences of 2.5% between the PCD measurement and the calculation.

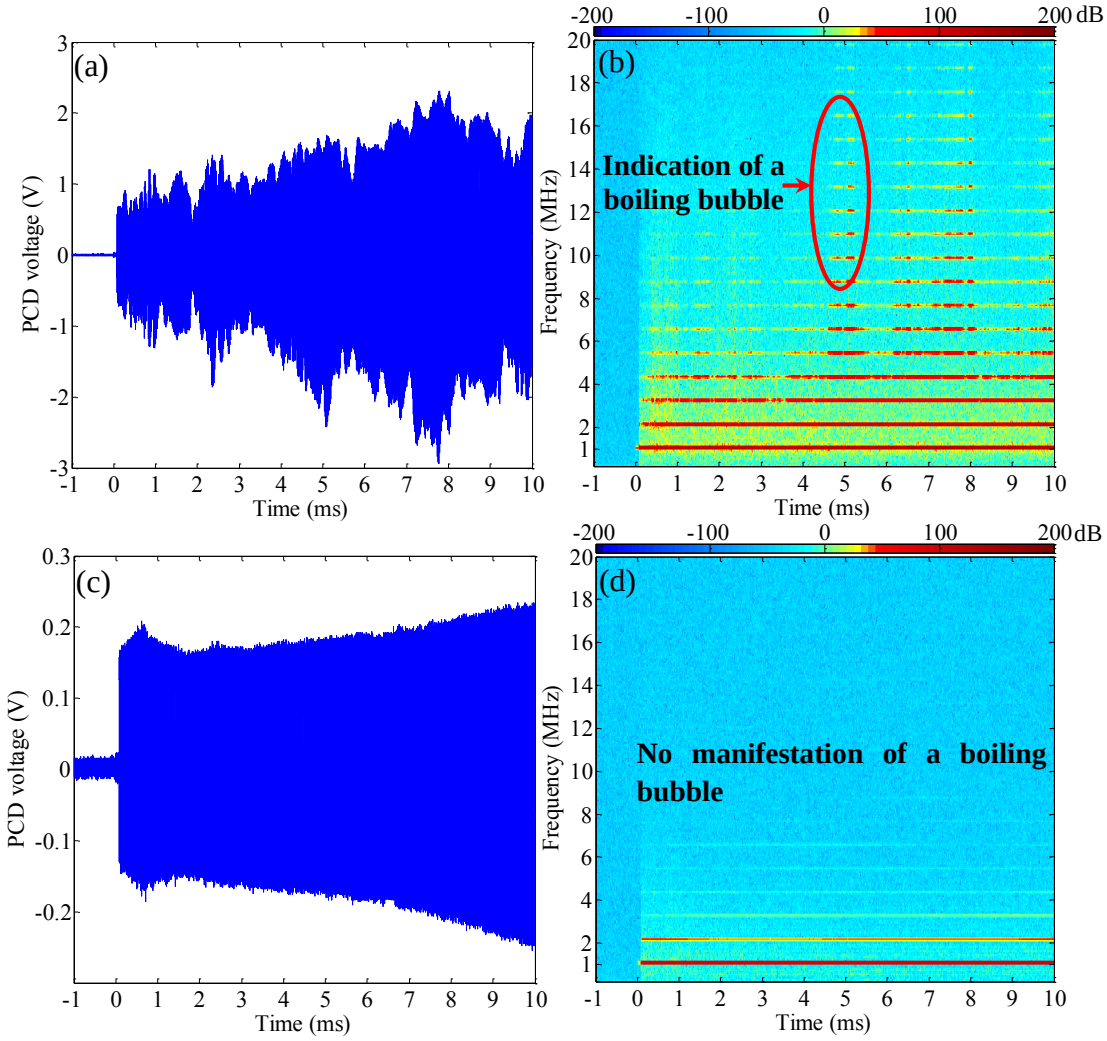

Figure 6.7. Recorded acoustic emissions resulting from cavitation activity at the HIFU focus during the boiling histotripsy and the thermal ablation exposures. (a) and (c) are the raw PCD voltage vs time plots obtained under the boiling histotripsy and the thermal ablation exposure conditions, respectively. (b) and (d) are the corresponding spectrograms. The time at 0 ms corresponds to the start of HIFU insonation.

Figure 6.8 shows calculated IC and SC doses over 4 ms prior to the onset of a boiling bubble. In both HIFU exposure conditions, SC dose increases (Figure 6.8(a)) while IC reduces (Figure 6.8(b)) with time. It is also noticed that cavitation dose (both SC and IC) under the boiling histotripsy insonation is greater relative to that under the thermal ablation exposure (see Figure 6.8 (a) and (b)). These experimental observations are in agreement with the numerical simulations displayed in Figure 6.8(c) and (d).

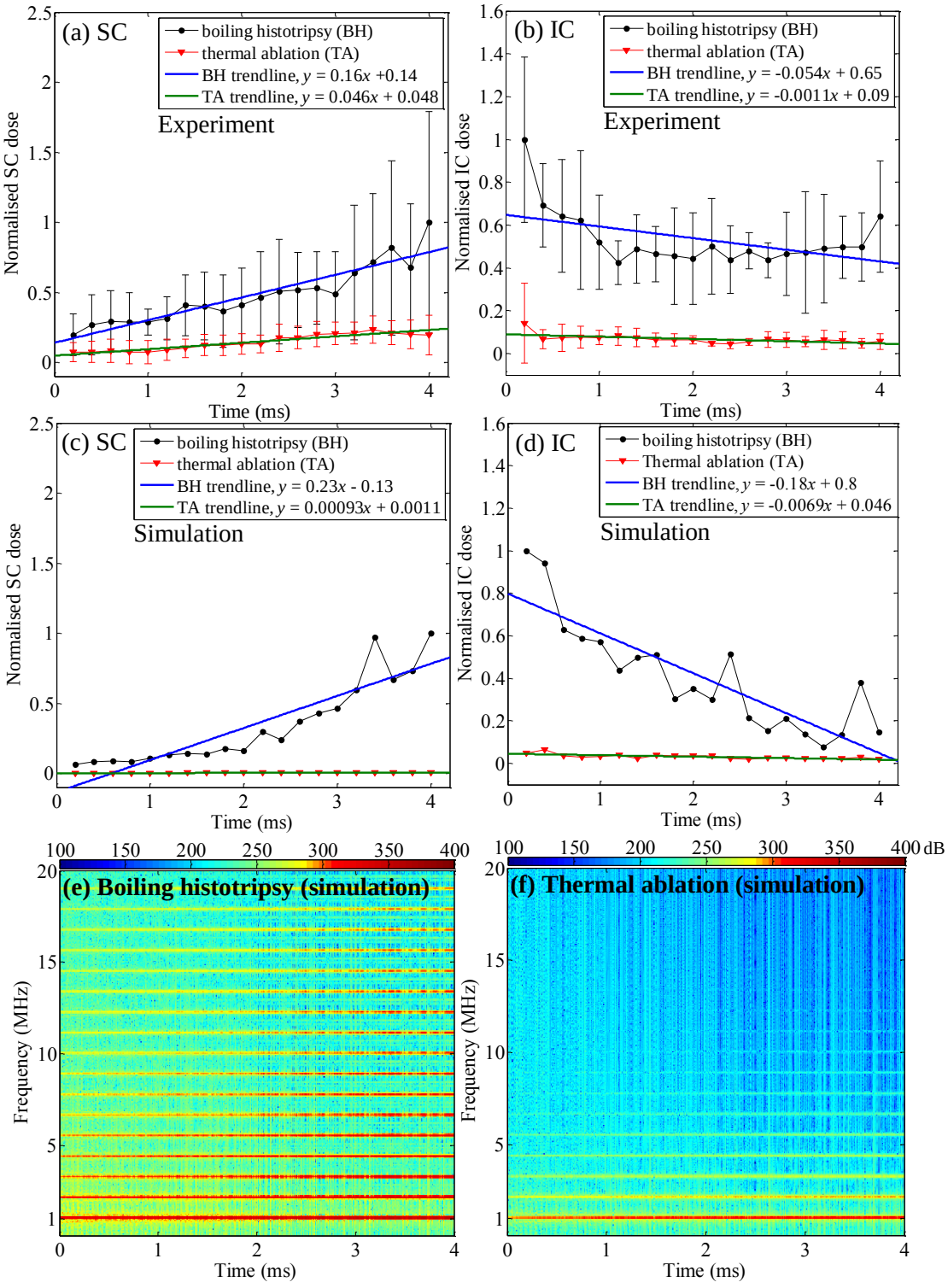

Figure 6.8. (a) and (b) are the experimentally obtained SC and IC doses under the boiling histotripsy (mean ± SD with n_s = 9) and the thermal ablation (mean ± SD, n_s = 4) exposures, respectively. (c) and (d) are the simulated SC and IC doses. (e) and (f) are the predicted spectrograms under the boiling histotripsy and the thermal ablation excitations, respectively.

6.2.2. *In vivo* experimental results

In one animal, the holder coupled with the HIFU transducer was placed lightly over the right upper quadrant of abdomen and the focal point of HIFU was adjusted to target the liver. In this way, the production of a cavity by the extracorporeal technique is confirmed and no skin burn is observed visually (see Figure 6.9). For the rest of the *in vivo* experiments, the liver was exteriorised and the transducer was directly placed over the liver surface. To examine the freshly created cavity, the animals were sacrificed immediately after cavity creation. Figure 6.10 (a) and (b) show a number of photographs of newly produced cavities in the exteriorised liver with different HIFU exposure conditions. On macroscopic examination, well-defined cavities are produced in the liver parenchyma with no evidence of thermal damage around the lesions. Furthermore, the size of a cavity increases with the number of HIFU pulses.

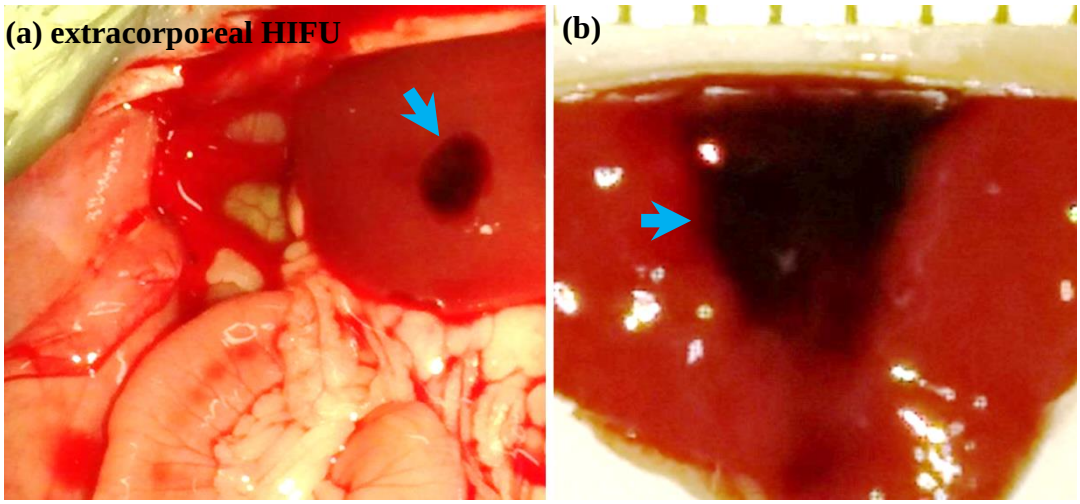

Figure 6.9. (a) A freshly created cavity by extracorporeal HIFU (i.e. the liver has not been exteriorised) with an electrical power of 200 W and 50 pulses. (b) Corresponding cross-sectioned lesion. The blue arrows indicate the cavity formation. The HIFU beam propagates from top to bottom.

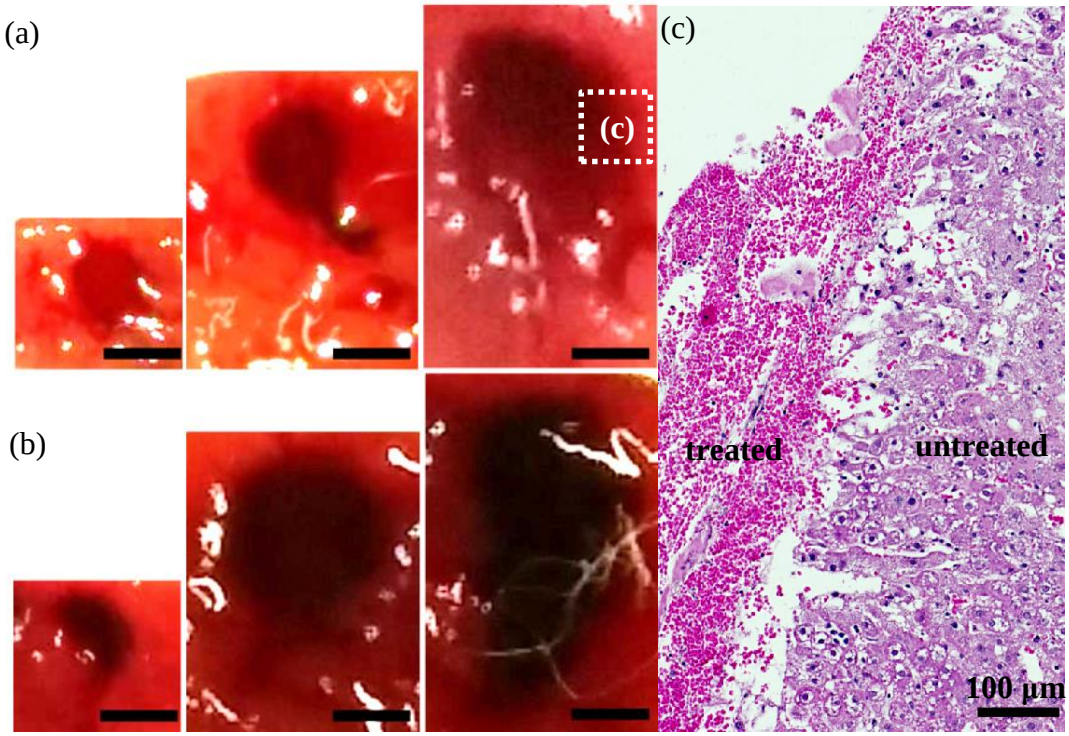

Figure 6.10. Cross-section of a liver lobe showing freshly created cavity in the exteriorised *in vivo* liver by HIFU. Upper row (a): Cavities produced by 150 W HIFU electrical power and, 5, 10 and 50 pulses, respectively (left to right), lower row (b): Cavities induced with 200 W and, 5, 10 and 50 pulses, respectively (left to right). The HIFU beam propagates from top to bottom. (c) A microscopic view of the highlighted area in (a). The margin of a newly created cavity without any sign of thermal damage is shown. Scale bars in (a) and (b) represent 1 mm.

On microscopic examination, no sign of thermal injury due to coagulative necrosis is observed around the margins of the freshly created cavities (i.e. the interface between the cavity and the surrounding tissue) (see Figure 6.10(c)). If thermal damage had occurred, more eosinophilic areas (stained a darker pink) with the appearances of a shrunken hepatocyte nuclei and granular cytoplasm would have appeared (Jones *et al* 2012, Wang *et al* 2013) (see Figure 6.11(b)).

The contents of the cavities are mainly the red blood cells (RBCs) and cellular debris. Some lysed RBCs (featuring red tinted area in Figure 6.12(a)) as well as few intact hepatocyte nuclei were also observed in the cavity (indicated by the blue arrows in Figure 6.12(b)).

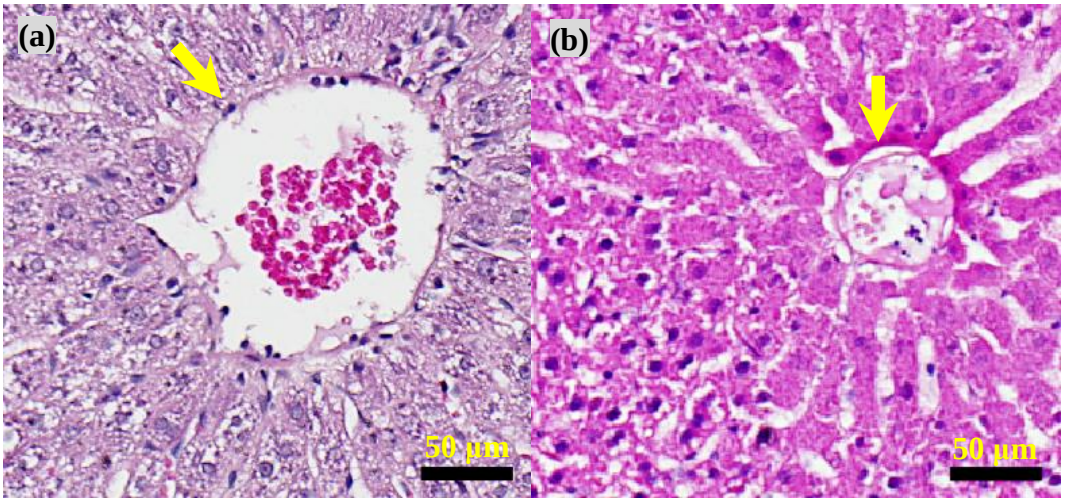

Figure 6.11. Examples of microscopic views of (a) a normal hepatic parenchyma and (b) a thermally ablated liver parenchyma by HIFU. The yellow arrows indicate blood vessels.

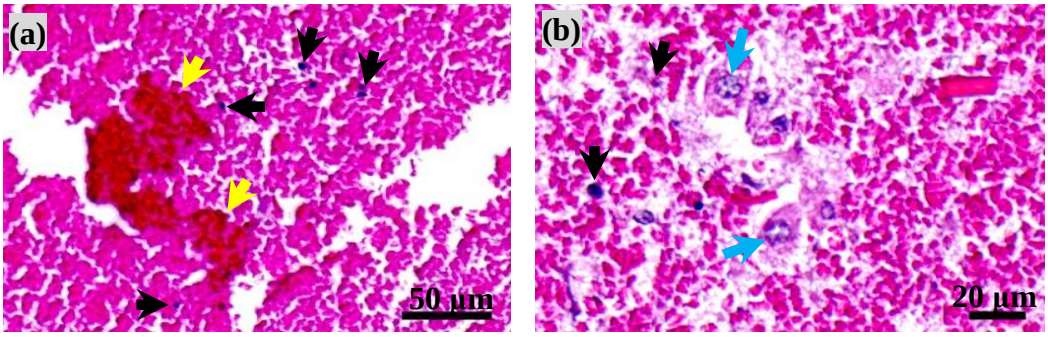

Figure 6.12. (a) Lysed RBCs (yellow arrows) and (b) intact hepatocytes nuclei (blue arrows) inside the cavity. The black arrows indicate cellular debris.

In Chapter 5, two different types of cavitation activity (i.e. a boiling bubble and cavitation clouds) were found to be the major mechanisms for the lesion creation (i.e. a "head" and a "tail" shaped lesions) during HIFU boiling histotripsy. Upon histological examination, broken hepatocyte plates and pits with ragged boundaries between the treated and untreated regions are noticed around the "head" shaped lesion (see Figure 6.13(c)-(e)). In contrast, the margins of the "tail" are sharply demarcated with smooth boundaries (see Figure 6.13(f) and (g)).

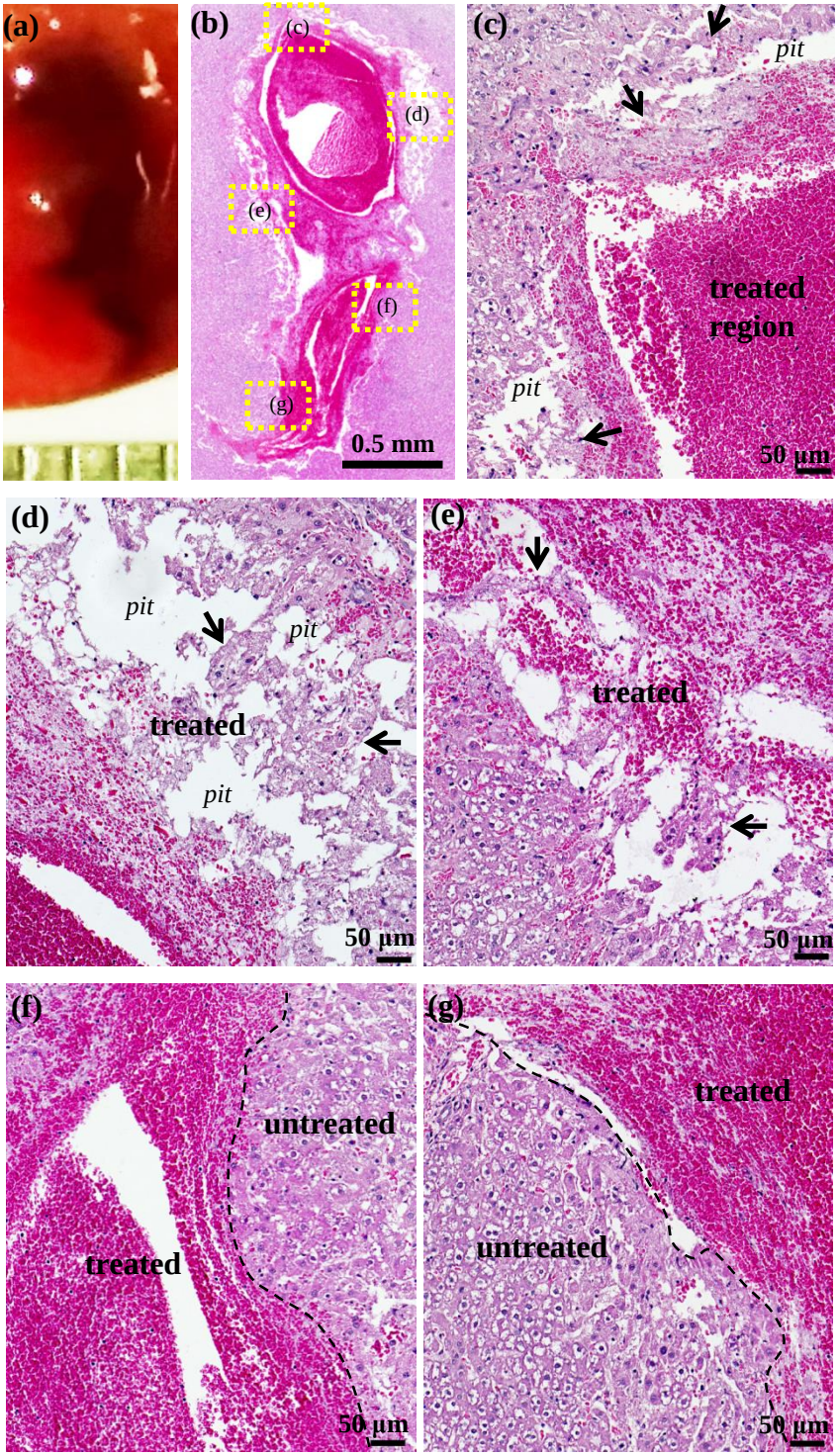

Figure 6.13. Histological examination around a freshly created cavity produced by an electrical power of 200 W (P_+ = 80 MPa, P_- = –15.6 MPa) with 10 HIFU pulses. (a) A photograph showing the cavity creation *in vivo*. The HIFU beam propagates from top to bottom. (b) Corresponding H&E stained lesion. Images (c) to (f) show the highlighted areas in (b) at higher magnifications. Arrows indicate broken hepatocyte plates.

Interestingly, with a setting of 150 W of electrical power (P_+ = 66 MPa, P_- = –14.1 MPa at the focus) and using five HIFU pulses, some of the cavities are partially fractionated with intact extracellular matrix and vascular network producing a decellularised cavity (see Figure 6.14). An intact vascular network inside the cavity is confirmed by anti-CD31 immunohistochemistry, which stains vascular endothelial cells as brown colour.

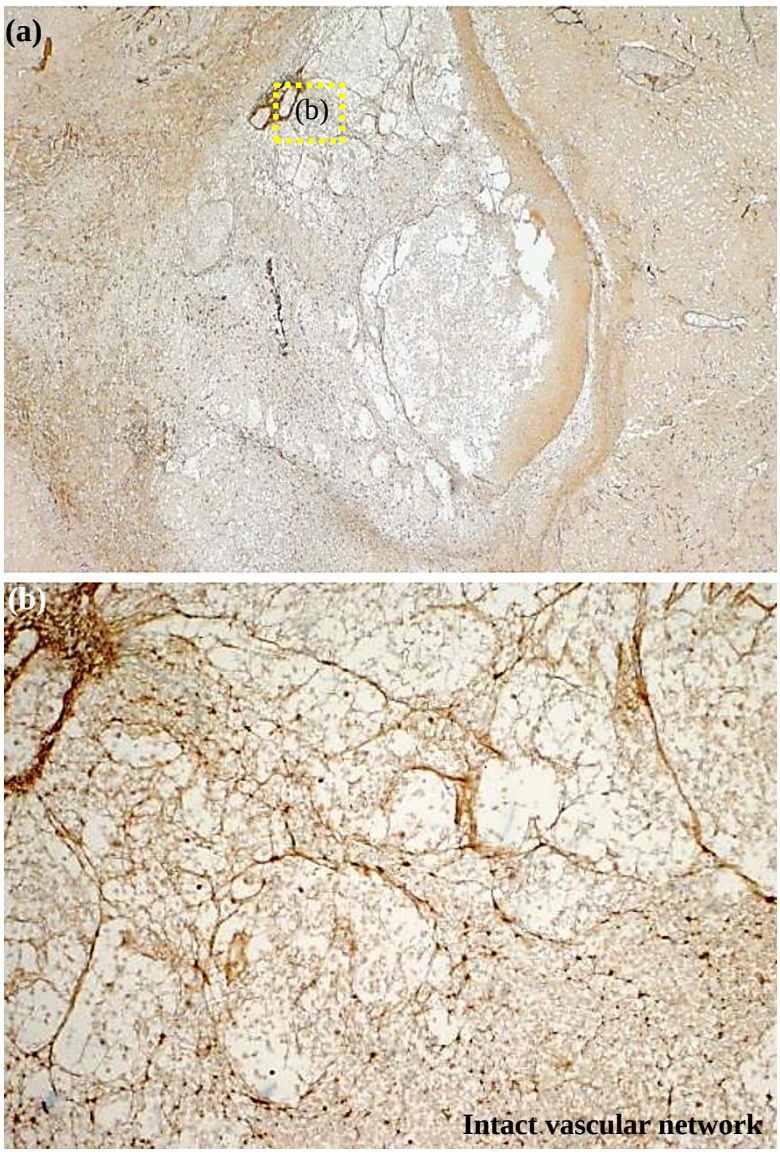

Figure 6.14. (a) CD-31 stained decellularised cavity is shown. (b) shows the highlighted area in (a) at higher magnification (100×). Extracellular matrix in the cavity remained intact and vascular network was stained (brown colour) by anti-CD-31 antibody.

6.3. Discussion

6.3.1. The formation of a cavity

Khokhlova *et al* (2014) have recently shown that by optimising the HIFU parameters, tissue fractionation and cavity formation is possible without any collateral thermal damage. The results presented in this Chapter concur with theirs and convincingly show that HIFU can be used to create a well-defined cavity inside the liver parenchyma with no evidence of coagulative necrosis at the periphery (see Figure 6.6 (a) and (b), Figure 6.9, Figure 6.10 and Figure 6.13). This is of paramount importance for cell therapy, as a raw margin with intact blood vessels may provide nutrients and oxygen supply to transplanted cells inside a cavity. Intra-hepatic cell delivery through a cavity will be performed in Chapter 7.

Mechanisms involved in the production of a tadpole shaped lesion during HIFU boiling histotripsy were investigated in Chapter 5. It was proposed that shear forces on tissue resulting from a rapid boiling bubble expansion (identified as stable cavitation) produce a "tail" shaped lesion, whereas emissions of micro jetting and shockwaves resulting from a cavitation cluster (identified as inertial cavitation) induce a "head" shaped lesion (see Figure 5.16 in Chapter 5). If this hypothesis is correct, one would expect there to be a difference in the nature of the damage in cellular structures between a "tail" and a "head". Based on histological examination of a freshly created cavity (see Figure 6.13 (c)-(g)), a number of broken hepatocytes plates and remnants of the interlobular septa (matrix) with some pits were observed around a "head" region. A similar form of cellular damage was observed in a number of cavitation cloud histotripsy studies (Parsons *et al* 2006, Lin 2014, Duryea *et al* 2015). Furthermore, the presence of pits is generally the result of inertial cavitation (Tezel and Mitragotri 2003). Contrary to the histologic observations of a "head" lesion, the margins of a "tail" shaped lesion were sharply demarcated between the treated and untreated regions with the absence of broken hepatic plates (see Figure 6.13(f) and (g)). This may provide the evidence of shear

stress-induced cell damage. These histological observations can support the proposed mechanisms for HIFU boiling histotripsy.

6.3.2. HIFU tissue decellularisation

Figure 6.14 shows a HIFU tissue sparing or partial decellularisation effect. A similar differential effect of HIFU was noticed in the kidney, causing fractionation of cortical cells but partially sparing the medulla and the collecting ducts (Lake *et al* 2008b, Vlaisavljevich *et al* 2014). Tissue decellularisation was also previously demonstrated in *ex vivo* porcine kidney and bovine liver using HIFU boiling histotripsy (Khokhlova *et al* 2015a). This tissue sparing effect is most probably due to the differences in the mechanical properties of different types of tissue, leading to a variation in the susceptibility to mechanically induced HIFU damage (Vlaisavljevich *et al* 2014). The fact that the blood vessels were intact inside the cavity (see Figure 6.14) suggests that this explanation is plausible.

An extracellular matrix (ECM) scaffold with intact blood vessels in a HIFU-induced decellularised lesion may enhance cell integration due to the fact that (a) three-dimensional support with an appropriate biological microenvironment promotes cell attachment and (b) cells cannot survive more than a distance of 200 μm away from a blood vessel (Wainwright 1995, Frerich *et al* 2001, Badylak 2004, Lovett *et al* 2009, Khokhlova *et al* 2015a). Further adjustment of the HIFU insonation protocol is expected to produce a complete decellularised lesion with intact ECM and vascular network. This would be a useful alternative to preparatory modalities, such as radiotherapy (Malhi *et al* 2002, Morán-Jiménez *et al* 2008), used to improve the cell integration in the recipient liver.

6.3.3. Monitoring HIFU boiling histotripsy and thermal ablation

As mentioned in Chapter 2, conventional ultrasound imaging systems can be used for precise targeting and monitoring of HIFU thermal ablation and boiling histotripsy in real time (Khokhlova *et al* 2006, Maxwell *et al* 2012, Khokhlova *et*

al 2015a). Over the course of both these type of HIFU exposures (i.e. thermal ablation and boiling histotripsy), a treatment site, however, appears as a hyperechoic region on a B-mode ultrasound image because HIFU-induced bubbles are highly reflective to ultrasound. The *ex vivo* experimental results shown in Figure 6.7 demonstrate that emitted acoustic signals during thermal ablation and boiling histotripsy exposures can be distinguished in the frequency domain. The acoustic emissions which occurred during the boiling histotripsy exposure consisted of higher order multiple harmonics with higher levels of broadband components in the spectrogram relative to those during thermal ablation insonation. These features were consistent with the numerical simulations shown in Figure 6.8(e) and (f). The significant differences in acoustic emissions are primarily due to the acoustic waveform and the peak pressure amplitudes at the HIFU focus. For example, the shockwave (P_+ = 82 MPa, P_- = –15.1 MPa at the HIFU focus) resulting from the boiling histotripsy excitation consists of higher order multiple harmonics in the frequency domain (see Figure 4.1 in Chapter 4). This yields a high degree of nonlinearity in the bubble oscillations and violent bubble collapses with larger amplitude short-duration pressure spikes (Pahk *et al* 2015). In contrast, the slightly distorted nonlinear wave excitation resulting from the thermal ablation exposure condition (P_+ = 13.4 MPa, P_- = –7.5 MPa at the HIFU focus) contains a lesser number of multiple harmonics with lower acoustic peak pressures (see Figure 4.1), resulting in a lower degree of nonlinearity in the radial bubble motions and less violent bubble collapses. These phenomena eventually lead to the significant differences in (a) the radiated pressures resulting from the bubble dynamics and (b) the scattered acoustic pressure fields by a bubble.

6.4. Summary

The objectives of this Chapter were to (a) investigate whether a mechanically fractionated lesion can potentially provide a site for cell injection and (b) distinguish acoustic emissions emitted during thermal ablation and boiling histotripsy processes. Both *ex*- and *in vivo* experiments were performed with morphological and histological analyses.

HIFU boiling histotripsy was successfully applied to create a mechanically fractionated lesion in *ex*- and *in vivo* livers. Upon morphological and histological observations, no sign of coagulative necrosis around the freshly created lesion was observed, and the boundary of the lesion was demarcated between the treated and untreated regions. These experimental results suggest that a cavity may act as a site for housing transplanted cells because intact blood vessels at the periphery may provide nutrients and oxygen supply to injected cells to survive. Intra-hepatic cell transplantation proposed in Chapter 1 will be performed in animal models in the following chapter.

In addition to the cavity formation, HIFU-induced tissue decellularisation was observed. This decellularised lesion consisted of an intact extracellular matrix and a vascular network with the absence of hepatocytes. Although the exact mechanism behind the HIFU decellularisation effect is unknown, it is most probably due to the high tensile strength of the endothelium and connective tissue, thus making it difficult for it to be mechanically fractionated.

Acoustic emissions were recorded during the thermal ablation and the boiling histotripsy insonations. Both the experimental and numerical results showed that higher order multiple harmonic components of the fundamental frequency with the elevation of broadband spectrum appeared during mechanical tissue fractionation process relative to those during thermal ablation process. These unique features can, therefore, be used to monitor HIFU treatments and predict the different types of cavitation activity for either a thermally or a mechanically induced lesion.

Chapter 7. Intra-hepatic hepatocyte transplantation mediated by HIFU boiling histotripsy

In Chapter 6, HIFU boiling histotripsy was successfully applied to produce a well-defined mechanically fractionated lesion inside the *in vivo* liver parenchyma with no discernible thermal damage such as coagulative necrosis at the periphery of the cavity. The main objective of this Chapter is to demonstrate the feasibility of the proposed HIFU mediated intra-hepatic hepatocyte transplantation in Nagase analbuminic rats, where the serum albumin level is initially nil. As described in Chapter 1, the proposed cell therapy involves creating a cavity inside the liver parenchyma by use of ultrasonic histotripsy and injecting healthy donor hepatocytes into the cavity which acts as a suitable hepatocyte receptor and which facilitates the successful uptake, proliferation and integration of transplanted hepatocyte cells.

7.1. Materials and methods

7.1.1. Animals

Male Sprague–Dawley rats (SDR), 6–8 week old and weighing 200–250 g, were obtained from the Charles-River Laboratories UK Ltd (Margate, Kent, UK). Nagase analbuminic rats (NAR) were bred at the Royal Free Hospital, London, UK. The animals were housed in a temperature controlled room (23 ± 2°C), with a relative humidity of 50 ± 10% and alternate light/dark conditions. They were given standard laboratory rodent chow. All animal experiments were conducted according to the Home Office guidelines under the UK Animals and Scientific Procedures Act 1986. All experiments were carried out under isoflurane general anesthesia.

7.1.2. HIFU experimental arrangement

The *in vivo* HIFU experimental set up used in the previous chapter was employed for the cell therapy experiments. A photograph of the experimental arrangement is shown in Figure 7.1. During the experiments, the customised holder coupled with

the 2.0 MHz HIFU source (Sonic Concepts H106, Bothell, WA, USA) was placed directly on the animal's explanted liver, and the HIFU focus was 5 mm below the surface of the liver. The thickness of the rat liver at the treatment site was 9 mm.

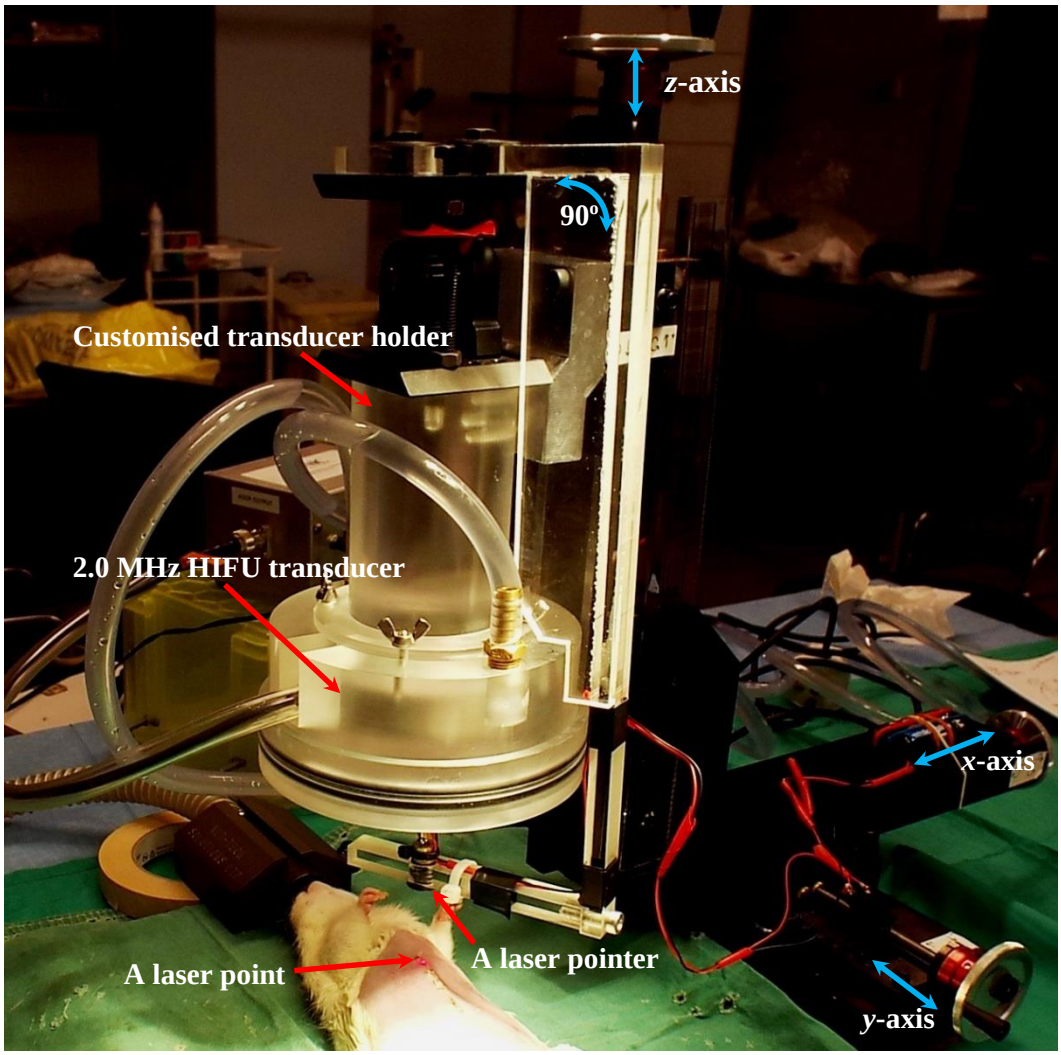

Figure 7.1. A photograph showing the *in vivo* experimental set-up used in this Chapter.

7.1.3. HIFU parameter optimisation and cavity creation

Because a replacement of 2%–5% of the liver mass (80–200 million cells/kg weight) with donor hepatocytes is necessary to restore liver function (Dhawan *et al* 2010, Gramignoli *et al* 2015), the delivery of 24–60 million cells was required for the cell

therapy experiments with Nagase analbuminic rats (weighing between 300–350 g). With an average hepatocyte concentration of 117 million cells/g in the liver (Sohlenius-Sternbeck 2006), the 2%–5% of the liver mass that needed to be removed by HIFU boiling histotripsy was calculated to be 0.2–0.5 g (194–484 μL). These values were obtained as follows:

- $2\%: \frac{1\,\text{g}}{117\times10^{6}\ \text{cells}} \times \left(\frac{80\times10^{3}\ \text{cells}}{1\,\text{g}} \times 300\,\text{g} \right) = 0.21\,\text{g} \text{ or } \frac{0.21\,\text{g}}{\frac{1.06\times10^{-3}\,\text{g}}{1\,\mu\text{L}}} = 194\,\mu\text{L}$
- $5\%: \frac{1\,\text{g}}{117\times10^{6}\ \text{cells}} \times \left(\frac{200\times10^{3}\ \text{cells}}{1\,\text{g}} \times 300\,\text{g} \right) = 0.51\,\text{g} \text{ or } 484\,\mu\text{L}$

Therefore, a minimum cavity volume of 194 μL was required. Khokhlova *et al* (2014) recently found that boiling histotripsy exposure settings used in unperfused *ex vivo* tissue can be employed as a valid substitute for *in vivo* experiments. They found that the lesions generated *in vivo* were similar to those produced in *ex vivo* tissue in size and shape. Thereupon, the HIFU parameter optimisation for *in vivo* experiments was carried out on an unperfused *ex vivo* chicken liver. It was assumed that acoustic and thermal properties of chicken liver were similar to those of rat liver. It was reported that the speed of sound in chicken liver was close to that in rat liver (e.g. $c_{0,\text{chicken}}$ = 1603 m/s and $c_{0,\text{rat}}$ = 1596 m/s at 36ºC) (Kumagai *et al* 2014, Martínez-Valdez *et al* 2015). An *ex vivo* chicken liver was placed directly under the HIFU transducer and the HIFU exposure conditions were varied to create cavities with different volumes. The HIFU exposure conditions are shown in Table 7.1. These settings were verified for the generation of a cavity with the *in vivo* experiments performed in Chapter 6.

Electrical power (W)	**Peak pressures at focus *in situ* (MPa)**	**Time to boil (ms)**	**Duty cycle (%)**	**Pulse length (ms)**	**Pulse repetition frequency (Hz)**	**Number of pulses**
150	P_+ = 66, P_- = –14.1	6.0	1	10	1	5,10,50
200	P_+ = 80, P_- = –15.6	2.7	1	10	1	5,10,50

Table 7.1. HIFU exposure settings used in the *ex vivo* experiments.

Immediately after the HIFU insonations, the *ex vivo* liver was cross-sectioned and the cavity measurements were taken using a digital caliper. The volume of the cavity was estimated by calculating the sum of volumes of a hemisphere and a cone, as this produces a good approximation of the "tadpole" shape of the cavity. The cavity was assumed to be axially symmetric. The cavities are shown in Figure 7.2.

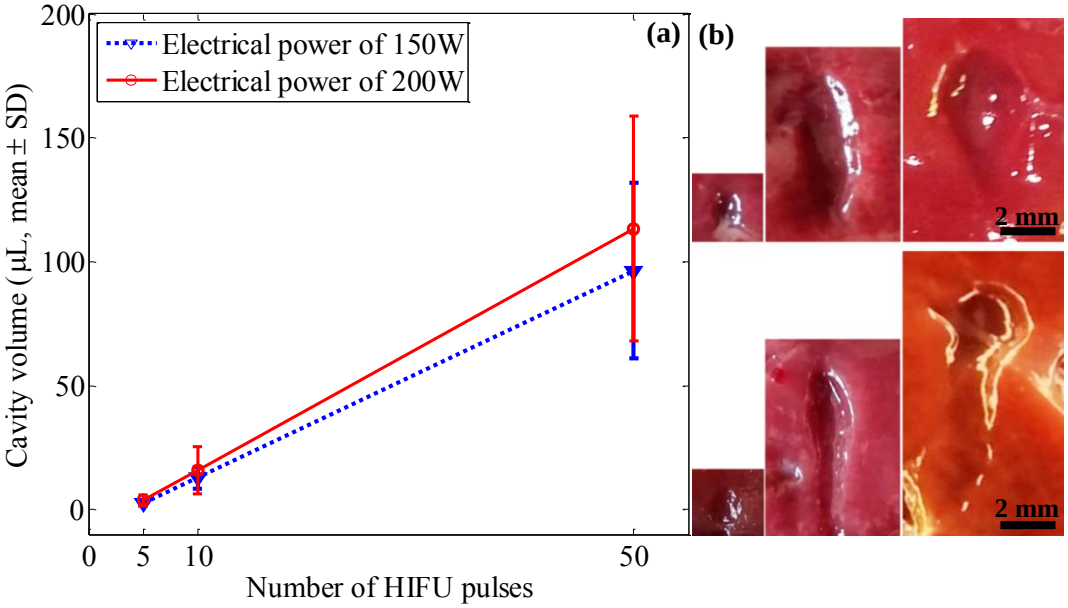

Figure 7.2. A graphical representation of the relationship between the *ex vivo* cavity volume and number of HIFU pulses is shown. The volumes are presented as the means ± standard deviations (SD) with n_s = 5. (b) Upper row: cavities produced by 150 W HIFU electrical power and 5, 10 and 50 pulses, respectively (left to right), lower row: cavities generated with 200 W and 5, 10 and 50 pulses, respectively (left to right). Each pulse contains a continuous 10 ms HIFU insonation.

7.1.4. Hepatocyte isolation and labelling with DiR xenolyte dye

Freshly isolated hepatocytes were used for injection in the recipient rats. For isolation of hepatocytes, a protocol provided by the Life Technologies (Paisley, UK) was used. Briefly, the liver was isolated *in situ* and flushed with phosphate buffered saline (PBS) followed by Liver Perfusion Medium (Life Technologies) through an 18G cannula (1.25 mm in diameter) placed inside the portal vein. The inferior vena cava was cut open to drain the effluent. This was followed by collagenase dispase enzymatic digestion (Liver Digest medium, Life Technologies) at 37°C for 10

minutes. Dispersed hepatocytes were filtered through a sterile nylon mesh and rinsed three times with Hepatocyte Wash Medium (Life Technologies). Hepatocytes were purified by Percoll density gradient separation and re-suspended in Williams' Medium E (Life Technologies). After viability check with a Trypan blue exclusion test under a microscope (dead cells are stained with a blue colour), cells were counted using a haemocytometer and incubated with Xenolyte DiR Fluorescent dye (320 µg/mL) (Perkin Elmer, Richmond, CA, USA) for 10 minutes at 37°C. This allowed for injected hepatocytes in a cavity to be monitored by using a noninvasive *in vivo* imaging system IVIS (Lumina, Perkin Elmer, Santa Clara, CA, USA). After three washes in ice cold PBS, cells were re-suspended in Matrigel (1:1 ratio) and kept on ice until injected into the cavity. Matrigel is a gelatinous protein mixture which is considered to be a reconstituted basement membrane extracellular matrix (ECM). In the cell therapy experiments, Matrigel was used to (a) provide a fibrous matrix for injected cells to survive and grow in a cavity and (b) stop an internal bleeding in a cavity as Matrigel (liquid at 4^{o}C) becomes a polymerised gel (solidified) at 37^{o}C (Arnaoutova *et al* 2009).

7.1.5. HIFU animal experiments

Eleven rats (seven Sprague–Dawley rats and four Nagase rats) were used for the cell therapy experiments (see Table 7.2 for more details). The Nagase rat is a mutant strain of the Sprague–Dawley rat, deficient in albumin production (Nagase *et al* 1979), which has widely been used for monitoring the biosynthetic and functional studies of transplanted hepatocytes in recipient animals (Oren *et al* 1999, David *et al* 2001, Ito *et al* 2007, Dhawan *et al* 2010, Liu *et al* 2012, Nishikawa *et al* 2015). In general, this Nagase animal model represents the metabolic liver diseases in patients with analbuminemia, Tyrosinemia Type I, Wilson's disease and Crigler-Najjar syndrome where the liver is incapable of producing the proteins or enzymes needed for replacement therapies such as hepatocyte or liver transplantation (Horslen and Fox 2004, Gómez *et al* 2007, Zhang *et al* 2007, Jorns *et al* 2012).

Animals	Numbers	Description
Sprague–Dawley rat (SDR)	7	Used SDR for isolating hepatocytes
Nagase analbuminemic rat (NAR)	4	Used NAR for cell transplantation to restore the liver function.

Table 7.2. Animals used in the cell therapy experiment. Eleven rats (7 Sprague–Dawley and 4 Nagase rats) were used in this Chapter.

Isoflurane-induced general anesthesia was used during the operative procedure. During the experiments, the livers were exteriorised to simplify the guidance of the needle into the cavity for injecting the cells. Without exteriorisation, ultrasound or magnetic resonance guidance would be needed to target the liver and guide the needle tip for cell injection. Such guidance methods are available (Chin *et al* 2008, Khokhlova *et al* 2015a), but the simpler exteriorisation approach was adopted and it is believed that this would not compromise the proposed cell therapy concept. A midline incision was introduced and the median and the left lateral liver lobes were taken outside of the abdominal cavity. The HIFU source was coupled to the exteriorised liver targeting the median lobe immediately right of the falciform ligament. A cavity was created in each of the three lobes including the right median, the left median and the left lateral lobes. A laser pointer was used to localise the centre of the cavity laterally. Immediately after creation of a cavity, 100 µL of freshly isolated normal hepatocytes (2×10^7 cells/100 µL) mixed in Matrigel was injected into the cavity by using a 29G needle (0.33 mm in diameter) (see Figure 7.3). Light pressure was applied on the injection site with a soft cotton bud until the Matrigel inside the cavity solidified to prevent leakage of cells from the injection site. During the procedure, normal saline (0.9% weight per volume of NaCl solution) was sprayed on the liver surface to keep it moist.

After visual confirmation of no bleeding at the injection site, the liver lobes were returned inside the abdominal cavity and the abdomen was closed in two layers. Localisation of the cells inside the cavity was confirmed with *in vivo* imaging system (IVIS) (Lumina, Perkin Elmer) images, and the animals were returned to the recovery room. The DiR dye-labelled cells inside the cavity were tracked

longitudinally with the IVIS, and the animals were sacrificed at 96 hours and 1 week after cell injection. Upon sacrifice, blood samples were collected for serological tests and the liver was dissected for the cells inside the cavity, to be checked with the IVIS. Sliced liver tissue was also collected for histopathological examination.

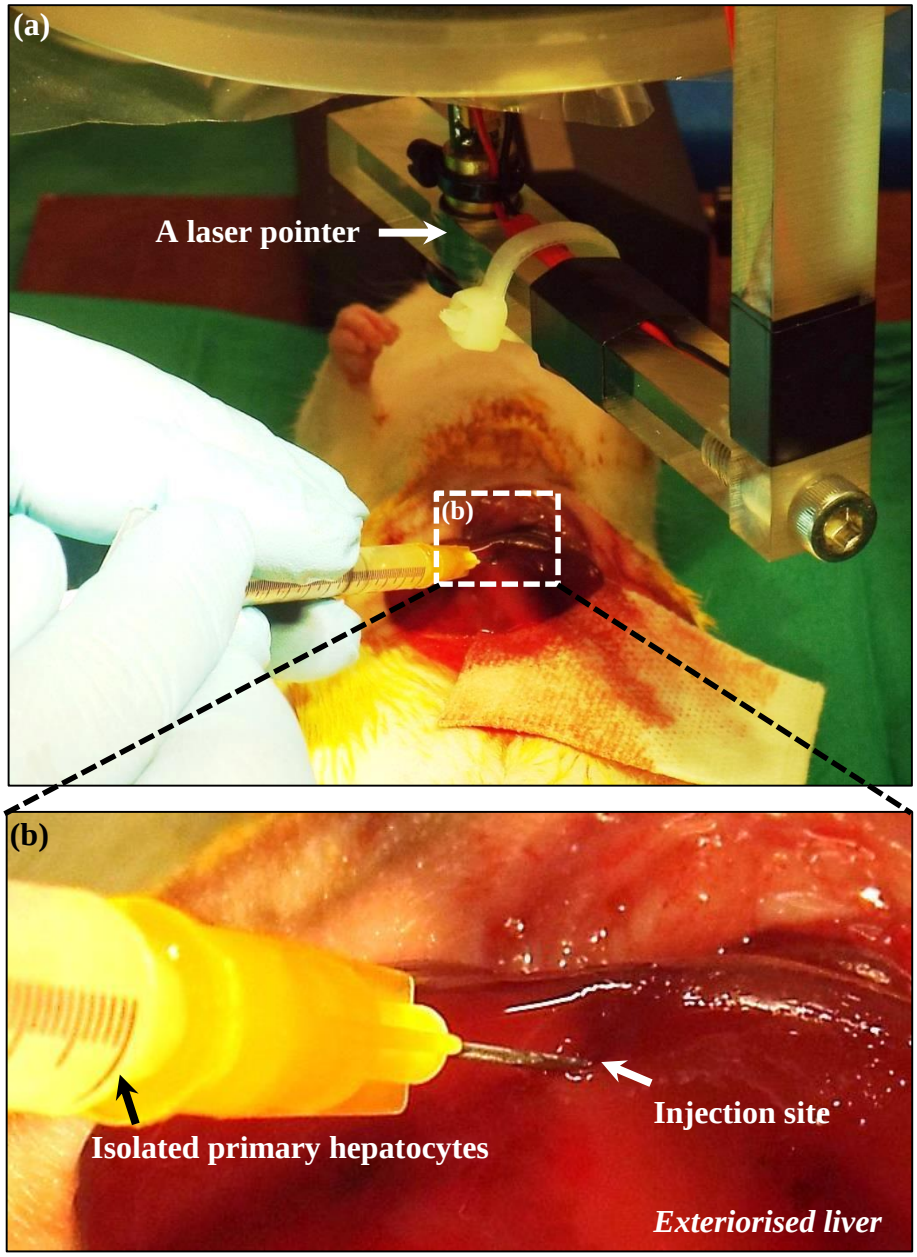

Figure 7.3. (a) Direct injection of primary hepatocytes into a cavity using a 29G needle (0.33 mm in diameter) guided by a laser pointer. (b) A magnified view of the highlighted area in (a).

7.1.6. Routine histopathology and immunohistochemistry

Paraffin-embedded tissue sections were used for hematoxylin and eosin (H&E), Ki-67 (a cellular marker for proliferation) and CD31 (a marker for vascular endothelial cells) staining. Immunostaining was performed by using a commercially available kit (ImmPRESS Universal Reagent, Vector Laboratories, Orton Southgate, Peterborough, UK). Briefly, the slides were dewaxed in xylene, rehydrated in graded alcohol and rinsed in PBS for 5 min. Antigen retrieval was done by immersing the slides in citrate buffer solution (pH 6.0) and autoclaved for 15 min. Endogenous peroxidase activity was quenched by incubating the slides with 3% hydrogen peroxide for 20 min. After incubation with the blocking serum, the sections were incubated with anti-Ki-67 and anti-CD31 primary antibodies (Rabbit polyclonal to Ki-67, Abcam, UK and Rabbit monoclonal to anti-CD31, Millipore Corporation, Watford, Hertfordshire, UK) and overnight at 4°C. Goat anti-Rabbit secondary antibody conjugated with IgG-HRP (immunoglobulin G and horseradish peroxidase) was applied for 30 min. Colour development was done with the peroxidase substrate DAB (3,3'-Diaminobenzidine tetrahydrochloride hydrate). Between steps, slides were rinsed with PBS.

7.1.7. Serum albumin and alanine transaminase (ALT) level measurement

To investigate the production of albumin by the injected hepatocytes and the hepatic enzyme ALT, blood samples were collected from the abdominal aorta (the largest artery in the abdomen which provides blood to the organs) from the Nagase analbuminemic rat before euthanasia. The blood samples were immediately placed into a centrifuge system (PRIMO R7590, Heraeus, Hanau, Germany) to collect plasma as it serves as the protein reserve, and stored at –80^{o}C. A clinical grade automated biochemical analyser was used for the measurements.

7.2. Results

This Chapter reports successful delivery of a large number of cells into the liver parenchyma by using HIFU tissue fractionation or boiling histotripsy. Initially, an *ex vivo* model was used for extensive optimisation of the HIFU protocol to create cavities of different sizes (see Figure 7.2). With an electrical power of 200 W (P_+ = 80 MPa, P_- = –15.6 MPa at the HIFU focus) and 50 HIFU pulses the largest cavities were produced with a volume of 113 ± 45 μL (mean ± SD with n_s = 5). The local thickness of the liver (9 mm) limited this maximum volume so that the axial extent of the cavity did not rupture the liver surface.

For the injection of hepatocytes into a recipient cavity, a minimum volume of 194 μL of the liver (2% of liver mass) has to be removed (see section 7.1.3). With the optimum HIFU setting the single cavity created had a volume of 113 μL, so three cavities were produced in three separate lobes of the recipient liver which corresponded to 3.5% of the liver mass removed. After injection of donor hepatocytes into the HIFU-created cavity, the injected cells inside the cavity were identified by IVIS imaging (see Figure 7.4). The injected cells were highlighted inside the liver parenchyma by IVIS imaging of the explanted liver as well (see Figure 7.4(a)). Dispersal of the cells to different organs was not observed (see Figure 7.5).

On microscopic examination, the cavity margin looked healed with thin compressed hepatic plates at the periphery of the cavity on day 4 (see Figure 7.6). Blood vessels and bile ducts were well preserved at the periphery of the cavity, indicating that HIFU might have differential tissue fractionating effects on different types of tissues. Liver in different stages of disease might have a range of mechanical properties. For eventual clinical application, the HIFU exposure conditions will need to be adjusted according to changes in the mechanical property of diseased liver (e.g. more stiff in cirrhotic liver and less stiff in fatty liver). Vlaisavljevich *et al* (2014) recently found a decrease in susceptibility to histotripsy damage for soft tissues of increased mechanical strength.

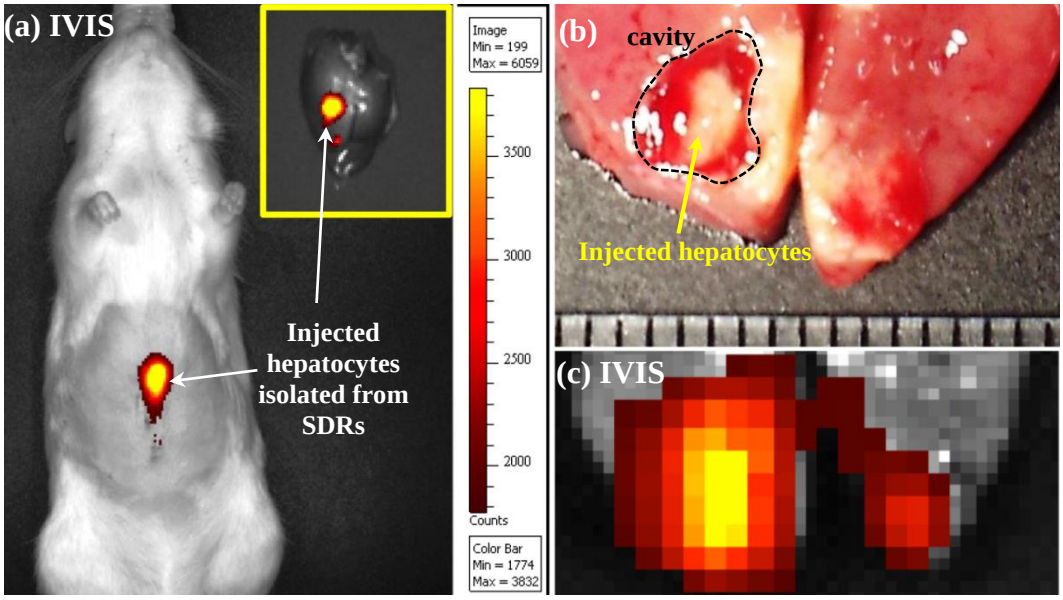

Figure 7.4. (a) IVIS image of the cavity in a Nagase rat at day 7 after injection of cells is shown. Cells were stained with DiR xenolyte (inset: IVIS image of the explanted liver showing elliptical cavity). (b) Corresponding cross-section of the cavity. (c) IVIS image of (b).

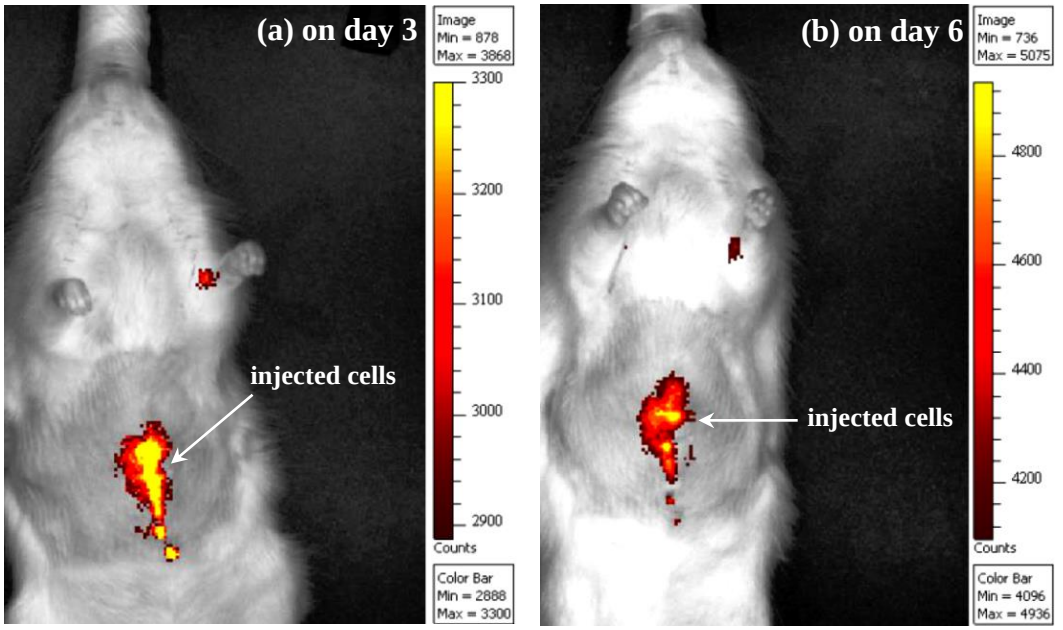

Figure 7.5. IVIS images of the injected cells in the recipient liver (a) at day 3 and (b) day 6. No dispersal of the transplanted cells to different organs is seen.

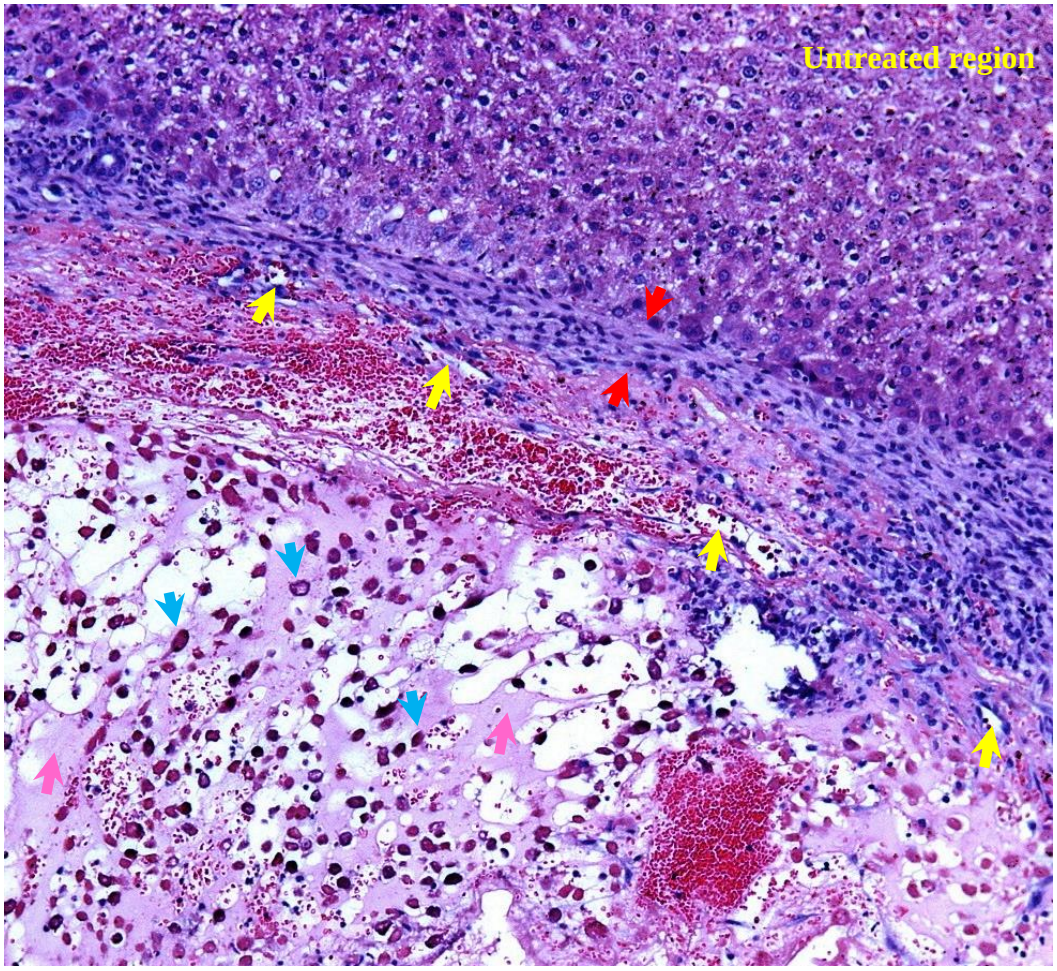

Figure 7.6. Healed margin with injected hepatocytes inside the cavity (stained with H&E). Red arrows show compressed hepatic plates at the boundary of the cavity and yellow arrows indicate intact blood vessels and bile ducts at the margin (100×). Blue and pink arrows represent transplanted hepatocytes and Matrigel scaffold inside the cavity, respectively.

Despite the fact that well-defined cavities were induced in the *in vivo* liver parenchyma with no evidence of coagulative necrosis, the cavity-alone may not be suitable for transplanted cells to survive, because there is no extracellular matrix inside the cavity. In the cell therapy experiments, Matrigel was, therefore, used to provide support for the cell growth. As shown in Figure 7.7, cells formed colonies of injected hepatocytes with many in the proliferative phase as detected by the Ki-67 staining. An intricate network of endothelial cells growing in the vicinity of hepatocyte clusters (i.e. angiogenesis) was also noticed in the cavity, some of them looking like nascent blood vessels (see Figure 7.8). Interestingly, host hepatocytes

in the untreated region did not proliferate (see the region within the dashed yellow line in Figure 7.7(c)).

As a proof of concept to restore the liver function, analbuminic rats (Nagase) were used for cell transplantation. On day 7, the plasma albumin level restored to 50% (mean 15 g/L) of the normal level (30 g/L, Oren *et al* 1999). Hepatic enzyme level was normal in all rats (mean ALT 55 IU/L).

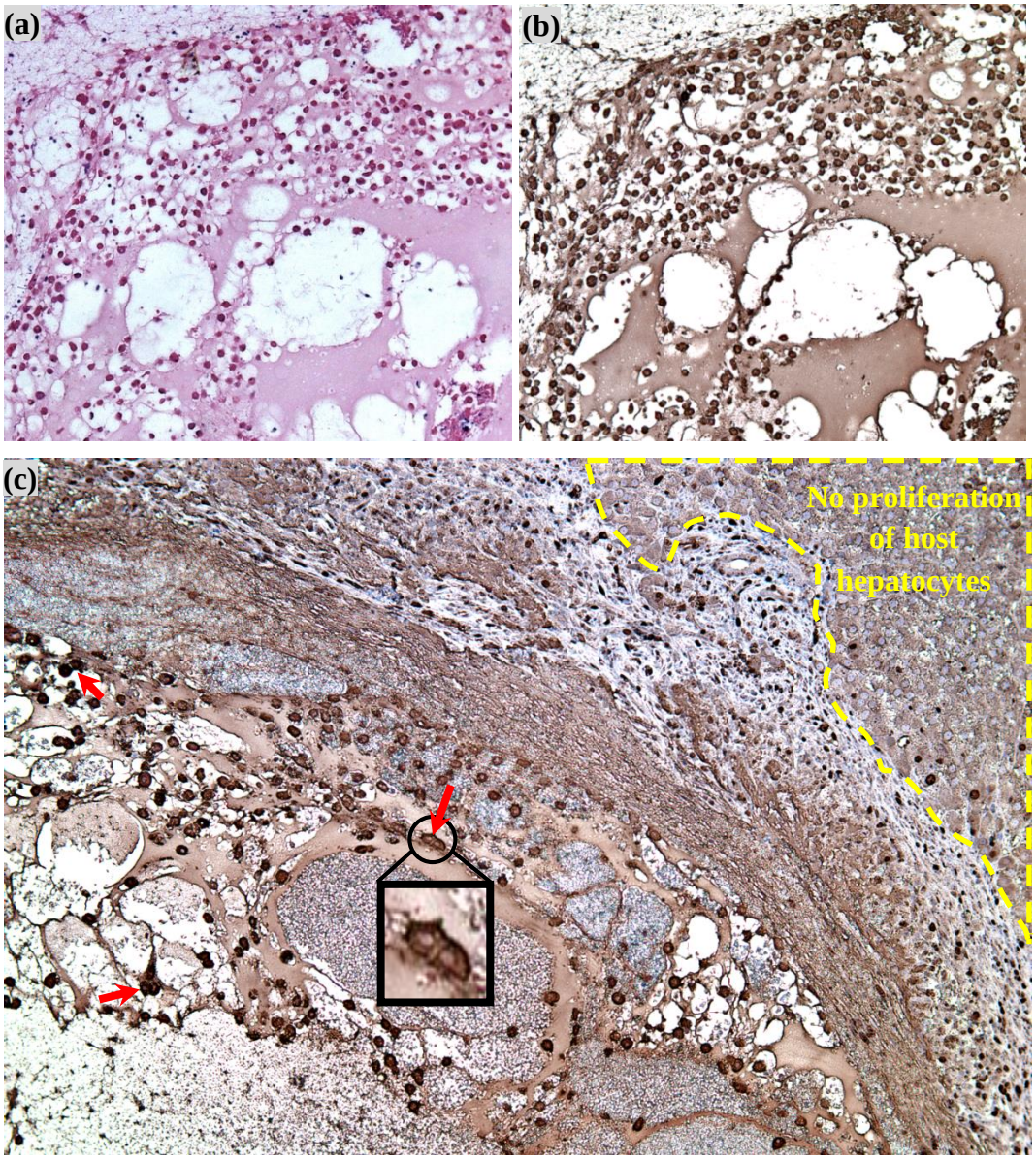

Figure 7.7. (a) Colonies of DiR and H&E stained hepatocytes inside the cavity at day 7. (b) Proliferating cells stained by Ki-67. (c) The margin of the cavity stained by Ki-67 is shown. Red arrows show strongly positive bi-nucleated cells inside the

cavity. The area within the dashed yellow line indicates the untreated liver parenchyma. Magnification 100×.

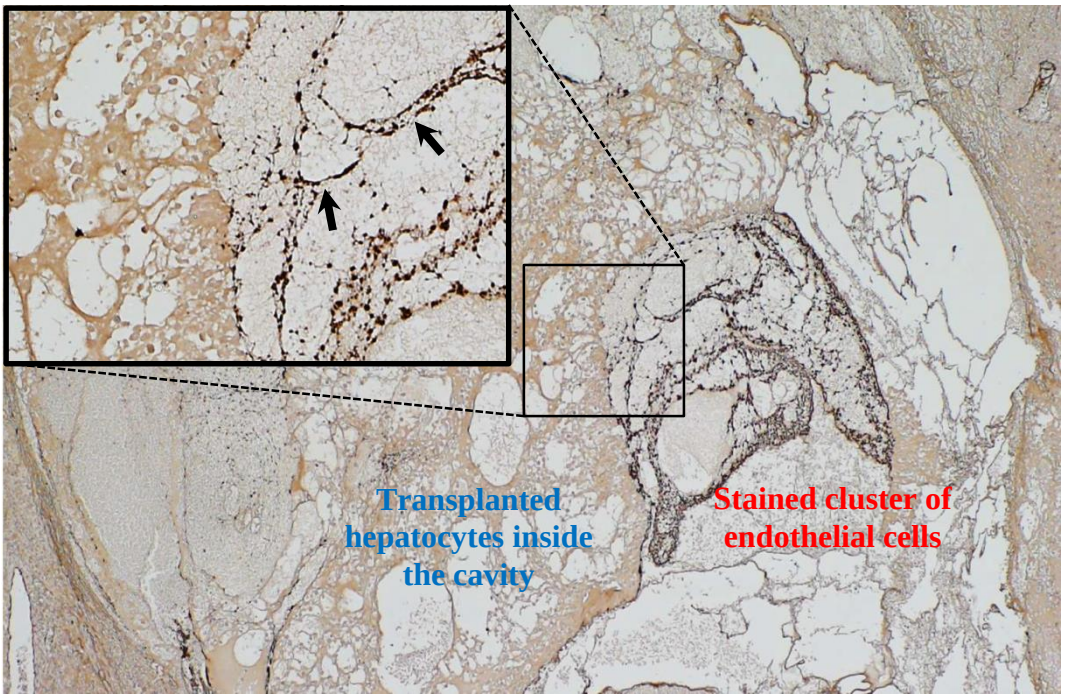

Figure 7.8. Growing nascent vascular network in the vicinity of proliferating hepatocytes inside the cavity is shown. The proliferating vascular endothelial cells (i.e. angiogenesis) stained by CD-31 antibody formed lumen like structure (indicated by a black arrow). Magnification 25×.

7.3. Discussion

With the advent of better choices of stem/progenitor cells, there is renewed interest in cell therapy for clinical applications. Despite a significant advance in cell choices, limited progress has been made to increase the efficiency of cell delivery and engraftment in solid organ. In this Chapter, at least 60 million hepatocytes were delivered into the liver parenchyma without using currently available preparatory damage to the recipient liver such as liver irradiation, partial hepatectomy, reperfusion injury or noxious chemical agents. As mentioned in Chapter 2, these iatrogenic methods have been used to induce extensive proliferation of transplanted cells. However, radiation-induced liver disease, host hepatocyte proliferation, the risk of portal thrombosis and the development of hepatocellular carcinoma are all possible side effects (Malhi *et al* 2002, Dhawan *et al* 2010, Fujii *et al* 2010, Jorns *et al* 2012, Schlachterman *et al* 2015). With HIFU boiling histotripsy, a small region of interest within the recipient liver can be precisely fractionated, whereas other methods of incurring liver damage target a specific liver lobe or the whole liver and induce more generalised damage. Since the cell destruction only appears at the HIFU focus, this ultimately triggers regenerative response at the treatment site in the recipient liver. This leads to the enhanced engraftment and proliferation of donor cells whilst inhibiting the ability of host hepatocytes to proliferate (see Figure 7.7(c)).

The number of delivered cells in the recipient liver could be further increased by creating additional cavities or by increasing the size of an individual cavity via the manipulation of HIFU pulses. Further work is necessary to investigate the variation of the size of a cavity in tissues with different mechanical properties and the relationship between the effectiveness of cell growth and the size of a cavity.

To the best of the author's knowledge, this is the first study reporting cell transplantation mediated by HIFU histotripsy. When cells are directly injected into the portal vein or hepatic artery, only 5%–20% of cells are integrated in the recipient liver. The chances of engraftment are increased when preparatory damage is caused

to the recipient liver before or after cell injection (Malhi *et al* 2002, Stéphenne *et al* 2006, Morán-Jiménez *et al* 2008, Turner *et al* 2011). In a recent study, Turner *et al* (2013) injected the cells directly into the liver parenchyma and were able to increase the cell engraftment by almost a factor of five by embedding the cells in hyaluronic acid hydrogel cross-linked with PEGDA (polyethylene glycol diacrylate) compared with injection of simple cell suspensions. However, to increase the cell engraftment, CCl_4 (Carbon tetrachloride, a noxious chemical agent) induced liver damage was still necessary and there was a risk of spillage of hyaluronan free cells into the abdominal cavity.

The *in vivo* experimental results together with histologic observations presented in this Chapter showed that direct injection of cells inside the cavity facilitated successful uptake, proliferation and integration of the transplanted hepatocytes in the recipient liver. Although Matrigel was used to provide temporary support for the transplanted cells, this could be further improved by implanting decellularised liver scaffold inside the cavity followed by cell transplantation or alternatively cells could be injected into the HIFU-induced decellularised liver bed (see Figure 6.14 in Chapter 6). The use of this novel technique was able to partially reverse liver functional albumin deficiency (mean 15 g/L). This relatively low albumin level could be attributable to an inadequate number of good quality cells or inadequate access of secreted albumin to the systemic circulation. Further study is necessary to include longer follow-up and better cell selection (endodermal or mesenchymal stem cells).

Although experiments on a control group with intra-portal cell transplantation were not performed in this thesis, the detected albumin level of 15 g/L by cell therapy after HIFU boiling histotripsy is almost eight times greater than that after intra-portal hepatocyte transplantation reported by Oren *et al* (1999). In their study, isolated primary donor hepatocytes were transplanted into Nagase analbuminemic rats intraportally, and serum albumin level of 2 g/L was first detected between the second and third weeks after the transplantation. The albumin level detected in this

study was, therefore, considered sufficient evidence for successful repair of liver function.

The advantages of the proposed novel approach include the following. First of all, HIFU could be used non-invasively to create a receptacle cavity of appropriate size in the targeted liver. A completely acellular or partially decellularised cavity could be created by adjusting the HIFU protocol, as major hepatic blood vessels and bile ducts have higher mechanical strength and are more resistant to histotripsy than hepatic parenchyma (Vlaisavljevich *et al* 2014). This decellularised lesion with intact extracellular matrix and vascular network would promote cell attachment and supply sufficient oxygen and nutrients to the transplanted cells to survive. Moreover, liver organoids created *ex vivo* from allogenic or xenogenic scaffolds and appropriate cells could be grafted inside the cavity for integration into the recipient liver. The second advantage associated with creation of the cavity would be the regenerative stimulus due to the partial loss of hepatocytes by HIFU inside the cavity, which will increase the survival of the transplanted cells and formation of nascent blood vessels in the vicinity of the growing cells. The third advantage lies with the secure placement of the cells inside the cavity without any spillage into the peritoneal cavity. Though further study is required before this technique can be used clinically, these early findings represent the first demonstration of a treatment that shows great promise for improving the outcomes of liver disease patients worldwide.

7.4. Summary

The aim of this Chapter was to demonstrate the feasibility of a proposed novel intra-hepatic hepatocyte transplantation mediated by HIFU. Nagase analbuminemic rats (serum albumin level was initially nil) were used in the cell therapy experiments. Initially, a number of cavities were produced to create damage to the recipient liver through HIFU boiling histotripsy. Healthy donor hepatocytes isolated from Sprague–Dawley rats (normal rats) were then injected directly into the cavities. The transplanted cells in the recipient animals were monitored by IVIS imagining. Animals were euthanised at 96 hours and one week after the cell injection. Upon sacrifice, the viability and functionality of the injected hepatocytes were investigated with histological and serological examinations.

The experimental results presented in this Chapter showed the high potential of the proposed hepatocyte transplantation for improving the outcome of cell therapy. It was observed that the transplanted cells were highlighted inside the recipient liver by IVIS imaging, and no dispersal of the transplanted cells to different organs occurred. Upon microscopic examination, blood vessels and bile ducts were preserved at the cavity margin and cells formed colonies of hepatocytes with many in the proliferative phase in the cavity. The growth of endothelial cells was also observed in the vicinity of transplanted hepatocytes. In addition to this, the diseased host hepatocytes in the untreated region did not proliferate. On serological observation, the proposed cell therapy had led to a partial reversal of a liver functional deficiency. A week after the transplantation, the plasma albumin level in Nagase rats was restored to 50% of the normal level.

Chapter 8. Conclusions

The main objectives of the work described in this thesis were (1) to investigate the mechanisms involved in the formation of a mechanically fractionated lesion produced by HIFU boiling histotripsy and (2) to demonstrate the feasibility of the proposed intra-hepatic hepatocyte transplantation in animal models. In this Chapter, the original contributions made in the thesis will be presented and summarised. Areas for future work will also be addressed and discussed in order to extend the existing work.

8.1. Contributions

The achievements of this thesis will be compared with the objectives outlined in Chapter 1 to assess the degree to which novel contributions have been made.

The review of previous work on hepatocyte transplantation and HIFU histotripsy was made in Chapter 2. It was established that:

- There was a requirement to develop an alternative to conventional intra-portal cell therapy in order to effectively deliver a large number of cells as well as to enhance the level of engraftment of transplanted hepatocytes;

- An improved understanding of the mechanisms behind the formation of a "tadpole" shaped lesion resulting from HIFU boiling histotripsy was needed.

This thesis proposed a novel approach for intra-hepatic cell delivery by using HIFU histotripsy to improve the low level of integration of transplanted cells currently associated with intra-portal cell injections. This new strategy was to induce damage to the recipient liver by producing a number of cavities inside the liver through use of HIFU and then injecting donor hepatocytes into the cavities, thus preconditioning the liver for repopulation.

Mechanisms involved in HIFU boiling histotripsy were investigated in Chapters 3 to 5 both numerically and experimentally, and the feasibility of the proposed cell therapy was demonstrated in Chapters 6 and 7.

In Chapter 3, numerical approaches to modelling the response of a single spherical gas-vapour bubble exposed to HIFU fields were described. The effects of the compressibility of the surrounding medium and heat and mass transfer on the bubble dynamics were included in the model. Additionally, the piecewise constant approximation method was introduced and adopted into the bubble model to describe bubble radial motions as a function of temperature variation from 20^{o}C to 100^{o}C. It was assumed that the temperature-dependent liver properties followed similar trends to those of water. The numerical bubble model was then compared and validated against other published results for the cases of a single bubble sonoluminescence and a lithotripsy bubble in water.

Chapter 4 described a Matlab implementation of the bubble model developed in Chapter 3 to study the dynamic behaviour of a bubble in the liver excited by HIFU boiling histotripsy waveform. The numerical results showed that the combination of the asymmetry in shockwaves and of water vapour transport caused rectified bubble growth at a boiling temperature of 100^{o}C. The growth rate of this exploding bubble, however, gradually decreased with the reduction of the surrounding temperature from 100^{o}C to 70^{o}C. It was suggested that the extent of rectified bubble growth is spatially confined to a localised super-heated region by shocks at the HIFU focus due to the significant differences in tissue temperatures inside and outside of the HIFU focal volume. In addition to this, it was also shown that a significant appearance of higher order multiple harmonic components of the fundamental frequency in the frequency domain for acoustic emitted signals indicated the formation of a boiling bubble during the course of HIFU exposure. Moreover, additional numerical simulations were performed to distinguish and compare the different types of acoustic cavitation activity which occurred as a result of thermally induced HIFU ablation and mechanically induced lesions caused by boiling histotripsy. It was clearly observed that higher order multiple harmonic

components with larger amplitudes, as well as higher levels of broadband emissions, appeared under the boiling histotripsy exposure case. The numerical observations mentioned above agreed well with the experimental results obtained as described in Chapters 5 and 6.

For Chapter 5, a high-speed camera was used to investigate the bubble dynamics produced at the HIFU focus, particularly the interaction of a boiling bubble with incoming shockwaves, in a tissue mimicking gel phantom during HIFU boiling histotripsy. The principle mechanisms responsible for lesion formation were found to lie in the combination of the boiling bubble together with a bubble cloud. It was observed that additional boiling bubbles were induced in a localised super-heated region by shockwaves followed by the generation of a cavitation cluster towards the HIFU source. This process was repeated and eventually resulted in a "tadpole" shaped mechanically fractionated lesion. Moreover, a simplified numerical model describing the scattering of the incident harmonic acoustic wave by a vapour bubble was used to interpret these experimental results. The experimental and numerical observations suggested that the overall size of a lesion created by boiling histotripsy is primarily dependent upon the extents of the super-heated region at the HIFU focus and the ultrasound wave backscattered by the original vapour bubble.

In Chapter 6, HIFU boiling histotripsy was successfully applied to create a mechanically fractionated lesion in both *ex*- and *in vivo* livers with no evidence of thermal damage at the boundary of the lesion. In addition to the cavity creation, a partially decellularised lesion with intact extracellular matrix and vascular network was observed. This indicated differential mechanical tissue fractionating effects on different types of tissues and suggests that HIFU boiling histotripsy has the potential to be used as a tissue or cell selective fractionation method.

Chapter 7 demonstrated the feasibility of the proposed intra-hepatic cell transplantation in Nagase analbuminemic rats. A large number of primary hepatocytes was successfully delivered into the cavities produced by HIFU boiling histotripsy. To the best of the author's knowledge, this was the first study reporting

cell transplantation mediated by HIFU histotripsy. The experimental results showed that the proposed cell therapy approach facilitated successful uptake, proliferation and integration of the transplanted hepatocytes in the recipient animal with the prevention of proliferation of the diseased host hepatocytes. These results demonstrated the high potential of HIFU histotripsy for improving the outcome of cell therapy in treating metabolic liver diseases.

8.2. Further work

It has been shown in the previous section that the objectives outlined in Chapter 1 have been achieved and that a number of original contributions have been made as a result of this work. However, as indicated throughout the thesis, there are a number of areas requiring further investigation.

8.2.1. Acoustic field characterisation of a shockwave

Perhaps the greatest area of uncertainty in this thesis is the lack of experimental measurement of the acoustic waveform and the pressure amplitudes of a shockwave at the HIFU focus. Although there was excellent agreement between the acoustic field measurement and the calculation under linear propagation conditions in water in Chapter 5, the validation of acoustic field simulations in the case of the presence of a shockwave at the HIFU focus is still required. Experimental measurement of the shockwave pressure waveform could be used (a) to validate simulated pressure fields, (b) as input acoustic pressure p_a into the Gilmore bubble equation (3.30) for more accurate bubble excitation modelling, and (c) to calculate the time t_b to reach a boiling temperature of 100^{o}C using weak shock theory (equation 3.77).

8.2.2. Numerical bubble model

Soft tissues can be described as a viscoelastic material (Yang and Church 2005). The numerical bubble model described in Chapter 3 could be further improved by adding a viscoelastic term to account for the strain-stress relation in soft tissue.

Yang and Church (2005) have rederived the Keller-Miksis bubble model, a modified version of the Herring-Trilling equation (3.2), and combined it with the linear Kelvin-Voigt viscoelastic model to investigate the behaviour of a single bubble driven by ultrasonic fields in soft tissue. The validity of this Keller-Miksis model is, however, limited to $\dot{R}/c_L \leq 1$. To the best of the author's knowledge, there is no published numerical work on the modified Gilmore bubble equation (3.30, valid up to $\dot{R}/c_L = 2.2$) which combines with a viscoelastic model. Instead, Ding and Gracewski (1994) introduced a viscoelastic membrane at the bubble-liquid interface in the Gilmore equation (3.30) to consider the effects of the nonlinear elasticity and strain rate dependent viscosity on the bubble response. The authors simply added an additional pressure contribution from the membrane and modified the viscosity term in equation (3.34a). This numerical approach could be adopted to improve the numerical bubble model formulated in Chapter 3 for exploring the bubble dynamics in soft tissues exposed to the fields of HIFU boiling histotripsy. The addition of the viscoelastic membrane would restrict the explosive growth of a bubble in response to a negative pressure phase.

8.2.3. Mechanisms of HIFU boiling histotripsy

In Chapter 5, it was proposed that (a) shear forces on tissue resulting from a rapid boiling bubble growth and (b) emissions of micro jetting and shockwaves from a cavitation cluster are to be the major mechanisms involved in boiling histotripsy. Specifically, the generation of boiling bubbles at the HIFU focus produces a "tail" shaped lesion and the production of bubble clouds in front of the boiling bubble towards the HIFU source creates a "head" shaped lesion. With a single-element passive cavitation detector, the dynamic behaviour of a boiling bubble and cavitation clouds corresponded to cavitation regimes which were identified as stable cavitation and inertial cavitation, respectively. These results could be further validated using a passive cavitation mapping (PAM) technique (Gyöngy and Coussios 2010) to evaluate the spatiotemporal distribution of acoustic cavitation activity with optical observations of radial motions using a high-speed camera.

8.2.4. Prediction of the size of a cavity

Prediction of the shape and size of a mechanically induced lesion at a given HIFU boiling histotripsy exposure condition would be of much interest for pretreatment planning. The results presented in this thesis clearly show a strong correlation between the cavity size and the number of HIFU pulses. It was suggested that the dimensions of a "tail" and a "head" shaped lesions are primarily dependent upon the extents of a localised super-heated region and the acoustic fields backscattered by a boiling bubble, respectively. In order to predict the lesion size, an accurate and reliable numerical model capable of dealing with scattering by localised heterogeneities (i.e. the presence of a boiling vapour bubble at the HIFU focus) for simulating acoustic and temperature fields, would be required. This is because a boiling bubble reflects and scatters most of the incident ultrasonic field (Wojcik *et al* 1995), and thereby the heat deposition pattern is significantly changed (Grisey *et al* 2016).

Two numerical approaches could be performed to predict the sizes of a "tail" and a "head" shaped lesions. First of all, the full wave Westervelt equation could be used to calculate the spatial distribution of acoustic pressure field around a boiling bubble. The KZK equation (3.72) used in this thesis is a one-way wave equation and thus does not model reflections, scattering and heterogeneities. The open source k-Wave MATLAB toolbox (Treeby and Cox 2010, Treeby *et al* 2012), which solves the Westervelt equation and accounts for heterogeneities and power law absorption, could be implemented. The experimental validation of k-Wave has been performed for nonlinear wave propagation in a homogenous medium (Wang *et al* 2012) as well as in a heterogeneous medium with simple geometric scatterers (Martin and Treeby 2015). The BHT equation (3.75) could then be used in combination with the Westervelt equation to simulate the spatiotemporal distribution of the temperature field. This would provide the change in the extent of a heated region (which is assumed to correspond to the size of a "tail" shaped lesion) as a function of time over an entire HIFU exposure.

Furthermore, finite element analysis might also be useful to assess the effects of a rapid bubble expansion on mechanical tissue fractionation. An analysis of mechanical stress around an oscillating bubble in a viscoelastic medium could be carried out using commercially available finite-element-method (FEM) software packages such as ANSYS® or COMSOL Multiphysics® which would be useful for investigating how much tissue volume can potentially be fractionated by rectified bubble growth.

Lastly, the size of a "head" shaped lesion could be predicted by plotting a computed contour plot of backscattered pressure fields by a boiling bubble, where the contour lines are equal to or above the cavitation clouds' threshold of –28 MPa (Maxwell *et al* 2013, Lin *et al* 2014). This would essentially represent the potential region that would be mechanically fractionated by the formation of a cavitation cluster. The numerical results of the lesion size prediction would then need to be compared with both *ex*- and *in vivo* experimental results.

8.2.5. HIFU mediated intra-hepatic cell transplantation

The feasibility of the proposed intra-hepatic hepatocyte transplantation was demonstrated in this thesis. Although it was shown that the plasma albumin level in the Nagase analbuminemic rat was restored to 50% of the normal level one week after the transplantation, a long-term follow-up (e.g. months after treatment) study with a large number of Nagase rats would be necessary for confirming the potential clinical benefits of the proposed novel cell therapy. This is because restored liver function several months after intra-portal hepatocyte transplantation tends to decline due to the low rate of long-term survival of transplanted cells (i.e. loss of the cell engraftment with time) (Bartlett and Newsome 2015). Furthermore, it would also be of interest to investigate the relationship between the size of a cavity and the effectiveness of cell growth as well as vascular endothelial growth factor VEGF.

The clinical outcome of hepatocyte transplantation is highly dependent upon the quality of the donor hepatocytes (Jorns *et al* 2012). The majority of published animal and clinical studies to date have used primary hepatocytes as a source of donor hepatocytes. However, the shortage of livers from which high quality hepatocytes can be isolated has led researchers to consider alternative sources of hepatocyte or hepatocyte-like cells (Bartlett and Newsome 2015). These include mesenchymal, embryonic or induced-pluripotent stems cells. Because of their potential for infinite replication and modulation of host immune responses (Gramignoli *et al* 2015), stem cells would be the ideal choice for cell replacement. HIFU-mediated stem cell-derived hepatocytes transplantation could therefore be a powerful clinical therapy and warrants further investigation.

8.2.6. HIFU-induced tissue decellularisation

For successful cell therapy, three-dimensional support with an appropriate mechanical and biological environment is necessary to facilitate cell attachment and proliferation. Preservation of intact vascular networks and extracellular matrix scaffold provides an ideal foundation for cellular repopulation (Guyette *et al* 2014; Khokhlova *et al* 2015a). Current decellularisation techniques use chemical or biological agents to remove the cellular material of an organ or tissue, leaving the matrix intact. These methods, however, are a lengthy processes (12 to 14 days) and can result in chemical alternations of the matrix (Guyette *et al* 2014). The possibility of using HIFU boiling histotripsy to create a decellularised lesion in an *in vivo* liver parenchyma was shown in this thesis. Further investigations need to be conducted to gain an improved understanding of the mechanisms behind HIFU decellularisation effects as well as to control the degree of intact extracellular matrix. The HIFU exposure parameters would need to be adjusted and optimised to achieve complete decellularisation with minimal connective tissue damage. For this goal to be realised, a large *in vivo* parametric study would need to be carried out to investigate the transition in lesion types from a cavity to a completely decellularised lesion. Alternatively, a three-dimensional collagen gel matrix consisting of different types of liver cells (i.e., hepatocytes, endothelial cells of blood vessels and epithelial

cells of bile duct) could be used as a liver analogue. Mouratidis *et al* (2016) have recently developed a human colon cancer cell line HT29 embedded in 3D collagen gel matrices suitable for cell exposure to HIFU fields. Their approach could be adopted to improve this analogue by embedding liver cells in the collagen gel. This liver analogue would then be exposed to different HIFU insonation conditions to examine the effects of HIFU on cell viability.

8.3. Summary

This Chapter has demonstrated that the aims and objectives defined at the start of the work have been achieved. A numerical model describing the response as a function of temperature variation of a single bubble in the liver exposed to HIFU boiling histotripsy fields has been developed. Mechanisms involved in HIFU boiling histotripsy, particularly the formation of a boiling bubble at the HIFU focus and its further interaction with incident shockwaves, were investigated both experimentally and numerically. Furthermore, the feasibility of the proposed hepatocyte transplantation has been demonstrated. Areas for future work have also been identified in this Chapter. These include:

- Characterising the acoustic field of a shockwave;
- Improving the numerical bubble model by adding a viscoelastic model;
- Modelling the acoustic and temperature fields in the case of a boiling bubble at the HIFU focus;
- Predicting the size of a histotripsy-induced lesion for a given HIFU exposure condition;
- Further investigations of the proposed novel intra-hepatic cell transplantation and of HIFU-induced tissue decellularisation.

References

Akulichev, V.A. 1971. *High-Intensity Ultrasonic Fields*. New York: Plenum.

Al-Bataineh, O., Jenne, J. and Huber, P. 2012. Clinical and future applications of high intensity focused ultrasound in cancer. *Cancer Treat. Rev.* **38**(5), pp.346-353.

Allen, S. and Hall, T. 2015. Real-time MRI feedback of cavitation ablation therapy (histotripsy). *Journal of Therapeutic Ultrasound*. **3**(Suppl 1), pp.O89.

Arnaoutova, I., George, J., Kleinman, H.K. and Benton, G. 2009. The endothelial cell tube formation assay on basement membrane turns 20: state of the science and the art. *Angiogenesis*. **12**(3), pp.267-274.

Aubry, J.F., Tanter, M., Pernot, M., Thomas, J.L. and Fink, M. 2003. Experimental demonstration of noninvasive transskull adaptive focusing based on prior computed tomography scans. *J. Acoust. Soc. Am.* **113**(84), pp.84-93.

Aubry, J.F., Pauly, K.B., Moonen, C., ter Haar, G., Ries, M., Salomir, R., Sokka, S., Sekins, K.M., Shapira, Y., Ye, F., Huff-Simonin, H., Eames, M., Hananel, A., Kassell, N., Napoli, A., Hwang, J.H., Wu, F., Zhang, L., Melzer, A., Kim, Y.S. and Gedroyc, W.M. 2013. The road to clinical use of high-intensity focused ultrasound for liver cancer: technical and clinical consensus. *Journal of Therapeutic Ultrasound*. **1**(13), pp.1-7.

Averkiou, M.A. and Hamilton, M.F. 1997. Nonlinear distortion of short pulses radiated by plane and focused circular pistons. *J. Acoust. Soc. Am*. **102**(5), pp.2539-2548.

Aymé-Bellegarda, E.J. 1990. Collapse and rebound of a gas-filled spherical bubble immersed in a diagnostic ultrasound field. *J. Acoust. Soc. Am*. **88**(2), pp.1054-1060.

Baccarani, U., Adani, G.L., Sanna, A., Avellini, C., Sainz-Barriga, M., Lorenzin, D., Montanaro, D., Gasparini, D., Risaliti, A., Donini, A. and Bresadola, F. 2005. Portal vein thrombosis after intraportal hepatocytes transplantation in a liver transplant recipient. *Transpl. Int.* **18**(6), pp.750-754.

Badylak, S.F. 2004. Xenogeneic extracellular matrix as a scaffold for tissue reconstruction. *Transpl. Immunol*. **12**(3), pp.367-377.

Bailey, M.R., Khokhlova, V.A., Sapozhnikov, O.A., Kargl, S.G. and Crum, L.A. 2003. Physical mechanisms of the therapeutic effect of ultrasound (a review). *Acoustical Physics.* **49**(4), pp.369-388.

Banerjee, P.K. 1994. *The Boundary Element Methods in Engineering*. London: McGraw-Hill.

Bartlett, D.C. and Newsome, P.N. 2015. Hepatocyte cell therapy in liver disease. *Expert Rev. Gastroenterol. Hepatol*. **9**(10), pp.1261-1272.

Basude, R. and Wheatley, M.A. 2001. Generation of ultraharmonics in surfactant based ultrasound contrast agents: use and advantages. *Ultrasonics* **39**(6), pp.437-444.

Battino, R., Rettich, T.R. and Tominaga, T. 1984. The solubility of nitrogen and air in liquids. *J. Phys. Chem. Ref. Data*. **13**(2), pp.563-600.

Battino, R. 1982. *IUPAC Solubility Data Series, Vol. 10, Nitrogen and Air*. Oxford: Pergamon.

Battino, R. 1981. *IUPAC Solubility Data Series, Vol. 7, Oxygen and Ozone*. Oxford: Pergamon.

Benenden National Health Report. 2015. *Liver transplant*. [Accessed 17 March 2016]. Available from: https://www.benenden.co.uk/media/1787810/Benenden-Report-2015_final-version.pdf.

Berberan-Santos, M.N., Bodunov, E.N. and Pogliani, L. 2008. The van der Waals equation: analytical and approximate solutions. *J. Mathematical Chemistry*. **43**(4), pp.1437-1457.

Bilaniuk, N. and Wong, G.S.K. 1993. Speed of sound in pure water as a function of temperature. *J. Acoust. Soc. Am.* **93**(3), pp.1609-1612.

Birkmayer, W. and Hornykiewicz, O. 1961. Der L-3,4-Dioxyphenylalanin (=DOPA)–Effekt bei der Parkinson-Akinese. *Wien. Klin. Wochenschr.* **73**(45), pp.787-788.

Bobkova, S., Gavrilov, L., Khokhlova, V., Shaw, A. and Hand, J. 2010. Focusing of high-intensity ultrasound through the rib cage using a therapeutic random phased array. *Ultrasound in Med. Biol.* **36**(6), pp.888-906.

Brenner, M.P., Hilgenfeldt, S. and Lohse, D. 2002. Single-bubble sonoluminescence. *Rev. Mod. Phys.***74**(2), pp.425-484.

Burgers, J.M. 1948. A mathematical model illustrating the theory of turbulence. *Advances in Applied Mechanics*. **1**, pp.171-199.

Calne, R.Y., White, D.J., Thiru, S., Evans, D.B., McMaster, P., Dunn, D.C., Craddock, G.N., Pentlow, B.D. and Rolles, K. 1978. Cyclosporin A in patients receiving renal allografts from cadaver donors. *The Lancet*. **312**(8104), pp.1323-1327.

Canney, M.S., Bailey, M.R., Crum, L.A., Khokhlova, V.A. and Sapozhnikov, O.A. 2008. Acoustic characterization of high intensity focused ultrasound fields: a

combined measurement and modeling approach. *J. Acoust. Soc. Am.* **124**(4), pp.2406-2420.

Canney, M.S., Khokhlova, V.A., Bessonova, O.V., Bailey, M.R. and Crum, L.A. 2010a. Shock-induced heating and millisecond boiling in gels and tissue due to high intensity focused ultrasound. *Ultrasound in Med. Biol.* **36**(2), pp.250-267.

Canney, M.S., Khokhlova, T.D., Khokhlova, V.A., Bailey, M.R., Hwang, J.H. and Crum, L.A. 2010b. Tissue erosion using shock wave heating and millisecond boiling in HIFU fields. *AIP Conf. Proc. 9th Int. Symp. on Therapeutic Ultrasound (ISTU 2009),24-29 September 2009, Aix-en-Provence, France.* **1215**(36), pp.36-39.

Chakma, S. and Moholkar, V.S. 2013. Numerical simulation and investigation of system parameters of sonochemical process. *Chinese Journal of Engineering.* **2013**, pp.1-14.

Chavrier, F., Chapelon, J.Y., Gelet, A. and Cathignol, D. 2000. Modeling of high-intensity focused ultrasound-induced lesions in the presence of cavitation bubbles. *J. Acoust. Soc. Am*. **108**(1), pp.432-440.

Chen, C., Liu, Y., Maruvada, S., Myers, M. and Khismatullin, D. 2012. Effect of ethanol injection on injection of cavitation and heating of tissues exposed to high-intensity focused ultrasound. *Phys. Med. Biol*. **57**(4), pp.937-961.

Chen, W.S., Lafon, C., Matula, T.J., Vaezy, S. and Crum, L.A. 2003a. Mechanisms of lesion formation in high intensity focused ultrasound therapy. *Acoustic. Res. Lett. Online*. **4**(2), pp.41-46.

Chen, W.S., Brayman, A.A., Matula, T.J. and Crum, L.A. 2003b. Inertial cavitation dose and hemolysis produced in vitro with or without optison. *Ultrasound in Med. Biol.* **29**(5), pp.725-737.

Chin, K.J., Perlas, A., Chan, V.W.S. and Brull, R. 2008. Needle visualization in ultrasound-guided regional anesthesia: challenges and solutions. *Regional Anesthesia and Pain Medicine*. **33**(6), pp.532-544.

Choi, M.J., Guntur, S.R., Lee, J.M., Paeng, D.G., Lee, K.I. and Coleman, A. 2011. Changes in ultrasonic properties of liver tissue *in vitro* during heating-cooling cycle concomitant with thermal coagulation. *Ultrasound in Med. Biol.* **37**(12), pp.2000-2012.

Choi, M.J., Guntur, S.R., Lee, K.I., Paeng, D.G. and Coleman, A. 2013. A tissue mimicking polyacrylamide hydrogel phantom for visualizing thermal lesions generated by high intensity focused ultrasound. *Ultrasound in Med. Biol.* **39**(3), pp.439-448.

Church, C.C. 1989. A theoretical study of cavitation generated by an extracorporeal shock wave lithotripter. *J. Acoust. Soc. Am.* **86**(1), pp.215-227.

Church, C.C., Labuda, C. and Nightingale, K. 2012. Should the mechanical index be revised for ARFI imaging? *IEEE Int. Ultras. Symp. Proc, 7-10 October 2012, Dresden, Germany.* **5**, pp.17-20.

Clement, G.T., White, J. and Hynynen, K. 2000. Investigation of a large-area phased array for focused ultrasound surgery through the skull. *Phys. Med. Biol*. **45**(4), pp.1071-1083.

Cleveland, R.O. and McAteer, J.A. 2007. The physics of shock wave lithotripsy. In: in Smith, A.D. ed. *Smith's Textbook on Endourology*. Hamilton: Decker, pp.317-332.

Clever, H.L. 1980. *IUPAC Solubility Data Series: Vol. 4, Argon*. Oxford: Pergamon Press.

Cobbold, R.S.C. 2007. *Foundations of Biomedical Ultrasound*. New York: Oxford University Press.

Colussi, A.J. and Hoffmann, M.R. 1999. Vapor supersaturation in collapsing bubbles. Relevance to the mechanisms of sonochemistry and sonoluminescence. *J. Phys. Chem.* **103**(51), pp.11336-11339.

Connor, C.W. and Hynynen, K. 2002. Bio-acoustic thermal lensing and nonlinear propagation in focused ultrasound surgery using large focal spots: a parametric study. *Phys. Med. Biol*. **47**(11), pp.1911-1928.

Coussios, C.C. and Roy, R.A. 2008 Applications of acoustics and cavitation to noninvasive therapy and drug delivery. *Annu. Rev. Fluid Mech.* **40**, pp.395-420.

Crum, L.A. 1984. Rectified diffusion. *Ultrasonics.* **22**(5), pp.215-223.

Darwish, A.A., Sokal, E., Stephenne, X., Najimi, M., De Goyet, J.D.V. and Reding, R. 2004. Permanent access to the portal system for cellular transplantation using an implantable port device. *Liver Transpl*. **10**(9), pp.1213-1215.

David, P., Alexandre, E., Audet, M., Chenard-Neu, M.P., Wolf, P., Jaeck, D., Azimzadeh, A. and Richert, L. 2001. Engraftment and albumin production of intrasplenically transplanted rat hepatocytes (Sprague-Dawley), freshly belated versus cryopreserved, into nagase analbuminemic rats (NAR). *Cell Transplantation*. **10**(1), pp.67-80.

Delgrosso, V.A. and Mader, C.W. 1972. Speed of sound in pure water. *J. Acoust. Soc. Am.* **52**(5), pp.1442-1446.

Dhawan, A., Puppi, J., Hughes, R.D. and Mitry, R.R. 2010. Human hepatocyte transplantation: current experience and future challenges. *Nat. Rev. Gastroenterol. Hepatol.* **7**(5), pp.288-298.

Ding, Z. and Gracewski, S.M. 1994. Response of constrained and unconstrained bubbles to lithotripter shock wave pulses. *J. Acoust. Soc. Am.* **96**(6), pp.3636-3644.

Dubinsky, T.J., Cuevas, C., Dighe, M.K., Kolokythas, O. and Hwang, J.H. 2008. High-intensity focused ultrasound: current potential and oncologic applications. *American J. Roentgenology*. **190**(1), pp.191-199.

Duck, F.A. 1990. *Physical properties of tissue: a comprehensive reference book*. London: Academic Press.

Duryea, A.P., Cain, C.A., Roberts, W.W. and Hall, T.L. 2015. Removal of residual cavitation nuclei to enhance histotripsy fractionation of soft tissue. *IEEE Trans. Ultrason. Ferroelectr. Freq. Control*. **62**(12), pp.2068-2078.

Everbach, E.C., Makin, I.R.S, Azadniv, M. and Meltzer, R.S. 1997. Correlation of ultrasound-induced hemolysis with cavitation detector output in vitro. *Ultrasound in Med. Biol.* **23**(4), pp.619-624.

Farny, C.H., Holt, R.G and Roy, R.A. 2009. Temporal and spatial detection of hifu-induced inertial and hot-vapor cavitation with a diagnostic ultrasound system. *Ultrasound in Med. Biol.* **35**(4), pp.603-615.

Forbes, S.J. and Rosenthal, N. 2014. Preparing the ground for tissue regeneration: from mechanism to therapy. *Nature Med*. **20**(8), pp.857-869.

Food and Drug Administration, Center for Devices and Radiological Health. *High intensity ultrasound system for prostate tissue ablation approval letter, October 9, 2015*. [Accessed 25 March 2016]. Available from: http://www.accessdata.fda.gov/cdrh_docs/pdf15/den150011.pdf.

Fox, I.J., Chowdhury, J.R., Kaufman, S.S., Goertzen, T.C., Chowdhury, N.R., Warkentin, P.I., Dorko, K., Sauter, B.V and Strom, S.C. 1998. Treatment of the

crigler-najjar syndrome type I with hepatocyte transplantation. *N. Engl. J. Med.* **338**(20), pp.1422-1426.

Frerich, B., Lindemann, N., Kurtz-Hoffmann, J. and Oertel, K. 2001. In vitro model of a vascular stroma for the engineering of vascularized tissues. *Int. J. Oral Maxillofacial Surg.* **30**(5), pp.414-420.

Fry, W.J., Barnard, J.W., Fry, F.J., Krumins, R.F. and Brennan, J.F. 1955. Ultrasonic lesions in the mammalian central nervous system. *Science*. **122** (3168), pp.517-518.

Fry, W.J., Mosberg, W.H., Barnard, J.W. and Fry, F.J. 1954. Production of focal destructive lesions in the central nervous system with ultrasound. *J. Neurosurg.* **11**(5), pp.471-478.

Fry, W.J. and Fry, F.J. 1960. Fundamental neurological research and human neurosurgery using intense ultrasound. *IRE Trans. Medical Electronics*. **7**(3), pp. 166-181.

Fujii, T., Fuchs, B.C., Yamada, S., Lauwers, G.Y., Kulu, Y., Goodwin, J.M., Lanuti, M. and Tanabe, K.K. 2010. Mouse model of carbon tetrachloride induced liver fibrosis: histopathological changes and expression of CD133 and epidermal growth factor. *BMC Grastroenterology*. **10**, pp.79-89.

Gaitan, D.F., Crum, L.A., Church, C.C. and Roy, R.A. 1992. Sonoluminescence and bubble dynamics for a single, stable, cavitation bubble. *J. Acoust. Soc. Am.* **91**(6), pp.3166-3183.

Gavrilov, L.R. and Hand, J.W. 2000. A theoretical assessment of the relative performance of spherical phased arrays for ultrasound surgery. *IEEE Trans. Ultrason. Ferr. Freq. Control.* **47**(1), pp.125-139.

Gélat, P., ter Haar, G. and Saffari, N. 2011. Modelling of the acoustic field of a multi-element HIFU array scattered by human ribs. *Phys. Med. Biol*. **56**(17), pp.5553-5581.

Gélat, P., ter Haar, G. and Saffari, N. 2012. Scattering of the field of a multi-element phased array by human ribs. *Journal of physics: Conference Series*. **353**, pp.012010.

Gélat, P., ter Haar, G. and Saffari, N. 2014. A comparison of methods for focusing the field of a HIFU array transducer through human ribs. *Phys. Med. Biol*. **59**(12), pp.3139-3171.

Gélat, P., ter Haar, G. and Saffari, N. 2015. An assessment of the DORT method on simple scatterers using boundary element modelling. *Phys. Med. Biol.* **60**(9), pp.3715-3730.

Gilmore, F.R. 1952. *The growth or collapse of a spherical bubble in a viscous compressible liquid*. Technical Report No.26-24. California Institute of Technology, Pasadena, California.

Gómez, J.L., Gunnerson, K.J., Song, M., Li, J. and Kellum, J.A. 2007. Effects of hypercapnia on BP in hypoalbuminemic and Nagase analbuminemic rats. *Chest*. **131**(5), pp.1295-1300.

Gramignoli, R., Vosough, M., Kannisto, K., Srinivasan, R.C. and Strom, S.C. 2015. Clinical hepatocyte transplantation: practical limits and possible solutions. *Eur. Sug. Res*. **54**(3), pp.162-177.

Grisey, A., Yon, S., Letort, V. and Lafitte, P. 2016. Simulation of high-intensity focused ultrasound lesions in presence of boiling. *Journal of Therapeutic Ultrasound*. **4**, pp.11-14.

Grossman, M., Raper, S.E., Kozarsky, K., Stein, E.A., Engelhardt, J.F., Muller, D., Lupien, P.J. and Wilson, J.M. 1994. Successful ex vivo gene therapy directed to liver in a patient with familial hypercholesterolaemia. *Nat. Genet*. **6**(4), pp.335-341.

Gustafson, E.K., Elgue, G., Hughes, R.D., Mitry, R.R., Sanchez, J., Haglund, U., Meurling, S., Dhawan, A., Korsgren, O. and Nilsson, B. 2011. The instant blood-mediated inflammatory reaction characterized in hepatocyte transplantation. *Transplantation.* **91**(6), pp.632-638.

Guyette, J.P., Gilpin, S.E., Charest, J.M., Tapias, L.F., Ren, X. and Ott, H.C. 2014. Perfusion decellularization of whole organs. *Nat. Protoc*. **9**(6), pp.1451-1468.

Gyöngy, M. and Coussios, C.C. 2010. Passive cavitation mapping for localization and tracking of bubble dynamics. *J. Acoust. Soc. Am.* **128**(4), pp.175-180.

Habka, D., Mann, D., Landes, R. and Soto-Gutierrez, A. 2015. Future economics of liver transplantation: a 20-year cost modeling forecast and the prospect of bioengineering autologous liver grafts. *PLOS ONE*. **10**(7), pp.1-21.

Hall, T.L., Fowlkes, J.B. and Cain, C.A. 2005. Imaging feedback of tissue liquefaction (histotripsy) in ultrasound surgery. *IEEE Ultrason. Symp. Proc., 18-21 September 2005, Rotterdam, Netherlands.* **3**, pp.1732-1734.

Hall, T.L., Hempel, C.R., Lake, A.M., Kieran, K., Ives, K., Fowlkes, J.B., Cain, C.A. and Roberts, W.W. 2008. Histotripsy for the treatment of BPH: evaluation in a chronic canine model. *IEEE Ultrason. Symp. Proc., 2-5 November 2008, Beijing, China.* pp.765-767.

Hall, T.L., Hempel, C.R., Wojno, K., Xu, Z., Cain, C.A. and Roberts, W.W. 2009. Histotripsy of the prostate: dose effects in a chronic canine model. *Urology*. **74**(4), pp.932-937.

Hamilton, M.F. and Blackstock, D.T. 2008. *Nonlinear Acoustic*. New York: Acoustical Society of America.

Hao, Y. and Prosperetti, A. 1999. The dynamics of vapour bubbles in acoustic pressure fields. *Phys. Fluids*. **11**(8), pp.2008-2019.

Hao, Y. and Prosperetti, A. 2002. Rectified heat transfer into translating and pulsating vapor bubbles. *J. Acoust. Soc. Am.* **112**(5), pp.1787-1797.

Haar, L., Gallagher, J.S. and Kell, G.S. 1984. *NBS/NRC Steam Tables*. New York: Hemisphere Publishing.

Herring, C. 1941. Theory of the pulsations of the gas bubble produced by an underwater explosion. *O.S.R.D. Rep. No. 236.*

Hertz, H. 1882. On the evaporation of liquids, especially mercury, in vacuo. *Ann. Phys. (Leipzig)*. **17**, p.177.

Hilgenfeldt, S., Brenner, M.P., Grossmann, S. and Lohse, D. 1998. Analysis of rayleigh-plesset dynamics for sonoluminescing bubbles. *J. Fluid Mech.* **365**, pp.171-204.

Hirschfelder, J.O., Curtiss, C.F. and Bird, R.B. 1964. *Molecular Theory of Gases and Liquids.* New York: Wiley.

Holt, R.G. and Roy, R.A. 2001. Measurements of bubble-enhanced heating from focused, mHz-frequency ultrasound in a tissue-mimicking material. *Ultrasound in Med. Biol*. **27**(10), pp.1399-1412.

Holzfuss, J. 2005. Unstable diffusion and chemical dissociation of a single sonoluminescing bubble. *Phys. Rev. E*. **71**, pp.1-5.

Holzfuss, J. 2008. Surface-wave instabilities, period doubling, and an approximate universal boundary of bubble stability at the upper threshold of sonoluminescence. *Physical Review E*. **77**, pp.1-10.

Hoogenboom, M., Eikelenboom, D., den Brok, M.H., Heerschap, A., Fütterer, J.J. and Adema, G.J. 2015. Mechanical high-intensity focused ultrasound destruction of soft tissue: working mechanisms and physiologic effects. *Ultrasound in Med. Biol*. **41**(6), pp.1500-1517.

Hoppo, T., Komori, J., Manohar, R., Stolz, D.B. and Lagasse, E. 2011. Rescue of lethal hepatic failure by hepatized lymph nodes in mice. *Gastroenterology*. **140**(2), pp.656-666.

Horslen, S.P. and Fox, I.J. 2004. Hepatocyte transplantation. *Transplantation*. **77**(10), pp.1481-1486.

Hughes, R.D., Mitry, R.R. and Dhawan, A. 2012. Current status of hepatocyte transplantation. *Transplantation*. **93**(4), pp.342-347.

Illing, R.O., Kennedy, J.E., Wu, F., ter Haar, G.R, Protheroe, A.S., Friend, P.J., Gleeson, F.V., Cranston, D.W., Phillips, R.R. and Middleton, M.R. 2005. The safety and feasibility of extracorporeal high-intensity focused ultrasound (HIFU) for the treatment of liver and kidney tumours in a western population. *Br. J. Cancer* **93**(8), pp.890-895.

Ito, M., Nagata, H., Yamamoto, T., Yoshihara, D., Fox, I.J. and Miyakawa, S. 2007. Intrasplenic hepatocyte transplantation prolonged the survival in Nagase analbuminemic rats with liver failure induced by common bile duct ligation. *Cell Transplantation*. **16**(5), pp.547-553.

Johansson, H., Lukinius, A., Moberg, L., Lundgren, T., Berne, C., Foss, A., Felldin, M., Källen, R., Salmela, K., Tibell, A., Tufveson, G., Ekdahl, K.N., Elgue, G.,

Korsgren, O. and Nilsson, B. 2005. Tissue factor produced by the endocrine cells of the islets of Langerhans is associated with a negative outcome of clinical islet transplantation. *Diabetes*. **54**(6), pp.1755-1762.

Jones, R.P., Kitteringham, N.R., Terlizzo, M., Hancock, C., Dunne, D., Fenwick, S.W., Poston, G.J., Ghaneh, P. and Malik, H.Z. 2012. Microwave ablation for ex vivo human liver and colorectal liver metastases with a novel 14.5 GHz generator. *Int. J. Hyperthermia.* **28**(1), pp.43-54.

Jorns, C., Ellis, E.C., Nowak, G., Fischler, B., Nemeth, A., Strom, S.C. and Ericzon, B.G. 2012. Hepatocyte transplantation for inherited metabolic diseases of the liver. *Journal of Internal Medicine*. **272**(3), pp.201-223.

Joseph, D.D. 1964. Variable viscosity effects on the flow and stability of flow in channels and pipes. *Phys. Fluids.* **7**, pp.1761-1771

Jung, S.E., Cho, S.H., Jang, J.H. and Han, J.Y. 2011. High-intensity focused ultrasound ablation in hepatic and pancreatic cancer: complications. *Abdom. Imaging.* **36**(2), pp.185-195.

Kamath, V., Prosperetti, A. and Egolfopoulos, F.N. 1993. A theoretical study of sonoluminescence. *J. Acoust. Soc. Am.* **94**(1), pp.248-260.

Khokhlova, T.D., Wang, Y.N., Simon, J.C., Cunitz, B.W., Starr, F., Paun, M., Crum, L.A., Bailey, M.R. and Khokhlova, V.A. 2014. Ultrasound-guided tissue fractionation by high intensity focused ultrasound in an in vivo porcine liver model *Proc. Natl. Acad. Sci. USA.* **111**(22), pp.8161-8166.

Khokhlova, T.D., Canney, M.S., Khokhlova, V.A., Sapozhnikov, O.A., Crum, L.A. and Bailey, M.R. 2011. Controlled tissue emulsification produced by high intensity focused ultrasound shock waves and millisecond boiling. *J. Acoust. Soc. Am.* **130**(5), pp.3498-3510.

Khokhlova, T.D. and Hwang, J.H. 2011. HIFU for palliative treatment of pancreatic cancer. *J. Gastrointest. Oncol*. **2**(3), pp.175-184.

Khokhlova, V.A., Bailey, M.R., Reed, J.A., Cunitz, B.W., Kaczkowski, P.J. and Crum, L.A. 2006. Effects of nonlinear propagation, cavitation, and boiling in lesion formation by high intensity focused ultrasound in a gel phantom. *J. Acoust. Soc. Am.* **119**(3), pp.1834-1848.

Khokhlova, V.A., Bobkova, S.M. and Gavrilov, L.R. 2010. Focus splitting associated with propagation of focused ultrasound through the rib cage. *Acoust. Phys.* **56**(5), pp.665-674.

Khokhlova, V.A., Fowlkes, J.B., Roberts, W.W., Schade, G.R., Xu, Z., Khokhlova, T.D., Hall, T.L., Maxwell, A.D., Wang, Y.N. and Cain, C.A. 2015a. Histotripsy methods in mechanical disintegration of tissue: towards clinical applications. *Int. J. Hyperthermia.* **31**(2), pp.145-162.

Khokhlova, V., Partanen, A., Maxwell, A., Khokhlova, T., Kreider, W., Bailey, M., Farr, N., Wang, Y.N., Schade, G. and Sapozhnikov, O. 2015b. Boiling histotripsy to mechanically fractionate tissue volumes in ex vivo bovine liver using a clinical MR-guided HIFU system. *J. Therapeutic Ultrasound*. **3**(Suppl 1), p.O88.

Kieran, K., Hall, T.L., Parsons, J.E., Wolf, J.S., Fowlkes, J.B., Cain, C.A. and Roberts, W.W. 2007. Refining histotripsy: defining the parameter space for the creation of nonthermal lesions with high intensity, pulsed focused ultrasound of the in vitro kidney. *J. Urol.* **178**(2), pp.672-676.

Kim, Y., Vlaisavljevich, E., Owens, G.E., Allen, S.P., Cain, C.A. and Xu, Z. 2014. In vivo transcostal histotripsy therapy without aberration correction. *Phys. Med. Biol*. **59**(11), pp.2553-2568.

Kim, Y., Wang, T.Y., Xu, Z. and Cain, C.A. 2011. Lesion generation through ribs using histotripsy therapy without aberration correction. *IEEE Trans. Ultrason. Ferroelectr. Freq. Control*. **58**(11), pp.2334-2343.

Kim, Y.S., Rhim, H., Choi, M.J., Lim, H.K. and Choi, D.I. 2008. High-intensity focused ultrasound therapy: an overview for radiologists. *Korean J. Radiol*. **9**(4), pp.291-302.

Kirkwood, J.G. and Bethe, H.A. 1942. The pressure wave produced by an underwater explosion. *O.S.R.D. Rep*. *558.*

Knudsen, M. 1915. Maximum rate of vaporazation of mercury. *Ann. Phys. (Leipzig)*. **47**, pp.697.

Kocken, J.M., Bouwman, E., Borel Rinkes, I.H.M, Sinaasappel, M. and Terpstra, O.T. 1997. Observations on initial cell loss after intraportal hepatocyte transplantation of 5'-Bromo-Deoxy-Uridine-labeled hepatocytes. *Eur. Surg. Res*. **29**(6), pp.411-420.

Kokudo, N., Takahashi, S., Sugitani, K., Okazaki, T. and Nozawa, M. 1999. Supplement of liver enzyme by intestinal and kidney transplants in congenitally enzyme-deficient rat. *Microsurgery* **19**(2), pp.103-107.

Korpel, A. 1980. Frequency approach to nonlinear dispersive waves. *J. Acoust. Soc. Am*. **67**(6), pp.1954-1958.

Korson, L., Drost-Hansen, W and Millero, F.J. 1969. Viscosity of water at various temperatures. *J. Phys. Chem.* **73**(1), pp.34-39.

Kravchenko, V.S. 1966. Empirical equation derived for temperature dependence of density of heavy water. *Soviet Atomic Energy.* **20**(2), p.212.

Kreider, W. 2008. *Gas-Vapor Bubble Dynamics in Therapeutic Ultrasound.* Ph.D. thesis, University of Washington.

Kreider, W., Bailey, M.R., Sapozhnikov, O.A., Khokhlova, V.A. and Crum, L.A. 2011a. The dynamics of histotripsy bubbles. *AIP Conf. Proc. 10th Int. Symp. on Therapeutic Ultrasound (ISTU 2010), 9-12 June 2010, Tokyo, Japan.* **1359**, pp.427-430.

Kreider, W., Crum, L.A., Bailey, M.R. and Sapozhnikov, O.A. 2011b. A reduced-order, single-bubble cavitation model with applications to therapeutic ultrasound. *J. Acoust. Soc. Am.* **130**(5), pp.3511–3530.

Kreider, W., Yuldashev, P.V., Sapozhnikov, O.A., Farr, N., Partanen, A., Bailey, M.R. and Khokhlova, V.A. 2013. Characterization of a multi-element clinical HIFU system using acoustic holography and nonlinear modelling. *IEEE Trans. Ultrason. Ferr. Freq. Control.* **60**(8), pp.1683-1698.

Kumagai, H., Yokoyama, K., Katsuyama, K., Hara, S., Yamamoto, H., Yamagata, T., Taniguchi, N., Hirota, N. and Itoh, K. 2014. A new method for measuring the speed of sound in rat liver ex vivo using an ultrasound system: correlation of sound speed with fat deposition. *Ultrasound in Med. Biol.* **40**(10), pp.2499-2507.

Kuznetsov, V.P. 1971. Equations of nonlinear acoustics. *Soviet Physical Acoustics*. **16**, pp.467-470.

Labelle, P., Inserra, C. and Béra, J.C. 2012. Cavitation level-acoustic intensity hysteresis: experimental and numerical characterization. *Proceedings of the Acoustics, 23-24 April 2012, Nantes, France.* pp.2551-2556.

Lafon, C., Zderic, V., Noble, M., Yuen, J., Kaczkowski, P., Sapozhnikov, O., Chavrier, F., Crum, L. and Vaezy, S. 2005. Gel phantom for use in high-intensity focused ultrasound dosimetry. *Ultrasound in Med. Biol.* **31**(10), pp.1383-1389.

Lake, A.M., Hall, T.L., Kieran, K., Fowlkes, J.B., Cain, C.A. and Roberts, W.W. 2008a. Histotripsy: minimally invasive technology for prostatic tissue ablation in an in vivo canine model. *Urology*. **72**(3), pp.682-686.

Lake, A.M., Xu, Z., Wilkinson, J.E., Cain, C.A. and Roberts, W.W. 2008b. Renal ablation by histotripsy-does it spare the collecting system? *J. Urol.* **179**(3), pp.1150-1151.

Landau, L.D. and Lifshitz, E.M. 2011. *Fluid Mechanics*. Oxford: Elsevier.

Lauterborn, W. 1976. Numerical investigation of nonlinear oscillations of gas bubbles in liquids. *J. Acoust. Soc. Am*. **59**(2), pp.283-293.

Lee, K.W., Lee, J.H., Shin, S.W., Kim, S.J., Joh, J.W., Lee, D.H., Kim, J.W., Park, H.Y., Lee, S.Y., Lee, H.H., Park, J.W., Kim, S.Y., Yoon, H.H., Jung, D.H., Choe, Y.H. and Lee, S.K. 2007. Hepatocyte transplantation for glycogen storage disease type Ib. *Cell Transplant*. **16**(6), pp.629-637.

Lee, S.W., Wang, X., Chowdhury, N.R. and Roy-Chowdhury J. 2004. Hepatocyte transplantation: state of the art and strategies for overcome existing hurdles. *Ann. Hepatol*. **3**(2), pp.48-53.

Lee, Y.S. and Hamilton, M.F. 1995. Time-domain modeling of pulsed finite-amplitude sound beams. *J. Acoust. Soc. Am*. **97**(2), pp.906-917.

Leighton, T.G. 1994. *The Acoustic Bubble*. London: Academic Press.

Lemmon, E.W., Jacobsen, R.T., Penoncello, S.G. and Friend, D.G. 2000. Thermodynamic properties of air and mixtures of nitrogen, argon and oxygen from 60 to 2000 K at pressures to 2000 MPa. *J. Phys. Chem. Ref. Data*. **29**(3), pp.331-385.

Leslie, T., Ritchie, R., Illing, R., ter Haar, G., Phillips, R., Middleton, M., Wu, F. and Cranston, D. 2012. High-intensity focused ultrasound treatment of liver tumours: post-treatment MRI correlates well with intra-operative estimates of treatment volume. *Br. J. Radiol.* **85**(1018), pp.1363-1370.

Lin, K.W. 2014. *Precise lesion formation in histotripsy therapy using strategic pulsing methods.* Ph.D. thesis, University of Michigan.

Lin, K.W, Kim, Y., Maxwell, A., Wang, T.Y., Hall, T.L, Xu, Z., Fowlkes, J.B. and Cain, C.A. 2014. Histotripsy beyond the intrinsic cavitation threshold using very short ultrasound pulses: microtripsy. *IEEE Trans. Ultrason. Ferroelectr. Freq. Control.* **61**(2), pp.251-265.

Liu, L., Yannam, G.R., Nishikawa, T., Yamamoto, T., Basma, H., Ito, R., Nagaya, M., Dutta-Moscato, J., Stolz, D.B., Duan, F., Kaestner, K.H., Vodovotz, Y., Soto-Gutierrez, A. and Fox, I.J. 2012. The microenvironment in hepatocyte regeneration and function in rats with advanced cirrhosis. *Hepatology.* **55**(5), pp.1529-1539.

Lizzi, F.L., Coleman, D.J., Driller, J., Franzen, L.A. and Jakobiec, F.A. 1978. Experimental, ultrasonically induced lesions in the retina, choroid, and sclera. *Invest. Ophthalmol. and Vis. Sci.* **17**(4), pp.350–360.

Lizzi, F.L., Coleman, D.J., Driller, J., Franzen, L.A. and Leopold, M. 1981. Effects of pulsed ultrasound on ocular tissue. *Ultrasound in Med. Biol.* **7**(3), pp.245-252.

Lovett, M., Lee, K., Edwards, A. and Kaplan, D.L. 2009.Vascularization strategies for tissue engineering. *Tissue Eng. Part B Rev.* **15**(3), pp.353-370.

Lynn, J.G. and Putnam, T.J. 1944. Histology of cerebral lesions produced by focused ultrasound. *Am. J. Pathol.* **20**(3), pp.637-649.

Lynn, J.G., Zwemer, R.L., Chick, A.J. and Miller, A.E. 1942. A new method for the generation and use of focused ultrasound in experimental biology. *J. Gen. Physiol.* **26**(2), pp.179-193.

Malhi, H., Gorla, G.R., Irani, A.N., Annamaneni, P. and Gupta S. 2002. Cell transplantation after oxidative hepatic preconditioning with radiation and ischemia-reperfusion leads to extensive liver repopulation. *Proc. Natl. Acad. Sci. USA.* **99**(20), pp.13114-13119.

Martin, E. and Treeby, B.E. 2015. Experimental validation of computational models for large-scale nonlinear ultrasound simulations in heterogeneous, absorbing fluid media. AIP Conf. Proc. *Recent Developments in Nonlinear Acoustics, 29 June-3 July 2015, Écully, France.* **1685**, p.070007.

Martínez-Valdez, R., Contreras M.V.H., Vera, A. and Leija, L. 2015. Sound speed measurement of chicken liver from 22^{o}C to 60^{o}C. *Physics Procedia*. **70**, pp.1260-1263.

Maruvada, S., Liu, Y., Pritchard, W.F., Herman, B.A. and Harris, G.R. 2012. Comparative study of temperature measurements in ex vivo swine muscle and a tissue-mimicking material during high intensity focused ultrasound exposures. *Phys. Med. Biol*. **57**(1), pp.1-19.

Matas, A.J., Sutherland, D.E.R., Steffes, M.W., Mauer, S.M., Lowe, A., Simmons, R.L. and Najarian, J.S. 1976. Hepatocellular transplantation for metabolic deficiencies: decrease of plasma bilirubin in gunn rats. *Science.* **192**(4242), pp.892-894.

Matula, T.J., Hilmo, P.R., Storey, B.D. and Szeri, A.J. 2002. Radial response of individual bubbles subjected to shock wave lithotripsy pulses in vitro. *Phys. Fluids.* **14**(3), pp.913-921.

Maxwell, A., Sapozhnikov, O., Bailey, M., Crum, L., Xu, Z., Fowlkes, B., Cain, C. and Khokhlova, V. 2012. Disintegration of tissue using high intensity focused ultrasound: two approaches that utilize shock waves. *Acoustics Today*. **8**, pp.24-37.

Maxwell, A.D., Cain, C.A., Hall, T.L., Fowlkes, J.B. and Xu, Z. 2013. Probability of cavitation for single ultrasound pulses applied to tissues and tissue-mimicking materials. *Ultrasound in Med. Biol.* **39**(3), pp.449-465.

Maxwell, A.D, Wang, T.Y., Cain, C.A., Fowlkes, J.B., Sapozhnikov, O.A., Bailey, M.R. and Xu, Z. 2011. Cavitation clouds created by shock scattering from bubbles during histotripsy. *J. Acoust. Soc. Am.* **130**(4), pp.1888-1898.

McLaughlan, J.R. 2008. *An investigation into the use of cavitation for the optimisation of high intensity focused ultrasound (HIFU) treatments*. Ph.D. thesis, University of London.

Miller, D.L. 1981. Ultrasonic detection of resonant cavitation bubbles in a flow tube by their second-harmonic emissions. *Ultrasonics*. **19(**5), pp.217-224.

Miller, D.L., Smith, N.B., Bailey, M.R., Czarnota, G.J., Hynynen, K. and Makin, I.R.S. 2012. Overview of therapeutic ultrasound applications and safety considerations. *J. Ultrasound Med.* **31**(4), pp.623-634.

Minsier, V. and Proost, J. 2008. Shock wave emission upon spherical bubble collapse during cavitation-induced megasonic surface cleaning. *Ultrasonics Sonochem.* **15**(4), pp.598-604.

Morán-Jiménez M.J., García-Bravo M., Méndez M., Gutiérrez-Vera, I., Grau, M., Navarro-Ordoñez, S., Fontanellas, A. and Enríquez-de-Salamanca, R. 2008. Bone marrow transplantation into hemochromatotic mice decreases hepatic and duodenal iron overload. *Int. J. Biochem. Cell Biol*. **40**(1), pp.135-146.

Mouratidis, P., Rivens, I. and ter Haar, G. 2016. Development of 3D collagen gel matrices suitable for cell exposure to high intensity focused ultrasound. Poster presentation at: *The 16th International Symposium on Therapeutic Ultrasound (ISTU 2016), 14-16 March 2016, Tel Aviv, Israel*.

Nagase, S., Shimamune, K. and Shumiya, S. 1979. Albumin-deficient rat mutant. *Science*. **205**(4406), pp.590-591.

Neppiras, E.A. 1980. Acoustic Cavitation. *Phys*. *Rep.* **61**(3), pp.159-251.

Neppiras, E.A. 1984. Acoustic cavitation series: part one: acoustic cavitation: an introduction. *Ultrasonics.* **22**(1), pp.25-28.

NHS Blood and Transplant. 2015. *Annual report on liver transplantation. Report for 2014/2015.* [Accessed 15 March 2016]. Available from: http://www.odt.nhs.uk/pdf/organ_specific_report_liver_2015.pdf.

Nishikawa, T., Bell, A., Brooks, J.M., Setoyama, K., Melis, M., Han, B., Fukumitsu, K., Handa, K., Tian, J., Kaestner, K.H., Vodovotz, Y., Locker, J., Soto-Gutierrez, A. and Fox, I.J. 2015. Resetting the transcription factor network reverses terminal chronic hepatic failure. *J. Clin. Invest.* **125**(4), pp.1533-1544.

Oren, R., Dabeva, M.D., Petkov, P.M., Hurston, E., Laconi, E. and Shafritz, D.A. 1999. Restoration of serum albumin levels in nagase analbuminemic rats by hepatocyte transplantation. *Hepatology*. **29**(1), pp.75-81.

Othmer, D.F. and Thakar, M.S. 1953. Correlating diffusion coefficients in liquids. *Ind. Eng. Chem.* **45**(3), pp.589-593.

Pahk, K.J., Dhar, D.K., Malago, M. and Saffari, N. 2015. Ultrasonic histotripsy for tissue therapy. *J. Phys. Conf. Ser*. **581**(1), pp.012001

Parsons, J.E., Cain, C.A., Abrams, G.D. and Fowlkes, J.B. 2006. Pulsed cavitational ultrasound therapy for controlled tissue homogenization. *Ultrasound in Med. Biol.* **32**(1), pp.115-129.

Pauly, H. and Schwan, H.P. 1971. Mechanism of absorption of ultrasound in liver tissue. *J. Acoust. Soc. Am.* **50**(2), pp.692-699.

Pennes, H.H. 1948. Analysis of tissue and arterial blood temperatures in the resting human forearm. *Journal of Applied Physiology*. **1**(2), pp.93-122.

Pernot, M., Aubry, J.F., Tanter, M., Thomas, J.L. and Fink, M. 2003. High power transcranial beam steering for ultrasonic brain therapy. *Phys. Med. Biol.* **48**(16), pp. 2577-2589.

Phelps, A.D. and Leighton, T.G. 1997. The subharmonic oscillations and combination-frequency subharmonic emissions from a resonant bubble: their properties and generation mechanisms. *Acta. Acust. United Ac*. **83**, pp.59-66.

Pierce, A.D. 1989. *Acoustics: an Introduction to Its Physical Principles and Applications.* New York: McGraw-Hill.

Pinton, G.F. 2007. *Numerical methods for nonlinear wave propagation in ultrasound*. Ph.D. thesis, Duke University.

Pishchalnikov, Y.A., Sapozhnikov, O.A., Bailey, M.R., Williams, J.C., Cleveland, R.O., Colonius, T., Crum, L.A., Evan, A.P. and McAteer, J.A. 2003. Cavitation bubble cluster activity in the breakage of kidney stones by lithotripter shockwaves. *J. Endourol.* **17**(7), pp.435-446.

Plesset, M.S. 1949. The dynamics of cavitation bubbles. *ASME Journal of Applied Mechanics*. **16**, pp.228-231.

Pless, G., Sauer, I.M. and Rauen, U. 2012. Improvement of the cold storage of isolated human hepatocytes. *Cell Transplant*. **21**(1), pp.23-37.

Poling, B.E., Prausnitz, J.M. and O'Connell, J.P. 2004. *The properties of gases and liquids*. New York: McGraw-Hill.

Powles, R.L., Clink, H., Sloane, J., Barrett, A.J., Kay, H.E.M and Mcelwain, T.J. 1978. Cyclosporin A for the treatment of graft-versus-host disease in man. *The Lancet*. **312**(8104), pp.1327-1331.

Puppi, J., Strom, S.C., Hughes, R.D., Bansal, S., Castell, J.V., Dagher, I., Ellis, E.C., Nowak, G., Ericzon, B.G., Fox, I.J., Gómez-Lechón, M.J., Guha, C., Gupta, S., Mitry, R.R., Ohashi, K., Ott, M., Reid, L.M., Roy-Chowdhury, J., Sokal, E., Weber, A. and Dhawan, A. 2012. Improving the techniques for human hepatocyte transplantation: report from a consensus meeting in London. *Cell Transplant*. **21**(1), pp.1-10.

Quaglia, A., Lehec, S.C., Hughes, R.D., Mitry, R.R., Knisely, A.S., Devereaux, S., Richards, J., Rela, M., Heaton, N.D., Portmann, B.C. and Dhawan, A. 2008. Liver after hepatocyte transplantation for liver-based metabolic disorders in children. *Cell Transplantation*. **17**(12), pp.1403-1414.

Rahimi, P. and Ward, C.A. 2005. Kinetics of evaporation: statistical rate theory approach. *Int. J. Thermodynamics*. **8**(1), pp.1-14.

Ribes-Koninckx, C., Ibars, E.P., Calzado Agrasot, M.Á., Bonora-Centelles, A., Miquel, B.P., Vila Carbó, J.J., Aliaga, E.D., Pallardó, J.M., Gómez-Lechón, M.J. and Castell, J.V. 2012. Clinical outcome of hepatocyte transplantation in four pediatric patients with inherited metabolic diseases. *Cell Transplant*. **21**(10), pp.2267-2282.

Ritchie, R.W., Leslie, T., Phillips, R., Wu, F., Illing, R., ter Haar, G., Protheroe, A. and Cranston, D. 2010. Extracorporeal high intensity focused ultrasound for renal tumours: a 3-year follow-up. *BJU Int.* **106**(7), pp.1004-1009.

Rijkhorst, E.J., Rivens, I., ter Haar, G., Hawkes, D. and Barratt, D. 2011. Effects of respiratory liver motion on heating for gated and model-based motion-compensated high-intensity focused ultrasound ablation. *Proc. 14th Int. Conf. Medical Image Computing and Computer-Assisted Intervention (MICCAI), 18-22 September 2011, Toronto, Canada.* pp.605-612.

Roberts, W.W., Hall, T.L., Ives, K., Wolf, J.S., Fowlkes, J.B. and Cain, C.A. 2006. Pulsed cavitational ultrasound: a noninvasive technology for controlled tissue ablation (histotripsy) in the rabbit kidney. *J. Urol.* **175**(2), pp.734-738.

Samiei, E., Shams, M. and Ebrahimi, R. 2011. A novel numerical scheme for the investigation of surface tension effects on growth and collapse stages of cavitation bubbles. *Eur. J. Mech. B-Fluids.* **30**(1), pp.41-50

Sanghvi, N.T., Fry, F.J., Bihrle, R., Foster, R.S., Phillips, M.H., Syrus, J., Zaitsev, A.V. and Hennige, C.W. 1996. Noninvasive surgery of prostate tissue by high-intensity focused ultrasound. *IEEE Trans. Ultrason. Ferroelectr. Freq. Control.* **43**(6), pp.1099-1110.

Sapareto, S.A. and Dewey, W.C. 1984. Thermal dose determination in cancer therapy. *Int. J. Radiation Oncology Biol. Phys. Med.* **10**(6), pp.787-800.

Sboros, V., MacDonald, C.A., Pye, S.D., Moran, C.M., Gomatam, J. and McDicken, W.N. 2002. The dependence of ultrasound contrast agents backscatter on acoustic pressure: theory versus experiment. *Ultrasonics.* **40**(1), pp.579-583.

Schade, G.R., Hall, T.L. and Roberts, W.W. 2012a. Urethral-sparing histotripsy of the prostate in a canine model. *Urology*. **80**(3), pp.730-735.

Schade, G.R., Keller, J., Ives, K., Cheng, X., Rosol, T.J., Keller, E. and Roberts, W.W. 2012b. Histotripsy focal ablation of implanted prostate tumor in an ACE-1 canine cancer model. *J. Urol*. **188**(5), pp.1957-1964.

Schade, G.R., Maxwell, A.D., Khokhlova, T., Wang, Y.N., Sapoznikov, O., Bailey, M.R. and Khokhlova, V. 2014. Boiling histotripsy of the kidney: preliminary studies and predictors of treatment effectiveness. *J. Acoust. Soc. Am.* **136**(4), p.2251.

Schlachterman, A., Craft, W.W., Hilgenfeldt, E., Mitra, A. and Cabrera, R. 2015. Current and future treatments for hepatocellular carcinoma. *World J. Gastroenterol.* **21**(28), pp.8478-8491.

Schlicher, R.K., Hutcheson, J.D., Radhakrishna, H., Apkarian, R.P. and Prausnitz, M.R. 2010. Changes in cell morphology due to plasma membrane wounding by acoustic cavitation. *Ultrasound in Med. Biol*. **36**(4), pp.677-692.

Shung, K.K. and Thieme, G.A. 1992. *Ultrasonic scattering in biological tissues*. Florida: CRC Press.

Sigal, S.H., Rajvanshi, P., Gorla, G.R., Sokhi, R.P., Saxena, R., Gebhard, D.R., Reid, L.M. and Gupta, S. 1999. Partial hepatectomy-induced polyploidy attenuates hepatocyte replication and activates cell aging events. *Am. J. Physiol.* **276**(5), pp.1260-1272.

Simon, J.C. 2013. *The thresholds and mechanisms of tissue injury by focused ultrasound*. Ph.D. thesis, University of Washington.

Simon, J.C., Sapozhnikov, O.A., Khokhlova, V.A., Wang, Y.N., Crum, L.A. and Bailey, M.R. 2012. Ultrasonic atomization of tissue and its role in tissue fractionation by high intensity focused ultrasound. *Phys. Med. Biol.* **57**(23), pp.8061-8078.

Simon, J.C., Sapozhnikov, O.A., Wang, Y.N., Khokhlova, V.A., Crum, L.A. and Bailey, M.R. 2015. Investigation into the mechanisms of tissue atomization by high-intensity focused ultrasound. *Ultrasound in Med. Biol*. **41**(5), pp.1372-1385.

Sohlenius-Sternbeck, A.K. 2006. Determination of the hepatocellularity number for human, dog, rabbit, rat and mouse livers from protein concentration measurements. *Toxicol. In Vitro*. **20**(8), pp.1582-1586.

Sokal, E.M., Smets, F., Bourgois, A., Van Maldergem, L., Buts, J.P., Reding, R., Bernard Otte, J., Evrard, V., Latinne, D., Vincent, M.F., Moser, A. and Soriano, H.E. 2003. Hepatocyte transplantation in a 4-year-old girl with peroxisomal biogenesis disease: technique, safety, and metabolic follow-up. *Transplantation*. **76**(4), pp.735-738.

Solovchuk, M., Sheu, T.W.H. and Thiriet, M. 2015. Multiphysics modelling of liver tumor ablation by high intensity focused ultrasound. *Commun. Comput. Phys*. **18**(4), pp.1050-1071.

Soneson, J.E. 2009. A user-friendly software package for HIFU simulation. *AIP Conf. Proc. 8th Int. Symp. on Therapeutic Ultrasound (ISTU 2008), 10-13 September, 2008, Minneapolis, United States.* **1113**, pp.165-169.

Soneson, J.E. and Myers, M.R. 2007. Gaussian representation of high-intensity focused ultrasound beams. *J. Acoust. Soc. Am*. **122**(5), pp.2526-2531.

Starzl, T.E., Marchioro, T.L., Von kaulla, K.N., Hermann, G., Brittain, R.S. and Waddell, W.R. 1963. Homotransplantation of the liver in humans. *Surg. Gynecol. Obstet*. **117**, pp.659-676.

Stéphenne, X., Najimi, M., Sibille, C., Nassogne, M.C., Smets, F. and Sokal, E.M. 2006. Sustained engraftment and tissue enzyme activity after liver cell

transplantation for argininosuccinate lyase deficiency. *Gastroenterology*. **130**(4), pp.1317-1323.

Storey, B.D. and Szeri, A.J. 2000. Water vapour, sonoluminescence and sonochemistry. *Proc. R. Soc. London. A.* **456**(1999), pp.1685-1709.

Stricker, L., Prosperetti, A. and Lohse, D. 2011. Validation of an approximate model for the thermal behavior in acoustically driven bubbles. *J. Acoust. Soc. Am.* **130**(5), pp.3243-3251.

Strom, S.C., Bruzzone, P., Cai, H., Ellis, E., Lehmann, T., Mitamura, K. and Miki, T. 2006. Hepatocyte transplantation: clinical experience and potential for future use. *Cell transplantation.* **15**(Suppl 1), pp.105-110.

Strom, S.C., Fisher, R.A., Thompson, M.T., Sanyal, A.J., Cole, P.E., Ham, J.M. and Posner, M.P. 1997a. Hepatocyte transplantation as a bridge to orthotopic liver transplantation in terminal liver failure. *Transplantation.* **63**(4), pp.559-569.

Strom, S.C., Fisher, R.A., Rubinstein, W.S., Barranger, J.A., Towbin, R.B., Charron, M., Mieles, L., Pisarov, L.A., Dorko, K., Thompson, M.T. and Reyes, J. 1997b. Transplantation of human hepatocytes. *Transplant. Proc*. **29**(4), pp.2103-2106.

Styn, N.R., Wheat, J.C., Hall, T.L. and Roberts, W.W. 2010. Histotripsy of vx-2 tumor implanted in a renal rabbit model. *J. Endourol*. **24**(7), pp.1145-1150.

Sullivan, D.A. 1981. Historical review of real-fluid isentropic flow models. *J. Fluids Eng.* **103**(2), pp.258-267.

ter Haar, G. 1995. Ultrasound focal beam surgery. *Ultrasound in Med. Biol*. **21**(9), pp.1089-1100.

ter Haar, G. 2015. Ultrasound bio-effects and safety considerations. In: Alonso, A., Hennerici, M.G. and Meairs, S. ed. *Translational neurosonology*. Basel: Karger, pp.23-30.

ter Haar, G. and Coussios, C. 2007. High intensity focused ultrasound: physical principles and devices. *Int. J. Hyperthermia*. **23**(2), pp.89-104.

Tezel, A. and Mitragotri, S. 2003. Interactions of inertial cavitation bubbles with stratum corneum lipid bilayers during low-frequency sonophoresis. *Biophysical Journal*. **85**(6), pp.3502-3512.

Toegel, R., Gompf, B., Pecha, R. and Lohse, D. 2000. Does water vapor prevent upscaling sonoluminescence? *Phys. Rev. Lett.* **85**(15), pp.3165-3168.

Toegel, R. and Lohse, D. 2003. Phase diagrams for sonoluminescing bubbles: a comparison between experiment and theory. *J. Chem. Phys.* **118**(4), pp.1863-1875.

Treeby, B.E. and Cox, B.T. 2010. k-Wave: MATLAB toolbox for the simulation and reconstruction of photoacoustic wave fields. *Journal of biomedical optics*. **15**(2), pp.021314.

Treeby, B.E., Jaros, J., Rendell, A.P. and Cox, B.T. 2012. Modeling nonlinear ultrasound propagation in heterogeneous media with power law absorption using a k-space pseudospectral method. *J. Acoust. Soc. Am.* **131**(6), pp.4324-4336.

Trilling, L. 1952. The collapse and rebound of a gas bubble. *J. Appl. Phys.* **23**(1), pp.14-17.

Tu, J., Matula, T.J., Brayman, A.A. and Crum, L.A. 2006a. Inertial cavitation dose produced in ex vivo rabbit ear arteries with optison® by 1-MHz pulsed ultrasound. *Ultrasound in Med. Biol.* **32**(2), pp.281-288.

Tu, J., Hwang, J.H., Matula, T.J., Brayman, A.A and Crum, L.A. 2006b. Intravascular inertial cavitation activity detection and quantification in vivo with optison. *Ultrasound in Med. Biol.* **32**(10), pp.1601-1609.

Turner, R.A., Wauthier, E., Lozoya, O., McClelland, R., Bowsher, J.E., Barbier, C., Prestwich, G., Hsu, E., Gerber, D.A. and Reid, L.M. 2013. Successful transplantation of human hepatic stem cells with restricted localization to liver using hyaluronan grafts. *Hepatology*. **57**(2), pp.775-784.

Turner, R., Lozoya, O., Wang, Y., Cardinale, V., Gaudio, E., Alpini, G., Mendel, G., Wauthier, E., Barbier, C., Alvaro, D. and Reid, L.M. 2011. Human hepatic stem cell and maturational liver lineage biology. *Hepatology*. **53**(3), pp.1035-1045.

Uddin Ahmed, H., Cathcart, P., Chalasani, V., Williams, A., McCartan, N., Freeman, A., Kirkham, A., Allen, C., Chin, J. and Emberton, M. 2012. Whole-gland salvage high-intensity focused ultrasound therapy for localized prostate cancer recurrence after external beam radiation therapy. *Cancer*. **118**(12), pp.3071-3078.

Vaezy, S., Andrew, M., Kaczkowski, P. and Crum, L. 2001. Image-guided acoustic therapy. *Annu. Rev. Biomed. Eng*. **3**(1), pp.375-390.

Vaezy, S. and Zderic, V. 2009. *Image-guided therapy systems*. Massachusetts: Artech House.

Vargaftik, N.B., Volkov, B.N and Voljak, L.D. 1983. International tables of the surface tension of water. *J. Phys. Chem. Ref. Data.* **12**(3), pp.817-820.

Vlaisavljevich, E., Kim, Y., Allen, S., Owens, G., Pelletier, S., Cain, C., Ives, K. and Xu, Z. 2013. Image-guided non-invasive ultrasound liver ablation using histotripsy: feasibility study in an in vivo porcine model. *Ultrasound in Med. Biol.* **39**(8), pp.1398-1409.

Vlaisavljevich, E., Kim, Y., Owens, G., Roberts, W., Cain, C. and Xu, Z. 2014. Effects of tissue mechanical properties on susceptibility to histotripsy-induced tissue damage. *Phys. Med. Biol*. **59**(2), pp.253-270.

Vokurka, K. 1986. Comparison of Rayleigh's, Herring's, and Gilmore's models of gas bubbles. *Acta. Acust. United Ac.* **59**(3), pp.214-219.

Voogt, M.J., Trillaud, H., Kim, Y.S., Mali, W.P., Barkhausen, J., Bartels, L.W., Deckers, R., Frulio, N., Rhim, H., Lim, H.K., Eckey, T., Nieminen, H.J., Mougenot, C., Keserci, B., Soini, J., Vaara, T., Köhler, M.O., Sokka, S. and Bosch, M. 2012 Volumetric feedback ablation of uterine fibroids using magnetic resonance-guided high intensity focused ultrasound therapy. *Eur. Radiol.* **22**(2), pp.411-417.

Wagner, W. and Pruß, A. 2002. The IAPWS formulation 1995 for the thermodynamic properties of ordinary water substance for general and scientific use. *J. Phys. Chem. Ref. Data.* **31**(2), pp.387-535.

Wainwright, D.J. 1995. Use of an acellular allograft dermal matrix (AlloDerm) in the management of full-thickness burns. *Burns*. **21**(4), pp.243-248.

Wang, K., Teoh, E., Jaros, J. and Treeby, B.E. 2012. Modelling nonlinear ultrasound propagation in absorbing media using the k-Wave toolbox: experimental validation. *IEEE Int. Ultrason. Symp., 7-10 October, Dresden, Germany.* pp.523-526.

Wang, Y.N., Khokhlova, T., Bailey, M., Hwang, J.H. and Khokhlova, V. 2013. Histological and biochemical analysis of mechanical and thermal bioeffects in boiling histotripsy lesions induced by high intensity focused ultrasound. *Ultrasound in Med. Biol.* **39**(3), pp.424-438.

Ward, C.A. and Fang, G. 1999. Expression for predicting liquid evaporation flux: statistical rate theory approach. *Physical Review E*. **59**(1), pp.429-440.

Watkin, N.A., ter Haar, G.R. and Rivens, I. 1996. The intensity dependence of the site of maximal energy deposition in focused ultrasound surgery. *Ultrasound in Med. Biol.* **22**(4), pp.483-491.

Webb, I.R., Payne, S.J. and Coussios, C.C. 2011. The effect of temperature and viscoelasticity on cavitation dynamics during ultrasonic ablation. *J. Acoust. Soc. Am.* **130**(5), pp.3458-3466.

Wells, P.N.T. 1975. Absorption and dispersion of ultrasound in biological tissue. *Ultrasound in Med. Biol*. **1**(4), pp.369-376.

Wojcik, G., Mould, J.J., Lizzi, F., Abboud, N., Ostromogilsky, M. and Vaughan, D. 1995. Nonlinear modeling of therapeutic ultrasound. *IEEE Int. Ultrason. Symp., 7-10 November 1995, Seattle, United States.* **2**, pp.1617-1622.

Wu, F., Wang, Z.B., Chen, W.Z., Zhu, H., Bai, Jin., Zou, J.Z., Li, K.Q., Jin, C.B., Xie, F.L. and Su, H.B. 2004. Extracorporeal high intensity focused ultrasound ablation in the treatment of patients with large hepatocellular carcinoma. *Ann. Surg. Oncol.* **11**(12), pp.1061-1069.

Xu, J., Bigelow, T.A. and Nagaraju, R. 2013. Precision control of lesions by high-intensity focused ultrasound cavitation based histotripsy through varying pulse duration. *IEEE Trans. Ultrason. Ferroelect. Freq. Control.* **60**(7), pp.1401-1411.

Xu, J., Bigelow, T.A. and Riesberg, G.M. 2012. Impact of preconditioning pulse on lesion formation during high-intensity focused ultrasound histotripsy. *Ultrasound in Med. Biol*. **38**(11), pp.1918-1929.

Xu, Z., Owens, G., Gordon, D., Cain, C. and Ludomirsky, A. 2010. Noninvasive creation of an atrial septal defect by histotripsy in a canine model. *Circulation*. **121**(6), pp.742-749.

Yahya, W., Kadri, N. and Ibrahim, F. 2014. Cell patterning for liver tissue engineering via dielectrophoretic mechanisms. *Seonsors.* **14**(7), pp.11714-11734.

Yang, X. and Church, C.C. 2005. A model for the dynamics of gas bubbles in soft tissue. *J. Acoust. Soc. Am*. **118**(6), pp.3595-3606.

Yasui, K. 1995. Effects of thermal conduction on bubble dynamics near the sonoluminescence threshold. *J. Acoust. Soc. Am.* **98**(5), pp.2772-2782.

Yasui, K. 1997. Chemical reactions in a sonoluminescing bubble. *J. Phys. Soc. Jpn.* **66**(9), pp.2911-2920.

Yu, T., Xiong, S., Mason, T.J. and Wang, Z. 2006. The use of a microbubble agent to enhance rabbit liver destruction using high intensity focused ultrasound. *Ultrasonics Sonochemistry.* **13**(2), pp.143-149.

Zhang, K.Y., Tung, B.Y. and Kowdley, K.V. 2007. Liver transplantation for metabolic liver diseases. *Clin. Liver Dis.* **11**(2), pp.265-281.

Zhou, H., Dong, X., Kabarriti, R., Chen, Y., Avsar, Y., Wang, X., Ding, J., Liu, L., Fox, I.J., Roy-Chowdhury, J., Roy-Chowdhury, N. and Guha, C. 2012. Single liver lobe repopulation with wildtype hepatocytes using regional hepatic irradiation cures jaundice in gunn rats. *PLOS ONE*. **7**(10), pp.1-7.

Zhou, Y. and Gao X.W. 2013. Variations of bubble cavitation and temperature elevation during lesion formation by high-intensity focused ultrasound. *J. Acoust. Soc. Am.* **134**(2), pp.1683-1694.

Zhou, Y., Kargl, S.G. and Hwang, J.H. 2011. The effect of the scanning pathway in high-intensity focused ultrasound therapy on lesion production. *Ultrasound in Med. Biol.* **37**(9), pp.1457-1468.

Zhou, Y. 2015. *Principles and applications of therapeutic ultrasound in healthcare.* New York: CRC Press.

Zhu, S., Cocks, F.H., Preminger, G.M. and Zhong, P. 2002. The role of stress waves and cavitation in stone comminution in shock wave lithotripsy. *Ultrasound in Med. Biol.* **28**(5), pp. 661-671.

Appendix A. Nondimensionalisation

The physical parameters used in the numerical bubble model described in Chapter 3 were nondimensionalised according to the following scheme:

$$\text{Length}\,(\mathrm{L}) = R_0; \quad \text{Temperature}\,(\theta) = T_0; \quad \text{Time}\,(\mathrm{T}) = (2\pi f_0)^{-1};$$

$$\text{Mole}\,(\mathrm{MOL}) = n_{0,\text{total}}; \quad \text{Mass}\,(\mathrm{M}) = R_{\text{gas}}\theta\,\mathrm{MOL}\,\mathrm{T}^2\mathrm{L}^{-2}$$

A superscript $*$ denotes nondimensionalised parameters.

$$R_0^* = R_0\frac{1}{\mathrm{L}}; \quad \dot{R}_0^* = \dot{R}_0\frac{\mathrm{T}}{\mathrm{L}}; \quad T_0^* = T_0\frac{1}{\theta}; \quad \rho_0^* = \rho_0\frac{\mathrm{L}^3}{\mathrm{M}}; \quad \rho_{\text{vap}}^{\text{sat}*} = \rho_{\text{vap}}^{\text{sat}}\frac{\mathrm{L}^3}{\mathrm{M}}; \quad \mu_0^* = \mu_0\frac{\mathrm{LT}}{\mathrm{M}};$$
$$\sigma_0^* = \sigma_0\frac{\mathrm{T}^2}{\mathrm{M}}; \quad c_0^* = c_0\frac{\mathrm{T}}{\mathrm{L}}; \quad p_0^* = p_0\frac{\mathrm{LT}^2}{\mathrm{M}}; \quad p_a^* = p_a\frac{\mathrm{LT}^2}{\mathrm{M}}; \quad f_0^* = f_0\,\mathrm{T};$$

$$n_{0,\mathrm{N}_2}^* = n_{0,\mathrm{N}_2}\frac{1}{\mathrm{MOL}}; \quad n_{0,\mathrm{O}_2}^* = n_{0,\mathrm{O}_2}\frac{1}{\mathrm{MOL}}; \quad n_{0,\mathrm{Ar}}^* = n_{0,\mathrm{Ar}}\frac{1}{\mathrm{MOL}}; \quad n_{0,\text{vap}}^* = n_{0,\text{vap}}\frac{1}{\mathrm{MOL}};$$
$$a_{\text{air}}^* = a_{\text{air}}\frac{\mathrm{T}^2\mathrm{MOL}^2}{\mathrm{ML}^5}; \quad a_{\text{vap}}^* = a_{\text{vap}}\frac{\mathrm{T}^2\mathrm{MOL}^2}{\mathrm{ML}^5}; \quad b_{\text{air}}^* = b_{\text{air}}\frac{\mathrm{MOL}}{\mathrm{L}^3}; \quad b_{\text{vap}}^* = b_{\text{vap}}\frac{\mathrm{MOL}}{\mathrm{L}^3};$$

$$\alpha_{\text{air}}^* = \alpha_{\text{air}}\frac{\mathrm{T}^3\theta^2}{\mathrm{ML}}; \quad \alpha_{\text{vap}}^* = \alpha_{\text{vap}}\frac{\mathrm{T}^3\theta^2}{\mathrm{ML}}; \quad \beta_{\text{air}}^* = \beta_{\text{air}}\frac{\mathrm{T}^3\theta}{\mathrm{ML}}; \quad \beta_{\text{vap}}^* = \beta_{\text{vap}}\frac{\mathrm{T}^3\theta}{\mathrm{ML}};$$
$$R_{\text{gas}}^* = R_{\text{gas}}\frac{\mathrm{MOLT}^2\theta}{\mathrm{ML}^2}; \quad K_{\mathrm{B}}^* = K_{\mathrm{B}}\frac{\mathrm{T}^2\theta}{\mathrm{ML}^2}; \quad N_{\mathrm{A}}^* = N_{\mathrm{A}} = \frac{N_{\mathrm{A}}}{\mathrm{MOL}}; \quad M_{\text{air}}^* = M_{\text{air}}\frac{\mathrm{MOL}}{\mathrm{M}};$$

$$M_{\text{vap}}^* = M_{\text{vap}}\frac{\mathrm{MOL}}{\mathrm{M}}; \quad M_{\mathrm{N}_2}^* = M_{\mathrm{N}_2}\frac{\mathrm{MOL}}{\mathrm{M}}; \quad M_{\mathrm{O}_2}^* = M_{\mathrm{O}_2}\frac{\mathrm{MOL}}{\mathrm{M}}; \quad M_{\mathrm{Ar}}^* = M_{\mathrm{Ar}}\frac{\mathrm{MOL}}{\mathrm{M}};$$
$$K_{\mathrm{H},\mathrm{O}_2}^* = K_{\mathrm{H},\mathrm{O}_2}\frac{\mathrm{T}^2\mathrm{MOL}}{\mathrm{L}^2\mathrm{M}}; \quad K_{\mathrm{H},\mathrm{N}_2}^* = K_{\mathrm{H},\mathrm{N}_2}\frac{\mathrm{T}^2\mathrm{MOL}}{\mathrm{L}^2\mathrm{M}}; \quad K_{\mathrm{H,Ar}}^* = K_{\mathrm{H,Ar}}\frac{\mathrm{T}^2\mathrm{MOL}}{\mathrm{L}^2\mathrm{M}};$$

$$D_{\mathrm{O}_2}^* = D_{\mathrm{O}_2}\frac{\mathrm{T}}{\mathrm{L}^2}; \quad D_{\mathrm{N}_2}^* = D_{\mathrm{N}_2}\frac{\mathrm{T}}{\mathrm{L}^2}; \quad D_{\mathrm{Ar}}^* = D_{\mathrm{Ar}}\frac{\mathrm{T}}{\mathrm{L}^2};$$
$$C_{\infty,\mathrm{O}_2}^* = C_{\infty,\mathrm{O}_2}\frac{\mathrm{L}^3}{\mathrm{MOL}}; \quad C_{\infty,\mathrm{N}_2}^* = C_{\infty,\mathrm{N}_2}\frac{\mathrm{L}^3}{\mathrm{MOL}}; \quad C_{\infty,\mathrm{Ar}}^* = C_{\infty,\mathrm{Ar}}\frac{\mathrm{L}^3}{\mathrm{MOL}}.$$

Appendix B. Programme codes

This appendix contains listings for the following programmes.

Programme	Description
waveform_from_KZK.m	MATLAB® code for replicating a simulated waveform (obtained from the HIFU Simulator 1.2) for a given number of acoustic cycles.
NGA_modeling_main_Air_h20.m	main MATLAB® code for numerically solving the bubble model described in Chapter 3.
NEOM_air_h20.m	MATLAB® code for solving the bubble model in the case of a sinusoidal excitation.
KZKNEOM_air_h20.m	MATLAB® code for solving the bubble model in the case of a shockwave excitation.

waveform_from_KZK.m

```
f=1.1e6; %driving ultrasonic frequency
XX=Xpeak; %acoustic waveform obtained from the HIFU Simulator 1.2
XX=1E-6*p0*XX*1E6; %dimensionalise acoustic pressure
cycles=100; %a number of acoustic cycles used
XX=repmat(XX,1,cycles);
timeXX=linspace(0,cycles/f,length(XX));
```

NGA_modeling_main_Air_h20.m

```
R0=1e-6; %initial bubble radius
Rdot0=0; %initial bubble wall velocity
T0=373.15; %ambient temperature
r=0.064; %a distance away from the centre of a bubble
f=1.1e6;
omega=2*pi*f; %angular frequency
cycles=100;
t_max=cycles/f;
fs=20000*f; %sampling frequency
delt=1/fs; %time-step

P0=1.01325*10^5; %ambient pressure
Pa=15e6;%acoustic pressure

m=5.527; %medium-dependent empirical constant
A=614.6e6; % medium-dependent empirical constant
B=A-P0; % medium-dependent empirical constant

O=1-T0/647.096;
o=T0-273.16;
sigma=0.2358*O^(1.256)*(1-0.625*O)*(0.056/0.07275); %liver surface tension
c=(1.40238744e3+5.03836171*o-5.81172916e-2*o^2+3.34638117e-4*o^3-1.48259672e-
6*o^4+3.16585020e-9*o^5)*(1575/1482.3); %speed of sound in liver as a function of temperature
```

```
rho=1000*(1-(T0-273.15-4)^2/(119000+1365*(T0-273.15)-4*(T0-273.15)^2))*(1060/1000);  %density of liver as a function of temperature
mu=1.779*(1.0019e-3)/(1+0.03367*(T0-273.15)+2.2099e-4*(T0-273.15)^2)*(9/1.046); %viscosity of liver as a function of temperature
rho_sat=322*exp(-2.03150240*O^(1/3)-2.68302940*O^(2/3)-5.38626492*O^(4/3)-17.2991605*O^(3)-44.7586581*O^(37/6)-63.9201063*O^(71/6)); %saturated density of water vapour.

%constants for the gas dynamics
Rgas=8.3144621; %universal gas constant
NA=6.02214179e23; %Avogadro's number
Kb=1.3806488e-23; %Boltzmann constant
Mair=28.97e-3; %molar mass of air
MN2=28e-3; %molar mass of nitrogen
M02=31.9988e-3; %molar mass of oxygen
Mar=39.95e-3; %molar mass of argon
Mh20=18.015268e-3; %molar mass of water vapour

theta_n2=3350; %characteristic vibrational temperature of N2
theta_02=2273; % characteristic vibrational temperature of O2
theta_h20_1=2295; % characteristic vibrational temperatures of H20
theta_h20_2=5255;
theta_h20_3=5400;

alpha_air=5.39e-5; %temperature dependent thermal conductivity of air
alpha_vap=9.98e-5; %temperature dependent thermal conductivity of H20
beta_air=0.0108; %thermal conductivity of air
beta_vap=-0.0119; %thermal conductivity of air

%number of molecules
Pv=610*exp((T0/273.16-1)*(22.486*(273.16/T0)+0.3182*T0/273.16-2.9558)); %vapour pressure
concentration_Nh20=Pv/(Kb*T0); %vapour molecules in the medium
Nvap0=concentration_Nh20*4*pi/3*R0^3; %vapour molecules in a bubble
Nair0=(P0*(4*pi/3*R0^3)/(Kb*T0)); %air molecules in a bubble

Nn2=Nair0*0.78; %number of N2 molecules
N02=Nair0*0.21; %number of O2 molecules
Nar=Nair0*0.01; %number of Ar molecules
N_tot=Nair0+Nvap0; %total number of molecules

%in moles
nair0=Nair0/(NA); %moles for air
nvap0=Nvap0/NA; %moles for H20
nn2=nair0*0.78; %moles for N2
n02=nair0*0.21; %moles for O2
nar=nair0*0.01; %moles for Ar
nair=nn2+n02+nar; %initial number of air moles
n_tot=nair+nvap0; %total number of moles

a_air=1.402e-1; %the Van der Waal constant a for air
a_h20=5.536e-1; %the Van der Waal constant a for H20
a_air_h20=sqrt(a_air*a_h20);
b_air=3.753e-5; %the Van der Waal constant b for air
b_h20=3.049e-5; %the Van der Waal constant b for H20

ln=@log;
Kh_N2=rho/(101325*MN2)*exp((-67.3877+86.3213/(T0/100)+24.7981*ln(T0/100))); %Henry's constant for N2
Kh_N2=1/Kh_N2;
Kh_02=rho/(101325*M02)*exp((-66.7354+87.4755/(T0/100)+24.4526*ln(T0/100))); %Henry's constant for O2
Kh_02=1/Kh_02;
Kh_Ar=rho/(101325*Mar)*exp((-57.6661+74.7627/(T0/100)+20.1398*ln(T0/100))); %Henry's constant for Ar
Kh_Ar=1/Kh_Ar;
```

```
C0_02=P0/Kh_02; %concentration of dissolved O2 in the medium
C0_N2=P0/Kh_N2; %concentration of dissolved N2 in the medium
C0_Ar=P0/Kh_Ar; %concentration of dissolved Ar in the medium

concentration=0.9;
Ci_02=C0_02*concentration; %physiological value of O2 concentration
Ci_N2=C0_N2*concentration; %physiological value of N2 concentration
Ci_Ar=C0_Ar*concentration; %physiological value of Ar concentration

V_N2=18.5; %diffusion volume of N2
V_02=16.3; %diffusion volume of O2
V_Ar=16.2; %diffusion volume of Ar

D_02=14e-5/(((mu*1000)^1.1)*(V_02^0.6))*0.01*0.01; %diffusivity of O2
D_N2=14e-5/(((mu*1000)^1.1)*(V_N2^0.6))*0.01*0.01; %diffusivity of N2
D_Ar=14e-5/(((mu*1000)^1.1)*(V_Ar^0.6))*0.01*0.01; %diffusivity of Ar

%nondimensionalised parameters
L=R0; %length
TIME=1/(omega); %time
MOL=n_tot; %mole
theta=T0; %temperature
M=Rgas*MOL*TIME^2*theta/L^2; %mass

nrho=rho*L^3/M;
nrho_sat=rho_sat*L^3/M;
nT0=T0/theta;
nmu=mu*L*TIME/M;
nR0=R0/L;
nr=r/L;
nRdot=Rdot0*TIME/L;
nP0=P0*L*TIME^2/M;
nf=f*TIME;
nsigma=sigma*TIME^2/M;
nPa=Pa*L*TIME^2/M;
nomega=2*pi*nf;
nA=A*L*TIME^2/M;
nB=B*L*TIME^2/M;
nc=c*TIME/L;

nnn2=nn2/MOL;
nn02=n02/MOL;
nnvap0=nvap0/MOL;
nnar=nar/MOL;
nn_tot=n_tot/MOL;

na_air=a_air*TIME^2*MOL^2/(M*L^5);
na_h20=a_h20*TIME^2*MOL^2/(M*L^5);
na_air_h20=sqrt(na_air*na_h20);
nb_air=b_air*MOL/L^3;
nb_h20=b_h20*MOL/L^3;
nb_air_h20=(0.5*(nb_air^(1/3)+nb_h20^(1/3)))^(1/3);

ntheta_n2=theta_n2/theta;
ntheta_02=theta_02/theta;
ntheta_h20_1=theta_h20_1/theta;
ntheta_h20_2=theta_h20_2/theta;
ntheta_h20_3=theta_h20_3/theta;

nRgas=Rgas*MOL*TIME^2*theta/(M*L^2);
nKb=Kb*TIME^2*theta/(M*L^2);
nNA=NA*MOL;
nMair=Mair*MOL/M;
nMh20=Mh20*MOL/M;
```

```
nMN2=MN2*MOL/M;
nM02=M02*MOL/M;
nMAr=Mar*MOL/M;

nalpha_air=alpha_air*TIME^3*theta^2/(M*L);
nalpha_vap=alpha_vap*TIME^3*theta^2/(M*L);
nbeta_air=beta_air*TIME^3*theta/(M*L);
nbeta_vap=beta_vap*TIME^3*theta/(M*L);

nKh_02=Kh_02*TIME^2*MOL/(L^2*M);
nKh_N2=Kh_N2*TIME^2*MOL/(L^2*M);
nKh_Ar=Kh_Ar*TIME^2*MOL/(L^2*M);

nD_02=D_02*TIME/L^2;
nD_N2=D_N2*TIME/L^2;
nD_Ar=D_Ar*TIME/L^2;

nCi_02=Ci_02*L^3/MOL;
nCi_N2=Ci_N2*L^3/MOL;
nCi_Ar=Ci_Ar*L^3/MOL;

kzkPac=XX;
nkzkPac=kzkPac*L*TIME^2/M;%
kzktime=timeXX;
nkzktime=kzktime/TIME;

%solver%%%
```

```
Ntot_kzk=nh20_kzk+n02_kzk+nN2_kzk+nAr_kzk; %with simulated waves
Nair_sin=(n02_sin+nN2_sin+nAr_sin).*nNA; %air molecules with sine waves
Nair_kzk=(n02_kzk+nN2_kzk+nAr_kzk).*nNA; %with simulated waves
Nh20_sin=nh20_sin.*nNA; %H20 molecules with sine waves
Nh20_kzk=nh20_kzk.*nNA; %with simulated waves
vol_sin=(4*pi/3)*SIN_Bubbledynamic.^3; %bubble volume(t) with sine waves
vol_kzk=(4*pi/3)*KZK_Bubbledynamic.^3; %with simulated waves
v_mix_sin=nNA*vol_sin./Ntot_sin; %molar mixture volume with sine waves
v_mix_kzk=nNA*vol_kzk./Ntot_kzk; %with simulated waves
a_sin=na_air*((Nair_sin)./(Ntot_sin)).^2+2*na_air_h20*((Nair_sin)./Ntot_sin).*(Nh20_sin./Ntot_sin)+na_h2
0*(Nh20_sin./Ntot_sin).^2;
a_kzk=na_air*((Nair_kzk)./(Ntot_kzk)).^2+2*na_air_h20*((Nair_kzk)./Ntot_kzk).*(Nh20_kzk./Ntot_kzk)+n
a_h20*(Nh20_kzk./Ntot_kzk).^2;
b_sin=nb_air*(Nair_sin./Ntot_sin).^2+2*nb_air_h20*(Nair_sin./Ntot_sin).*(Nh20_sin./Ntot_sin)+nb_h20*(
Nh20_sin./Ntot_sin).^2;
b_kzk=nb_air*(Nair_kzk./Ntot_kzk).^2+2*nb_air_h20*(Nair_kzk./Ntot_kzk).*(Nh20_kzk./Ntot_kzk)+nb_h2
0*(Nh20_kzk./Ntot_kzk).^2;
nPg_initial_sin=nRgas*temp_sin./(v_mix_sin-b_sin)-a_sin./(v_mix_sin).^2; %pressure(t) inside the bubble
with sine waves
nPg_initial_kzk=nRgas*temp_kzk./(v_mix_kzk-b_kzk)-a_kzk./(v_mix_kzk).^2; %with simulated waves
Pw_sin=nPg_initial_sin-2*nsigma./SIN_Bubbledynamic-
4*nmu*SIN_Wall_velocity./SIN_Bubbledynamic; %pressure at bubble wall
Pw_kzk=nPg_initial_kzk-2*nsigma./KZK_Bubbledynamic-
4*nmu*KZK_Wall_velocity./KZK_Bubbledynamic; %pressure at bubble wall

nPac_sin=-nPa*sin(nomega*time);
T=linspace(delt,max(t_max),length(nkzkPac));
nPac_kzk=interp1(T,nkzkPac,linspace(delt,max(t_max),length(Pw_kzk)));

H_sin=m/(m-1)*nA^(1/m)/nrho*((Pw_sin+nB).^((m-1)/m)-(nP0+nPac_sin+nB).^((m-1)/m));
H_kzk=m/(m-1)*nA^(1/m)/nrho*((Pw_kzk+nB).^((m-1)/m)-(nP0+nPac_kzk'+nB).^((m-1)/m));
G_sin=SIN_Bubbledynamic.*(H_sin+0.5*((SIN_Wall_velocity).^2));
G_kzk=KZK_Bubbledynamic.*(H_kzk+0.5*((KZK_Wall_velocity).^2));

Pr_sin=nA*((2/(m+1)+((m-1)/(m+1))*(1+(G_sin.*(m+1)./(nr*(nc^2)))).^(0.5)).^((2*m)/(m-1)))-
nB; %radiated pressure
Pr_kzk=nA*((2/(m+1)+((m-1)/(m+1))*(1+(G_kzk.*(m+1)./(nr*(nc^2)))).^(0.5)).^((2*m)/(m-1)))-
nB; %radiated pressure
Pr_sin=Pr_sin*M/(L*TIME^2); %dimensionalise radiated pressure
Pr_kzk=Pr_kzk*M/(L*TIME^2); %dimensionalise radiated pressure

%Fast fourier transform FFT
dt_sin=t_max/length(Pr_sin);
dt_kzk=t_max/length(Pr_kzk);
df_sin=1/((length(Pr_sin))*dt_sin);
df_kzk=1/((length(Pr_kzk))*dt_kzk);
aa_sin=fft(Pr_sin,length(Pr_sin));
aa_kzk=fft(Pr_kzk,length(Pr_kzk));
nn_sin=1:length(Pr_sin)/2;
nn_kzk=1:length(Pr_kzk)/2;
xx_sin=nn_sin*df_sin;
xx_kzk=nn_kzk*df_kzk;
PP_sin=(aa_sin).*conj(aa_sin);
PP_kzk=(aa_kzk).*conj(aa_kzk);

%Figure%%%
```

```
figure(3)
plot(realtime*1e6,nh20_sin*MOL*NA/Nvap0);
title('SIN water h20'); ylabel('Normalised_number of vapour molecules'); xlabel('time[\mus]'); axis('tight')
figure(4)
plot(realtime*1e6,(nN2_sin+n02_sin+nAr_sin)*MOL*NA/Nair0);
title('SIN gas (N2+o2+Ar)'); ylabel('normalized number of air molecules'); xlabel('time[\mus]'); axis('tight')
figure(5)
plot(realtime*1e6,temp_sin*theta);
title('sin Temp'); xlabel('time[\mus]'); ylabel('Temperature [K]'); axis('tight')
figure(6)
plot(realtime*1e6,Pr_sin/1e6);
title('SIN Radiated pressure at r'); xlabel('time[\mus]'); ylabel('Radiated pressure [MPa]'); axis('tight')
figure(7)
plot(xx_sin,PP_sin(1:length(Pr_sin)/2));
title('FFT sin scattered pressure'); xlabel('Frequency [Hz]'); ylabel('FFT amplitude'); axis('tight')

%Simulated wave excitation case
rrealtime=timetime*TIME;
figure(8)
plot(rrealtime*1e6,KZK_Bubbledynamic*L*1e6);
title('KZK Radius'); xlabel('time [\mus]'); ylabel('Radius [\mum]'); axis('tight')
figure(9)
plot(rrealtime*1e6,KZK_Wall_velocity*L/TIME);
title('KZK wall velocity'); xlabel('time [\mus]'); ylabel('wall velocity [m/s]'); axis('tight')
figure(10)
plot(rrealtime*1e6,nh20_kzk*MOL*NA/Nvap0);
title('KZK water h20'); ylabel('Normalised number of vapour molecules'); xlabel('time[\mus]'); axis('tight')
figure(11)
plot(rrealtime*1e6,(nN2_kzk+n02_kzk+nAr_kzk)*MOL*NA/Nair0);
title('KZK gas (N2+o2+Ar)'); ylabel('normalized number of air molecules'); xlabel('time[\mus]'); axis('tight')
figure(12)
plot(rrealtime*1e6,temp_kzk*theta);
title('KZK Temp'); xlabel('time[\mus]'); ylabel('Temperature [K]'); axis('tight')
figure(13)
plot(rrealtime*1e6,Pr_kzk/1e6);
title('KZK Radiated pressure at r'); xlabel('time[\mus]'); ylabel('Radiated pressure [MPa]'); axis('tight')
figure(14)
plot(xx_kzk,PP_kzk(1:length(Pr_kzk)/2));
title('FFT,kzk scattered pressure'); xlabel('Frequency [Hz]'); ylabel('FFT amplitude'); axis('tight')
%%%%%%%%%%%%%%%%%%%%%%%%%%%%%%%%%%%%%%%%%%%%%%%%%%%%%%%%%%%%%%%%%%%%%%%%%%%%
```

NEOM_air_h20.m

```
function [bubble_dyn]=NEOM_air_h20(t,r)
m=evalin('base','m');
nc=evalin('base','nc');
nrho=evalin('base','nrho');
nP0=evalin('base','nP0');
nmu=evalin('base','nmu');
nA=evalin('base','nA');
nB=evalin('base','nB');
nsigma=evalin('base','nsigma');
nomega=evalin('base','nomega');
nPa=evalin('base','nPa');
nnn2=evalin('base','nnn2');
nn02=evalin('base','nn02');
nnar=evalin('base','nnar');
nT0=evalin('base','nT0');
ntheta_n2=evalin('base','ntheta_n2');
ntheta_02=evalin('base','ntheta_02');
ntheta_h20_1=evalin('base','ntheta_h20_1');
ntheta_h20_2=evalin('base','ntheta_h20_2');
ntheta_h20_3=evalin('base','ntheta_h20_3');
nRgas=evalin('base','nRgas');
```

```
nKb=evalin('base','nKb');
nNA=evalin('base','nNA');
nMh20=evalin('base','nMh20');
nrho_sat=evalin('base','nrho_sat');
nalpha_air=evalin('base','nalpha_air');
nalpha_vap=evalin('base','nalpha_vap');
nbeta_air=evalin('base','nbeta_air');
nbeta_vap=evalin('base','nbeta_vap');
na_air=evalin('base','na_air');
na_h20=evalin('base','na_h20');
na_air_h20=evalin('base','na_air_h20');
nb_air=evalin('base','nb_air');
nb_h20=evalin('base','nb_h20');
nb_air_h20=evalin('base','nb_air_h20');
nKh_02=evalin('base','nKh_02');
nKh_N2=evalin('base','nKh_N2');
nKh_Ar=evalin('base','nKh_Ar');
nD_02=evalin('base','nD_02');
nD_N2=evalin('base','nD_N2');
nD_Ar=evalin('base','nD_Ar');
nCi_02=evalin('base','nCi_02');
nCi_N2=evalin('base','nCi_N2');
nCi_Ar=evalin('base','nCi_Ar');

bubble_dyn=zeros(7,1);
dR=zeros(7,1);

R=r(1); %R(t)
Rdot=r(2); %Rdot(t)
nh20=r(3); %nh2O(t)
nn02=r(4); %nO2(t)
nnn2=r(5); %nN2(t)
nnar=r(6);  %nAr(t)
T=r(7); %temp(t)

ntot=nh20+nn02+nnn2+nnar; %number of total mole inside the bubble
Ntot=ntot*nNA; %number of total molecules inside the bubble
Nh20=nh20*nNA; %number of h20 molecules inside the bubble
nair=nn02+nnn2+nnar; %number of air moles
Nair=nair*nNA; %number of air molecules
vol=(4*pi/3)*R^3; %bubble volume
vol_dot=4*pi*R^2*Rdot; %rate of bubble volume change
v_mix=nNA*vol/Ntot;%mixture molar volume
rho_h20=nMh20*(nh20/ntot)/v_mix; %density of h20 in the bubble

Cv_n2=nnn2*nNA*nKb*(5/2+(ntheta_n2/T)^2*(exp(ntheta_n2/T))/((exp(ntheta_n2/T)-1)^2)); %heat
capacity N2
Cv_n02=nn02*nNA*nKb*(5/2+(ntheta_02/T)^2*(exp(ntheta_02/T))/((exp(ntheta_02/T)-1)^2)); %heat
capacity O2
Cv_h20=nh20*nNA*nKb*(6/2+(((ntheta_h20_1/T)^2*(exp(ntheta_h20_1/T))/((exp(ntheta_h20_1/T)-
1)^2))+((ntheta_h20_2/T)^2*(exp(ntheta_h20_2/T))/((exp(ntheta_h20_2/T)-
1)^2))+((ntheta_h20_3/T)^2*(exp(ntheta_h20_3/T))/((exp(ntheta_h20_3/T)-1)^2)))); %heat capacity H2O
Cv_ar=nnar*nNA*nKb*3/2; %heat capacity Ar
Cv=Cv_n2+Cv_n02+Cv_h20+Cv_ar; %heat capacity of mixture

alpha=0.14; %accommodation coefficient for evaporation and condensation
Dnh20_DT=(4*pi*R^2*alpha/(nMh20)*(sqrt(8*nRgas*nT0/(pi*nMh20))/4)*(nrho_sat-rho_h20));   %change
of molar rate of H20

ramda_air=nalpha_air*T+nbeta_air; %temperature dependence thermal conductivity of air
ramda_vap=nalpha_vap*T+nbeta_vap; %temperature dependence thermal conductivity of H20
ramda_mixx=0.5*(((nh20/ntot)*ramda_vap+(nair/ntot)*ramda_air)+((nh20/ntot)/ramda_vap+(nair/ntot)/ramd
a_air)^(-1)); %temp. dependence thermal conductivity of mixture
a=na_air*((Nair)/(Ntot))^2+2*na_air_h20*((Nair)/Ntot)*(Nh20/Ntot)+na_h20*(Nh20/Ntot)^2;
```

```
b=nb_air*(Nair/Ntot)^2+2*nb_air_h20*(Nair/Ntot)*(Nh20/Ntot)+nb_h20*(Nh20/Ntot)^2;
B1=b/v_mix;
y=B1+0.6250*(B1)^2+0.2869*(B1)^3+0.115*(B1)^4;
ramda_mix=B1*(1/y+1.2+0.755*y)*ramda_mixx; %density dependence thermal conductivity of mixture

sp_n2=(7/2)*nKb*nnn2*nNA/vol; %specific heat capacity N2
sp_02=(7/2)*nKb*nn02*nNA/vol; %specific heat capacity O2
sp_ar=2.5*nKb*nnar*nNA/vol; %specific heat capacity Ar
sp_h20=(4)*nKb*nh20*nNA/vol; % specific heat capacity H20
sp=sp_n2+sp_02+sp_h20+sp_ar; % specific heat capacity mixture

X=ramda_mix/sp; %thermal diffusivity of mixture
Lth=min(R/pi,sqrt(R*X/(abs(Rdot)))); %thermal boundary layer
DQ_DT=4*pi*R^2*ramda_mix*(nT0-T)/Lth; %rate of heat transferred to the bubble
nPac=-nPa*sin(nomega*t); %sinusoidal excitation
nPg_initial=nRgas*T/(v_mix-b)-a/(v_mix)^2; %pressure inside the bubble
DPg_DR=-nRgas*T*((nNA/Ntot)*4*pi*R^3/3-b)^(-
2)*(4*pi*nNA/Ntot*R^2)+2*a*((nNA/Ntot)*4*pi*R^3/3)^(-3)*(4*pi*R^2*nNA/Ntot);

Pw=nPg_initial-2*nsigma/R-4*nmu*Rdot/R; %pressure at the bubble wall
DPw_DR=DPg_DR+2*nsigma/(R^2)+4*nmu*Rdot/(R^2);

H=m/(m-1)*nA^(1/m)/nrho*((Pw+nB)^((m-1)/m)-(nP0+nPac+nB)^((m-1)/m));%difference in liquid enthalpy
between the bubble wall and infinity
DH_DR=nA^(1/m)/nrho*(Pw+nB)^(-1/m)*DPw_DR;

C=sqrt((nc^2)+(m-1)*H); %speed of sound at the bubble wall

dR(1)= Rdot;

dR(2)=-3/2*(Rdot^2)/R*((1-Rdot/(3*C))/(1-Rdot/C))+1/R*((1+Rdot/C)/(1-Rdot/C))*H+1/C*Rdot*DH_DR;

dR(3)=Dnh20_DT;

nCs_02=nPg_initial*(nn02/ntot)/nKh_02; %saturated O2 concentration in liquid at the bubble wall
nCs_N2=nPg_initial*(nnn2/ntot)/nKh_N2; %saturated N2 concentration in liquid at the bubble wall
nCs_Ar=nPg_initial*(nnar/ntot)/nKh_Ar; %saturated Ar concentration in liquid at the bubble wall

Length_02=min(sqrt(R*nD_02/abs(Rdot)),R/pi); %diffusion boundary layer O2
Length_N2=min(sqrt(R*nD_N2/abs(Rdot)),R/pi); %diffusion boundary layer N2
Length_Ar=min(sqrt(R*nD_Ar/abs(Rdot)),R/pi); %diffusion boundary layer Ar

dR(4)=-4*pi*R^2*nD_02*(nCs_02-nCi_02)/Length_02;
dR(5)=-4*pi*R^2*nD_N2*(nCs_N2-nCi_N2)/Length_N2;
dR(6)=-4*pi*R^2*nD_Ar*(nCs_Ar-nCi_Ar)/Length_Ar;

A=(ntheta_h20_1/T)/(exp(ntheta_h20_1/T)-1); %h20
B=(ntheta_h20_2/T)/(exp(ntheta_h20_2/T)-1); %h20
C1=(ntheta_h20_3/T)/(exp(ntheta_h20_3/T)-1); %h20
D=(ntheta_n2/T)/(exp(ntheta_n2/T)-1); %n2
E=(ntheta_02/T)/(exp(ntheta_02/T)-1); %o2

AAA=-4*pi*R^2*nD_02*(nCs_02-nCi_02)/Length_02; %rate of change O2
BBB=-4*pi*R^2*nD_N2*(nCs_N2-nCi_N2)/Length_N2; %rate of change N2
CCC=-4*pi*R^2*nD_Ar*(nCs_Ar-nCi_Ar)/Length_Ar; %rate of change Ar
ar_loss=(5/2*nT0-3/2*T)*nKb*nNA*CCC; %energy loss due to Ar diffusion
h20_loss=(8/2*nT0-6/2*T-T*(A+B+C1))*nKb*nNA*Dnh20_DT; %H2O loss
n2_loss=(7/2*nT0-5/2*T-T*(D))*nKb*nNA*BBB; %N2 loss
o2_loss=(7/2*nT0-5/2*T-T*(E))*nKb*nNA*AAA; %O2 loss

dR(7)=DQ_DT/Cv-nPg_initial*vol_dot/Cv+(ar_loss+h20_loss+n2_loss+o2_loss)/Cv;
bubble_dyn = dR;
end
%%%
```

KZKNEOM_air_h20.m

```
function [KZKbubble_dyn]=KZKNEOM_air_h20(t,r)
m=evalin('base','m');
nc=evalin('base','nc');
nrho=evalin('base','nrho');
nP0=evalin('base','nP0');
nmu=evalin('base','nmu');
nA=evalin('base','nA');
nB=evalin('base','nB');
nsigma=evalin('base','nsigma');
nomega=evalin('base','nomega');
nPa=evalin('base','nPa');
nnn2=evalin('base','nnn2');
nn02=evalin('base','nn02');
nnar=evalin('base','nnar');
nT0=evalin('base','nT0');
ntheta_n2=evalin('base','ntheta_n2');
ntheta_02=evalin('base','ntheta_02');
ntheta_h20_1=evalin('base','ntheta_h20_1');
ntheta_h20_2=evalin('base','ntheta_h20_2');
ntheta_h20_3=evalin('base','ntheta_h20_3');
nRgas=evalin('base','nRgas');
nKb=evalin('base','nKb');
nNA=evalin('base','nNA');
nMh20=evalin('base','nMh20');
nrho_sat=evalin('base','nrho_sat');
nalpha_air=evalin('base','nalpha_air');
nalpha_vap=evalin('base','nalpha_vap');
nbeta_air=evalin('base','nbeta_air');
nbeta_vap=evalin('base','nbeta_vap');
na_air=evalin('base','na_air');
na_h20=evalin('base','na_h20');
na_air_h20=evalin('base','na_air_h20');
nb_air=evalin('base','nb_air');
nb_h20=evalin('base','nb_h20');
nb_air_h20=evalin('base','nb_air_h20');
nkzkPac=evalin('base','nkzkPac');
nkzktime=evalin('base','nkzktime');
nKh_02=evalin('base','nKh_02');
nKh_N2=evalin('base','nKh_N2');
nKh_Ar=evalin('base','nKh_Ar');
nD_02=evalin('base','nD_02');
nD_N2=evalin('base','nD_N2');
nD_Ar=evalin('base','nD_Ar');
nCi_02=evalin('base','nCi_02');
nCi_N2=evalin('base','nCi_N2');
nCi_Ar=evalin('base','nCi_Ar');

KZKbubble_dyn=zeros(7,1);
dR=zeros(7,1);

R=r(1); %R(t)
Rdot=r(2); %Rdot(t)
nh20=r(3); %nh2O(t)
nn02=r(4); %nO2(t)
nnn2=r(5); %nN2(t)
nnar=r(6);  %nAr(t)
T=r(7); %temp(t)
ntot=nh20+nn02+nnn2+nnar;
Ntot=ntot*nNA; %number of total molecules inside the bubble
Nh20=nh20*nNA; %number of h20 molecules inside the bubble
nair=nn02+nnn2+nnar; %number of air moles
Nair=nair*nNA; %number of air molecules
```

```
vol=(4*pi/3)*R^3; %bubble volume
vol_dot=4*pi*R^2*Rdot; %rate of bubble volume change
v_mix=nNA*vol/Ntot;%mixture molar volume
rho_h20=nMh20*(nh20/ntot)/v_mix; %density of h20 in the bubble

Cv_n2=nnn2*nNA*nKb*(5/2+(ntheta_n2/T)^2*(exp(ntheta_n2/T))/((exp(ntheta_n2/T)-1)^2)); %heat
capacity of N2
Cv_n02=nn02*nNA*nKb*(5/2+(ntheta_02/T)^2*(exp(ntheta_02/T))/((exp(ntheta_02/T)-1)^2)); %heat
capacity O2
Cv_h20=nh20*nNA*nKb*(6/2+(((ntheta_h20_1/T)^2*(exp(ntheta_h20_1/T))/((exp(ntheta_h20_1/T)-
1)^2))+((ntheta_h20_2/T)^2*(exp(ntheta_h20_2/T))/((exp(ntheta_h20_2/T)-
1)^2))+((ntheta_h20_3/T)^2*(exp(ntheta_h20_3/T))/((exp(ntheta_h20_3/T)-1)^2)))); %heat capacity H2O
Cv_ar=nnar*nNA*nKb*3/2; %heat capacity Ar
Cv=Cv_n2+Cv_n02+Cv_h20+Cv_ar; %heat capacity of mixture

alpha=0.14; %accommodation coefficient for evaporation and condensation
Dnh20_DT=(4*pi*R^2*alpha/(nMh20)*(sqrt(8*nRgas*nT0/(pi*nMh20))/4)*(nrho_sat-rho_h20)); %change
of molar rate of H20

ramda_air=nalpha_air*T+nbeta_air; %temperature dependence thermal conductivity of air
ramda_vap=nalpha_vap*T+nbeta_vap; %temperature dependence thermal conductivity of H20
ramda_mixx=0.5*(((nh20/ntot)*ramda_vap+(nair/ntot)*ramda_air)+((nh20/ntot)/ramda_vap+(nair/ntot)/ramd
a_air)^(-1)); %temp. dependence thermal conductivity of mixture
a=na_air*((Nair)/(Ntot))^2+2*na_air_h20*((Nair)/Ntot)*(Nh20/Ntot)+na_h20*(Nh20/Ntot)^2;
b=nb_air*(Nair/Ntot)^2+2*nb_air_h20*(Nair/Ntot)*(Nh20/Ntot)+nb_h20*(Nh20/Ntot)^2;
B1=b/v_mix;
y=B1+0.6250*(B1)^2+0.2869*(B1)^3+0.115*(B1)^4;
ramda_mix=B1*(1/y+1.2+0.755*y)*ramda_mixx; %density dependence thermal conductivity of mixture

sp_n2=(7/2)*nKb*nnn2*nNA/vol; %specific heat capacity N2
sp_02=(7/2)*nKb*nn02*nNA/vol; %specific heat capacity O2
sp_ar=2.5*nKb*nnar*nNA/vol; %specific heat capacity Ar
sp_h20=(4)*nKb*nh20*nNA/vol; % specific heat capacity H20
sp=sp_n2+sp_02+sp_h20+sp_ar; % specific heat capacity mixture

X=ramda_mix/sp; %thermal diffusivity of mixture
Lth=min(R/pi,sqrt(R*X/(abs(Rdot)))); %thermal boundary layer
DQ_DT=4*pi*R^2*ramda_mix*(nT0-T)/Lth; %rate of heat transferred to the bubble

nPac2=nkzkPac;
if  ~any(nkzktime - t)
    indx = (nkzktime - t)== 0;
    nPac2 = nkzkPac(indx);
else
    indx_low = find((nkzktime - t)<0,1,'last');
    indx_up  = find((nkzktime - t)>0,1,'first');
    nPac2 = interp1([nkzktime(indx_low) nkzktime(indx_up)],[nPac2(indx_low) nPac2(indx_up)],t);
end

nPg_initial=nRgas*T/(v_mix-b)-a/(v_mix)^2; %pressure inside the bubble
DPg_DR=-nRgas*T*((nNA/Ntot)*4*pi*R^3/3-b)^(-
2)*(4*pi*nNA/Ntot*R^2)+2*a*((nNA/Ntot)*4*pi*R^3/3)^(-3)*(4*pi*R^2*nNA/Ntot);

Pw=nPg_initial-2*nsigma/R-4*nmu*Rdot/R; %pressure at the bubble wall
DPw_DR=DPg_DR+2*nsigma/(R^2)+4*nmu*Rdot/(R^2);

H=m/(m-1)*nA^(1/m)/nrho*((Pw+nB)^((m-1)/m)-(nP0+nPac2+nB)^((m-1)/m));%difference in liquid
enthalpy between the bubble wall and infinity
DH_DR=nA^(1/m)/nrho*(Pw+nB)^(-1/m)*DPw_DR;
C=sqrt((nc^2)+(m-1)*H); %speed of sound at the bubble wall

dR(1)= Rdot;

dR(2)=-3/2*(Rdot^2)/R*((1-Rdot/(3*C))/(1-Rdot/C))+1/R*((1+Rdot/C)/(1-Rdot/C))*H+1/C*Rdot*DH_DR;
```

```
dR(3)=Dnh20_DT;

nCs_02=nPg_initial*(nn02/ntot)/nKh_02; %saturated O2 concentration in liquid at the bubble wall
nCs_N2=nPg_initial*(nnn2/ntot)/nKh_N2; %saturated N2 concentration in liquid at the bubble wall
nCs_Ar=nPg_initial*(nnar/ntot)/nKh_Ar; %saturated Ar concentration in liquid at the bubble wall

Length_02=min(sqrt(R*nD_02/abs(Rdot)),R/pi); %diffusion boundary layer O2
Length_N2=min(sqrt(R*nD_N2/abs(Rdot)),R/pi); %diffusion boundary layer N2
Length_Ar=min(sqrt(R*nD_Ar/abs(Rdot)),R/pi); %diffusion boundary layer Ar

dR(4)=-4*pi*R^2*nD_02*(nCs_02-nCi_02)/Length_02;
dR(5)=-4*pi*R^2*nD_N2*(nCs_N2-nCi_N2)/Length_N2;
dR(6)=-4*pi*R^2*nD_Ar*(nCs_Ar-nCi_Ar)/Length_Ar;

A=(ntheta_h20_1/T)/(exp(ntheta_h20_1/T)-1); %h20
B=(ntheta_h20_2/T)/(exp(ntheta_h20_2/T)-1); %h20
C1=(ntheta_h20_3/T)/(exp(ntheta_h20_3/T)-1); %h20
D=(ntheta_n2/T)/(exp(ntheta_n2/T)-1); %n2
E=(ntheta_02/T)/(exp(ntheta_02/T)-1); %o2

AAA=-4*pi*R^2*nD_02*(nCs_02-nCi_02)/Length_02; %rate of change O2
BBB=-4*pi*R^2*nD_N2*(nCs_N2-nCi_N2)/Length_N2; %rate of change N2
CCC=-4*pi*R^2*nD_Ar*(nCs_Ar-nCi_Ar)/Length_Ar; %rate of change Ar
ar_loss=(5/2*nT0-3/2*T)*nKb*nNA*CCC; %energy loss due to Ar diffusion
h20_loss=(8/2*nT0-6/2*T-T*(A+B+C1))*nKb*nNA*Dnh20_DT; %H2O loss
n2_loss=(7/2*nT0-5/2*T-T*(D))*nKb*nNA*BBB; %N2 loss
o2_loss=(7/2*nT0-5/2*T-T*(E))*nKb*nNA*AAA; %O2 loss

dR(7)=DQ_DT/Cv-nPg_initial*vol_dot/Cv+(ar_loss+h20_loss+n2_loss+o2_loss)/Cv;
KZKbubble_dyn = dR;
end
%%%%%%%%%%%%%%%%%%%%%%%%%%%%%%%%%%%%%%%%%%%%%%%%%%%%%%%%%%%%%%%%%%%%%%%%%%%%%%%
```

Appendix C. Camera Experiments

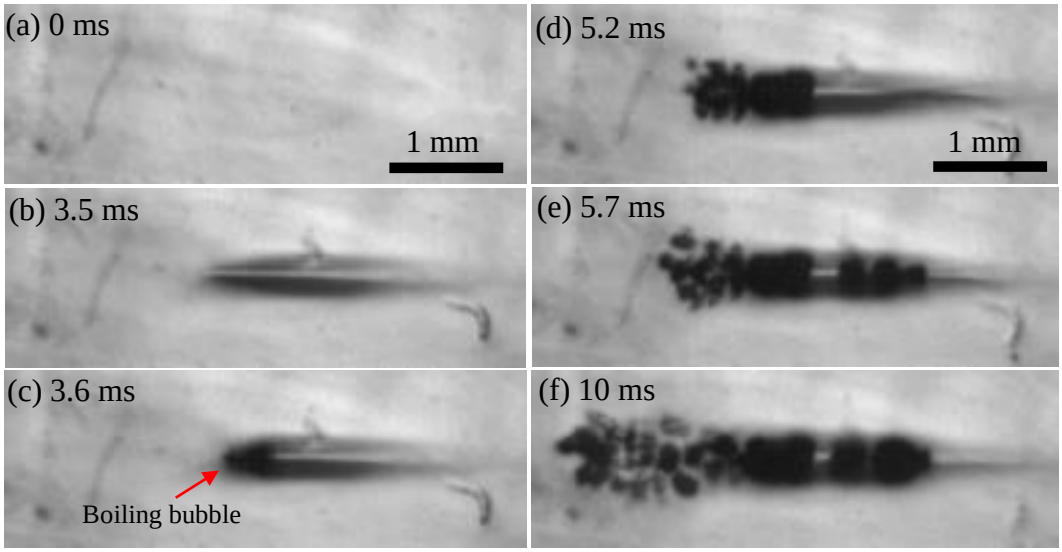

Figure C.1. A sequence of high speed camera images (a)-(f) obtained in an optically transparent tissue phantom during the single 10 ms HIFU insonation with an electrical power of 200W (P_+ = 85.4 MPa; P_- = –15.6 MPa at the HIFU focus). Images were captured at a 15,000 fps. The HIFU beam propagates from left to right. The time at 0 ms corresponds to the start of the HIFU exposure. The corresponding PCD vs time plot as well as its spectrogram are shown in Figure C.2.

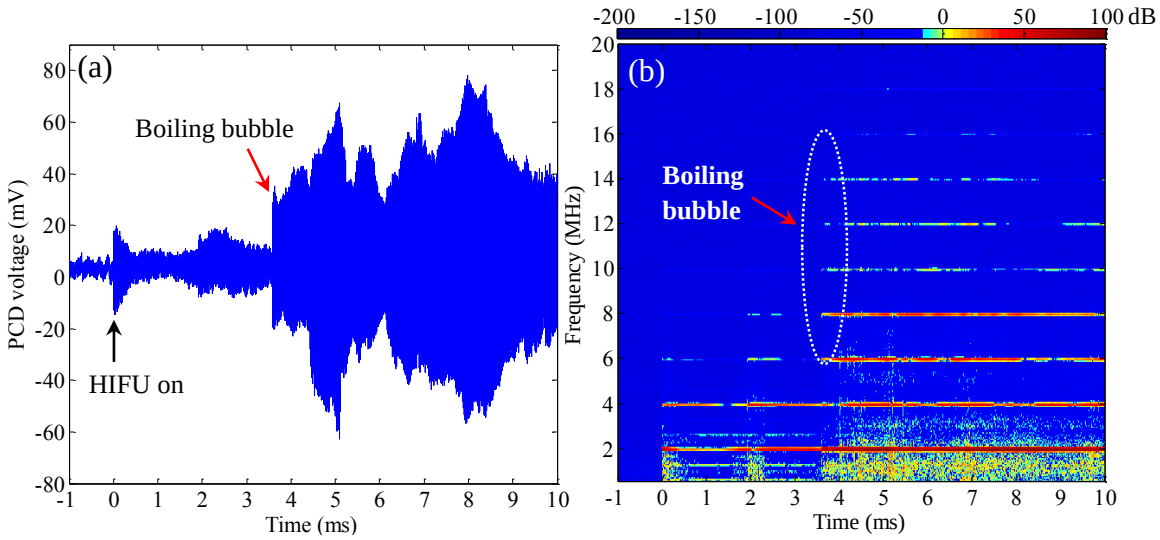

Figure C.2. Acoustic emission emitted at the HIFU focus in the gel during the single 10 ms HIFU pulse. (a) shows the PCD voltage vs time plot and (b) is the corresponding spectrogram. Acoustic emissions were recorded at a sampling rate of 0.5 GHz. The time at 0 ms represents the start of the HIFU insonation.

Appendix D. Journal Paper Reprints